Modelling Catalyst Layers in PEM Fuel Cells: Effects of Transport Limitations and Non-Uniform Platinum Loading

by

David Hans Schwarz
B.Sc., University of Alberta, 1987

A Thesis Submitted in Partial Fulfillment of the
Requirements for the Degree of

MASTER OF APPLIED SCIENCE

in the Department of Mechanical Engineering

Supervisor: Dr. N. Djilali

Abstract

The performance of proton exchange membrane (PEM) fuel cells depends on the composition and structure of the catalyst layers. Experimental observations reveal that state-of-the-art catalyst layers consist of microporous agglomerates of carbon black-supported catalyst sites bound together by polymer electrolyte. In between the agglomerates are macropores which provide pathways for the transport of gaseous reactants. The active surface is limited to the catalyst sites located on the surfaces of the agglomerates in contact with polymer electrolyte. Improving the performance of PEM fuel cells depends on the optimisation of catalyst layer composition and structure for large active surfaces and low transport resistances. This optimisation requires a detailed modelling of the reactions and mass transport in catalyst layers in order to find ways to increase the effectiveness of the catalyst layers for a given precious metal loading.

In this work, three-dimensional, multicomponent and multiphase transport simulations are performed using a new PEM fuel cell implementation (Li & Becker, 2004) in the general purpose commercial computational fluid dynamics (CFD) software package FLUENT™ (Fluent Inc., 2001), which has been further improved by taking into account the detailed composition and structure of the catalyst layers using a multiple thin-film agglomerate model. In this model, it is assumed that thin films of polymer electrolyte and liquid water surround the catalyst sites and, therefore, that the reactants in the gas phase must dissolve into the water and diffuse across both the water and polymer electrolyte

films, before reacting at the catalyst sites on the surfaces of the agglomerates in contact with polymer electrolyte.

From previous modelling studies, it is well known that PEM fuel cell performance is affected by the transport limitations associated with the low concentration of oxygen in air and the restriction of the porous media to gas transport. In the multiple thin-film agglomerate model, there are further transport limitations associated with the thin films of polymer electrolyte and liquid water. The effects of the thin films of polymer electrolyte and liquid water on PEM fuel cell performance are explored by varying the thickness of the thin films in the CFD simulations. It is found that the presence of the thin film of polymer electrolyte has a substantial negative effect on PEM fuel cell performance. For polymer electrolyte films greater than 1000 nm in thickness, current densities become negligible. Also, although the transport limitation associated with the thickness of the thin film of liquid water is found to be small compared to that associated with the thickness of the thin film of polymer electrolyte, the presence of liquid water in the cathode gas diffusion and catalyst layers decreases the volumetric fraction available for the transport of gaseous reactants and has a substantial negative effect on PEM fuel cell performance. As liquid water saturation in the cathode approaches one (i.e. the gas diffusion and catalyst layers are fully flooded) CFD simulations predict that current densities become negligible.

From previous modelling studies, it is also well known that the distribution of electrochemical reactions in the catalyst layers is highly dependent on the complex interaction of activation and ohmic effects as well as the contributions from transport limitations and the variations in local and overall current densities. Available data on catalyst layer composition and structure are used in the CFD simulations to predict reaction rate distributions in the catalyst layers. Based on these results, variations in local catalyst loading are implemented in the CFD simulations for a given precious metal loading in an attempt to improve PEM fuel cell performance. Improved performance is obtained for increased catalyst loading adjacent to the membrane at low and medium current densities. However, in general, PEM fuel cell performance is higher for uniform

catalyst loading. Thus, optimising platinum loading and reducing costs through better catalyst utilisation is accomplished primarily by causing the reaction regions to expand and fill the entire catalyst layers.

Supervisor: Dr. N. Djilali, (Department of Mechanical Engineering)

Table of Contents

List of Tables

List of Figures

Nomenclature

Symbol	Description	Units
$\hat{a}$	Activity of water vapour and liquid water	-
a	Exponent of porosity in effective diffusion coefficients	-
b	Exponent of gas saturation in effective diffusion coefficients	-
b_{H_2}	Exponent of hydrogen concentration in anodic exchange current density	-
b_{O_2}	Exponent of oxygen concentration in cathodic exchange current density	-
c	Concentration of gas	kmol m^{-3}
c_f	Concentration of fixed negative charge sites in dry membrane	kmol m^{-3}
c_i	Concentration of gas species i	kmol m^{-3}
c_i^{ref}	Reference concentration of gas species i	kmol m^{-3}
c_r	Concentration of dissolved reactant r at the catalyst sites located at the inner surface of the thin film of polymer electrolyte	kmol m^{-3}
$c_{r,b}$	Concentration of dissolved reactant r at the outer	kmol m^{-3}

	surface of the thin film of liquid water	
$c_{r,\,mw}$	Concentration of dissolved reactant r at boundary between thin films of polymer electrolyte and liquid water	kmol m^{-3}
c_s	Rate of condensation of water vapour	s^{-1}
c_w	Concentration of liquid water	kmol m^{-3}
$c_{P,\,i}$	Specific heat at constant pressure of gas species i	J $(kg\ K)^{-1}$
$c_{P,\,s}$	Specific heat at constant pressure of solid	J $(kg\ K)^{-1}$
d_{gc}	Side dimensions of gas channels	m
d_i	Driving force for diffusion of species i	m^{-1}
$\hat{D}_{ij}$	Fick's diffusion coefficients for gas species i and j	$m^2\ s^{-1}$
$\hat{D}_{ij}^{\circ}$	Fick's diffusion coefficients for gas species i and j at reference temperature and pressure	$m^2\ s^{-1}$
$\hat{D}_{ij}^{eff}$	Effective Fick's diffusion coefficients for gas species i and j	$m^2\ s^{-1}$
$\mathcal{D}_{ij}$	Stefan-Maxwell binary diffusion coefficients for gas species i and j	$m^2\ s^{-1}$
$\mathcal{D}_{ij}^{\circ}$	Stefan-Maxwell binary diffusion coefficients for gas species i and j at reference temperature and pressure	$m^2\ s^{-1}$
$\mathcal{D}_{ij}^{eff}$	Effective Stefan-Maxwell binary diffusion coefficients for gas species i and j	$m^2\ s^{-1}$
$D_{H^+}^{eff}$	Effective diffusion coefficient for protons in polymer electrolyte	$m^2\ s^{-1}$
D_{λ}	Fick's self-diffusion coefficient for liquid water in polymer electrolyte	$m^2\ s^{-1}$
D_{λ}^{eff}	Effective Fick's self-diffusion coefficient for liquid water in polymer electrolyte	$m^2\ s^{-1}$

$\mathcal{D}_{r\text{-}m}$	Stefan-Maxwell binary diffusion coefficient for reactant r dissolved in polymer electrolyte	$m^2\ s^{-1}$
$\mathcal{D}_{r\text{-}m}^{eff}$	Effective Stefan-Maxwell binary diffusion coefficient for reactant r dissolved in polymer electrolyte	$m^2\ s^{-1}$
$\mathcal{D}_{r\text{-}w}$	Stefan-Maxwell binary diffusion coefficient for reactant r dissolved in liquid water	$m^2\ s^{-1}$
$\mathcal{D}_{r\text{-}w}^{eff}$	Effective Stefan-Maxwell binary diffusion coefficient for reactant r dissolved in liquid water	$m^2\ s^{-1}$
f_r	Fugacity of the reactant r in gas	Pa
$f_{r,w}$	Fugacity of the reactant r dissolved in liquid water	Pa
F	Faraday's constant	$C\ kmol^{-1}$
h	Enthalpy per unit mass of gas	$J\ kg^{-1}$
h_i	Enthalpy per unit mass of gas species i	$J\ kg^{-1}$
h_w	Enthalpy per unit mass of liquid water	$J\ kg^{-1}$
h_{wg}	Latent heat per unit mass of water released due to condensation	$J\ kg^{-1}$
$H_{r,w}$	Henry's law constant for the solubility of the reactant r in liquid water	Pa
i	Current density (i.e. total current produced in PEM fuel cell divided by superficial area of MEA)	$A\ m^{-2}$
$\vec{i}_m$	Superficial current density of protons	$A\ m^{-2}$
$\vec{i}_s$	Superficial current density of electrons	$A\ m^{-2}$
$i_{0,a}$	Exchange current density in anode catalyst layer	$A\ m^{-2}$
$i_{0,c}$	Exchange current density in cathode catalyst layer	$A\ m^{-2}$
$i_{0,a}^{ref}$	Exchange current density in anode catalyst layer at reference concentrations	$A\ m^{-2}$
$i_{0,c}^{ref}$	Exchange current density in cathode catalyst layer at reference concentrations	$A\ m^{-2}$

I	Total current produced in PEM fuel cell	A
$\vec{j}_i$	Diffusive mass flux of gas species i	kg m^{-2} s^{-1}
J	Leverett J-function	-
$\vec{J}_w$	Superficial mass flux of liquid water in polymer electrolyte	kg m^{-2} s^{-1}
k	Thermal conductivity of multicomponent gas	W $(m\ K)^{-1}$
k_i	Thermal conductivity of gas species i	W $(m\ K)^{-1}$
k_s	Thermal conductivity of solid	W $(m\ K)^{-1}$
k_{total}	Total thermal conductivity	W $(m\ K)^{-1}$
k_w	Thermal conductivity of liquid water	W $(m\ K)^{-1}$
l_{gc}	Length of gas channels	m
l_m	Thickness of thin film of polymer electrolyte	m
l_w	Thickness of thin film of liquid water	m
l	Thickness of thin film of gas	m
M	Mean molecular weight of gas	kg $kmol^{-1}$
M_a	Mean molecular weight of gas in anode	kg $kmol^{-1}$
M_c	Mean molecular weight of gas in cathode	kg $kmol^{-1}$
M_{dry}	Equivalent weight of dry polymer electrolyte	kg $kmol^{-1}$
M_i	Molecular weight of species i	kg $kmol^{-1}$
n	Number of species in gas	-
$\vec{N}_i$	Superficial molar flux of species i	kmol m^{-2} s^{-1}
N_r	Molar flux of dissolved reactant r	kmol m^{-2} s^{-1}
$N_{r,m}$	Molar flux of dissolved reactant r in thin film of polymer electrolyte	kmol m^{-2} s^{-1}
$N_{r,w}$	Molar flux of dissolved reactant r in thin film of liquid water	kmol m^{-2} s^{-1}
P	Pressure of gas	Pa or atm
P°	Reference pressure	Pa or atm

P_c	Capillary pressure	Pa
P_f	Pressure of fluid f	Pa
P_i	Pressure of gas species i	Pa or atm
P_{sat}	Saturation pressure	Pa or atm
P_w	Pressure of liquid water	Pa
$\vec{q}$	Conductive heat flux	$W\ m^{-2}$
Q_a	Mass flow rate of multicomponent gas at inlet of anode gas channel	$kg\ s^{-1}$
Q_c	Mass flow rate of multicomponent gas at inlet of cathode gas channel	$kg\ s^{-1}$
r_m	Rate of mass condensation per unit volume due to phase change of water vapour into liquid water in polymer electrolyte	$kg\ m^{-3}\ s^{-1}$
r_w	Rate of mass condensation per unit volume due to phase change of water vapour into liquid water	$kg\ m^{-3}\ s^{-1}$
R	Gas constant	$J\ (kmol\ K)^{-1}$
RH	Relative humidity of gas	%
s	Saturation of liquid water	-
s_{im}	Immobile saturation of liquid water	-
s_f	Saturation of fluid f	-
$s_{g,\,im}$	Immobile saturation of gas	-
s_{mea}	Superficial area of MEA	m^2
$\vec{S}$	Rate of momentum production of gas per unit volume	$N\ m^{-3}$
S_f	Rate of mass production of fluid f per unit volume	$kg\ m^{-3}\ s^{-1}$
S_g	Rate of mass production of gas per unit volume	$kg\ m^{-3}\ s^{-1}$
S_h	Rate of heat production per unit volume	$W\ m^{-3}$

S_i	Rate of mass production of gas species i per unit volume	kg m^{-3} s^{-1}
S_s	Electronic current production per unit volume	A m^{-3}
S_m	Protonic current production per unit volume	A m^{-3}
S_w	Rate of mass production of liquid water per unit volume	kg m^{-3} s^{-1}
t_{cl}	Thickness of catalyst layers	m
t_{gdl}	Thickness of gas diffusion layers	m
t_m	Thickness of membrane	m
T	Temperature	K or °C
T°	Reference temperature	K
$\vec{v}$	Superficial velocity of gas	m s^{-1}
$\vec{v}_f$	Superficial velocity of fluid f	m s^{-1}
$\vec{v}_i$	Superficial velocity of species i	m s^{-1}
$\vec{v}_m$	Superficial velocity of liquid water in polymer electrolyte	m s^{-1}
$\vec{V}$	Intrinsic velocity of liquid water	m s^{-1}
V_i	Molecular diffusion volume of species i	-
V_i	Volume fraction of species i	-
V_{oc}	Open-circuit potential	V
x	Coordinate in x-direction	m
x_i	Mole fraction of gas species i	-
x_r	Mole fraction of reactant r in gas	-
$x_{r,w}$	Mole fraction of reactant r dissolved in liquid water	-
y	Coordinate in y-direction	m
y_i	Mass fraction of gas species i	-
y_r	Mass fraction of reactant r in gas corresponding to	-

	concentration of dissolved reactant at the catalyst sites located at the inner surface of the thin film of polymer electrolyte	
$y_{r,b}$	Mass fraction of reactant r in gas at boundary with thin film of liquid water	-
z	Coordinate in z-direction	m
z_i	Ionic charge number of species i	-
$\alpha_{a,a}$	Anodic transfer coefficient in anode catalyst layer	-
$\alpha_{a,c}$	Anodic transfer coefficient in cathode catalyst layer	-
$\alpha_{c,a}$	Cathodic transfer coefficient in anode catalyst layer	-
$\alpha_{c,c}$	Cathodic transfer coefficient in cathode catalyst layer	-
β	Fraction of change in enthalpy of formation in Reaction (1.3) released as heat in cathode catalyst layer	-
γ	Surface tension between liquid water and gases	N m^{-1}
γ_r	Fugacity coefficient of reactant r in gas phase	-
Γ	Tortuosity factor	-
$\Delta c_{r,m}$	Change in concentration of dissolved reactant r in thin film of polymer electrolyte	kmol m^{-3}
$\Delta c_{r,w}$	Change in concentration of dissolved reactant r in thin film of liquid water	kmol m^{-3}
$\Delta \bar{g}_f^\circ$	Change in Gibbs free energy of formation in Reaction (1.3) at operating temperature and reference pressure	J $kmol^{-1}$
$\Delta \bar{h}_f^\circ$	Change in enthalpy of formation in Reaction (1.3) at operating temperature and pressure	J $kmol^{-1}$
$\Delta \bar{s}_a^\circ$	Change in entropy in Reaction (1.1) at reference temperature and pressure	J (kmol K)$^{-1}$

$\Delta\bar{s}_c^\circ$	Change in entropy in Reaction (1.2) at reference temperature and pressure	J (kmol K)$^{-1}$
ζ_a	Stoichiometric flow rate at inlet of anode gas channel	-
ζ_c	Stoichiometric flow rate at inlet of cathode gas channel	-
η_a	Activation overpotential in anode catalyst layer	V
η_c	Activation overpotential in cathode catalyst layer	V
θ	Contact angle of liquid water in porous medium	°
κ	Permeability of porous medium	m^2
κ_f	Permeability of porous medium to fluid f	m^2
$\kappa_{r,f}$	Relative permeability of porous medium to fluid f	m^2
λ	Concentration of liquid water divided by the concentration of fixed negative charge sites in the polymer electrolyte	-
μ_i	Chemical potential of species i	J kmol^{-1}
$\bar{\mu}_i$	Electrochemical potential of species i	J kmol^{-1}
μ	Viscosity of multicomponent gas	kg (m s)$^{-1}$
μ_f	Viscosity of fluid f	kg (m s)$^{-1}$
μ_i	Viscosity of gas species i	kg (m s)$^{-1}$
μ_w	Viscosity of liquid water	kg (m s)$^{-1}$
ξ	Active surface area per unit volume in catalyst layers	m^{-1}
ρ	Density of gas	kg m^{-3}
ρ_{dry}	Density of dry polymer electrolyte	kg m^{-3}
ρ_f	Density of fluid f	kg m^{-3}
ρ_i	Density of gas species i	kg m^{-3}
ρ_s	Density of solid	kg m^{-3}

ρ_w	Density of liquid water	kg m^{-3}
σ_{ij}	Diffusion collision diameter for species i and j	Å
σ_m	Electrical conductivity of protons in polymer electrolyte	S m^{-1}
σ_m^{eff}	Effective electrical conductivity of protons	S m^{-1}
σ_s^{eff}	Effective electrical conductivity of electrons	S m^{-1}
τ	Tortuosity	-
τ	Viscous stress tensor	Pa
ϕ_m	Electrical potential in polymer electrolyte	V
ϕ_s	Electrical potential in solid	V
φ	Porosity	-
φ_{cl}	Porosity of catalyst layers	-
φ_f	Volumetric fraction of fluid f	-
φ_{gdl}	Porosity of gas diffusion layers	-
$\varphi_{C/Pt}$	Volumetric fraction of carbon in gas diffusion layers and carbon and platinum in catalyst layers	-
φ_m	Volumetric fraction of polymer electrolyte	-
φ_w	Volumetric fraction of liquid water in polymer electrolyte	-
Φ_{ij}	Dimensionless quantities in semiempirical formulas for viscosities and thermal conductivities of multicomponent gases	-
$\Omega_{D,ij}$	Diffusion collision integral for species i and j	-

Acknowledgements

This thesis would not have been possible without the help and encouragement of various people. In this regard, I would first like to thank my supervisor, Ned Djilali, for his support and guidance, and especially for agreeing to take on another student and securing financial support from the University of Victoria and the Department of Mechanical Engineering. Also, I would like to thank the other professors, post-doctoral fellows and students in the Department of Mechanical Engineering for many useful discussions. In this regard, a special thanks to Jay Sui for allowing numerous interruptions to his work.

Sue Walton and Lawrence Pitt at IESVic deserve much credit for creating a great environment in which to work and socialise. I would also like to thank the office staff in the Department of Mechanical Engineering for all their assistance. I acknowledge the support of the staff at Fluent Inc., who provided me with training and technical assistance, and Goncalo Pedro in the UVic CFD Lab for maintaining the computing facilities and providing help.

Thanks go out to all my good friends in the Department of Mechanical Engineering, who have provided me with such an excellent support network. Special thanks to my office-mates Ruth, Jeff and David, and also to Matt for taking over the organisation of "IESVic Fridays". Finally, I acknowledge my life-long partner, Susan Skone, without whose support this thesis would not have been possible.

Chapter 1

Proton Exchange Membrane Fuel Cells

Proton exchange membrane (PEM) fuel cells operate at relatively low temperatures (i.e. below 100 °C), yielding quick start-up times, and also have the potential for achieving high performances with respect to energy efficiencies, power densities and lifetimes. It is for these reasons that PEM fuel cells are being considered as power sources for transportation, small-scale power generation and portable power applications. Another advantage of PEM fuel cells is the use of a solid polymer as an electrolyte for the transport of protons, which reduces both manufacturing and safety complications. However, in order for PEM fuel cells to reach commercialisation, technological advances must still be achieved in various areas of fuel cell design, with the goal of reducing costs and increasing performance.

1.1 Introduction

Figure 1.1 shows a typical design for a single PEM fuel cell, which is placed in series with other fuel cells to form a stack.

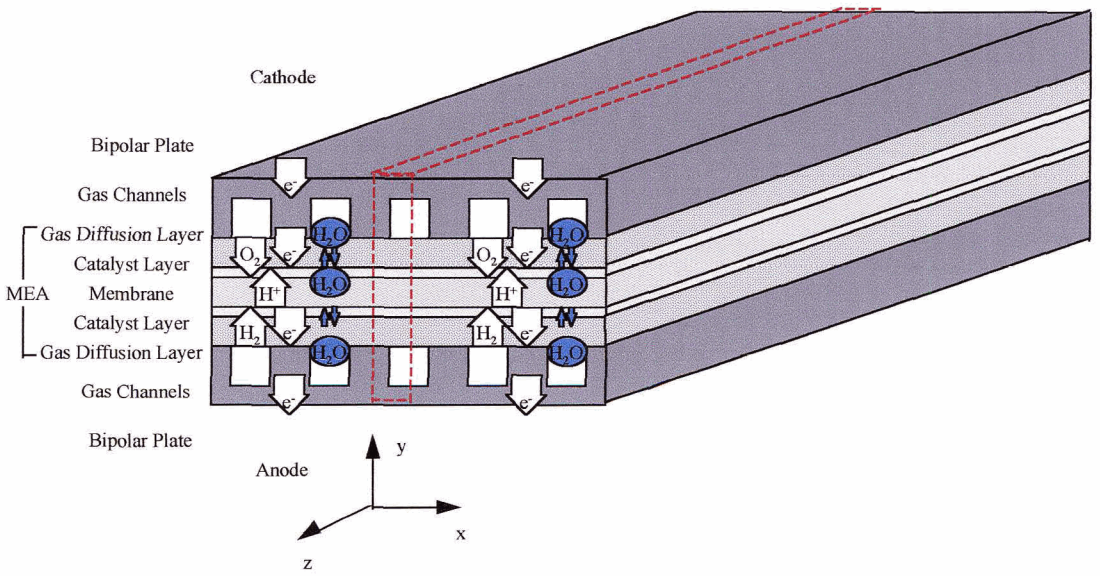

Figure 1.1 - Proton exchange membrane fuel cell.

As can be seen in Figure 1.1, numerous gas channels are made in solid graphite bipolar plates. Fuel composed of humidified hydrogen or hydrogen-rich reformate (produced from carbon feedstocks) on the anode side and oxidant composed of humidified oxygen or air on the cathode side flow through the gas channels, while the highly conductive bipolar plates are responsible for transporting electrons. The bipolar plates also serve as mechanical supports and are corrosion resistant. The gas channels and bipolar plates contact the backing surfaces of a membrane-electrode assembly (MEA), which is composed of porous gas diffusion electrodes with gas diffusion and catalyst layers located on either side of a solid polymer electrolyte membrane separating the anode and cathode sides of the fuel cell. The membrane is composed of perfluorosulphonic acid (PFSA) polymer, the most common of which is Nafion®, the registered trademark of DuPont.

In the catalyst layers, Reactions (1.1) and (1.2), which are electrochemical in nature, occur at catalyst sites in the anode and cathode, respectively, as a result of adsorption of

the reactants and conversion to and desorption of the products by the catalyst surface, yielding Reaction (1.3) for the overall fuel cell.

$$2H_2 + \rightarrow 4H^+ + 4e^- \quad (1.1)$$

$$O_2 + 4H^+ + 4e^- \rightarrow 2H_2O \quad (1.2)$$

$$2H_2 + O_2 \rightarrow 2H_2O \quad (1.3)$$

Reactions (1.1) and (1.2) are commonly referred to as the hydrogen oxidation and oxygen reduction reactions, respectively. In order for Reaction (1.1) to occur, hydrogen must be transported through the anode from the gas channels into the gas diffusion and catalyst layers via the gas diffusion layer surfaces in contact with the gas channels. The product electrons are transported in the opposite direction from the catalyst layer to the bipolar plate through the gas diffusion layer surfaces in contact with the bipolar plate. In order for Reaction (1.2) to occur, oxygen must be transported through the cathode from the gas channels into the gas diffusion and catalyst layers, while the product protons from Reaction (1.1) in the anode are transported through the solid polymer electrolyte membrane to the cathode catalyst layer. Electrons from Reaction (1.1) are simultaneously transported through the cathode from the bipolar plate to the catalyst layer. In a stack, each bipolar plate serves as both an anode and a cathode in adjacent fuel cells. However, in a single fuel cell the bipolar plates are connected through an external circuit. In both cases the bipolar plates act as conduits for electron transport from the anode to the cathode. Finally, the product water from Reaction (1.2) must be transported from the cathode catalyst layer to the gas channels in the form of water vapour and/or liquid water and out of the fuel cell.

Figure 1.2 shows a typical design for one side of a PEM fuel cell MEA, composed of a porous gas diffusion electrode, with substrate, diffusion and catalyst (or active) layers, and a solid polymer electrolyte membrane.

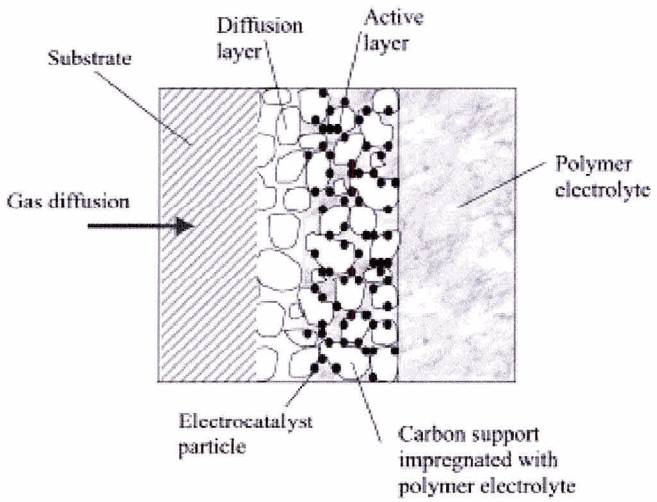

Figure 1.2 - One side of a PEM fuel cell MEA (Costamagna & Srinivasan, 2001b).

The main purpose of the substrate or backing layer in porous gas diffusion electrodes is to provide mechanical support. A hydrophobic (i.e. wet-proofed) carbon cloth or paper commonly serves as the substrate. The carbon cloth or paper is wet-proofed by coating it with polytetrafluoroethylene (PTFE) which is extremely hydrophobic. PTFE is also sold as Teflon®, the registered trademark of DuPont.

A mix of high surface area carbon black particles (about 20 - 40 nm in size) and PTFE is generally applied to one side of the wet-proofed carbon cloth or paper, partially penetrating and filling the open spaces of the carbon cloth or paper, and forming a porous diffusion layer on the substrate. In this case, the PTFE not only provides wet-proofing, but also binds the high surface area carbon black particles into a cohesive layer. A final layer consisting of catalysed carbon black (i.e. platinum catalyst grains, 2 - 4 nm in size, supported on high surface area carbon black particles), with or without PTFE, is then deposited on the diffusion layer, although this catalyst layer can also be deposited on the membrane. The catalyst layer is also impregnated with polymer electrolyte in order to provide a continuous pathway of polymer electrolyte to the membrane for the transport of protons. Thus the electrode is composed of three layers (i.e. a wet-proofed carbon cloth

or paper partially impregnated with carbon black and PTFE, a diffusion layer composed of carbon black and PTFE, and a catalyst layer), although it is normally assumed that there are only two (i.e. substrate/diffusion and catalyst) layers. The thickness of the substrate/diffusion (or gas diffusion) layer is normally about 200 - 400 μm, while the thickness of the catalyst layer is 100 μm or less, with state-of-the-art catalyst layers closer to 10 μm (Costamagna & Srinivasan, 2001b).

The gas diffusion layers of porous gas diffusion electrodes consist of a matrix of carbon black solid, which forms an interconnected network for the conduction of electrons surrounded by PTFE (which is an electronic insulator), and voids or pores between the matrix, which provide pathways for the transport of gases and liquid water. Catalyst layers consist of a matrix of catalysed carbon black solid, which forms an interconnected network for the conduction of electrons, and polymer electrolyte, which provides continuous pathways inside the pores for the transport of protons and is also an electronic insulator. However, depending on the degree of impregnation of polymer electrolyte, the voids or pores between the catalysed carbon black particles can be entirely filled with polymer electrolyte, as shown in Figure 1.2, or some of the pores can be open. Also, depending on whether or not the catalyst layers have been wet-proofed with PTFE, open pores can be filled with gas or liquid water. Thus, in the catalyst layers the transport of reactants can be through gas, liquid water or polymer electrolyte phases, where the resistance to reactant transport is significantly less through the gas phase than through either the liquid water or polymer electrolyte phases.

Even though the structures of the gas diffusion and catalyst layers are obviously very complicated, they are usually described as continuous media with effective transport parameters, electron conductivities, and (in the case of the catalyst layers) proton conductivities. Also, it is usually assumed that the polymer-electrolyte and uncatalysed or catalysed carbon black solid matrix phases have their own electrical potentials, which govern the transport of protons in the catalyst layers and electrons in the gas diffusion or catalyst layers, respectively. The differences between these potentials in the catalyst layers,

which are called activation overpotentials, are responsible for driving Reaction (1.1) in the anode and Reaction (1.2) in the cathode from equilibrium in order to consume or produce electrical currents of protons and electrons. The kinetics of Reactions (1.1) and (1.2) in the catalyst layers depend on the available surface area of catalyst and the concentrations of reactants at the catalyst sites. The reactant concentrations depend in turn on the complicated transport of the reactants from the gas channels to the catalyst sites.

The performance of PEM fuel cells is strongly dependent on reaction kinetics and therefore also on the transport of reactants. In general, performance losses in PEM fuel cells occur mainly at the catalyst layers, where the irreversible nature of the reactions causes activation overpotentials and transport limitations are important at high reaction rates. In PEM fuel cells, the slow kinetics (i.e. reaction rate) associated with Reaction (1.2) causes considerably higher activation overpotentials in the cathode catalyst layer compared with the anode catalyst layer (where Reaction (1.1) has much faster kinetics). However, poisoning of catalyst sites by carbon monoxide present in the fuel stream due to reforming can increase activation overpotentials in the anode catalyst layer. In general, the majority of performance losses associated with transport limitations occur in the cathode. The low concentration of oxygen in air (since air is primarily used as the oxidant stream), the restriction of the porous media to gas transport, and the formation of water in Reaction (1.2) which floods the catalyst sites, all result in substantial losses in the cathode due to transport limitations, particularly at high reaction rates. These so called concentration overpotentials can be partially overcome by pressurising the reactant gas stream at the cathode, which improves the kinetics of Reaction (1.2) and enhances oxygen transport.

The performance of a PEM fuel cell can be illustrated by plotting voltage versus current density (i.e. current divided by the projected area of the catalyst layers parallel to the gas diffusion/catalyst layer interfaces), or a polarisation curve. Figure 1.3 shows a typical polarisation curve for a PEM fuel cell.

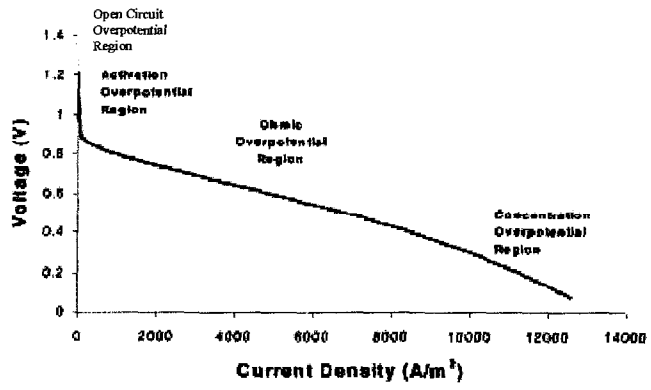

Figure 1.3 - Polarisation curve for a PEM fuel cell (after Baschuk & Li, 2000).

The polarisation curve can be divided into four regions characterised by open circuit, activation, ohmic and concentration overpotentials. In the first region at open circuit (i.e. zero current density), the electrical potential departs from its reversible value of approximately 1.2 V due to the extremely poor kinetics of Reaction (1.2), which allows competing reactions (i.e. oxide formation and the oxidation of organic impurities) to occur preferentially, thus setting up a mixed potential of about 1.0 - 1.12 V for the fuel cell (Parthasarathy et al., 1992). At low current densities after open circuit, behaviour of the polarisation curve is semi-exponential, being determined by the activation overpotential of Reaction (1.2) in the cathode. As the current density increases, activation overpotential also increases. However, in the ohmic overpotential region, activation losses increase at a slower rate than ohmic losses (which behave linearly) and, as a result, the overall behaviour becomes linear. Ohmic losses are due to a number of factors, including resistance to the transport of electrons in the solid matrix of the gas diffusion and catalyst layers and, to a lesser degree, in the bipolar plates. In general, however, ohmic losses are primarily due to resistance to the transport of protons in the polymer electrolyte of the catalyst layers and membrane.

Finally, at high current densities, limitations in oxygen transport become dominant (i.e. the rate at which oxygen can be supplied becomes limited), causing the concentration of oxygen to decrease at catalyst sites in the cathode. This lack of oxygen limits the rate of Reaction (1.2), resulting in a steep increase in concentration overpotential and a rapid decrease in potential with increasing current density, as shown in Figure 1.3. The limitations in oxygen transport are primarily due to the production of water in the cathode catalyst layer causing flooding, which blocks the transport of oxygen. In general, limitations in oxygen transport are far worse when air rather than oxygen is used as the oxidant, because the accumulation of nitrogen in the pores of the cathode leads to the formation of an additional barrier for oxygen transport.

In order to improve the performance of PEM fuel cells, it is thus necessary to reduce the overpotential encountered at open circuit and the activation overpotential in the cathode. Although this can be done by increasing the operating pressure to about 3 - 5 atm, which increases the open circuit potential, compression has an associated energy penalty. Reducing the activation overpotential can be done by significantly enhancing the kinetics of Reaction (1.2) (i.e. through an increase in the available catalyst surface area). Also, minimising the ohmic overpotential losses (due primarily to proton transport through polymer electrolyte) is vital for attaining high power densities in PEM fuel cells. Finally, transport problems need to be addressed in the design of PEM fuel cells.

Other areas of concern for PEM fuel cells are water and thermal management. These are strongly interrelated because water management is dependent on the equilibrium of water between its gas and polymer-electrolyte phases, which in turn depends strongly on the temperature. The polymer electrolyte in the catalyst layers and membrane of PEM fuel cells needs to be well-hydrated in order to maintain sufficient proton transport for satisfactory fuel cell performance. However, for fuel cells operating close to 100 °C (higher operating temperatures are desirable in order to improve the kinetics of Reaction (1.2) and minimise oxygen transport limitations), evaporative losses become significant and the polymer electrolyte tends to dry out, increasing the resistance to proton transport.

Thus a major problem with PEM fuel cells is maintaining hydration of the polymer electrolyte in the membrane and catalyst layers, and in order to reduce the water carried away by exiting gases due to evaporation, the reactant gas streams must be adequately humidified.

A conflicting problem is that water formed at the cathode can cause flooding. This effect is enhanced by the migration of protons through the membrane due to the attraction between the polar water molecules and the protons. This attraction results in the transport of water though the membrane from the anode to the cathode, an effect which is proportional to the current density and is called electro-osmotic drag. At low current densities, the concentration gradient set up in the MEA due to the production of water at the cathode and the electro-osmotic drag is sufficiently high such that diffusion from the cathode to the anode balances the electro-osmotic drag. However, at high current densities, the transport of water due to electro-osmotic drag occurs at a rate greater than that at which it can be restored by diffusion. Thus, for maximum water retention, differential pressurisation (i.e. higher pressure on the cathode side than on the anode side) needs to be applied during operation of the PEM fuel cell in order to balance the electro-osmotic drag by convective flow.

Finally, even though PEM fuel cells are very efficient systems, at high current densities approximately 50 % of the power produced is dissipated as heat. This loss of electrochemical power is due to ohmic heating and the irreversible heat generation associated with the activation overpotentials, together with the reversible heat generation, of Reactions (1.1) and (1.2). This heat has to be removed from the fuel cell to prevent the polymer electrolyte from drying out. The two main methods of removing heat are air-cooling and liquid-cooling. Because of the small temperature differential between the fuel cell and its surroundings, the use of air-cooling is satisfactory only at low current densities, and at high current densities liquid-cooling is found to be necessary.

1.2 Catalyst Layers

In general, the performances of PEM fuel cells are strongly influenced by the catalyst layers, including the processes involved in the manufacturing of the catalyst layers and the compositions of catalyst, carbon black support, PTFE and polymer electrolyte used in the various manufacturing methods. No matter what manufacturing method and compositions are used in the preparation of catalyst layers, the fundamental goal is to achieve good contact between polymer electrolyte and the catalyst sites for the transport of protons, while creating a matrix of catalysed carbon black solid for the transport of electrons and open pores for the transport of reactants. Thus the performance of PEM fuel cells is significantly influenced by the structure of the catalyst layers. In general, differences in manufacturing methods and compositions manifest themselves as differences in catalyst layer structure; it is therefore important to understand the relationships between manufacturing methods and the compositions and structures of catalyst layers in order to maximise PEM fuel cell performances. Finally, in the catalyst layers, the nature of the processes involved in the transport of reactants to the catalyst sites depends on the structures of the catalyst layers.

1.2.1 Manufacturing

Kumar et al. (1995) outlined a typical manufacturing process for PEM fuel cell catalyst layers and associated MEA in the 1980s and early 1990s. First a substrate was prepared by wet-proofing carbon cloth or paper with PTFE emulsion. Next, a diffusion layer consisting of carbon black particles and PTFE was applied to the substrate by a spraying technique. Finally, a catalyst layer was applied to the diffusion layer by spraying it with a slurry of carbon-black supported platinum and PTFE. The gas diffusion and catalyst layers were then compacted and sintered. The catalyst layers thus prepared were then impregnated with polymer electrolyte solution before hot pressing gas diffusion and catalyst layers to

either side of a membrane to form an MEA. Kumar et al. (1995) noted that a wide variation in PEM fuel cell performance could be attained using catalyst layers with the same compositions if the manufacturing method was altered, for instance by changing the compaction and sintering processes, which effects the structure of the catalyst layers.

Since the late 1990s, two modes of preparing and applying catalyst layers during MEA fabrication have been employed, with the catalyst layers deposited either on the gas diffusion layers, followed by membrane addition, or on the membrane followed by gas diffusion layer additions. In both cases, the catalyst layers are either prepared first and then applied or, alternatively, formed during application. Also, in both cases the final step is hot pressing the membrane, catalyst layers, and gas diffusion layers to form an MEA.

Methods for catalyst layer preparation and application to a gas diffusion layer include spreading, spraying, powder deposition, impregnation and electro-deposition (Mehta & Cooper, 2003). Spreading consists of preparing a catalysed carbon black and PTFE dough by mechanical mixing, and then rolling the dough on a wet-proofed carbon cloth or paper using a heavy stainless steel cylinder. Spraying consists of preparing an active dispersion of catalysed carbon black suspended in a mixture of water, alcohol and solubilised PTFE and polymer electrolyte, and then repeatedly spraying and sintering the mixture onto wet-proofed carbon cloth or paper, followed by a final rolling step. The sintering prevents the re-dissolving of components into the next layer, while rolling produces a structure with lower porosity, but greater mechanical strength. In catalyst powder deposition, catalysed carbon black, PTFE and polymer electrolyte powder are mechanically mixed and then applied onto wet-proofed carbon cloth or paper, followed by rolling and sintering. In the impregnation method, the catalyst layer is brushed with polymer electrolyte solubilised in a mixture of alcohol and water. Alternatively, catalysed carbon black, PTFE and polymer electrolyte are pre-mixed in alcohol and water, and the resulting solution is brushed on the gas diffusion layer. Electro-deposition involves impregnation of a porous gas diffusion layer with polymer electrolyte, in which the usual cations have been exchanged for a cationic complex of platinum, followed by electro-deposition of platinum from this

complex onto the carbon black/PTFE matrix of the gas diffusion layer. This results in deposition of platinum only at sites that are accessed effectively by both polymer electrolyte and carbon black.

Methods for catalyst layer preparation and application to a membrane include evaporative deposition, dry spraying, catalyst decaling and painting (Mehta & Cooper, 2003). In evaporative deposition, a catalyst metal salt is evaporatively deposited onto a membrane from an aqueous solution. After deposition of the salt, metallic platinum is produced through a reduction of the metal salt by immersion of the entire membrane in a solution of $NaBH_4$. In dry spraying, catalysed carbon black, PTFE, and polymer electrolyte powder are mixed, then atomised and sprayed directly onto the membrane, with the layer fixed by either hot pressing or rolling. The catalyst decaling method involves the preparation of an ink, by thoroughly mixing catalysed carbon black and solubilised polymer electrolyte, for casting onto a PTFE blank and transfer to the membrane by hot pressing. After the blank is peeled away, a thin catalyst layer is left on the membrane. Alternatively, ink is painted directly onto a membrane, which is then baked to dry the ink.

Sputtering can also be used as a single step option for catalyst layer preparation and application to either the gas diffusion layer or membrane (Mehta & Cooper, 2003). In this method, a thin layer of platinum metal catalyst is sputter deposited onto the gas diffusion layer or membrane and then rolled. To enhance the performance, a mixture of carbon black powder and solubilised polymer electrolyte is brushed on the catalyst, then dried, before sputter depositing another layer of catalyst.

1.2.2 Composition

Differences in compositions of catalyst, carbon black support, PTFE and polymer electrolyte used in the manufacturing of catalyst layers have large effects on PEM fuel cell performance. Also, the compositions of catalyst layers influence their structure, and the

performance of PEM fuel cells are in turn influenced by the structure of the catalyst layers. Thus it is important to understand the relationship between catalyst layer compositions and structure, and their influence on fuel cell performance, in order to optimise the compositions of catalyst layers.

1.2.2.1 Catalyst

In PEM fuel cells, platinum or platinum alloys provide the best catalytic activity (i.e. the smallest activation overpotentials) for both Reaction (1.1) at the anode and Reaction (1.2) at the cathode. Unfortunately, platinum is prohibitively expensive, and in order to reduce the costs associated with PEM fuel cells, platinum loading (i.e. the amount of platinum) in catalyst layers must be decreased while performance is maintained or improved. In this regard, it is of vital importance to attain higher utilisations of the available surface area of catalyst, thereby improving performance, through optimisation of the composition and structure of the catalyst layers.

Until the 1980s, satisfactory PEM fuel cell performance was only attained using pure platinum particles (10 - 20 nm in size) as catalysts in the active layers of porous gas diffusion electrodes with high platinum loadings of 4 mg cm^{-2} (Costamagna & Srinivasan, 2001a). Later, in the 1980s and 1990s, improvements in catalyst layer design allowed the same level of performance to be attained for electrodes with much lower platinum loadings of 0.4 mg cm^{-2} (Ticianelli et al., 1988a; b). The first of these design improvements was the use of smaller platinum grains (2 - 4 nm in size) supported on high surface area carbon black particles. This allowed for a higher degree of platinum dispersion (i.e. for identical platinum loadings, more small platinum grains are preferable to less large grains since the overall catalyst surface area increases, improving platinum utilisation and therefore performance). Also, a reduction in the thickness of the catalyst layers from 100 to 50 to 25 μm was attained by using platinum grains supported on carbon black with platinum weight percentages of 10, 20 and 40 wt %, respectively, while maintaining the same platinum

loading of 0.4 mg cm^{-2} (and therefore similar activation overpotentials) by decreasing the amount of carbon black. This decrease in the thickness of the catalyst layers significantly improved the performance of PEM fuel cells by reducing concentration and ohmic overpotentials, particularly at high current densities, due to improved supply of reactant gases and protons to catalyst sites through shorter pathways in the catalyst layers. Fuel cell performance was also increased by applying some of the total platinum loading as a sputtered film on the surface of the catalyst layers in contact with the membrane, thereby reducing the ohmic overpotential associated with the transport of protons by providing a higher concentration of catalyst sites closer to the membrane.

Another improvement in catalyst layer design was due to extension of the three-dimensional reaction zone by impregnating catalyst layers (containing carbon-black supported platinum and PTFE) with solubilised polymer electrolyte through a brushing process, in an attempt to partially fill the catalyst layers with polymer electrolyte (Ticianelli et al., 1988a; b). This process overcame fuel cell performance problems related to lack of protonic access to the majority of catalyst sites not in intimate contact with the membrane. Nevertheless, the inability of the impregnation technique to effectively access all of the catalyst sites in the active layer since polymer electrolyte was found to a depth of only about 10 μm (Ticianelli et al., 1991), resulted in low catalyst utilisations of 5 - 25 %. Finally, improvements in fuel cell performance were also attained by hot pressing MEAs in order to obtain a good contact between the electrodes and membrane, improving electron and proton conductivity across the interface and minimising ohmic overpotentials.

The highly porous catalyst layers obtained through typical MEA fabrication processes in the 1980s and 1990s enabled a better dispersion of platinum catalyst than the pure platinum catalyst layers employed previously, and a more favourable structure was created for the transport of gaseous reactants. However, the low catalyst utilisations allowed for further reductions in platinum loading, and also for further improvements in fuel cell performance, by reducing the thickness of catalyst layers with even higher platinum utilisations in the mid 1990s. It was at this time that high performances of PEM fuel cells

with even lower platinum loadings of 0.1 mg cm^{-2} for the cathode and 0.05 mg cm^{-2} for the anode were achieved by very thin catalyst layers, on the order of 10 μm and 5 μm, respectively (Wilson et al., 1995; Escribano & Aldebert, 1995). These catalyst layers were composed of highly intermixed carbon-black supported platinum and polymer electrolyte, with or without PTFE, deposited on either the gas diffusion layers or either side of a supported membrane, before hot-pressing the electrodes and supported membrane to form a MEA. The supported membranes were prepared by impregnation of polymer electrolyte into microporous PTFE mesh. The recast film of polymer electrolyte in the supported membrane resulted in a higher protonic conductivity and better mechanical strength than that of commercial polymer electrolyte film.

In contrast to typical catalyst layers in the 1980s and 1990s, the thin-film catalyst layers can contain no PTFE, although the presence of polymer electrolyte similarly binds the carbon-black supported platinum into a cohesive layer. In general, the increased content of polymer electrolyte (and therefore higher platinum catalyst utilisations) allows for small thicknesses of the catalyst layers, which greatly minimises the concentration and ohmic overpotentials. In general, the thin-film catalyst layers have shown the best PEM fuel cell performances to date, and high utilisations of platinum in the range 45 - 60 % can be obtained for these catalyst layers (Costamagna & Srinivasan, 2001a). This is essential in regards to reducing the loading, and hence the cost, of platinum in PEM fuel cells. With such high utilisations currently achievable, further reductions in platinum loading seem unlikely in future and are also no longer necessary since, for the required amounts, platinum is no longer cost-prohibitive for developing PEM fuel cells.

1.2.2.2 Carbon Black

Uchida et al. (1996) investigated the effects of the structure of the carbon black particles used to support the platinum catalyst grains on the structure of catalyst layers and the corresponding performance of PEM fuel cells. This was done by preparing supported

platinum catalyst using various electron-conducting carbon black particles with different surface areas, but at the same concentrations and platinum loadings. The carbon black particles were produced either by the oil-furnace process or the acetylene process. The surface area and pore volume distribution of the carbon black particles were measured by a nitrogen adsorber, while the platinum grain size and platinum surface area of the catalysed carbon black were measured by a carbon monoxide adsorber. Catalyst layers were then prepared using a mixture of catalysed carbon black and an optimal amount of polymer electrolyte colloidal solution. As a result of cross-linking among the polymer electrolyte chains adsorbed on the carbon black supports by ultrasonic treatment, the mixture was transformed into a paste, which was then spread over a wet-proofed carbon paper gas diffusion layer. The pore-volume distributions of the resulting catalyst layers with the various carbon black particles were measured using mercury porosimetry. The resulting electrodes were finally hot-pressed on both sides of a polymer electrolyte membrane and PEM fuel cell performance tests were performed using humidified hydrogen and oxygen as the reactant gases.

The mercury porosimetry measurements showed that the pore-volume distribution of the catalyst layers is significantly affected by the type of carbon black support. Catalyst layers with acetylene carbon black particles have a larger porosity than those with oil-furnace carbon black particles. This is because the adsorption of polymer electrolyte by acetylene carbon black particles is greater than that by oil-furnace carbon black particles, resulting in better binding in the catalyst layer and also increased contact between proton-conducting polymer electrolyte and catalyst sites on the carbon black particles. Thus the PEM fuel cells with acetylene carbon black particles showed better performances than those with oil-furnace carbon black particles, since the increased contact between polymer electrolyte and catalyst sites increases catalyst utilisation, which significantly enhances the rate of Reaction (1.2) and therefore reduces the activation overpotential in the cathode.

Uchida et al. (1996) showed that platinum grain size increases and overall surface area decreases with decreasing surface area of the carbon black particles. This is because the

platinum grains are adsorbed on the various carbon black particles at regular intervals of about 10 nm. In the case of carbon black particles with smaller surface areas, such that the number of platinum grains is greater than that of adsorption sites on the carbon black, the platinum grains are adsorbed onto previously adsorbed platinum grains. Consequently the adsorbed platinum grains increase in size with a decrease in carbon black surface area, and the overall platinum surface area decreases since there are fewer grains with less overall surface area compared with the case where more adsorption sites are present on the carbon black. Also, Ticianelli et al. (1991) showed an increase in platinum grain sizes (i.e. 2, 3 and 4 nm) on carbon black particles when the percentage weight ratio of platinum to carbon black is increased (i.e. 10, 20 and 40 wt %, respectively). Using electron microscopy, Siegel et al. (2003) showed that platinum grains have a tendency to clump together, thereby reducing the surface area available for reactions and decreasing catalyst utilisation.

The results from Uchida et al. (1996) for the pore-volume distribution measurements of the individual carbon black particles, which have diameters in the range of 10 to 40 nm, showed that the carbon black particles consist primarily of pores smaller than 8 nm and that most of their surface area is in these pores. Platinum grains are typically smaller than the pore diameters and are adsorbed on the internal surfaces of the pores. The platinum grains in these pores do not catalyse the PEM fuel cell reactions, because polymer electrolyte is much larger than the pore diameters and the polymer electrolyte cannot contact the platinum. Thus, although carbon black particles with higher pore volumes and surface areas have a higher overall surface area of platinum grains, most of this surface area does not catalyse the fuel cell reactions and platinum utilisation is low. Alternatively, carbon black particles with lower pore volumes and lower surface areas have lower overall surface area of platinum grains, but the platinum grains are larger and restricted to the external surface of the carbon black particles where they can be in contact with polymer electrolyte and catalyse the reactions, resulting in high platinum utilisation. Consequently, PEM fuel cell performance in the activation overpotential region at low current densities increases with smaller pore volumes and surface areas for similar types of carbon black

particles. This indicates that the platinum utilisation increases with a decrease in pore volume and surface area. Thus PEM fuel cells with acetylene carbon black particles, which have the smallest pore volumes and surface areas, show the best performance.

1.2.2.3 PTFE

Ridge et al. (1989) studied the effects of varying PTFE content in catalyst layers using 5, 10, 15, 25 and 35 wt % PTFE. The 10 wt % PTFE catalyst layers yielded the best PEM fuel cell performances, although the variation in performances for all of the samples was not very large. The lower PTFE-content catalyst layers yielded better performances due to the presence of PTFE in the catalyst layers, which decreases catalyst utilisation and therefore increases the activation overpotential (since PTFE coats catalyst sites, blocking reactants from reaching them). Also, higher PTFE contents may cause drying of the polymer electrolyte, which increases the ohmic overpotential. Finally, higher PTFE contents reduce the pore space available for the transport of reactants, increasing the concentration overpotential, even though the hydrophobic property of PTFE is desirable for enhancing water expulsion and assisting in the transport of reactants. Thus the best performances are obtained at lower PTFE contents, although it is not possible to reduce the content to zero since PTFE is necessary to avoid flooding of the catalyst layers.

Giorgi et al. (1998) studied the effects of the amount of PTFE on porosities in the catalyst layers and on the performance of fuel cells. For their study, catalyst layers with low platinum loadings of 0.1 mg cm^{-2} were made using the spraying fabrication method. Results of scanning electron microscopy show the presence of numerous pores at 10 wt % PTFE. At higher contents of 20 and 40 wt % it appears that the PTFE fills the entire surface of the layer, but then at 60 wt % large cracks develop. Nevertheless, results of mercury porosimetry reveal that the porosities of the catalyst layers decrease for increasing PTFE content. Performance tests of fuel cells incorporating these catalyst layers at high current densities are similar to the results of Ridge et al. (1989) with fuel cell

performance steadily decreasing with increasing PTFE content. This is due to the presence of PTFE decreasing catalyst utilisation and increasing drying of the polymer electrolyte, which increases the activation and ohmic overpotentials, respectively, and to the decrease in porosities which causes transport limitations and increases the concentration overpotential. However, at low current densities, the performance is minimised at 20 wt % PTFE rather than steadily decreasing, probably because of the appearance of the cracks (seen in the scanning electron microscopy) which enhance transport to some of the catalyst sites that then dominate the reactions at low current densities. In contrast, at high current densities, all of the catalyst sites are necessary and the effect of the overall decrease in porosities is predominant.

One solution to the problem of PTFE decreasing catalyst utilisation is to support PTFE on uncatalysed carbon black. In this way the PTFE does not directly coat the catalysed carbon black and block the catalyst sites. Uchida et al. (1995) investigated the effect of uncatalysed carbon-black supported PTFE on PEM fuel cell performance. At high current densities, performance increases with the content of uncatalysed carbon-black supported PTFE until an optimum amount is reached, after which the performance decreases. This is because concentration overpotential is dominant at high current densities and increasing the content of hydrophobic PTFE decreases the effects of flooding by exhausting product water, thus increasing space for the reactant gases in the pores and enhancing their transport. This occurs until the presence of an excessive amount of PTFE restricts the pores, resulting in transport limitations, and causes drying of the polymer electrolyte in the catalyst layers. However, at low current densities the performance steadily decreases with an increase in the content of PTFE, due to decreasing catalyst utilisation. This occurs because some of the PTFE also binds to catalysed carbon black and the contact area between polymer electrolyte and catalyst decreases, increasing the activation overpotential, which is dominant at low current densities. Thus the results showed that the highest fuel cell performance was achieved for optimal contents of PTFE.

1.2.2.4 Polymer Electrolyte

Ticianelli et al. (1988b) studied effects of the amount of catalyst-layer polymer electrolyte on the performance of PEM fuel cells. Their experimental results show that an increase in the amount of polymer electrolyte in the catalyst layer increases fuel cell performance at low current densities. This is due to improved continuity of polymer electrolyte from the membrane to the catalyst layer and an increase of contact between polymer electrolyte and catalyst sites in the active layer. This results in improved catalyst utilisation during fuel cell operation. At high current densities, the increase in polymer electrolyte content has a positive effect on performance up to an optimal content, after which the performance starts to decrease rapidly. This is because catalyst layers have poor protonic conductivity for low polymer electrolyte content, resulting in poor fuel cell performance at all current densities. However, although the proton conductivity increases as the polymer electrolyte content increases, increased polymer electrolyte inside the pores of the catalyst layer introduces transport limitations (by retarding the transport of reactant gases to the catalyst sites and by blocking product water from flowing out of the cathodic catalyst layer, causing flooding). These effects are enhanced at high current densities and thus there is an optimal polymer electrolyte content which minimises both ohmic losses and the overpotential due to transport limitations.

Uchida et al. (1995) investigated the influence of polymer electrolyte on the morphology of catalyst layers and the resulting PEM fuel cell performances. Results of performance tests of fuel cells incorporating catalyst layers without PTFE agree with the results of Ticianelli et al. (1988b) at high current densities. They show that performance improves with an increase of polymer electrolyte, due to an increase in catalyst utilisation, until an optimal content of polymer electrolyte is reached (after which performance decreases due to the presence of excessive amounts of polymer electrolyte causing transport limitations). However, at low current densities fuel cell performance does not change with increasing polymer electrolyte content until the presence of excessive amounts of polymer electrolyte causes a decrease in performance. Thus the results showed

that the highest fuel cell performance was achieved for optimal contents of polymer electrolyte.

Cheng et al. (1999) investigated the influence of polymer electrolyte on catalyst utilisation in thin-film catalyst layers deposited either on the gas diffusion layers or on the membrane. For catalyst layers composed of only catalysed carbon black and polymer electrolyte deposited on the membrane, the results of cyclic voltammetry analyses showed that catalyst utilisation is 45 %. Thus even though polymer electrolyte is uniformly distributed in the catalyst layers, it still does not contact all of the catalyst sites. For catalyst layers composed of catalysed carbon black and PTFE deposited on gas diffusion layers, proton conductivity is provided by impregnating the catalyst layers with polymer electrolyte; in this case catalyst utilisation is influenced by the degree of polymer electrolyte impregnation, which can be quite low. However, when the catalyst layers were sufficiently impregnated with polymer electrolyte by an immersion technique, rather than by using the conventional practice of brushing, it was found that catalyst utilisations can reach as high as 78 %.

These results are explained on the basis of scanning and transmission electron microscopy analyses which reveal that, although the distribution of polymer electrolyte in catalyst layers made directly from polymer electrolyte is basically uniform, some thick polymer electrolyte layers and clumps are observed. Alternatively, in immersed catalyst layers, the distribution of polymer electrolyte is more uniform. Thus when polymer electrolyte is sufficiently impregnated into the catalyst layer by means of the immersion method, fairly high catalyst utilisations can be obtained, in excess of those obtained for catalyst layers made directly from polymer electrolyte, due to a more uniform distribution of polymer electrolyte and therefore more contact between catalyst sites and polymer electrolyte.

1.2.3 Structure

Ticianelli et al. (1991) studied the structure of catalyst layers made by the polymer electrolyte impregnation manufacturing method using scanning and transmission electron microscopy. Their results show that the catalysed carbon black particles are bound together into numerous clusters, or agglomerates, probably due to the presence of the PTFE used as a wet-proofing agent. Cheng et al. (1999) also presented scanning and transmission electron microscopy results showing that the structures of catalyst layers made by polymer electrolyte impregnation (using the immersion manufacturing method) change significantly with PTFE content. When the weight ratio of PTFE to catalysed carbon black is five to one, no large-scale structure is observed and the catalyst layers appear homogeneous on a macroscopic scale (i.e. they have a macro-homogeneous structure). As a result, the catalyst layers have few pores for the transport of reactants, yielding the low performances discussed in Section 1.2.2.3. However, at a ratio of one to one, an agglomerate structure is seen with numerous pores. Finally, Siegel et al. (2003) analysed catalyst layers manufactured by ElectroChem Inc. using electron microscopy. Macropores can be seen in the catalyst layers on the order of 1000 nm in size, whereas nanoscale micropores are surprisingly absent from the images.

Uchida et al. (1995) investigated the influence of PTFE and polymer electrolyte on the structure of catalyst layers and the resulting PEM fuel cell performances. Their measurements using mercury porosimetry showed that catalyst layers made (by the polymer electrolyte impregnation manufacturing method) from catalysed carbon black and uncatalysed carbon-black supported PTFE, followed by impregnation with solubilised polymer electrolyte, have two distinct pore distributions; one for micropores with sizes in the range of 20 - 40 nm, and one for macropores with sizes in the range of 40 - 1000 nm. The micropores are spaces between the catalysed or uncatalysed carbon black particles in the agglomerates identified by Ticianelli et al. (1991), and the macropores are spaces between individual agglomerates.

Uchida et al. (1995) showed that the volume of macropores increases with increasing PTFE content and decreases with increasing polymer electrolyte content. However, the volume of the micropores is independent of the content of both PTFE and polymer electrolyte. Thus PTFE and polymer electrolyte are found only in the macropores. This is because they cannot penetrate into the micropores due to their large molecular sizes, which restrict them to the surface of agglomerates as binding agents or to the spaces between individual agglomerates. Thus reactions (i.e. the utilised surface area of catalyst) are limited to the surfaces of macropores in the active layers where catalyst sites on carbon black in the agglomerates are in contact with polymer electrolyte. Since catalyst sites are not only found on the surface of the macropores, but are also uniformly distributed in the agglomerates, and polymer electrolyte does not penetrate deep into the active layer, low catalyst utilisations of 15 to 25 % are found for this fabrication method. Therefore a need exists for higher catalyst loadings of 0.4 mg cm^{-2} (compared to the state-of-the-art loadings of 0.1 mg cm^{-2}) to increase the contact area between catalyst sites and polymer electrolyte.

Fischer et al. (1998) used pore-forming additives to create additional porosity in thin-film catalyst layers and they investigated the resulting effects on PEM fuel cell performances. Catalyst layers were prepared by applying a slurry consisting of catalysed carbon black, polymer electrolyte solution, glycerol and water onto a polymer electrolyte membrane. The solvents were subsequently removed by heating to at least 150 °C, which also improved the contact between polymer electrolyte in the catalyst layer and the membrane. Catalyst layers prepared in this manner had an overall porosity of about 35 %. To provide the catalyst layers with additional porosity, different kinds of pore-forming additives were added to the catalyst slurry. Catalyst layers prepared by adding volatile pore-forming additives to the catalyst slurry, which decomposed during the heating process, had overall porosities of 42 - 48 %. Adding salt crystals, which were removed by dissolving the salt in sulphuric acid, resulted in overall porosities of 65 %. Hydrophobic gas diffusion layers were then applied to the different catalyst layers and the resulting MEAs were used in fuel cell performance tests. The results showed that, although the

electronic conductivity of the catalyst layers prepared using pore-forming additives is lower than that of the catalyst layers prepared without using additives, this decreased conductivity does not seem to impair the performance of fuel cells. Also, the performance of fuel cells using catalyst layers without additional porosity, or with volatile or salt additives, increases with the overall porosity due to decreasing resistance to the transport of reactants.

Eikerling & Kornyshev (1998) presented a model for the structure of catalyst layers, which is based primarily on the experimental results of Uchida et al. (1995).

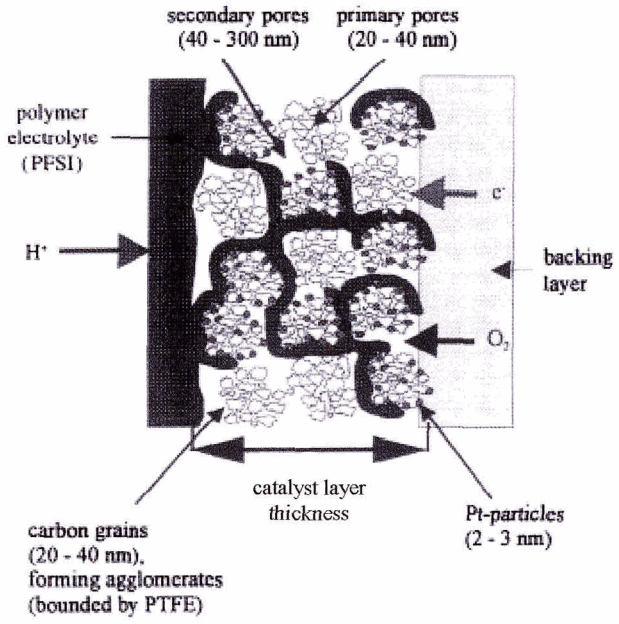

Figure 1.4 - Cathode catalyst layer (Eikerling & Kornyshev, 1998).

As seen in Figure 1.4, cathode catalyst layers are bound on one side by a polymer electrolyte membrane, which supplies protons to the catalyst layers. On the other side there is a porous gas-diffusion electrode-backing layer, which supplies electrons and

oxygen. Both the gas-diffusion electrodes and the catalyst layers are composed of carbon black particles, each 20 - 40 nm in size. The presence of uncatalysed carbon-black supported PTFE, which has a relatively large molecular size compared to the carbon black particles, causes the particles to form interconnected agglomerates (up to 1000 nm in size) bound on the outside by PTFE. Inside the agglomerates there are micropores, similar in size to the carbon black particles, which are too small for the PTFE to penetrate, while between the agglomerates there are macropores similar in size to the agglomerates themselves.

In the catalyst layers, carbon black particles are also used to support platinum grains, 2 - 3 nm in size; excess PTFE and polymer electrolyte, which extends from the membrane, bind the catalysed carbon black particles into agglomerates similar to the PTFE bound agglomerates composed of uncatalysed carbon black particles. In general, polymer electrolyte is found on the surfaces of agglomerates and also in the macropores, but it cannot penetrate into the micropores due to its relatively large molecular size. The result is a triple interface of proton-conducting polymer electrolyte, electron-conducting carbon black particles and oxygen transport macropores in the presence of platinum grains, which catalyse Reaction (1.2). The product water is prevented from flooding the macropores and blocking oxygen transport by the hydrophobic nature of PTFE. Also, because PTFE is a binding agent, more PTFE content in the catalyst layer results in tighter bound individual agglomerates, yielding larger macropores, while free space in the macropores decreases with more polymer electrolyte content. This explains the results of Uchida et al. (1995) where it was shown that the volume of macropores increases with increasing PTFE content and decreases with increasing polymer electrolyte content.

Increasing polymer electrolyte content (which increases proton conductivity) therefore comes at the expense of reduced oxygen transport space in the macropores. Also, although increasing PTFE content increases the oxygen transport space through larger macropores, the smaller agglomerates will have less surface area and therefore less platinum grains in contact with polymer electrolyte, resulting in less reactions. In general,

based on the model of Eikerling & Kornyshev (1998), it is obvious that in order to avoid non-utilisation of expensive catalyst, platinum grains should be loaded only onto the outer surfaces of agglomerates in contact with polymer electrolyte. Also, optimising the PTFE and polymer electrolyte content of catalyst layers is obviously a difficult task of balancing competing tendencies, made even more difficult since the optimisation will change depending on the desired fuel cell operating parameters.

1.2.4 Transport

In general, transport through porous media (due to convection, ordinary molecular diffusion, Knudsen diffusion and surface migration) depends on the pore structure (i.e. pore size, distribution and interconnectivity). Since the pore structure cannot be determined easily, transport equations taking the pore structure into account tend to be very complex and inaccurate. However, from a macroscopic point of view, detailed modelling of the relationship between the porous solid matrix and the transport properties of the pore network is not necessary, since most porous media are macroscopically uniform and can therefore be treated as pseudo-homogeneous media. Thus simple continuum equations are used to describe the transport properties, with effective coefficients accounting for the porous nature of the media instead of the usual coefficients applicable for bulk fluids. The effective coefficients depend on macro-properties of the porous media, such as porosity and tortuosity, as well as on the bulk coefficients. Therefore, ordinary molecular diffusion in porous media is governed by Fick's first law, or by the Stefan-Maxwell equations for multicomponent gases, and by Fick's first law for multicomponent liquids, all with effective diffusion coefficients.

Knudsen diffusion, which only occurs for gas phases if the pore sizes are comparable to the mean free path (such that collisions between molecules and the surface walls of the pores are as important as ordinary intermolecular collisions), is governed by Fick's first law with an effective Knudsen diffusion coefficient. If there is viscous (i.e. convective)

flow due to a difference in total pressure across the porous media, then there will be a direct contribution to the flux from forced convective laminar flow, or permeation, through the pores. This effect can be modelled using either Darcy's law with effective permeabilities, or Fick's first law with effective diffusion coefficients determined under the assumption of Poiseuille flow. Finally, in the porous media, molecules adsorbed on the surfaces of the solid matrix may still have considerable mobility through site hopping, and this migration of molecules in the adsorbed phase (along surface walls of the solid matrix) is referred to as surface diffusion or migration. Surface migration can be assumed to be governed by Fick's first law, with effective surface diffusion coefficients.

In general, the structures of the catalyst layers in PEM fuel cells will determine whether or not ordinary molecular diffusion and viscous flow dominate the transport of reactants to the catalyst sites, or if Knudsen diffusion and surface migration also need to be taken into account. In the macropores of the catalyst layers, which are located between the agglomerates and are similar in size to the agglomerates themselves, the large pore diameters of up to 1000 nm imply that Knudsen diffusion and surface migration are negligible. However, pore diameters are only 20 - 40 nm for micropores inside the agglomerates, and therefore Knudsen diffusion and surface migration are probably not negligible. Thus, if transport in the catalyst layers is dominated by flow through the macropores (i.e. the volume of the macropores is much larger than that of the micropores), it is usually assumed that the transport is by ordinary molecular diffusion and, if there are pressure gradients, also convection. However, if transport in the catalyst layers is dominated by flow through the microporous agglomerates (i.e. the volume of the micropores greatly exceeds that of the macropores, due to a decrease in the available pore volume of the macropores; for instance because of flooding of the macropores by water) it is also important to consider Knudsen diffusion and surface migration as well as ordinary molecular diffusion and convection.

In general, in the case of multicomponent liquids, the ordinary molecular diffusive, convective and surface migration fluxes through the pores can simply be added. However,

in the case of multicomponent gases, if pore sizes are comparable to the mean free path, Knudsen diffusion must also be taken into account. Currently, there are three standard models available to describe multicomponent transport for combined molecular and Knudsen diffusion: the dusty gas model (DGM), the cylindrical pore or mean transport-pore model (MTPM) and the binary friction model (BFM). These models are based on the Stefan-Maxwell description of ordinary multicomponent diffusion. The DGM is the most frequently used model. This model treats the solid matrix as one species in the multicomponent gas, consisting of giant "dust" molecules uniformly distributed in space and held fixed (i.e. motionless) by external forces.

The MTPM assumes that gas transport takes place in a collection of straight cylindrical capillaries, or transport-pores, which penetrate a solid at various angles and, therefore, with various lengths. Also, the capillaries have various radii which are distributed about a mean value, with the width of this distribution characterised by the mean-squared value of the radii. In this model, molecular and Knudsen diffusion are considered to function as parallel resistances to flow through intermolecular and molecular-wall interactions. In both the DGM and MTPM models, any fluxes due to convection and surface migration can simply be added to the diffusional flux through the pores. Also, both models are identical except for prediction of the dependence of effective permeability coefficients, for each component in the Darcy (i.e. convective) flow terms, on the composition of the gaseous mixture and macroscopic geometrical parameters of the porous media.

In contrast to both the DGM and MTPM, the BFM repudiates the concept of parallel Knudsen and viscous flow in porous media, since these flows are assumed to be limiting forms of the same phenomena of momentum transfer to the pore walls (through molecular-wall collisions in the Knudsen and molecular regimes, respectively). The DGM and MTPM models assume that the diffusive (i.e. ordinary molecular and Knudsen) flows combine by the additivity of momentum transfer, while the convective flow is combined by the additivity of fluxes. In contrast, the BFM does not separate Knudsen diffusion and

viscous convection, and combines both with molecular diffusion by the additivity of momentum transfer. The incorporation of surface migration into the BFM model of transport in a porous medium is similar to that for the DGM and MTPM models, with the surface migration flux simply added to the diffusional flux.

Capek & Seidel-Morgenstern (2001) studied the ability of the DGM, MTPM and BFM models to describe experimental responses for various catalysed porous agglomerates used in industrial catalysis. The MTPM model was found to describe transport in agglomerates with intermediate pore sizes better than the DGM and BFM models, especially for ternary mixtures of gases. In contrast, the MTPM and DGM models predicted transport in agglomerates with large pore sizes equally well, while BFM predictions were inferior. However, in general, the prediction potential of all three models was found to be satisfactory.

In general, transport models such as the DGM, MTPM and BFM models are still relatively complicated and depend on many macroscopic parameters, some of which cannot be determined easily. Thus, instead of a detailed description of the complex internal transport of reactants through catalysed porous agglomerates, an effective bulk diffusion coefficient is commonly used in Fick's first law, which lumps together all relevant transport phenomena and which, in general, is measured experimentally. For catalysed porous agglomerates this approach has proven to be very useful, provided that the agglomerates can be regarded as macroscopically homogeneous.

Veldsink et al. (1995) studied transport accompanied by electrochemical reactions in catalysed porous agglomerates using Fick's first law with an effective bulk diffusion coefficient and the DGM. The results show that Fick's first law is satisfactorily accurate to estimate the reactant transport in different agglomerates, and that the results deviate only slightly from the reactant transport predicted using the DGM. The results also show that pressure in the agglomerates does not seriously affect the reactant transport and therefore demonstrates that pressure-driven (i.e. convective) flow can be omitted from the reactant

flux expression without significant loss of accuracy. The effects of convective flux are generally negligible since the pressure-drops over the agglomerates are typically very small.

In general, when reactants diffuse into catalysed porous agglomerates, simultaneous reaction and diffusion have to be considered when obtaining an expression for the overall rate of conversion of the reactants. Assuming single pseudo-homogeneous expressions for the kinetics of the overall reactions, which depend on the surface area of the catalyst per unit volume of the agglomerates and the local concentrations of reactants, and employing Fick's first law (with an effective bulk diffusion coefficient) for mass transport of the reactants, a factor describing catalysed porous agglomerate effectiveness-of-reactant-conversion can be calculated. This agglomerate effectiveness factor is defined as the ratio of the amount of reactants converted by an agglomerate to the amount that would have been converted if conditions at catalyst sites located on the external surface of the agglomerate were to prevail at catalyst sites inside the agglomerate as well. Reactant conversion rates for the agglomerates are then given by the kinetic rate expression for the concentrations of reactants at the external surfaces of the agglomerates, multiplied by the effectiveness factor. In the model presented by Eikerling & Kornyshev (1998) for the structure of catalyst layers in PEM fuel cells (in which reactions are limited to the external surfaces of the agglomerates where catalyst sites are in contact with polymer electrolyte), the effectiveness factor has a value of one.

Chapter 2

Catalyst Layer Models

Modelling studies have been conducted to aid in optimising the composition and structure of catalyst layers, electrodes and MEAs, as well as PEM fuel cell operating conditions, in order to attain improved performances. These studies have allowed better understanding of the physical and electrochemical processes taking place in PEM fuel cells. In this chapter a number of different catalyst layer models are presented, with discussions of their relevant limitations and advantages based on the results of modelling studies. A final recommendation is given for implementation of an optimal catalyst layer model.

Since catalyst layers in PEM fuel cells have relatively small thicknesses, many studies have simplified their models by treating catalyst layers as infinitely thin interfaces between the membrane and gas diffusion layers, relegating them to boundary conditions for the solution of the model. Some of these studies are listed as follows: Springer et al. (1991), Nguyen & White (1993), Amphlett et al. (1995), West & Fuller (1996), Wohr et al. (1998), Yi & Nguyen (1998, 1999), Singh et al. (1999), Dutta et al. (2000, 2001), He et al. (2000), Shimpalee & Dutta (2000), Natarajan & Nguyen (2001, 2003), Wang et al. (2001), Berning et al. (2002), Djilali & Lu (2002), You & Liu (2002), Costamagna (2003) and Stockie et al. (2003).

Other studies have only partially considered the effects of catalyst layer structures on performance. Gurau et al. (1998) took into account electrical potential and current density in the polymer electrolyte of the catalyst layers, but the catalyst layers were considered to have negligible thickness in the solution of the transport equations. Finally, some studies have made simplifications equivalent to stating boundary conditions concerning variables found in the catalyst layers. Fuller & Newman (1993) used bulk concentrations of each reactant species in their respective phases for reaction kinetics. Kulikovsky (2002a; b) assumed the oxygen concentration was constant throughout the cathode catalyst layer.

In general, one-dimensional models typically consider transport processes perpendicular to the gas diffusion/catalyst layer interfaces. However, the gas channels and the bipolar plates alternate contact with the gas diffusion layers, which makes the gas transport and electronic current density two-dimensional. Also, concentrations are not uniform along the gas channels, which makes the transport processes three-dimensional. Therefore additional effects are encountered as a result of these changes in the directions parallel to the gas diffusion/catalyst layer interfaces and, in order to study these effects, it is necessary to consider models that are not one-dimensional.

2.1 Porous Catalyst Layers

For simple electrodes, electrochemical reactions are restricted to well-defined interfaces (often plane surfaces) between catalytic and electron-conducting metals and electrolyte. However, as described in Chapter 1, PEM fuel cells have catalyst layers consisting of porous matrices of platinum catalyst supported on carbon black. An electrolyte penetrates the void spaces of the porous matrix and there is a complex interface between the catalyst sites, the electron-conducting matrix and the electrolyte extending throughout the interiors of the catalyst layers. Thus, relative to solid electrodes, porous catalyst layers are superior in that they provide a much larger contact area between catalyst sites and electrolyte.

Models of porous catalyst layers can either be microscopic in nature, with exact considerations of the complicated structure, or macroscopic in nature, with some averaging over the random structure of the catalyst layers. Thus, macroscopic models contain parameters which describe the overall features of porous catalyst layers, such as porosity and tortuosity, and effective electronic and ionic conductivities and diffusion coefficients. Parameters are also included for reaction kinetics, such as the active surface area of contact between catalyst sites and electrolyte per unit volume of the catalyst layers (which is used instead of the active surface area due to the complicated structure of the contact interface). In contrast, microscopic models have many more parameters based on the complicated structure. Considering that it is advantageous in parametric studies to minimise the total number of parameters, macroscopic models are better suited for use in PEM fuel cell studies versus microscopic models, based on the total number of model parameters. Also, because macroscopic parameters are difficult to predict, there have been many experimental studies conducted to determine accurate values for these parameters, which may then be used in modelling studies of PEM fuel cells. Finally, because of the inherent averaging techniques employed in computational fluid dynamics (CFD), macroscopic models are better suited for CFD implementations than microscopic models. Thus, macroscopic models of porous catalyst layers in fuel cells are reviewed in this chapter, and are the focus of this thesis, while microscopic models are not considered here.

2.2 Liquid Electrolyte

Porous catalyst layers are commonly used in contact with liquid electrolytes, such as the potassium hydroxide solution found in alkaline fuel cells and the concentrated phosphoric acid found in phosphoric acid fuel cells. The PEM fuel cell models for porous catalyst layers in contact with polymer electrolyte are based on models developed

previously for fuel cells with liquid electrolytes. It is therefore important to understand these liquid electrolyte models.

2.2.1 Macro-Homogeneous Models

General equations describing the behaviour of porous catalyst layers (consisting of electron-conducting matrix in contact with an electrolytic solution) were developed by Newman & Tobias (1962), for the case where all reactants are ionic constituents of the solution. In their model, the liquid electrolyte was considered to fully penetrate the porous catalyst layer and completely fill the void spaces. Such models are commonly referred to as macro-homogeneous, since the catalyst layers are macroscopically uniform as a result - if it is also assumed that the matrix has a uniform structure (i.e. porosity and tortuosity). Thus the catalyst layers are macroscopically considered to be homogeneous domains of electrolyte and solid matrix, in which the transport of dissolved reactants and electrons (in the electrolyte and matrix, respectively) are simply superposed onto each other. This is in contrast to the standard definition of a homogeneous system as being composed of only one phase. Systems made up of more than one phase are generally referred to as heterogeneous and, therefore, macro-homogeneous models are also commonly referred to as pseudo-homogeneous models. Also, it is usually assumed that the matrix and electrolyte have their own electrical potentials, which govern two current densities, one in the matrix and one in the electrolyte. The difference between the potentials is responsible for driving electrochemical reactions which consume or produce the two current densities.

The equations governing transport phenomena in the porous catalyst layers for the macro-homogeneous model of Newman & Tobias (1962) are Ohm's law for the conduction of electrons in the matrix, and the Nernst-Planck equation for ionic species transport in the electrolyte due to convection, diffusion and migration. The Nernst-Planck equation is based on dilute solution theory and simplifies to Ohm's law for migration if convection and diffusion are neglected. The Butler-Volmer equation is used to express the

local rate of reaction as a function of the various concentrations and the potential jump at the catalyst-electrolyte interface. Finally, conservation of charge, which states that changes in the two current densities are equal in magnitude and opposite in sign, can be replaced by the more restrictive, but often justifiable, assumption of electroneutrality (i.e. no net charge) in the solid matrix and electrolyte phases.

Assuming isothermal and steady-state conditions for their macro-homogeneous model of porous catalyst layers, Newman & Tobias (1962) derived one-dimensional analytical and numerical results perpendicular to the bulk electrolyte/catalyst layer interface. They used linear and Tafel (i.e. neglecting the back reaction rate) approximations of the Butler-Volmer equation, valid at low and high current densities, respectively. The results show that when electrolytic conductivity is relatively high with respect to the reaction kinetics, for low current densities and high electronic conductivity or small thickness of the catalyst layers, the electrochemical reactions occur uniformly over the catalyst layers. On the other hand, when activation overpotential and the thickness of the catalyst layers are relatively high compared to electrolytic conductivity, reactions occur in a thin region adjacent to the bulk electrolyte/catalyst layer interface. The results also show that when the concentrations of reactants become depleted in the catalyst layers as a result of transport limitations, the distribution of electrochemical reactions is shifted towards a thin region adjacent to the reactant supply interface, where the concentrations of reactants are greater. Finally, for uniform reactant concentrations, the reaction distribution in the catalyst layers becomes less uniform with increasing current densities, increasing thickness of the catalyst layers, or increases in the sum of the effective resistivities of the electrolytic and solid phases.

2.2.2 Agglomerate Models

Unlike macro-homogeneous models that are based on a structure in which the catalyst layer has no pores through which gas can be transported to the catalyst sites, and reactant

transport in the catalyst layers is solely through dissolved species in the liquid electrolyte, some models assume that reactants are transported through the catalyst layer to the reaction sites predominantly in a gas phase. Such models are commonly referred to as agglomerate models because they are based on an assumed agglomerate structure for the catalyst layers. Such a structure occurs for catalyst layers in which PTFE is present, binding catalysed carbon black particles into a cohesive network of interconnected microporous agglomerates surrounded by macropores and imparting some hydrophobic character to the catalyst layer. In this case pores in the layer are only partially filled with liquid electrolyte, leaving some of the pores free to be filled with gas. Also, potassium hydroxide and phosphoric acid preferentially fill the micropores, leaving the macropores filled with gas, due to capillary effects.

2.2.2.1 Flooded

The flooded agglomerate model used by Ridge et al. (1989) was first introduced by Giner & Hunter (1969) for cathode catalyst layers in alkaline fuel cells although, in this case, the model was applied to a PEM-sulphuric acid test cell cathode - where the sulphuric acid acted as a liquid electrolyte and a source of protons. In this model, the macropores in the catalyst layers provide gas diffusion pathways, while the micropores that make up the agglomerates are flooded with liquid electrolyte. The transport of oxygen in the macropores is described by the Stefan-Maxwell equations for multicomponent gas diffusion. Once the oxygen diffuses through the macropores of the catalyst layers, it dissolves into the micropores of the flooded agglomerates according to Henry's law, under the assumption that dissolved oxygen is in equilibrium with gaseous oxygen in the macropores, before reacting at the catalyst sites. The concentration of oxygen in the Butler-Volmer equation is the concentration of oxygen dissolved in the electrolyte at the surface of the agglomerates, multiplied by an effectiveness factor which takes into account the simultaneous diffusion and conversion of the reactants in the agglomerates. The concentration of protons in the Butler-Volmer equation is also transport-limited with the

flux of protons in the liquid electrolyte given by the Nernst-Planck equation, but in which convection is neglected. Finally, Ohm's law is used for the electronic current density in the solid matrix phase.

Assuming isothermal and steady-state conditions, Ridge et al. (1989) derived one-dimensional numerical results perpendicular to the bulk electrolyte/catalyst layer interface which show that fuel cell performances increase asymptotically with decreasing characteristic agglomerate radius. This is because smaller agglomerates have shorter diffusion paths for dissolved oxygen. However, a certain point is reached when the characteristic agglomerate radius is small enough to prevent diffusion limitations from hindering fuel cell performance. Also, if the agglomerates become too small, then their interconnectivity is reduced and limitations in electronic conductivity need to be considered. Finally the results show that limitations associated with the transport of protons have a large effect on fuel cell performance.

2.2.2.2 Thin-Film, Flooded

Iczkowski & Cutlip (1980) described the behaviour of porous fuel cell cathodes in concentrated phosphoric acid electrolyte using a thin-film, flooded agglomerate model. In this model, illustrated in Figure 2.1, excess liquid electrolyte is assumed to form a thin film around the agglomerates. In contrast, the flooded agglomerate model of Ridge et al. (1989) is similar to that shown in Figure 2.1, except that the electrolyte film is not present - due to the assumption that capillary effects are sufficiently strong and all of the liquid electrolyte is found inside the agglomerates.

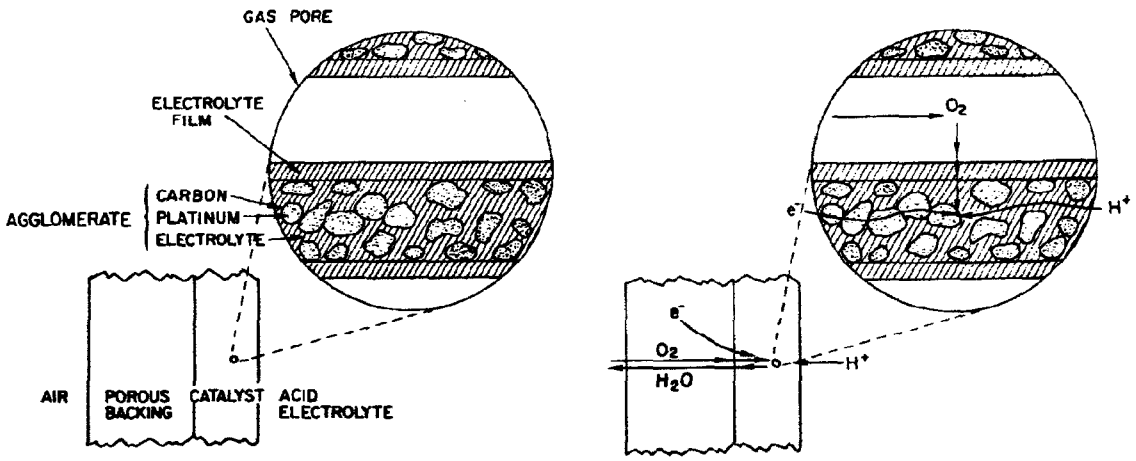

Figure 2.1 - Thin-film, flooded agglomerate model for fuel cell cathode (Iczkowski & Cutlip, 1980).

In the thin-film, flooded agglomerate model of Iczkowski & Cutlip (1980), oxygen first dissolves into and diffuses across the thin film of liquid electrolyte covering the agglomerates, before diffusing through the flooded micropores of the agglomerates and reacting at catalyst sites along the way. In general, the model accounts for diffusion of oxygen in the gas-filled macropores, diffusion of dissolved oxygen in the liquid electrolyte, electrochemical reaction of oxygen dissolved in electrolyte within the agglomerates, and current of electrons through the solid matrix and transport of protons in the electrolyte, as shown in Figure 2.1. The model assumes that product water from the electrochemical reactions evaporates into the gas in the macropores and then diffuses out through the catalyst and gas diffusion layers and into the gas channels.

In the model of Iczkowski & Cutlip (1980), as in the model of Ridge et al. (1989), the transport of oxygen in the macropores is described by the Stefan-Maxwell equations for multicomponent gas diffusion. These equations are valid for ordinary molecular diffusion, in which retardation of the gas flow is due to collisions with other molecules. However, according to Iczkowski & Cutlip (1980) the macropores in the catalyst layer are narrow

enough such that distances between gas pores' walls can be on the order of the mean free path of the molecules. Therefore oxygen molecules are slowed by collisions with the pore walls as well as by collisions with other gas molecules. Thus, unlike the model of Ridge et al. (1989), in the model of Iczkowski & Cutlip (1980), the Stefan-Maxwell equations are modified by considering combined ordinary molecular and Knudsen diffusion. This is done through use of the mean transport-pore model discussed in Chapter 1. Assuming that equilibrium conditions apply, Henry's law is then used to relate the partial pressure of oxygen in the catalyst layer macropores to the concentration of dissolved oxygen at the surface of the thin film of liquid electrolyte. Diffusion through the film, which is considered thin in comparison with the characteristic radius of the agglomerates, is approximated by the linearised version of Fick's first law for a flat, thin film. After the oxygen diffuses across the film, it diffuses into the micropores of the agglomerate and diffuses towards the centre of the agglomerate, reacting at available catalyst sites along the way. The overall rate of reaction in the agglomerate is obtained by multiplying the Butler-Volmer equation for the rate of the reaction, assumed to be first-order in oxygen concentration, by the concentration of dissolved oxygen at the surface of the agglomerate and also by an effectiveness factor depending on the relative rates of diffusion and reaction, the geometry of the agglomerates, and the distribution of catalyst sites and polymer electrolyte in the agglomerates. Finally, Ohm's law is used for electronic and protonic current densities (i.e. the model does not account for diffusion of protons or convection in the Nernst-Planck equation, since the protons are assumed to have a constant concentration in the stationary concentrated phosphoric acid electrolyte).

Assuming isothermal and steady-state conditions for the thin-film, flooded agglomerate model in porous fuel cell cathodes with concentrated phosphoric acid electrolyte, Iczkowski & Cutlip (1980) derived one-dimensional numerical results perpendicular to the bulk electrolyte/catalyst layer interface that show the relative contributions of diffusional and ohmic losses to the total voltage loss for transport processes. These results are summarised in Figure 2.2 for transport processes at a current density of 200 mA cm^{-2} using base case parameters determined by fitting the model to

experimental data. Note that activation losses, although not shown, are much larger than the losses associated with the transport processes.

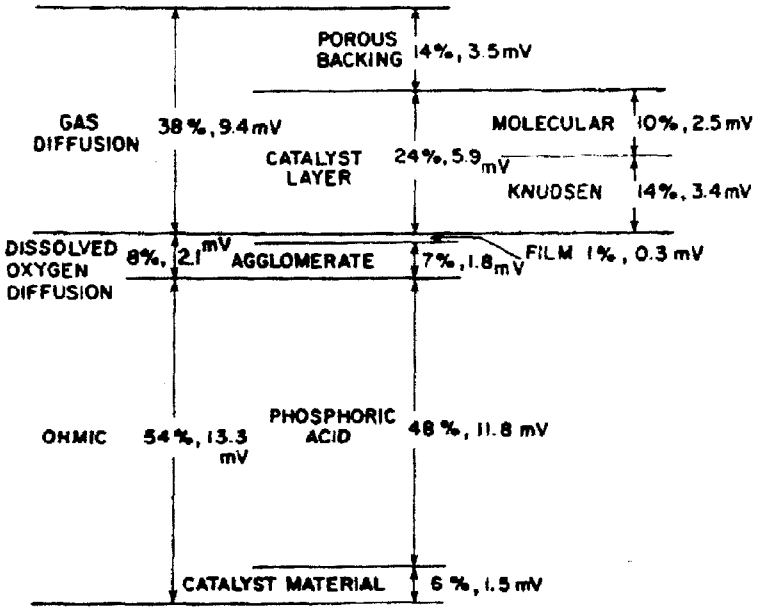

Figure 2.2 - Transport losses in a phosphoric acid fuel cell cathode at 200 mA cm^{-2} (Iczkowski & Cutlip, 1980).

According to Figure 2.2, 54 % of the total transport losses are due to ohmic resistances in the catalyst layer. Most of this ohmic loss occurs in the phosphoric acid electrolyte, with only a small fraction due to electronic resistance in the catalysed carbon-black solid matrix. The next most important loss is due to gas diffusion, which accounts for 38 % of the voltage loss. Both the porous backing (i.e. gas diffusion) and catalyst layers account for gas diffusion losses. For the catalyst layer, Knudsen diffusion is found to be slightly more important than molecular diffusion. Least important are the losses due to the diffusion of dissolved oxygen in the thin film of liquid electrolyte outside and the liquid electrolyte inside the agglomerates, which account for only 8 % of the total voltage loss.

The very small voltage loss calculated for the thin film of liquid electrolyte indicates that such films are infinitesimally thin in the cathode at low current densities, although they are probably much thicker at high current densities due to the presence of excess product water.

2.3 Polymer Electrolyte

In PEM fuel cells, porous catalyst layers are in contact with polymer electrolyte. For thin-film catalyst layers composed of catalysed carbon black and polymer electrolyte, and with or without PTFE, microporous agglomerates are formed because of the presence of the polymer electrolyte or PTFE. Between the individual agglomerates there are macropores in which polymer electrolyte is exclusively found due to its large molecular size not allowing penetration into the micropores. For catalyst layers in which the content of polymer electrolyte is very high, the macropores between the agglomerates can be considered to be entirely filled with polymer electrolyte. This yields a macro-homogeneous structure if the porosity is dominated by the macropores, allowing for transport to occur only in the polymer electrolyte. Alternatively, for catalyst layers with smaller polymer electrolyte content, the polymer electrolyte does not entirely fill the macropores and some of the macropores are open, as are the micropores, allowing for gas and liquid water transport. In general, such structures for the catalyst layers in PEM fuel cells are referred to as agglomerate.

2.3.1 Macro-Homogeneous Models

Bernardi & Verbrugge (1991, 1992) developed a macro-homogeneous model for PEM fuel cell catalyst layers, in which polymer electrolyte is considered to fully penetrate the catalyst layers and completely fill the void spaces of the porous matrix, such that there is

only polymer electrolyte and no gas phase in the pores of the catalyst layers. The overall model for a PEM fuel cell takes into account transport of reactants (supplied at the gas channels) through wet-proofed pores in the gas diffusion layers (lined by PTFE) to the interfaces between the gas diffusion and catalyst layers. There the reactants dissolve from the gas phase into the polymer-electrolyte phase of the catalyst layers according to Henry's law and are transported towards catalyst sites by convection and diffusion (which is given by Fick's first law). The Butler-Volmer equation is used to describe kinetics of the electrochemical reactions at catalyst sites. The Stefan-Maxwell equations for multicomponent diffusion are used to model gas phase transport through the wet-proofed pores in the gas diffusion layers. Also, in the gas diffusion layers, the transport of liquid water, given by Darcy's law, takes place in wetted pores not lined by PTFE. In general, the liquid water in the gas diffusion layers, and in the polymer electrolyte of the catalyst layers and membrane, provide continuous pathways for the transport of water. Thus, water produced by electrochemical reactions in the cathode catalyst layer flows out of the catalyst layer and either through the membrane and anode or through the cathode. The water then flows out into the gas channels in the form of liquid water and also water vapour.

The direction of water flow through the PEM fuel cell will depend on the relative magnitudes of electro-osmotic drag in the polymer electrolyte versus convection due to pressure gradients, both of which are incorporated into the model through Schlogl's equation (Bernardi & Verbrugge, 1991). However, the polymer electrolyte in the catalyst layers and membrane is assumed to be fully hydrated, such that the water content in the polymer electrolyte is uniform and there is no diffusion of liquid water. The model also takes into account the transport of electrons through the solid matrix, governed by Ohm's law, and the transport of protons from the anode to cathode catalyst layers through the polymer electrolyte. Under the assumption of electroneutrality, the proton concentration in the polymer electrolyte is taken to be constant and diffusion is not a mode of protonic transport. Thus, protonic transport in the polymer electrolyte is described by an equation

derived from the Nernst-Planck equation, which accounts for only the ohmic and convective modes of protonic transport through the polymer electrolyte.

Assuming isothermal and steady-state conditions, Bernardi & Verbrugge, (1991, 1992) obtained one-dimensional numerical solutions perpendicular to the membrane/catalyst layer interfaces for a PEM fuel cell operated with air and hydrogen and a differential pressurisation of 5 and 3 atm at the cathode and anode, respectively. Figure 2.3 shows profiles of dissolved oxygen concentration in the polymer electrolyte phase of the membrane and in the cathode catalyst layer for various current densities. The corresponding oxygen gas mole fraction (i.e. partial pressure) in the cathode gas diffusion layer is also shown.

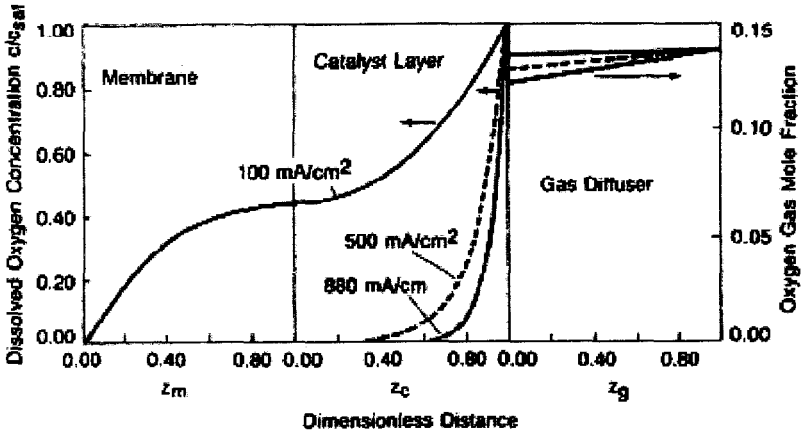

Figure 2.3 - Oxygen profiles in PEM fuel cell membrane/cathode assembly (Bernardi & Verbrugge, 1991).

Figure 2.3 shows that the oxygen mole fraction profile in the gas diffusion layer is almost flat, demonstrating that no transport limitations take place in the gas diffusion layer. In the catalyst layer, the dissolved oxygen concentration is almost uniform at low current densities. At high current densities, the region of the catalyst layer adjacent to the

membrane is depleted of dissolved oxygen, because the oxygen cannot diffuse fast enough to replenish what is consumed by the electrochemical reaction in this region. As a consequence, the electrochemical reaction rate is almost uniform throughout the catalyst layer at low current densities while, at higher current densities, the electrochemical reaction is restricted to a thin region of the catalyst layer adjacent to the gas diffusion layer, as shown in Figure 2.4.

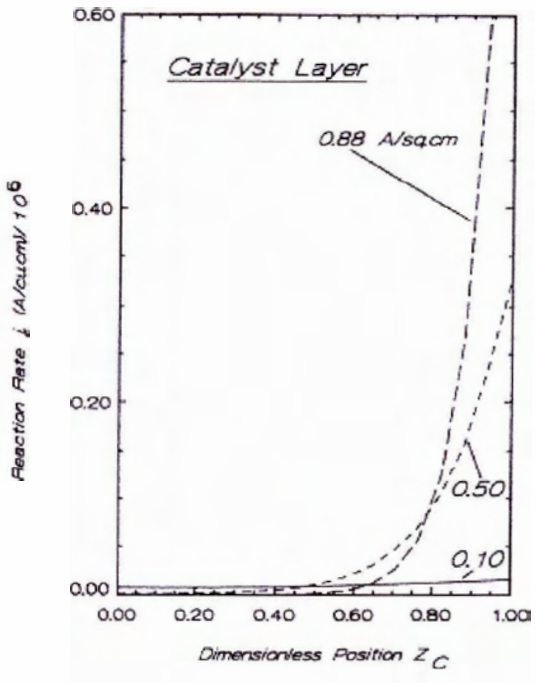

Figure 2.4 - Reaction rate distribution in PEM fuel cell cathode catalyst layer (Bernardi & Verbrugge, 1991).

Figure 2.5 shows superficial velocity for the liquid water phase in the gas diffusion layers and in the polymer electrolyte of the catalyst layers and membrane at different current densities (i.e. velocity is referred to the projected area parallel to the gas diffusion/catalyst layer interfaces of the entire MEA rather than of the phase).

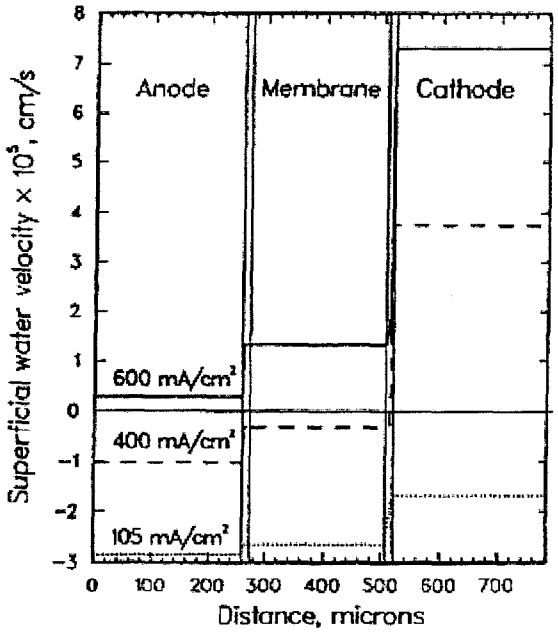

Figure 2.5 - Water velocity distribution in the MEA of a PEM fuel cell (Bernardi & Verbrugge, 1992).

Figure 2.5 shows that at low current densities (i.e. 105 mA cm^{-2}), pressure driven convective flow is the most important effect, causing water to flow from the gas channel/diffusion layer interface of the cathode to that of the anode. Under these conditions, even though water is produced at the cathode catalyst layer by the electrochemical reaction, liquid water must be supplied at the gas channel/diffusion layer interface of the cathode. This can be done by humidifying the air in the gas channel on the cathode side at a temperature higher than the operating temperature of the fuel cell, such that liquid water condenses at the gas channel/diffusion layer interface of the cathode. The reverse situation occurs at high current densities (i.e. 600 mA cm^{-2}) where electro-osmotic drag dominates, transporting enough water from the anode to the cathode to force water produced at the cathode to flow against the differential pressurisation. Thus, in this case the anode needs to be supplied with water instead of the cathode. In the intermediate case

at 400 mA cm^{-2} water production at the cathode catalyst layer is the dominant effect, causing water to flow out both sides of the fuel cell from the cathode catalyst layer. This situation arises due to a balance between the differential pressurisation and the electro-osmotic drag. For this type of flow pattern, it should not be necessary to supply water to the fuel cell to keep the polymer electrolyte in the catalyst layers and membrane in a fully-hydrated state. However, the model of Bernardi & Verbrugge (1991, 1992) does not take into account evaporative water losses from the fuel cell (due to heat generation) and, in general, an external water supply to both the anode and the cathode is found to be necessary for PEM fuel cells.

Bernardi & Verbrugge (1991, 1992) also showed that the volume fraction of the cathode gas diffusion layer available for gas transport should be at least 20 % in order to avoid transport limitations. Thus they concluded that the cathode gas diffusion layer must contain a large amount of hydrophobic PTFE in order to prevent flooding and maintain a high porosity for gas phase transport. Also, since the effective diffusion coefficient of oxygen in polymer electrolyte is relatively low, they note, that according to experimental data, the layer of polymer electrolyte surrounding the cathode catalyst sites cannot exceed 1 μm in thickness. Thus, since a typical state-of-the-art catalyst layer is on the order of 10 μm, their results show that the macro-homogeneous model, in which polymer electrolyte completely fills the pores of the catalyst layer, does not fit the experimental data. This suggests that only a fraction of the catalyst layer is filled with polymer electrolyte.

Springer et al. (1993) also used a macro-homogeneous model of the cathode catalyst layer similar to that of Bernardi & Verbrugge (1991, 1992), with gaseous oxygen dissolving into the polymer electrolyte phase at the gas diffusion/catalyst layer boundary. They argued that if ordinary gas-phase diffusion conditions were to exist in catalyst layer macropores, which they considered unlikely, the small thickness of typical state-of-the-art catalyst layers precludes the development of a significant reactant pressure drop through the gas phase in the catalyst layer. Therefore the concentration of dissolved oxygen at the gas phase/polymer electrolyte phase interface is the same no matter where the interface is

located with respect to the gas diffusion/catalyst layer boundary. Thus the difference between macro-homogeneous and agglomerate models is the thickness of the polymer electrolyte film in the catalyst layers and the detailed distribution of the catalyst sites inside of the film (i.e. randomly distributed or in agglomerates, respectively). The set of equations governing transport phenomena in this model include the Stefan-Maxwell equations for multicomponent diffusion in the porous gas diffusion layer, Henry's law at the gas diffusion/catalyst layer interface for oxygen dissolving from the gaseous phase into the polymer electrolyte phase, and Fick's first law for transport of dissolved oxygen through the polymer electrolyte film. The authors noted that although both liquid water and polymer electrolyte phases are present in the catalyst layer, a single condensed phase bulk diffusivity is a good description for reactant transport through the catalyst layer. Ohm's law is used for protonic current density in the polymer electrolyte phase, while the electronic conductivity in the gas diffusion and catalyst layers is considered to be large enough such that the electrical potential in the solid matrix is constant. Finally, the electrochemical reaction kinetics is given by the Tafel approximation of the Butler-Volmer equation.

Assuming isothermal and steady-state conditions for the macro-homogeneous model, Springer et al. (1993) derived one-dimensional numerical results perpendicular to the gas diffusion/catalyst layer boundary. The results showed that when both oxygen diffusivity and protonic conductivity are sufficiently high relative to the current density, reactions take place uniformly throughout the catalyst layer. In contrast, if the oxygen diffusivity cannot match the current density, reactions in the catalyst layer are confined to a thin region of the catalyst layer adjacent to the gas diffusion layer. If protonic conductivity is the limiting factor, reactions in the catalyst layer are confined to a thin region adjacent to the membrane. In both of these later cases, there is a higher activation overpotential associated with the non-uniformity of the reaction rate. The results of Springer et al. (1993) also showed that thicker catalyst layers under the conditions of limited diffusivity and conductivity increase performance at the low current densities dominated by activation overpotential due to the increase in catalyst loading. However, at higher current

densities, ohmic and concentration overpotentials are dominant and the additional thickness of the catalyst layer serves only as an added barrier to the transport of protons and reactants, causing a decrease in performance in spite of the increase in catalyst loading. Finally, in order to match experimental polarisation curves, relatively high values of oxygen diffusivity, compared to experimentally determined values, were used by Springer et al. (1993). Their results thus show that the macro-homogeneous model does not provide an accurate description of the cathode catalyst layer of PEM fuel cells.

2.3.2 Agglomerate Models

In contrast to liquid electrolytes which preferentially flood the micropores of the agglomerates and come into contact with catalyst sites throughout the agglomerates, leaving the macropores open, polymer electrolyte cannot penetrate the micropores of the agglomerates. Polymer electrolyte is therefore only found in the macropores covering the surfaces of the agglomerates, coming into contact only with those catalyst sites which are on the surfaces of the agglomerates. Thus in the agglomerate models for catalyst layers in PEM fuel cells, the micropores are open, as are the macropores for smaller polymer electrolyte contents.

2.3.2.1 No-Film

Eikerling & Kornyshev (1998) developed a mathematical model for PEM fuel cell cathode catalyst layers based on an agglomerate structure of the catalyst layers. In this model, under the assumption that oxygen diffusion through macropores is the dominant transport mechanism, the Stefan-Maxwell equations are used for oxygen transport. Ohm's law is used for protonic transport through the polymer electrolyte, based on the assumption of electroneutrality and neglecting convection. Equations for reaction kinetics are used under the assumption of a linear dependence on oxygen partial pressure. This

dependence on oxygen partial pressure is equivalent to assuming that there is a triple interface of proton-conducting polymer electrolyte, electron-conducting carbon black particles and oxygen transport macropores at the catalyst sites. Thus in the agglomerate model of Eikerling & Kornyshev (1998), there are no films of polymer electrolyte or liquid water obstructing the transport of oxygen to the catalyst sites. Such models are referred to as no-film models.

In their model, Eikerling & Kornyshev (1998) assumed that cathode catalyst layers operate under isobaric, isothermal and steady-state conditions. The protonic current density at the membrane/catalyst layer interface and the total pressure and oxygen partial pressure at the gas diffusion/catalyst layer interface are set as boundary conditions. At sufficiently small overpotentials (i.e. in the activation overpotential region), a linearised approximation of the Butler-Volmer equation for reaction kinetics was used, allowing a full one-dimensional analytical solution to be derived perpendicular to the gas diffusion/catalyst layer interface. The analytical solution reveals that the overpotential is inversely proportional to the square root of both the utilised catalyst surface area (i.e. the triple interface) per unit volume and the rate constant of the electrochemical reaction. Thus fuel cell performance improves with better catalyst utilisation and reaction kinetics. Also, a reaction penetration depth, measured from the membrane/catalyst layer interface, was defined as part of this model, which is also inversely proportional to the square root of both the utilised catalyst surface area per unit volume and the rate constant of the electrochemical reaction. This reaction penetration depth determines the active region of the catalyst layer (i.e. where reactions are occurring) and as this depth decreases, the overpotential of the catalyst layer decreases. If the thickness of the catalyst layer is greater than this depth, then the catalyst located outside of the active region is not utilised, resulting in an inefficient use of expensive platinum catalyst, but with the benefit of a decrease in overpotential losses due to the increase in platinum loading. However, if the thickness is less than the reaction penetration depth, the catalyst utilisation becomes homogeneous throughout the catalyst layer, but PEM fuel cell performance will decrease due to an increase in overpotential losses resulting from the reduction in catalyst loading.

Thus the reaction penetration depth can be considered to be an optimal catalyst layer thickness, providing a good compromise between higher catalyst utilisation and lower overpotential losses.

At high overpotentials, Eikerling & Kornyshev (1998) used a Tafel approximation for the Butler-Volmer equation. The results of a full numerical solution show that as oxygen diffusion becomes slower relative to protonic conductivity, the active region of the catalyst layer becomes progressively smaller near the gas diffusion layer as the current density increases. The remaining inactive region was shown to give an increased ohmic contribution to the overpotential. In the limit of fast oxygen diffusion, for small activation overpotentials and current densities, the active region is confined to a thin region near the membrane. However, as the current density increases and oxygen depletion becomes a factor, the active region moves towards the gas diffusion layer - as is the case for slow oxygen diffusion at lower current densities. Finally, in the oxygen depletion regime at the highest current densities, the concentration contribution to the overpotential decreases with decreasing catalyst layer thickness due to a reduction of transport limitations, and the optimal catalyst layer thickness will be smaller than the reaction penetration depth. Also, it is important to note that the reaction penetration depth decreases exponentially with increasing activation overpotential for Tafel kinetics. Thus, although this depth is an optimal catalyst layer thickness at low current densities, the depth will vary with the operating current density of the fuel cell.

Eikerling & Kornyshev (1998) also studied the effect of polymer electrolyte content on oxygen diffusivity, protonic conductivity and utilised catalyst surface area per unit volume. Their studies were conducted using percolation theory for random, composite media. Results showed that oxygen and proton transport space in the macropores decrease and increase, respectively, with increasing polymer electrolyte content, leading to a decrease in oxygen diffusivity and an increase in protonic conductivity. However, the utilised catalyst surface area per unit volume first increases and then decreases as the content of polymer electrolyte is increased, yielding an optimal polymer electrolyte content. This occurs

because more polymer electrolyte initially increases the contact interface between catalyst sites and polymer electrolyte, but later causes excess polymer electrolyte to block oxygen from reaching the catalyst sites.

Bevers et al. (1997) used a model for PEM fuel cell cathodes similar to the model of Eikerling & Kornyshev (1998), but their model is based on a cylindrical structure for the carbon black and catalysed carbon black solid matrix in the gas diffusion and catalyst layers, respectively, as shown in Figure 2.6.

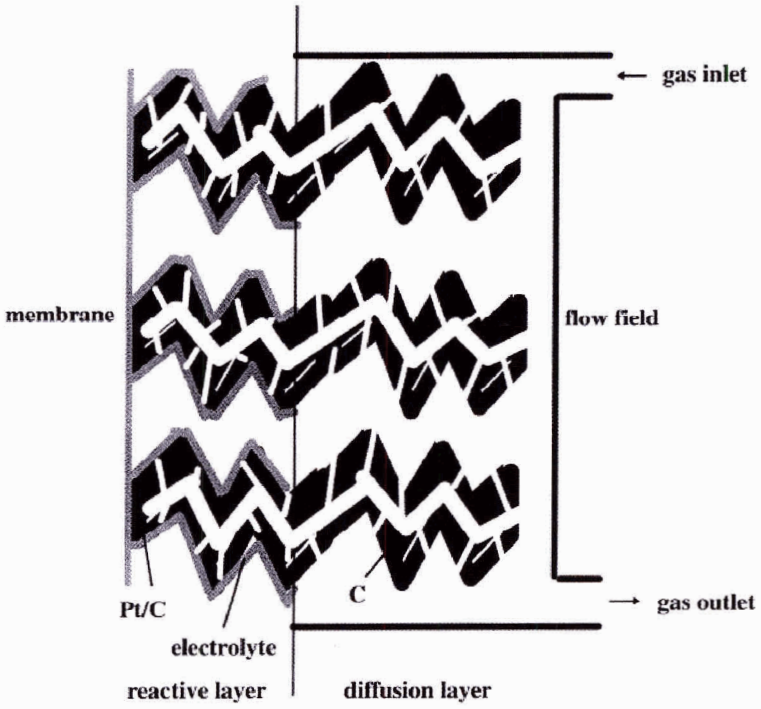

Figure 2.6 - Cylindrical structure for PEM fuel cell cathode (Bevers et al., 1997).

In the Bevers et al. (1997) model oxygen is transported through gas-filled pores inside the solid cylindrical matrix in the gas diffusion and reactive (i.e. catalyst) layers. The oxygen

then reacts at platinum sites on the surface walls of the cylinders, which are also in contact with pores partially filled by polymer electrolyte - such that a triple interface of gas-filled pores, proton-conducting polymer electrolyte and electron-conducting carbon black particles exists at the catalyst sites in the reactive layer. Thus, the overall rate of reaction can be obtained by multiplying the Butler-Volmer equation for the rate of reaction (using the partial pressure of oxygen at the surface walls of the cylinders) by the surface area of catalyst found on the surface of the cylinders. Under the assumption that pores in the gas diffusion and catalyst layers have relatively small diameters, oxygen transport is considered to be due to combined multicomponent molecular and Knudsen diffusion as given by the dusty gas model. Convection (i.e. differential total pressurisation) is also included using Fick's first law with effective diffusion coefficient determined under the assumption of Poiseuille flow. Protonic and electronic current densities are both given by Ohm's law. Liquid water transport in the gas diffusion and catalyst layers is considered to be due to diffusion as given by Fick's first law, and not convection.

Also, since more liquid water closes the pores to gas transport for increasing current densities, and because oxygen transport is much smaller through water-filled versus gas-filled pores, this model accounts for transport limitations (due to water flooding) by allowing the gas diffusion and catalyst layer porosities to decrease with increasing amounts of liquid water. Finally, the model takes into account a detailed energy balance equation rather than assuming isothermal conditions. The energy balance equation includes reversible heat generation of the electrochemical reaction and heat generation due to the irreversible activation overpotential. Heat conduction in the solid phase (neglecting heat conduction in the other phases due to their much lower thermal conductivities) and heat convection in the liquid water and gas phases are considered under the assumption of local thermal equilibrium between the phases.

Assuming steady-state conditions for their cylindrical model, Bevers et al. (1997) performed one-dimensional simulations perpendicular to the gas diffusion/catalyst layer interface using large diffusion coefficients for liquid water - such that there is rapid water

transport and therefore no flooding. Results show the influence of characteristic pore size, which is proportional to the Knudsen diffusion coefficient, and porosity of the gas diffusion and catalyst layers on fuel cell performances. These two parameters have a major influence on concentration overpotential, such that fuel cell performances decrease with lower characteristic pore size and/or porosity, causing transport limitations in molecular and Knudsen diffusion. Also, most of the reactions occur in a thin region of the catalyst layer adjacent to the gas diffusion layer for small characteristic pore sizes or porosities in these layers, resulting in an increase in ohmic overpotential due to higher resistance to protonic conduction.

Kulikovsky et al. (1999) used a no-film agglomerate model for PEM fuel cell cathode catalyst layers similar to the model of Eikerling & Kornyshev (1998). In this model, it is assumed that a triple interface of gas-filled pores, proton-conducting polymer electrolyte and electron-conducting carbon black particles exists at the catalyst sites. Oxygen diffuses through the pores of the catalyst layers and reacts at catalyst sites on the surfaces of the agglomerates, where the Tafel approximation of the Butler-Volmer equation is used for the reaction kinetics. Due to the assumption of constant pressurisation such that there is no convection, the primary mechanism of gas transport in the gas diffusion layer is assumed to be due to ordinary molecular diffusion in the macropores. However, in the catalyst layer, with macropores partially filled by polymer electrolyte, the role of micropores in gas transport is assumed to be of increased importance and, as a result, Knudsen diffusion is also taken into account. In the gas diffusion layer, the Stefan-Maxwell equations are used to describe gas transport and in the catalyst layer, the combined molecular and Knudsen diffusion is described using the dusty gas model. Finally, the electronic and protonic current densities are both given by Ohm's law.

Assuming isothermal and steady-state conditions for the no-film, agglomerate model, Kulikovsky et al. (1999) performed two-dimensional simulations (with one dimension perpendicular to the gas diffusion/catalyst layer interface and the second perpendicular to the inlet to outlet direction of the gas channel) for high and low values of electronic

conductivity. Their results showed that for low values of electronic conductivity relative to oxygen diffusivity, the rate of electrochemical reactions in the catalyst layer is much higher opposite the bipolar plate than the gas channels, where "dead zones" with small reaction rates are formed. Thus platinum loading in these zones may be reduced without significant loss in performance. In contrast, for high values of electronic conductivity relative to oxygen diffusivity, the rate of reactions in the catalyst layer is much higher opposite the gas channels than the bipolar plate and two concentrated streams of electronic current arise around the edges of the gas channels. These concentrated streams may lead to local overheating of the fuel cell. In this case, platinum loading may be reduced in the dead zones in the catalyst layer opposite the bipolar plate. Similar values of electron conductivity and oxygen diffusivity lead to a more uniform distribution of reaction rate and the absence of concentrated streams of electronic current. Thus the results of Kulikovsky et al. (1999) show that by locally reducing platinum loading it is possible to significantly decrease the cost/performance ratio of PEM fuel cell catalyst layers. In general, low electronic conductivity results from porosities that are too high. Therefore a decrease in electronic conductivity is offset by an improvement in gas transport. Also, for low electronic conductivity, current is distributed along the bipolar plates more uniformly, resulting in less local overheating and dead zones in the catalyst layer opposite the gas channels allow for the removal of platinum with almost no loss in performance. This suggests that electrodes with low conductivity, but high permeability to gases, should have better overall performance.

You & Liu (2001) presented a model for the cathode catalyst layer of PEM fuel cells similar to that of Bevers et al. (1997), in which it is assumed that the catalyst layer has a cylindrical structure. In the You & Liu (2001) model, oxygen concentration is set as a boundary condition at the gas diffusion/catalyst layer interface and Fick's first law is used for oxygen diffusion through wet-proofed pores in the catalyst layer. The Butler-Volmer equation is used for the kinetics of the electrochemical reaction under the assumption of a linear dependence on oxygen concentration in the gaseous phase. The protonic current density is set as a boundary condition at the membrane/catalyst layer interface and Ohm's

law is used for the transport of protons under the assumption that convection and diffusion can be neglected. Finally, the solid matrix is assumed to have a much higher electrical conductivity than the protonic conductivity in the polymer electrolyte, such that the electrical potential in the solid matrix can be considered constant.

Assuming isothermal and steady-state conditions for their cylindrical model, You & Liu (2001) derived one-dimensional numerical results perpendicular to the gas diffusion/catalyst layer interface for a range of overpotential values at the membrane/catalyst layer interface. At high overpotentials, oxygen concentration becomes zero at the membrane/catalyst layer interface and the current density reaches a maximum due to oxygen transport limitations. For further increases in overpotential, the reaction kinetics increases and most oxygen is consumed in a thin region of the catalyst layer close to the gas diffusion/catalyst layer interface. Results for varying values of protonic conductivity reveal that at high conductivities the reactions are diffusion-controlled, and most of the reactions occur in a thin region close to the gas diffusion/catalyst layer interface, especially at high overpotentials. However, when protonic conductivity is low, the reactions are controlled by protonic conductivity and, as such, most of the reactions occur in a thin region close to the membrane/catalyst layer interface. Also, the overall current density is lower when the protonic conductivity is low. At low protonic conductivities, overpotential decreases from the membrane interface to the gas diffusion layer interface, causing the reaction rate to drop significantly in the direction of the gas diffusion layer, resulting in lower overall current density.

The results of You & Liu (2001) also reveal that if the porosity of the catalyst layer is high, the resistance to oxygen transport is low and the limiting current density is high, whereas if the porosity is low, oxygen transport resistance is high and the limiting current density is low. At low porosities oxygen is quickly consumed and thus only a thin region of the catalyst layer close to the gas diffusion/catalyst layer interface is active. At higher porosities the whole catalyst layer is active. Thus the overall current density increases with porosity although, unfortunately, increases in porosity are limited by the requirement of

sufficient polymer electrolyte in the catalyst layer to ensure good protonic conductivity. Finally, the results of You & Liu (2001) show that high catalyst surface areas yield high current densities which, if the limiting current density is low, results in part of the catalyst layer becoming inactive. Alternatively, low areas do not provide enough sites for the reactions, yielding lower overall current densities. Thus there exists an optimal catalyst surface area which provides enough sites for the reactions, while limiting the catalyst loading, and this optimal value depends on the operating conditions.

2.3.2.2 Thin-Film

Rho et al. (1994) considered a thin-film, agglomerate model for catalyst layers, similar to that of Iczkowski & Cutlip (1980), except that in this case the model is applied to PEM fuel cells with polymer electrolyte rather than the concentrated phosphoric acid electrolyte considered by Iczkowski & Cutlip (1980). In the model of Rho et al. (1994), it is similarly assumed that a thin film of electrolyte surrounds the agglomerates. The set of equations governing transport phenomena in this model include the Stefan-Maxwell equations for multicomponent gas diffusion through wet-proofed macropores in the gas diffusion and catalyst layers, and Henry's law for dissolution of gaseous reactants into the polymer electrolyte film surrounding the catalyst sites. Fick's first law, in its flat thin-film approximation, is used to describe diffusion of dissolved reactants to the catalyst sites on the surface of the agglomerates, and Ohm's law is used for the transport of protons through the polymer electrolyte to the catalyst sites. After the dissolved reactants have diffused across the polymer electrolyte film, they react at catalyst sites on the surface of the agglomerates in contact with polymer electrolyte. Thus, the overall rate of reaction for each agglomerate can be obtained by multiplying the Butler-Volmer equation for the rate of reaction, using the concentration of dissolved reactant at the surface of the agglomerate, by the surface area of catalyst found on the surface of the agglomerate. In this case, there is no effectiveness factor for reactions occurring inside the agglomerate,

since no polymer electrolyte is found inside the agglomerate and the presence of the polymer electrolyte is necessary for the transport of protons.

Assuming isothermal and steady-state conditions for the thin-film agglomerate model, Rho et al. (1994) derived one-dimensional numerical results perpendicular to the gas diffusion/catalyst layer interface for a PEM fuel cell cathode. The results show that an increase in operating temperature at low pressures improves reaction kinetics and oxygen transport, but also reduces oxygen partial pressures. This is due to an increase of water vapour pressure in the assumed saturated condition, such that the performance at low pressures is more or less temperature independent. However, at higher operating pressures, the later effect is smaller, and performance increases with temperature. Worse fuel cell performances are observed for decreasing either the solubility of oxygen (e.g. by decreasing oxygen partial pressure) or the diffusion coefficient of dissolved oxygen in the polymer electrolyte phase. One of the main factors for high performances of PEM fuel cells is the relatively high solubility of oxygen in polymer electrolyte, which is at least an order of magnitude higher than in phosphoric acid electrolyte. Results at low current densities show that gas diffusion layer thickness has very little effect on fuel cell performances because oxygen transport is considerably faster in the gas phase than in the polymer electrolyte phase (i.e. the diffusion coefficients differ by about two orders of magnitude). However, the sudden decreased performance observed in the concentration overpotential region at high current densities can be attributed to transport limitations in the gas phase of the catalyst and gas diffusion layers. This is due to a significant decrease in macroporosity available for gas phase transport resulting from partial flooding by water droplets or films. In general, these transport limitations can be minimised by increasing the porosity or oxygen partial pressure or by decreasing the thickness of the gas diffusion layer.

Siegel et al. (2003) presented a model for PEM fuel cells, based on a thin-film, flooded agglomerate structure, similar to that of Iczkowski & Cutlip (1980). In the thin-film flooded agglomerate model, macropores in the catalyst layer provide gas diffusion

pathways, while the micropores that make up the agglomerates are flooded with liquid electrolyte. The agglomerates are also surrounded by a thin film of liquid electrolyte. However, unlike liquid electrolyte, polymer electrolyte cannot penetrate the micropores of the agglomerates, and thus is only found as a thin film surrounding the agglomerates. Thus this model is not appropriate for PEM fuel cells, although the similar thin-film agglomerate model of Rho et al. (1994) is appropriate. The only difference between these two models is the existence of an effectiveness factor in the thin-film flooded agglomerate model which accounts for reactions occurring inside the flooded agglomerate for liquid electrolyte rather than just on the agglomerate surface for polymer electrolyte. Setting the effectiveness factor equal to one in this case results in the two models being identical and thus the results presented by Siegel et al. (2003) can also be made applicable to PEM fuel cells.

The model of Siegel et al. (2003) includes anode and cathode gas channels with laminar fuel and oxidant flow, respectively, along the surfaces of the MEA, reactant diffusion into the gas diffusion layers, and reactant gas flows through the macropores of the gas diffusion and catalyst layers by convection and diffusion. This is followed by dissolution into and diffusion through the thin film of polymer-electrolyte to the agglomerates, through which the reactants diffuse, reacting at catalyst sites along the way. The governing transport equations used in the mathematical model include Darcy's law for gas phase convection through the porous gas diffusion and catalyst layers and Fick's law for gaseous species diffusion, with effective diffusion coefficients calculated using an approximate solution to the full set of Stefan-Maxwell equations. The dissolved reactant concentration at the gas macropore/polymer-electrolyte interface is determined using Henry's law, with diffusion to the agglomerate surfaces given by the linearised version of Fick's first law for a flat thin film.

Inside the agglomerates, there are transport limitations due to oxygen diffusion. The impact of this effect on the electrochemical reactions is characterised by an effectiveness factor in the Butler-Volmer equation used for reaction kinetics. Also, in the Butler-Volmer

equation the electrical potential associated with transport of electrons through the solid matrix is assumed to be constant over each catalyst layer due to the relatively high electronic conductivities. Water dissolved in the polymer electrolyte phase of the catalyst layers and in the membrane is transported by diffusion and electro-osmotic drag, but convective transport is neglected - based on the assumption that pressure differences are not sufficient to cause significant Darcy flow. Flooding of the gas diffusion and catalyst layers by liquid water is not taken into account. Ohm's law is used for protonic current density in the membrane and polymer electrolyte in the catalyst layers. Finally, the model includes a detailed energy balance equation, with source terms for reversible and irreversible heat generation in the electrochemical reactions, and ohmic heating due to protonic current resistance, rather than assuming isothermal conditions.

Assuming steady-state conditions, Siegel et al. (2003) derived computational solutions in two dimensions (one perpendicular to the gas diffusion/catalyst layer interfaces and the second parallel to the gas channels from inlet to outlet) using parameters based on the observed agglomerate structure of catalyst layers manufactured by ElectroChem Inc. and quantified using image analysis and enhancement software. Their results show that as porosity and associated permeability of the catalyst layers decrease, the resistance to reactant transport by convection and diffusion increases, resulting in an increase of the concentration overpotential. However, as porosity decreases, there is also an associated increase in the pore volume fraction of polymer electrolyte, which improves protonic conductivity, causing a decrease in the ohmic overpotential. The ElectroChem Inc. catalyst layers are relatively thick (i.e. 100 μm), with relatively long reactant transport and ionic conduction pathways, and therefore they are particularly sensitive to changes in reactant permeability and ionic conductivity. Thus for catalyst layer porosities greater (less) than the observed optimal porosity, fuel cell performances drop off rapidly - due to a faster rate of increase in ohmic (concentration) overpotential than the associated rate of decrease in concentration (ohmic) overpotential.

2.3.2.3 Multiple Thin-Film

Baschuk & Li (2000) considered a model for the cathode catalyst layer, similar to the thin-film agglomerate model of Rho et al. (1994). In this model, it is also assumed that a thin film of polymer electrolyte surrounds the agglomerates, however this model takes into account the effects of variable degrees of water flooding in the catalyst layer (i.e. not flooded, partially flooded and fully flooded). This is accomplished by including another thin film of liquid water surrounding the thin film of polymer electrolyte and allowing the liquid water film to have variable thickness as shown in Figure 2.6 for the partially flooded case. Thus this approach can be described as a multiple thin-film agglomerate model.

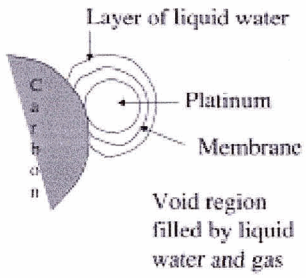

Figure 2.7 - Partially flooded catalyst layer (Baschuk & Li, 2000).

Another feature of the model is that it also allows flooding of the cathode gas diffusion layer by liquid water. In general, in the cathode, oxygen supplied at the gas channels diffuses through wet-proofed macropores in the gas diffusion and catalyst layers, and dissolves into the outer liquid water film surrounding the agglomerates from the gas phase according to Henry's law. Oxygen then diffuses across both the outer liquid water and inner polymer electrolyte films and reacts at catalyst sites on the surface of the agglomerates in contact with polymer electrolyte. Thus, the overall rate of reaction for each agglomerate can be obtained by multiplying the Butler-Volmer equation for the rate

of reaction, using the concentration of dissolved oxygen at the surface of the agglomerate, by the surface area of catalyst found on the surface of the agglomerate.

In this model oxygen transport in the macropores of the gas diffusion and catalyst layers is determined using Fick's first law with a bulk diffusion coefficient of oxygen in humidified air, assuming that the macropores within the gas diffusion and catalyst layers are sufficiently large that Knudsen diffusion can be neglected. Oxygen transport in the thin layers of liquid water and polymer electrolyte are modelled using the linearised version of Fick's first law for a flat thin film (assuming that these films are thin in comparison with the characteristic radius of the agglomerates) with diffusion coefficients of oxygen in liquid water and polymer electrolyte, respectively. Also, the model takes into account liquid water transport in the polymer electrolyte of the catalyst layers and membrane as a result of electro-osmotic drag and convection due to pressure gradients. Diffusion is neglected, however, since it is assumed that the polymer electrolyte is fully hydrated, such that the water content in the polymer electrolyte is uniform. Finally, assuming electroneutrality in the polymer electrolyte, protonic transport is given by Ohm's law, together with a term due to convection.

Assuming isothermal and steady-state conditions for the multiple thin-film agglomerate model, Baschuk & Li (2000) derived one-dimensional results perpendicular to the gas diffusion/catalyst layer interface. Using the set of design parameters for a given PEM fuel cell, the degree of flooding in the cathode catalyst layer was varied by changing the thickness of the liquid water film. The degree of flooding in the gas diffusion layer was also varied, changing the concentration of oxygen available for reaction at the catalyst sites (and therefore the concentration overpotential in the cathode catalyst layer), until the model polarisation curve was consistent with experimental data for the same fuel cell. Results show that cell voltage is minimally affected by water flooding in the cathode catalyst layer. This is because the diffusion coefficient of dissolved oxygen in liquid water is much higher than that in polymer electrolyte, and therefore the transport resistance of polymer electrolyte film in the catalyst layer dominates the overall resistance of the films

surrounding the agglomerates. Thus the added resistance due to an increase in the thickness of the liquid water film has only a small effect. In contrast, a small amount of liquid water in the gas diffusion layer can severely decrease performance at high current densities, because of the decrease in available macropores for gas diffusion in the much thicker gas diffusion layer. In general, the results also show that increasing temperature and decreasing pressure both improve fuel cell performance by reducing the amount of liquid water flooding through increased evaporation and decreased condensation, respectively.

2.3.3 Comparison of Macro-Homogeneous and Agglomerate Models

Broka & Ekdunge (1997) compared two models for cathode catalyst layers in PEM fuel cells: a macro-homogeneous model similar to that of Springer et al. (1993) and a thin-film flooded agglomerate model similar to that of Siegel et al. (2003). For oxygen transport in cathode catalyst layers, Broka & Ekdunge (1997) assumed that oxygen diffuses from the gas diffusion/catalyst layer interface towards the catalyst sites either through only polymer electrolyte (for the case of the macro-homogeneous model in which the entire catalyst layer is filled by polymer electrolyte), or first through gas-filled macropores and then through polymer electrolyte (in the case of the thin-film flooded agglomerate model).

In the macro-homogeneous model, Fick's first law is used for the transport of dissolved oxygen through the polymer electrolyte in the catalyst layer. However, in the thin-film flooded agglomerate model, diffusion of oxygen through the gas phase in the catalyst layer macropores is neglected, since the resistance to oxygen transport is significantly less through the gas phase than through the polymer-electrolyte phase. Only diffusion of oxygen through the film of polymer electrolyte surrounding the agglomerates is taken into account. This film, considered thin in comparison with the radius of the agglomerates, is approximated by the linearised version of Fick's first law for a flat thin

film. Inside the agglomerates, the effect of transport limitations (due to oxygen diffusion) on the electrochemical reactions is characterised by an effectiveness factor in the Tafel approximation for the Butler-Volmer equation used for reaction kinetics. Finally, the potential gradient in the solid matrix phase is neglected, since electronic conductivity in the carbon black solid structure is much higher than protonic conductivity in the polymer electrolyte, while Ohm's law is used for protonic transport in the polymer electrolyte.

Broka & Ekdunge (1997) derived numerical results in one dimension perpendicular to the gas diffusion/catalyst layer interface using the same model parameters for both the macro-homogenous and thin-film flooded agglomerate models, and assuming isothermal and steady-state conditions. Simulated polarisation curves for the two models show that the thin-film flooded agglomerate model gives lower overpotentials compared with experimental data. In contrast, the macro-homogeneous model predicts considerably higher overpotentials due to the fact that, at high current densities, oxygen does not penetrate into the inner part of the catalyst layer, resulting in a very uneven reaction distribution. Increasing the value of the oxygen diffusivity relative to experimentally determined values in the macro-homogeneous model results in oxygen concentration profiles (and therefore reaction rates) that are more evenly distributed over the catalyst layer and lower overpotentials.

In contrast, the thin-film flooded agglomerate model gives a more uniformly distributed reaction rate in the catalyst layer, since the gaseous oxygen concentration is constant throughout the catalyst layer. In this case, the highest reaction rates are obtained in the inner part of the catalyst layer adjacent to the membrane, where the highest overpotential values are found. Concentration overpotential in the thin-film flooded agglomerate model is dependent on the transport restriction of the thin film surrounding the agglomerates, with small increases in film thickness causing relatively large increases in concentration overpotential. Thus the simulations of catalyst layer structure indicate that the thin-film flooded agglomerate model gives a better representation of the catalyst layer than the macro-homogeneous model. This indicates that the high performance of PEM

fuel cells is due to gas macropores which enable utilisation of the entire depth of the catalyst layer even at high current densities.

Gloaguen & Durand (1997) and Gloaguen et al. (1998) both compared a macro-homogeneous model for cathode catalyst layers to a flooded agglomerate model, similar to the model of Ridge et al. (1989), in which the micropores that make up the agglomerate are flooded with liquid electrolyte. However, this model is not appropriate for PEM fuel cells, although the agglomerate model of Bevers et al. (1997) is appropriate. The only difference between these two models is the existence of an effectiveness factor in the flooded agglomerate model. When this factor is set equal to one the two models become identical, and thus the results of Gloaguen & Durand (1997) and Gloaguen et al. (1998) can also be made applicable to PEM fuel cells. In the macro-homogeneous model of Gloaguen & Durand (1997) and Gloaguen et al. (1998), Fick's first law and Ohm's law are used to describe the distribution of oxygen concentration and the protonic current density, respectively, in the catalyst layer. In the flooded agglomerate model, once the oxygen diffuses through the gas-filled macropores of the catalyst layer, it dissolves directly into the micropores of the flooded agglomerate and diffuses towards the centre of the agglomerate, reacting at available catalyst sites along the way. In this case, the effects of oxygen transport in gas-filled macropores and flooded agglomerates, as well as Ohm's law for protonic current density, are simulated using the effectiveness factor. In both models, a Tafel approximation is used for the reaction kinetics.

Gloaguen & Durand (1997) and Gloaguen et al. (1998) derived numerical results in one dimension perpendicular to the gas diffusion/catalyst layer interface. They used the same model parameters for both the macro-homogenous and flooded agglomerate models, assuming isothermal and steady-state conditions. Polarisation curves for the two models were compared with experimental data obtained for catalyst layers made from catalysed carbon black powder suspended in polymer electrolyte solution both with or without PTFE. Results show that, for the macro-homogeneous model, overpotential in the cathode is considerably overestimated due to oxygen diffusion limitations. In contrast, there is

good agreement between the numerical and experimental results for the flooded agglomerate model. These results are consistent with those of Broka & Ekdunge (1997). Thus, the assumption that oxygen diffuses only through the polymer electrolyte phase cannot be valid in the case of PEM fuel cell cathode catalyst layers, and the presence of gas-filled macropores is essential for the higher rate of oxygen transport to the catalyst sites observed in experimental data.

2.3.4 Assessment of Catalyst Layer Models

Many studies of PEM fuel cell catalyst layers have been presented in this chapter. In general, these studies are based on parameters characterising catalyst layer composition and structure, the transport of reacting species and reaction kinetics. The studies introduced and discussed here have all assumed different models for the composition and structure of the catalyst layers. In this section, an overall summary of existing models is presented, and a recommendation is made for implementation of an appropriate catalyst layer model for PEM fuel cell simulations.

Bernardi & Verbrugge (1991, 1992) and Springer et al. (1993) presented macro-homogeneous models for catalyst layers based on similar models previously applied to catalyst layers in contact with liquid electrolyte. Their models of charge and mass transport coupled to electrochemical reactions assume that polymer electrolyte completely fills the catalyst layer pores, such that the catalyst layers are a homogeneous domain of polymer electrolyte and solid matrix in which the transport of protons, dissolved reactants and electrons are simply superposed onto each other.

Eikerling & Kornyshev (1998) and Kulikovsky et al. (1999) presented catalyst layer models based on an assumed structure of microporous agglomerates separated by macropores, and Bevers et al. (1997) developed a catalyst layer model based on an assumed cylindrical structure. In all three of these models, a triple interface of gaseous

reactant transport pores, proton-conducting polymer electrolyte and electron-conducting carbon black particles is assumed to exist at the catalyst sites. Rho et al. (1994) considered a thin-film agglomerate model for PEM fuel cell catalyst layers, in which reactants diffuse through interconnected gas-filled macropores in the catalyst layer before dissolving into a thin film of polymer electrolyte surrounding catalyst sites on the surfaces of the agglomerates.

Baschuk & Li (2000) considered a multiple thin-film agglomerate model for the cathode catalyst layer, similar to that of Rho et al. (1994). In this model, it is also assumed that a thin film of polymer electrolyte surrounds the agglomerates. However, this model additionally accounts for transport limitations due to water flooding in the catalyst layer through the inclusion of another thin film of liquid water surrounding the thin film of polymer electrolyte. By varying the thickness of the thin film of liquid water, the catalyst layer is allowed to be fully flooded, partially flooded or not flooded.

In general, the conclusions which can be drawn from the modelling studies reviewed in this chapter are as follows:

- Results derived by Bernardi & Verbrugge (1991, 1992) and Springer et al. (1993) for their macro-homogeneous models do not fit the experimental data, suggesting that only a fraction of the catalyst layers are filled with polymer electrolyte.
- Results derived by Rho et al. (1994), Bevers et al. (1997) and Baschuk & Li (2000), among others, show that agglomerate models satisfactorily predict experimental data.
- Comparisons of polarisation curves derived from PEM fuel cell simulations for agglomerate and macro-homogeneous catalyst layer models with experimental data show that the agglomerate models give better predictions than the macro-homogeneous models (Broka & Ekdunge, 1997; Gloaguen & Durand, 1997; Gloaguen et al., 1998).

Thus the results from modelling studies show that agglomerate models for PEM fuel cell catalyst layers better predict experimental data than macro-homogeneous models. In general, the success of agglomerate models arises from the fact that a trade-off exists between proton conductivity and reactant transport as the limiting processes in catalyst layers, since polymer electrolyte enhances proton conductivity but restricts the transport of reactants.

The modelling results reviewed in this chapter are in agreement with those from experimental studies of catalyst layers reviewed in Chapter 1. These also suggests an agglomerate structure for the catalyst layers since:

- The structure of catalyst layers observed in SEM and TEM micrographs by Ticianelli et al. (1991), Cheng et al. (1999) and Siegel et al. (2003) is found to consist of agglomerates bound together by PTFE or polymer electrolyte. Macropores between the agglomerates provide pathways for the transport of reactants.
- Using the results of experimental techniques such as mercury porosimetry, Uchida et al. (1995) showed that polymer electrolyte is found only in macropores, due to its large molecular size not allowing penetration into agglomerate micropores. Thus polymer electrolyte is restricted to agglomerate surfaces as a binding agent or to the spaces between individual agglomerates.
- The experimental results of Ticianelli et al. (1988b) and Uchida et al. (1995) indicate that, for a given catalyst layer, there is an optimal amount of polymer electrolyte which depends on the thickness of the catalyst layer. This optimal value yields a lower volume fraction of polymer electrolyte in the catalyst layer than would be the case if void spaces of the porous matrix were completely filled by polymer electrolyte, which contradicts the fundamental assumption of the macro-homogeneous model.

Thus the results of both experimental and modelling studies show that agglomerate models for PEM fuel cell catalyst layers are more appropriate than macro-homogeneous models.

However, of the agglomerate models presented in this chapter, it remains to determine the most appropriate model for PEM fuel cell simulations. For PEM fuel cells the active surface is limited to the catalyst sites located on the external surface of the agglomerates in contact with polymer electrolyte (since polymer electrolyte is necessary for the transport of protons). In the models of Eikerling & Kornyshev (1998), Kulikovsky et al. (1999) and Bevers et al. (1997) the catalyst sites are also directly in contact with the reactants in the gas-filled pores, forming a triple interface together with the polymer electrolyte and solid matrix. However, in the models of Rho et al. (1994) and Baschuk & Li (2000), the catalyst sites are completely covered by polymer electrolyte, and the reactants must dissolve into and diffuse through polymer electrolyte before reaching the catalyst sites. The models of Rho et al. (1994) and Baschuk & Li (2000) are therefore considered more appropriate for PEM fuel cell simulations, since it is probable that a thin film of polymer electrolyte surrounds the utilised catalyst sites for the following reasons:

- The geometrical complexity of the triple interface in the models of Eikerling & Kornyshev (1998), Kulikovsky et al. (1999) and Bevers et al. (1997), limits the potential reaction surface area and should result in much lower values for catalyst utilisation than those determined experimentally for thin-film catalyst layers by Cheng et al. (1999).
- Based on the experimental results outlined above, the agglomerates are bound together by polymer electrolyte. As a result, a film of polymer electrolyte should cover the agglomerates and therefore also the catalyst sites on the external surfaces of the agglomerates.

Finally, in comparing the models of Rho et al. (1994) and Baschuk & Li (2000), it is noted that flooding of the catalyst layers by liquid water is common in PEM fuel cells (as discussed in Chapter 1). Since polymer electrolyte is composed of PFSA polymer, which has both a hydrophobic PTFE backbone and side chains with hydrophilic sulphonic acid heads, the flooding causes thin films of liquid water to form on hydrophilic surface regions

of polymer electrolyte. As a result, transport limitations occur, since reactants must dissolve into and diffuse through the liquid water before reaching the polymer electrolyte surrounding the catalyst sites. These transport limitations should be taken into account since they will cause concentration overpotentials. The model of Baschuk & Li (2000) includes these considerations and is recommended for implementation in PEM fuel cell simulations.

Thus, of the various agglomerate models presented in this chapter, it is concluded that the most appropriate model for PEM fuel cell catalyst layers is the multiple thin-film agglomerate model of Baschuk & Li (2000). Therefore the CFD implementation of PEM fuel cell catalyst layers in this thesis is based on this model. The model of Baschuk & Li (2000) is isothermal and one-dimensional and it is adapted for non-isothermal and three-dimensional implementation in Chapter 4. First, however, the basic model used for the entire PEM fuel cell is presented in Chapter 3.

Chapter 3

Proton Exchange Membrane Fuel Cell Model

In general, the results of previous macroscopic modelling studies show that macro-homogeneous models for PEM fuel cell membranes are consistent with experimental results. For PEM fuel cell gas diffusion and catalyst layers, however, agglomerate models better predict experimental results than macro-homogeneous models. In this chapter, a PEM fuel cell model is presented, which is herein referred to as the thesis model. In the thesis model, agglomerate models are used for the catalyst and gas diffusion layers and a macro-homogeneous model is used for the membrane. As discussed in Chapter 2, an appropriate model to consider for PEM fuel cell catalyst layers is the multiple thin-film agglomerate model, and this model is presented in Chapter 4. In order to include the effects due to alternating contact of the gas channels and bipolar plates with the gas diffusion layers and changing concentrations along the gas channels on transport processes in PEM fuel cells, the thesis model is fully three-dimensional. Also, because the governing equations in the macroscopic models used in the thesis model are strongly non-linear, analytical solutions are only available under simplified conditions. In order to obtain general solutions for the thesis model, essential for design and optimisation, a CFD implementation is necessary. Based on compatibility, a new PEM fuel cell implementation (Li & Becker, 2004) in the general purpose CFD software package FLUENT™ (Fluent Inc., 2001) is chosen for the implementation of the thesis model.

3.1 Equations and Boundary Conditions

In the thesis model, steady-state conditions are assumed to apply. The set of agglomerate model equations governing transport of reactants in the gas diffusion and catalyst layers includes Fick's first law for diffusion of the gaseous phase through wet-proofed macropores - with effective diffusion coefficients calculated using an approximate solution to the full set of Stefan-Maxwell equations, and an assumption that the macropores are large enough such that Knudsen diffusion can be neglected. For the multiple thin-films in the catalyst layers, Henry's law is used for the dissolution of gaseous reactants into the outer liquid water film. Fick's first law, in its flat thin-film approximation, is used for diffusion of dissolved reactants through the outer liquid water film and inner polymer electrolyte film to the catalyst sites on the surfaces of the agglomerates. The overall rate of reaction for each catalyst layer agglomerate can be obtained by multiplying the Butler-Volmer equation (using the concentration of dissolved reactant at the surface of the agglomerate) by the surface area of catalyst found on the agglomerate surface.

Ohm's law is used for both electron transport through the bipolar plates and solid matrix in the gas diffusion and catalyst layers and proton transport through the membrane and polymer electrolyte in the catalyst layers. Liquid water transport through the membrane is governed by electro-osmotic drag and diffusion. In the catalyst and gas diffusion layers liquid water transport is described by Darcy's law, taking into account capillary pressure and relative permeability as a function of liquid water saturation. Diffusional limitations of reactants, due to a reduction in porosity of the gaseous phase caused by the presence of liquid water, is also taken into account.

The temperature distribution in the PEM fuel cell is governed by the conservation of energy equation, taking into account local heat production in the catalyst layers due to the activation overpotentials and reversible changes in entropy of the electrochemical

reactions. Heat production in the catalyst layers and membrane due to ohmic resistance, and the heat associated with evaporation and condensation of water, are also taken into account.

The thesis model is based on the typical design for a single fuel cell with straight gas channels, a schematic of which is shown in Figure 1.1 together with an associated co-ordinate system. Note that this schematic, which is an interior cross-sectional view along the z-axis of the PEM fuel cell, is not to scale, nor is a typical number of gas channels for a fuel cell shown. In this schematic, many more channels are assumed to be present in the positive and negative x-directions. In general, although not shown in Figure 1.1, gaskets (i.e. seals) in PEM fuel cells prevent leakage of the gaseous, liquid water and protonic phases at external boundaries of the MEA with normals in the positive and negative x- and z-directions (i.e. the gaskets form impermeable walls, as do the bipolar plates in the positive and negative y-directions). Note that protonic current arises from the flow of a charged ionic species and therefore behaves as a fluid rather than as a current carried by electrons. Gaskets are also electrical insulators (i.e. they do not conduct electrons) and have poor thermal conductivity (i.e. they form adiabatic boundaries).

It is further assumed that there is no transfer of electrical current and that negligible heat exchange occurs between the surrounding environment and external boundaries of the bipolar plates (with normals in the positive and negative x- and z-directions). Thus there is no flux of gases, liquid water or heat and protons or electrons (i.e. no current densities) through the external boundaries of the entire fuel cell in the positive and negative x- and z-directions, except for the fluxes of gases, liquid water and heat through the inlets and outlets of the gas channels. Moreover, because the volume enclosed by boundaries marked with dashed lines in Figure 1.1 is symmetric across the boundary surfaces with normals in the positive and negative x-directions, any fluxes through the volume boundaries in the positive and negative x-directions must be caused by the external boundary conditions in the positive and negative x-directions. Thus, since there are no fluxes through the external boundaries in the positive and negative x-directions,

there must also be no fluxes through the boundary surfaces of this volume with normals in the positive and negative x-directions. Finally, this volume is extended throughout the PEM fuel cell in the positive and negative z-directions to the external boundaries, and the resulting volume can be assumed to be representative of the fuel cell as a whole, and therefore is used as the thesis model volume.

In the thesis model, it is assumed that both the anode and cathode bipolar plates and gas channels are identical, x-axis dimensions of the gas channels and the bipolar plates between the gas channels are equal, and that the gas channels have equal dimensions in the x- and y-directions (i.e. are square). Also, it is assumed that the anode and cathode gas diffusion layers are identical. Although state-of-the-art, thin-film anode catalyst layers can be thinner than cathode catalyst layers, for operation with hydrogen-rich reformate, carbon monoxide poisoning requires the use of thicker anode catalyst layers. As a result, it is assumed in the thesis model that the anode and cathode catalyst layers are identical. Finally, the length of the thesis model corresponds to gas channels lengths, as measured from the inlets to the outlets in contact with the MEA. The dimensions of the thesis model (Wang et al., 2003) are presented in Table 3.1. These dimensions, together with all the other relevant parameters presented subsequently for the thesis model, are also summarised in Appendix A.

Table 3.1 - Dimensions of thesis model.

Parameter	Description	Value
d_{gc}	Side dimensions of gas channels	1×10^{-3} m
l_{gc}	Length of gas channels	7×10^{-2} m
s_{mea}	Superficial area of MEA	7×10^{-5} m^2
t_{gdl}	Thickness of gas diffusion layers	2.6×10^{-4} m
t_{cl}	Thickness of catalyst layers	1.29×10^{-5} m
t_m	Thickness of membrane	5.1×10^{-5} m

In the thesis model, it is assumed that the gas diffusion and catalyst layers are homogeneous and isotropic porous media in which the volumetric fractions occupied by carbon in the gas diffusion layers and carbon/platinum in the catalyst layers are the same (i.e. $\varphi_{C/Pt} = 0.40$). The remaining volumetric fraction in the gas diffusion layers not occupied by carbon and the assumed porosity of $\varphi_{gdl} = 0.40$ (Wang et al., 2003) is occupied by PTFE (i.e. 0.20). This is a similar PTFE volumetric fraction as in the modelling study of Bernardi & Verbrugge (1991). In the catalyst layers, the volumetric fraction occupied by polymer electrolyte is assumed to be $\varphi_m = 0.25$, and the porosity is assumed to be $\varphi_{cl} = 0.25$ (You & Liu, 2001). For the carbon/platinum volumetric fraction of 0.40, this yields a PTFE volumetric fraction of 0.10, similar to the thin-film catalyst layers of Escribano & Aldebert (1995).

PEM fuel cells operate at relatively low temperatures and, in the thesis model, it is assumed that the operating temperature of the fuel cell is 70 °C (343.15 K). Although the thesis model is not isothermal, an approximate operating temperature of 70 °C is maintained by setting the temperatures of gases entering the gas channels to 70 °C. Also, although the thesis model is not isobaric, an approximate operating pressure of 3 atm (303,975 Pa) for the anode and cathode gases is maintained by setting the pressures of gases leaving the anode and cathode gas channels to 3 atm. The fuel and oxidant enter the gas channels at prescribed mass flow rates and it is assumed in the thesis model that both flow in the same direction. Finally, the relative humidities of gases entering the anode and cathode gas channels are assumed to be 100 % (Wang et al., 2003).

3.1.1 Bipolar Plates

The bipolar plates are made of graphite which is normally quite porous. However, the bipolar plates are manufactured using techniques that make the graphite more dense and

minimise the porosity available for the transport of gases. In one such method, Bulk Molding Compounds Inc. manufactures thermoset resin bipolar plates by compounding vinyl ester resin with graphite powder, followed by compression molding to make non-porous graphite bipolar plates. In general, these composite plates are better than pure graphite plates because they are more durable and also cheaper and quicker to manufacture.

In the thesis model, the bipolar plates are assumed to be porous media, although with extremely low porosity, and therefore minimal transport of gases, such that these plates are considered to form impermeable walls and have zero gas velocities inside. Thus the bipolar plates only allow for the conduction of electrons and heat. The conduction of electrons is given by Ohm's law, which states that:

$$\vec{i}_s = -\sigma_s^{eff}\,\vec{\nabla}\phi_s \tag{3.1}$$

where $\vec{i}_s$ is the superficial current density of electrons, σ_s^{eff} is the effective electrical conductivity of electrons and ϕ_s is the electrical potential in the solid graphite phase. Note that the superficial current density and effective electrical conductivity refer to the entire porous medium rather than just to the solid graphite phase. Taking the gradient of Equation (3.1) yields:

$$\vec{\nabla}\cdot\left(\sigma_s^{eff}\vec{\nabla}\phi_s\right)+S_s=0 \tag{3.2}$$

where the source term S_s, given by:

$$S_s = \vec{\nabla}\cdot\,\vec{i}_s \tag{3.3}$$

is the production or consumption of electrical current per unit volume, which is positive for the production of electrical current. Note that the production of electrical current

corresponds to the consumption of electrons since, by convention, current density is defined as the flow of positive charges. The current density of electrons is therefore in the opposite direction to the flow of electrons. Note that in the bipolar plates the source term is equal to zero since there are no electrochemical reactions.

As discussed previously in Section 3.1, for the thesis model, the boundary conditions applied to Equation (3.2) at boundary surfaces of the bipolar plates (with normals in the positive and negative x- and z-directions) require that the normal superficial current densities of electrons (i.e. the normal gradients of electrical potential in the solid phase) are equal to zero. In the case of a single fuel cell, at the external boundary surfaces of the bipolar plates with normals in the positive and negative y-directions, it is assumed that the electrons are transported through highly conductive solid metal plates in contact with the bipolar plates before being transported from the anode to cathode through an external circuit. A fixed potential difference load is applied between the anode and cathode and (as a result of the relatively high conductivity of the metal plates) the electrical potentials are assumed to be uniform at the bipolar plate external boundary surfaces. Since the anode is similar to a Standard Hydrogen Electrode, which by definition has a potential of zero, the electrical potential is set equal to zero at the external anode bipolar plate boundary. The electrical potential at the external cathode bipolar plate boundary is then equal to the potential difference load minus any contact resistances.

At boundaries between the bipolar plates and the gas channels, the normal superficial electronic current densities (i.e. the normal gradients of electrical potential in the solid phase) are set equal to zero, since the gases and liquid water in the gas channels act as electrical insulators. It is important to note that, unlike fluids, the flow of electrons does not obey a no-slip condition along boundaries between different phases (i.e. there is a surface conduction of electrons). At the boundaries of the bipolar plates with the gas diffusion layers, the superficial electronic current densities are continuous, although there can be discontinuities in the electrical potential due to contact resistances.

In the bipolar plates, the heat flux due to conduction, $\vec{q}$, is given by Fourier's law, which states that:

$$\vec{q} = -k_{total}\vec{\nabla}T \tag{3.4}$$

where k_{total} is the total thermal conductivity of the porous medium, which is effectively the thermal conductivity of the solid graphite phase, k_s, and T is the temperature. Taking the gradient of Equation (3.4), with $k_{total} = k_s$, yields:

$$\vec{\nabla}\cdot\left(k_s\vec{\nabla}T\right) + S_h = 0 \tag{3.5}$$

where the source term S_h (i.e. the rate of production or consumption of heat energy per unit volume, which is positive for heat production) is given by:

$$S_h = \vec{\nabla}\cdot\vec{q} = \frac{i_s^2}{\sigma_s^{eff}} \tag{3.6}$$

Equation (3.6) takes into account the ohmic heat generated by the flow of electrons in the bipolar plates and assumes that steady-state conditions apply, such that the heat produced in the bipolar plates must be conducted away.

As discussed previously in Section 3.1, for the thesis model, the boundary conditions applied to Equation (3.5) at the external boundaries of the bipolar plates (with normals in the positive and negative x- and z-directions) require that the normal heat fluxes due to conduction (i.e. the normal gradients of temperature) are equal to zero. In the case of a single fuel cell, at the external boundaries of the bipolar plates (with normals in the positive and negative y-directions), it is assumed that the solid metal plates in contact with the bipolar plates have relatively high thermal conductivities. It is also assumed that the metal plates are exposed to external cooling flows, which are sufficient to maintain a

uniform desired operating temperature for the PEM fuel cell in the metal plates, such that the temperature at the external boundary surfaces of the bipolar plates (with normals in the positive and negative y-directions) can be set equal to the operating temperature if local thermal equilibrium is assumed. Finally, at the boundaries of the bipolar plates with the gas channels and diffusion layers, the heat fluxes due to conduction are continuous.

In the thesis model, the bipolar plates are assumed to be BMC 940 vinyl ester thermosets manufactured by Bulk Molding Compounds Inc. These plates have the following properties: a density of the solid of $\rho_s = 1.8 \times 10^3$ kg m^{-3}, a specific heat of the solid of $c_{P,s} = 9.4 \times 10^2$ J (kg K)$^{-1}$, an effective electrical conductivity of $\sigma_s^{eff} = 7.5 \times 10^3$ S m^{-1} and a thermal conductivity of the solid of $k_s = 31.5$ W (m K)$^{-1}$ at 70 °C - which varies only slightly with temperature in the typical operating range of PEM fuel cells and thus can be considered a constant. These values are stated in the technical data sheet supplied by Bulk Molding Compounds Inc. (2001), although it is important to note that the BMC 940 bipolar plates have different values for the specific heat, and the electrical and thermal conductivities, in and through the plane of compression (i.e. perpendicular and parallel to the molding pressure, respectively). Averages of these non-isotropic values are used for the bipolar plates in the thesis model.

3.1.2 Gas Channels

The velocities, $\vec{v}$, of the multicomponent gases in the anode and cathode gas channels are determined by applying the fundamental conservation laws. The conservation of mass can be expressed in the form of the steady-state equation of continuity (Bird, Stewart & Lightfoot, 2002):

$$\vec{\nabla} \cdot (\rho \vec{v}) = S_g \tag{3.7}$$

where ρ is the density. The source term S_g is the rate of production or consumption of the total mass of gases per unit volume, which is positive for mass production. Also, although the flow of the gases is assumed to be incompressible, the density is not a constant because compositions of the gases vary as a result of electrochemical reactions occurring in the PEM fuel cell. The source term S_g is equal to zero in the anode and cathode gas channels because there are no electrochemical reactions occurring, and phase changes in the gas channels are neglected in the thesis model.

The conservation of linear momentum for steady-state flow in the absence of external body forces (i.e. neglecting gravity) yields (Bird, Stewart & Lightfoot, 2002):

$$\vec{\nabla}\cdot\left(\rho\vec{v}\vec{v}\right)+\vec{\nabla}P+\vec{\nabla}\cdot\tau=\vec{S} \tag{3.8}$$

where P is the thermodynamic pressure and τ is the viscous stress tensor. The vector source term $\vec{S}$ is the rate of production or consumption of linear momentum of the gases per unit volume, which is positive for momentum production. This source term is also assumed to be equal to zero in the anode and cathode gas channels. Finally, assuming that the gases are isotropic Newtonian fluids with no dilatational (i.e. bulk) viscosity, the viscous stress tensor is given by (Bird, Stewart & Lightfoot, 2002):

$$\tau=-\mu\left[\vec{\nabla}\vec{v}+\left(\vec{\nabla}\vec{v}\right)^{t}\right]+\frac{2}{3}\mu\left(\vec{\nabla}\cdot\vec{v}\right)\delta \tag{3.9}$$

where μ is the viscosity of the multicomponent gas as defined below and δ is the unit tensor.

The temperatures, T, of the gases in the anode and cathode gas channels are determined by applying the fundamental law of conservation of energy. Assuming steady-state conditions and that Fourier's law applies for heat conduction, the conservation of

energy for multicomponent gases (composed of n species) in the absence of external body forces (i.e. neglecting gravity) can be expressed in the following form (Bird, Stewart & Lightfoot, 2002):

$$\vec{\nabla}\cdot\left[\rho\left(\tfrac{1}{2}v^2 + h\right)\vec{v}\right] = \vec{\nabla}\cdot\left(k\,\vec{\nabla}T - \sum_{i=1}^{n} h_i \vec{j}_i - \tau\cdot\vec{v}\right) + S_h \tag{3.10}$$

where h is the enthalpy per unit mass, k is the thermal conductivity of the multicomponent gas (as defined below), h_i is the enthalpy per unit mass, and $\vec{j}_i$ is the diffusive mass flux of species i in the gas (as defined below). Note that Equation (3.10) is similar to Equation (3.5) but with the additional terms on the left hand side representing convection of kinetic energy and enthalpy and the additional terms on the right hand side representing enthalpy diffusion and viscous dissipation.

In Equation (3.10), assuming ideal gases, the enthalpy per unit mass, h, is given in terms of the enthalpies per unit mass, h_i, of the different species i, which are in turn given in terms of the specific heat at constant pressure of species i, $c_{p,i}$, by:

$$h = \sum_{i=1}^{n} y_i h_i = \sum_{i=1}^{n} y_i \int_{T^\circ}^{T} c_{p,i}\, dT \tag{3.11}$$

where y_i is the mass fraction as defined below. Note that enthalpies of the species at the reference temperature of T° = 298.15 K cancel out in Equation (3.10) and therefore are neglected in Equation (3.11).

For the typical operating conditions in PEM fuel cells, the effects of kinetic energy convection, enthalpy diffusion and viscous dissipation are relatively small and therefore are neglected in the thesis model. Thus Equation (3.10) simplifies to:

$$\vec{\nabla}\cdot\left(\rho h\vec{v}\right) = \vec{\nabla}\cdot\left(k\,\vec{\nabla}T\right) + S_h \tag{3.12}$$

In the anode and cathode gas channels the source term S_h is equal to zero, since there are no electrochemical reactions occurring and phase changes in the gas channels are neglected in the thesis model.

In general, for a multicomponent gas composed of n species, ρ_i is the mass density, $c_i = \rho_i / M_i$ is the molar density or concentration of species i with molecular weight M_i, $\rho = \sum_{i=1}^{n} \rho_i$ is the total mass density, $c = \sum_{i=1}^{n} c_i$ is the total concentration of the gas, $y_i = \rho_i / \rho$ is the mass fraction, and $x_i = c_i / c$ is the mole fraction of species i, such that $\sum_{i=1}^{n} y_i = 1$ and $\sum_{i=1}^{n} x_i = 1$. The mean molecular weight, M, of the gas is given by:

$$M = \frac{\rho}{c} = \frac{1}{\sum_{i=1}^{n} y_i / M_i} = \sum_{i=1}^{n} x_i M_i \tag{3.13}$$

Also, the mole fractions for an ideal gas can be expressed in terms of the partial pressure, P_i, of species i and the total gas pressure, P, as $x_i = P_i / P$.

The mass fractions of the species in the anode and cathode gas channels are determined by applying the fundamental law of conservation of mass to each species (Bird, Stewart & Lightfoot, 2002), which for steady-state conditions yields:

$$\vec{\nabla}\cdot\left(\rho y_i \vec{v}\right) = -\vec{\nabla}\cdot\vec{j}_i + S_i \tag{3.14}$$

where the source term S_i is the rate of production or consumption of mass of gas species i per unit volume, which is positive for mass production. In the gas channels the source

terms are equal to zero since there are no electrochemical reactions occurring and phase changes are neglected. In Equations (3.10) and (3.14):

$$\vec{j}_i = \rho_i(\vec{v}_i - \vec{v}) \tag{3.15}$$

is the diffusive mass flux of species i with velocity $\vec{v}_i$ with respect to the mass average velocity, $\vec{v}$, given by:

$$\vec{v} = \frac{\sum_{i=1}^{n} \rho_i \vec{v}_i}{\sum_{i=1}^{n} \rho_i} = \frac{1}{\rho} \sum_{i=1}^{n} \rho_i \vec{v}_i = \sum_{i=1}^{n} y_i \vec{v}_i \tag{3.16}$$

Assuming that Fick's first law for multicomponent species applies (Taylor & Krishna, 1993), the diffusive mass fluxes are given by:

$$\vec{j}_i = -\rho \sum_{j=1}^{n-1} \hat{D}_{ij} \vec{\nabla} y_j \quad \text{for} \quad i = 1,...,n-1 \tag{3.17}$$

where $\hat{D}_{ij}$ are the Fick's diffusion coefficients. Note that by using Equations (3.15) and (3.16), it can be shown that $\sum_{i=1}^{n} \vec{j}_i = 0$. Using the relation $\sum_{i=1}^{n} y_i = 1$, it can also be shown that $\sum_{i=1}^{n} \vec{\nabla} y_i = 0$. Thus there are only $n-1$ independent diffusive mass fluxes and gradients of mass fractions for n-component systems. Substituting Equation (3.17) into Equation (3.14) yields the following equations which can be solved for the species mass fractions:

$$\vec{\nabla} \cdot (\rho y_i \vec{v}) = \vec{\nabla} \cdot \left(\rho \sum_{j=1}^{n-1} \hat{D}_{ij} \vec{\nabla} y_j \right) + S_i \quad \text{for} \quad i = 1,...,n-1 \tag{3.18}$$

However, a more appropriate method for determining the mass fractions of the species in the anode and cathode gas channels is to apply the Stefan-Maxwell equations (Taylor & Krishna, 1993):

$$\vec{d}_i = \sum_{j=1}^{n} \frac{\left(x_i \vec{N}_j - x_j \vec{N}_i\right)}{c\mathcal{D}_{ij}} = \sum_{j=1}^{n} \frac{x_i x_j}{\mathcal{D}_{ij}} \left(\frac{\vec{j}_j}{\rho_j} - \frac{\vec{j}_i}{\rho_i} \right) \tag{3.19}$$

where $\vec{N}_i = c_i \vec{v}_i$ is the molar flux of species i and $\mathcal{D}_{ij}$ are the Stefan-Maxwell binary diffusion coefficients. In general, for non-ideal, electrolytic fluids in the absence of external body forces other than those due to electrical fields, and assuming that the condition of electroneutrality is met, the driving force for diffusion of species i, $\vec{d}_i$, is given by (Taylor & Krishna, 1993):

$$\vec{d}_i = \frac{x_i}{RT} \left(\vec{\nabla} \bar{\mu}_i \right)_{T,P} + \left(V_i - y_i\right) \frac{\vec{\nabla} P}{cRT} \tag{3.20}$$

where R is the gas constant, and V_i is the volume fraction and $\bar{\mu}_i = \mu_i + z_i F \phi_m$ is the electrochemical potential per unit mole of species i. In this expression for electrochemical potential, μ_i is the chemical potential per unit mole and z_i is the ionic charge number of species i, while F is Faraday's constant and ϕ_m is the electrical potential in the electrolyte (i.e. the polymer electrolyte in PEM fuel cells). The subscripts T and P in Equation (3.20) indicate that gradients of the electrochemical potentials are to be calculated under constant temperature and pressure conditions. Also, for ideal fluids, the gradients of the chemical potentials are given by:

$$\left(\vec{\nabla} \mu_i \right)_{T,P} = \left[\vec{\nabla} \left(RT \ln x_i \right) \right]_{T,P} \tag{3.21}$$

Thus, neglecting the gradient in pressure term, which is very small for typical operating conditions in PEM fuel cells, the driving forces for ideal electrolytic fluids are given by:

$$\vec{d}_i = \left(\vec{\nabla} x_i\right)_{T,P} + \frac{x_i z_i F \vec{\nabla}\phi_m}{RT} \tag{3.22}$$

and, for ideal non-electrolytic fluids, the driving forces are given by:

$$\vec{d}_i = \left(\vec{\nabla} x_i\right)_{T,P} \tag{3.23}$$

In general, the Stefan-Maxwell binary diffusion coefficients, $Đ_{ij}$, which are symmetric, (i.e. $Đ_{ij} = Đ_{ji}$) are related to the diffusion coefficients in Fick's first law for multicomponent species, $\hat{D}_{ij}$, which are not necessarily symmetric (Taylor & Krishna, 1993). Thus Equation (3.18) can be solved for the species mass fractions with Fick's diffusion coefficients given in terms of the Stefan-Maxwell binary diffusion coefficients. Using Equations (3.17), (3.19) and (3.23) for ideal two-component systems, with associated definitions and relationships as given, it can be shown that $\hat{D}_{11} = Đ_{12}$. In the thesis model it is assumed that humidified hydrogen gas enters the anode gas channel and, therefore, the appropriate diffusion coefficient in Equation (3.18) is $\hat{D}_{11} = Đ_{H_2-H_2O}$. For ideal three-component systems, such as humidified air, which is assumed to enter the cathode gas channel in the thesis model, it can be shown that (in matrix notation) the Fick's diffusion coefficients are given by:

$$\begin{bmatrix} \hat{D}_{11} & \hat{D}_{12} \\ \hat{D}_{21} & \hat{D}_{22} \end{bmatrix} = \frac{M_1 M_2 M_3 Đ_{12} Đ_{13} Đ_{23}}{M\left(x_1 Đ_{23} + x_2 Đ_{13} + x_3 Đ_{12}\right)} [Đ] \begin{bmatrix} \frac{x_1}{M_3} + \frac{(1-x_1)}{M_1} & x_1\left(\frac{1}{M_3} - \frac{1}{M_2}\right) \\ x_2\left(\frac{1}{M_3} - \frac{1}{M_1}\right) & \frac{x_2}{M_3} + \frac{(1-x_2)}{M_2} \end{bmatrix} \tag{3.24}$$

where the matrix which contains the Stefan-Maxwell binary diffusion coefficients is given by:

$$[Đ] = \begin{bmatrix} \dfrac{x_1}{Đ_{12}M_2} + \dfrac{x_2}{Đ_{23}M_3} + \dfrac{x_3}{Đ_{23}M_2} & x_1\left(\dfrac{1}{Đ_{12}M_2} - \dfrac{1}{Đ_{13}M_3}\right) \\ x_2\left(\dfrac{1}{Đ_{12}M_1} - \dfrac{1}{Đ_{23}M_3}\right) & \dfrac{x_1}{Đ_{13}M_3} + \dfrac{x_2}{Đ_{12}M_1} + \dfrac{x_3}{Đ_{13}M_1} \end{bmatrix} \tag{3.25}$$

The Stefan-Maxwell binary diffusion coefficients for ideal gases can be estimated from the kinetic theory of gases (Taylor & Krishna, 1993):

$$Đ_{ij} = \left(1.883 \times 10^{-2}\right) \frac{T^{3/2}}{P} \frac{\sqrt{1/M_i + 1/M_j}}{\sigma_{ij}^{\,2}\,\Omega_{D,\,ij}} \tag{3.26}$$

where the diffusion coefficient is in units of $m^2\ s^{-1}$, the temperature is in units of K, the pressure is in units of Pa, and the molecular weights are in units of kg $kmol^{-1}$. Values of both σ_{ij}, which is a characteristic length or collision diameter in units of Å, and the diffusion collision integral $\Omega_{D,\,ij}$, which is a dimensionless function of temperature, can be found in tables for species i and j (e.g. Bird, Stewart & Lightfoot, 2002). However, Equation (3.26) assumes nonpolar gases and, as a result, excludes the water vapour found in PEM fuel cells. Instead an empirical relation which is slightly more accurate than Equation (3.26) is used (Cussler, 1997):

$$Đ_{ij} = \left(1.01325 \times 10^{-2}\right) \frac{T^{1.75}}{P} \frac{\sqrt{1/M_i + 1/M_j}}{\left(V_i^{1/3} + V_j^{1/3}\right)^2} \tag{3.27}$$

where the diffusion coefficient, temperature, pressure and molecular weights have the same units as in Equation (3.26). The pressure and molecular weight dependences in Equations (3.26) and (3.27) are identical and, taking into account the temperature

dependence of the diffusion collision integral $\Omega_{D,ij}$ in Equation (3.26), the temperature dependences are similar between the two equations as well.

In Equation (3.27), the V_i and V_j terms are dimensionless molecular diffusion volumes, which are given in Table 3.2 for the species in the thesis model (Cussler, 1997), together with the respective molecular weights (Lide, 2003). These values are used in Equation (3.27) to calculate the values for the binary diffusion coefficients at the reference temperature of 298.15 K and pressure of 1 atm (101,325 Pa), which are also given in Table 3.2.

Table 3.2 - Stefan-Maxwell diffusion coefficients at 298.15 K and 101,325 Pa.

Molecular weight		Diffusion volume		Binary diffusion coefficient	
Symbol	Value (kg kmol^{-1})	Symbol	Value (-)	Symbol	Value (m^2 s^{-1})
M_{H_2}	2.016	V_{H_2}	7.07	$\mathcal{D}^{\circ}_{H_2-H_2O}$	8.79×10^{-5}
M_{H_2O}	18.015	V_{H_2O}	12.7	$\mathcal{D}^{\circ}_{H_2O-O_2}$	2.64×10^{-5}
M_{O_2}	31.999	V_{O_2}	16.6	$\mathcal{D}^{\circ}_{H_2O-N_2}$	2.64×10^{-5}
M_{N_2}	28.013	V_{N_2}	17.9	$\mathcal{D}^{\circ}_{O_2-N_2}$	2.07×10^{-5}

In the cathode of the PEM fuel cell, the binary diffusion coefficients at the operating temperature of 343.15 K, pressure of 3 atm (303,975 Pa) and relative humidity of 100 % are shown in Table 3.3, together with the values for the mole fractions of the species as calculated subsequently. Using these values and the values for the molecular weights in Table 3.2, the Fick's diffusion coefficients are calculated using Equations (3.24) and

(3.25), assuming that water vapour is species 1, oxygen is species 2 and nitrogen is species 3.

Table 3.3 - Diffusion coefficients in cathode at 343.15 K and 303,975 Pa.

Mole fraction		Binary diffusion coefficient		Fick's diffusion coefficient	
Symbol	Value (-)	Symbol	Value ($m^2\ s^{-1}$)	Symbol	Value ($m^2\ s^{-1}$)
x_{H_2O}	0.102	$Đ_{H_2O-O_2}$	1.13×10^{-5}	$\hat{D}_{11}$	1.13×10^{-5}
x_{O_2}	0.189	$Đ_{H_2O-N_2}$	1.13×10^{-5}	$\hat{D}_{12}$	1.92×10^{-8}
x_{N_2}	0.709	$Đ_{O_2-N_2}$	8.84×10^{-6}	$\hat{D}_{21}$	-5.28×10^{-7}
				$\hat{D}_{22}$	9.04×10^{-6}

Table 3.3 shows that the off-diagonal coefficients in the Fick's diffusion matrix are small compared to the diagonal coefficients (i.e. less than 6 %). Considering that the Stefan-Maxwell binary diffusion coefficients themselves are accurate to an average of only about 8 % (Cussler, 1997), the off-diagonal coefficients can be justifiably neglected. Also, the value of $\hat{D}_{11}$ is the same as the value of $Đ_{H_2O-O_2}$ and $Đ_{H_2O-N_2}$, which arises from the fact that binary diffusion coefficients for water vapour are the same in both oxygen and nitrogen and the Fick's diffusion coefficient is effectively a binary coefficient for water vapour in air. As well, this implies that $\hat{D}_{11}$ should not depend on the nitrogen/oxygen mole ratio in the air and should have a constant value, even for oxygen-depleted gas in the cathode catalyst layer. Finally, the value of $\hat{D}_{22}$ differs from the value of $Đ_{O_2-N_2}$ by only about 2 %, which arises from the fact that diffusion of oxygen in the humidified air is predominately through nitrogen. Considering that the water vapour mole fraction remains relatively constant throughout the cathode of the PEM fuel cell in the thesis model (as

shown in Chapter 5), the value of $\hat{D}_{22}$ should agree approximately with that of $\mathcal{D}_{O_2-N_2}$. Thus in Equation (3.18), for the multicomponent gas in the cathode, the Fick's diffusion coefficients are simply taken to be $\hat{D}_{11} = \mathcal{D}_{H_2O-N_2}$ and $\hat{D}_{22} = \mathcal{D}_{O_2-N_2}$, while the off-diagonal coefficients are set equal to zero.

All of the equations given above for the flows in the anode and cathode gas channels were derived under the implicit assumption of single-phase gas flows. This is justified because although liquid water can exist in the gas channels, the saturation, s, of liquid water (i.e. the volumetric fraction of the total fluid volume, which in this case is the total volume, occupied by liquid water) in the gas channels is assumed to be small under normal operating conditions. Phase changes between water vapour and liquid water are also considered negligible since the time-scale of the gas flows is short (i.e. the gas flows are relatively fast). The presence of the liquid water therefore has no effect on the conservation of mass and linear momentum for the gas flows.

For small saturations, the conduction and convection of heat by the liquid phase also has only a small effect on the overall heat flows and can be neglected. Heat associated with phase changes between water vapour and liquid water are also considered negligible. The presence of liquid water therefore has no effect on conservation of energy for the gas flows. Assuming that local thermal equilibrium applies, temperatures of the gas and liquid phases are equal and no energy equation is required for the liquid water. Also, in the thesis model, it is assumed that the liquid water is transported as a fine mist and that drag forces on the liquid water are sufficient for the mist to have the same velocity as the gases. Therefore no linear momentum equation needs to be solved for the liquid water. Finally, liquid water saturation is solved for using the steady-state equation of continuity applied to liquid water (Nield & Bejan, 1992):

$$\vec{\nabla} \cdot \left(\rho_w s \vec{V} \right) = S_w \tag{3.28}$$

where ρ_w is the density, $\vec{V}$ is the intrinsic velocity and $s\vec{V}$ is the superficial velocity of liquid water, and the source term S_w is the rate of production or consumption of mass of liquid water per unit volume (which is positive for mass production).

The density of liquid water is essentially constant for the typical variations in temperature and pressure found in PEM fuel cells, and the value of 977.9 kg m^{-3} at the operating temperature and pressure (Linstrom & Mallard, 2003) is used in the thesis model. The intrinsic velocity is the actual physical velocity of the liquid water, which is assumed to be equal to the velocity, $\vec{v}$, of the gases. The superficial velocity is defined as the velocity of liquid water averaged with respect to the local volume in the gas channels composed of both liquid water and gas, where the gas phase does not contribute to the velocity of the liquid water. Equation (3.28) is therefore rewritten as:

$$\vec{\nabla}\cdot\left(\rho_w s\vec{v}\right) = S_w \tag{3.29}$$

Note that since the gases are assumed to occupy most of the gas channels (i.e. the volumetric fraction or saturation of the gases is equal to one), $\vec{v}$ is both the intrinsic and superficial velocity of the gases in the gas channels, and the analogous equation to Equation (3.29) for the gases is simply Equation (3.7). In Equation (3.29), the source term is equal to zero in the anode and cathode gas channels because there are no electrochemical reactions occurring and phase changes in the gas channels are neglected in the thesis model.

In general, the assumptions made in the thesis model for liquid water transport in the gas channels are not physically justifiable since liquid water forms larger droplets on the gas diffusion layer surfaces in the gas channels and not a fine mist in the gases (Nam & Kaviany, 2003). The assumption of small liquid water saturations with negligible effect on the gases is, however, probably justifiable under normal operating conditions. In contrast, large liquid water saturations in the gas channels should lead to bridging and eventual

blocking of the entire gas channels by plugs, resulting in a temporary failure of the PEM fuel cell until the plugs are cleared. These effects are inherently unsteady and cannot be dealt with using the steady-state conditions assumed in the thesis model. Thus, since the liquid water saturations can be assumed small, and therefore the effects on the gases neglected, the actual mechanism by which liquid water is transported in the gas channels is not significant. Making the simplifying assumption that liquid water is transported as a fine mist with the same velocity as the gases is a reasonable approximation - in that it allows for liquid water to be transported to or from the gas diffusion layers through the gas channels from the inlets or to the outlets, respectively. Finally, note that most models developed previously do not model liquid water transport in the gas channels at all, and as such the thesis model represents an improvement in the handling of liquid water transport.

In summary, the flows in the anode and cathode gas channels are determined by assuming steady-state conditions for ideal gases in the absence of external body forces, and by applying the fundamental laws of conservation of total mass to yield Equation (3.7) for the gases and Equation (3.29) for liquid water. Conservation of linear momentum, energy and species yields Equations (3.8), (3.12) and (3.18), respectively, all of which are for the gases. With the appropriate physical properties and boundary conditions, these equations can be solved for the velocity, $\vec{v}$, pressure, P, temperature, T, species mass fractions, y_i, and liquid water saturation, s, since all other variables are known functions of these variables. Note that the density, ρ, is calculated from the ideal gas law $P = cRT$, which using Equation (3.13) yields:

$$\rho = \frac{P}{RT\sum_{i=1}^{n} y_i / M_i} \tag{3.30}$$

In this case the pressure P is the operating pressure of 303,975 Pa for the anode and cathode gases in the thesis model. The gas flows are assumed to be incompressible, such

that density changes only result from variable compositions of the gases due to the electrochemical reactions occurring in the fuel cell.

The viscosities of the multicomponent gases, μ, are necessary to solve Equation (3.8) and (3.9), and the thermal conductivities of the multicomponent gases, k, are necessary to solve Equation (3.12). In the thesis model, similar semiempirical formulas (Bird, Stewart & Lightfoot, 2002) are used for the viscosities of the multicomponent gases:

$$\mu = \sum_{i=1}^{n} \frac{x_i \mu_i}{\sum_{j=1}^{n} x_j \Phi_{ij}} \tag{3.31}$$

and for the thermal conductivities of the multicomponent gases:

$$k = \sum_{i=1}^{n} \frac{x_i k_i}{\sum_{j=1}^{n} x_j \Phi_{ij}} \tag{3.32}$$

where in both Equations (3.31) and (3.32) the dimensionless quantities Φ_{ij} are given by:

$$\Phi_{ij} = \frac{1}{\sqrt{8}} \left(1 + \frac{M_i}{M_j}\right)^{-1/2} \left[1 + \left(\frac{\mu_i}{\mu_j}\right)^{1/2} \left(\frac{M_j}{M_i}\right)^{1/4}\right]^2 \tag{3.33}$$

and where μ_i and k_i are the viscosities and thermal conductivities of the species in the multicomponent gases, respectively, at the PEM fuel cell operating temperature and pressure. The specific heats at constant pressure, $c_{p,i}$, of the multicomponent gas species in Equation (3.11) are also taken at the PEM fuel cell operating temperature and pressure. Finally, since variations around the operating temperature and pressure in PEM fuel cells are typically small, the viscosities and thermal conductivities are assumed to be constant -

as are the specific heats, which vary only slightly over the temperatures ranging from the reference temperature to the operating temperature. The values used in the thesis model are shown in Table 3.4 for the fuel cell operating temperature and pressure, except for the water vapour pressure which is the saturation pressure at the fuel cell operating temperature (Linstrom & Mallard, 2003).

Table 3.4 - Gas species properties at 343.15 K and 303,975 Pa.

	Viscosity, μ_i kg (m s)$^{-1}$	Thermal conductivity, k_i W (m K)$^{-1}$	Specific heat, $c_{p,i}$ J (kg K)$^{-1}$
Hydrogen, H_2	9.8173×10^{-6}	0.20704	14424
Water vapour, H_2O	1.1260×10^{-5}	0.022068	1986.2
Oxygen, O_2	2.2912×10^{-5}	0.030162	929.86
Nitrogen, N_2	1.9855×10^{-5}	0.028729	1044.5

In order to solve the equations as outlined previously for variables in the gas channels, appropriate boundary conditions include the mass fractions of gas species at the inlets of the anode and cathode gas channels. It is assumed that gas entering the anode gas channel is composed of humidified hydrogen at a relative humidity, RH, of 100 %. The relative humidity is given by $RH = 100\left(P_{H_2O}/P_{sat}\right)\%$, where the saturation pressure of water vapour, P_{sat}, in units of atmospheres, is given in terms of the temperature, T, in units of degrees Celsius by (Springer et al., 1991):

$$\log P_{sat} = -2.1794 + 0.02953\,T - 9.1837\times10^{-5}\,T^2 + 1.4454\times10^{-7}\,T^3 \qquad (3.34)$$

At the operating temperature of 70 °C (343.15 K), the saturation pressure of water vapour has a value of 0.307 atm. Finally, the mole and mass fractions of the gas species at the operating pressure, P, of 3 atm (303,975 Pa) are given by:

$$\begin{aligned} x_{H_2O} &= \frac{P_{H_2O}}{P} = \frac{P_{sat}}{P}\left(\frac{RH}{100}\right) = 0.102 \\ x_{H_2} &= 1 - x_{H_2O} = 0.898 \\ y_{H_2O,\,a} &= x_{H_2O}\frac{M_{H_2O}}{M_a} = \frac{x_{H_2O}M_{H_2O}}{x_{H_2O}M_{H_2O} + x_{H_2}M_{H_2}} = 0.505 \\ y_{H_2} &= 1 - y_{H_2O,\,a} = 0.495 \end{aligned} \tag{3.35}$$

In Equation (3.35), M_a is the mean molecular weight of the gas which has a value of 3.65 kg kmol^{-1}. Also, assuming that the gas entering the cathode gas channel is composed of humidified air (with nitrogen/oxygen mole ratio of 0.79/0.21) at 100 % relative humidity, mole and mass fractions of the gas species at the operating pressure of 3 atm and temperature of 70 °C are given by:

$$\begin{aligned} x_{H_2O} &= 0.102 \\ x_{O_2} &= \frac{1 - x_{H_2O}}{1 + x_{N_2}/x_{O_2}} = 0.189 \\ x_{N_2} &= 1 - x_{H_2O} - x_{O_2} = 0.709 \\ y_{H_2O,\,c} &= x_{H_2O}\frac{M_{H_2O}}{M_c} = \frac{x_{H_2O}M_{H_2O}}{x_{H_2O}M_{H_2O} + x_{O_2}M_{O_2} + x_{N_2}M_{N_2}} = 0.066 \\ y_{O_2} &= x_{O_2}\frac{M_{O_2}}{M_c} = \frac{x_{O_2}M_{O_2}}{x_{H_2O}M_{H_2O} + x_{O_2}M_{O_2} + x_{N_2}M_{N_2}} = 0.218 \\ y_{N_2} &= 1 - y_{H_2O,\,c} - y_{O_2} = 0.716 \end{aligned} \tag{3.36}$$

In Equation (3.36), M_c is the mean molecular weight of the gas which has a value of 27.7 kg kmol^{-1}.

As mentioned previously in this chapter, the gases enter the anode and cathode gas channels at prescribed mass flow rates, Q_a and Q_c, respectively, where the gases are assumed to be of uniform compositions and the flows incompressible and laminar. It is common practice in PEM fuel cell models to set the stoichiometric flow rates at the anode, ζ_a, and cathode, ζ_c, which are ratios of the amounts of hydrogen and oxygen added to the anode and cathode gas channels, respectively, to the amounts that are consumed by Reactions (1.1) and (1.2) in the corresponding catalyst layers. In order to set these rates, the total current produced in the PEM fuel cell, I, which is equal to the current density, i, multiplied by the superficial area of the MEA, s_{mea}, must be known in advance.

Using Reactions (1.1) and (1.2) to relate the molar rate of hydrogen and oxygen consumed per molar rate of electrons produced in the PEM fuel cell (i.e. I/F, where Faraday's constant, F, is the molar charge of electrons), the mass flow rate is given in terms of the stoichiometric flow rate at the anode by:

$$Q_a = \zeta_a \frac{is_{mea}}{2F} \frac{M_{H_2}}{y_{H_2}} = \zeta_a \frac{is_{mea}}{2F} \frac{M_a}{x_{H_2}} \tag{3.37}$$

and at the cathode by:

$$Q_c = \zeta_c \frac{is_{mea}}{4F} \frac{M_{O_2}}{y_{O_2}} = \zeta_c \frac{is_{mea}}{4F} \frac{M_c}{x_{O_2}} \tag{3.38}$$

Wang et al. (2003) provide experimental results in the form of polarisation curves for a single PEM fuel cell with superficial area of the MEA of 7.2 × 7.2 cm and constant volumetric flow rates of 1200 and 2200 standard cubic centimetres per minute (sccm), where "standard" is referenced to 273.15 K and 101,325 Pa, at the anode and cathode, respectively. Flow rates of pure hydrogen and dry air (i.e. before humidification) are measured and set using an MKS mass flow controller. Using the ideal gas law $c = P/RT$,

and correcting for unit conversions from cubic centimetres per minute to cubic metres per second, 1 sccm is equivalent to mass flow rates of Q_a = (7.44 × 10^{-10} kmol s^{-1}) M_a and Q_c = (7.44 × 10^{-10} kmol s^{-1}) M_c at the anode and cathode, respectively. Using Equation (3.37), with mole fraction of pure hydrogen equal to 1, and Equation (3.38), with mole fraction of oxygen in dry air equal to 0.21 (assuming a nitrogen/oxygen mole ratio of 0.79/0.21), the stoichiometric flow rates for a current density of i = 1 A cm^{-2} are found to be ζ_a = 3.32 and ζ_c = 2.56 at the anode and cathode, respectively.

In the thesis model, with an MEA superficial area of s_{mea} = 7 × 10^{-5} m^2, and for a current density of i = 1 A cm^{-2} (i.e. 1× 10^4 A m^{-2}), these stoichiometric flow rates are equivalent to mass flow rates of Q_a = 4.90 × 10^{-8} kg s^{-1} for humidified hydrogen (with y_{H_2} = 0.495) and Q_c = 6.82 × 10^{-7} kg s^{-1} for humidified air (with y_{O_2} = 0.218). Since only half the gas channels are included in the model volume, the mean gas velocities are $2Q_aRT/M_aPd_{gc}^2$ = 0.252 m s^{-1} and $2Q_cRT/M_cPd_{gc}^2$ = 0.462 m s^{-1}, respectively, at the inlets of the anode and cathode gas channels. An operating temperature of 343.15 K and pressure of 303,975 Pa are assumed, and both of these velocities are much less than the speed of sound in the gases, such that the assumption of incompressible flows is physically justifiable.

The Reynolds numbers are $Re_a = 2Q_a/\mu_a d_{gc}$ = 9.3 and $Re_c = 2Q_c/\mu_c d_{gc}$ = 68, respectively, at the inlets of the anode and cathode gas channels. Viscosities of saturated hydrogen and air are calculated using a simple mass fraction average of the viscosity values for species in Table 3.4, such that μ_a = 1.05 × 10^{-5} kg (m s)$^{-1}$ and μ_c = 2.00 × 10^{-5} kg (m s)$^{-1}$. Both of these Reynolds numbers are small enough such that the assumption of laminar flows is physically justifiable. Finally, for laminar flow the entrance length (i.e. developing profile region) before establishing fully developed flow is $0.06\,Re_a d_{gc}$ = 5.6 × 10^{-4} m and $0.06\,Re_c d_{gc}$ = 4.1 × 10^{-3} m in the anode and cathode gas channels, respectively (White, 1999). These values, when compared to the length of the gas channels (7 × 10^{-2}

m), show that the flow is fully developed within 0.8 % and 5.8 % of the anode and cathode gas channel lengths, respectively, such that entrance effects are not important.

In the thesis model, the boundary conditions also include setting the liquid water saturations equal to zero at the anode and cathode gas channel inlets. Thus, appropriate boundary conditions for the velocities, $\vec{v}$ (i.e. the mass flow rates, Q_a and Q_c), density, ρ (i.e. using the ideal gas law), temperature, T, pressure, P, species mass fractions, y_i, and liquid water saturations, s, have been set. Note that appropriate boundary conditions for pressure are set at the outlets to the anode and cathode gas channels (Wang et al., 2003), which assists in the CFD solutions by accounting for the possibility of back flow.

Finally, the gas channels are bounded on three sides by the bipolar plates and on one side by the gas diffusion layers. It is assumed that the bipolar plates form impermeable walls and that the fluid flows obey no-slip conditions - such that velocities of the gases and liquid water, and diffusive mass fluxes (i.e. gradients in mass fractions) of the gas species, are equal to zero at the boundaries. In contrast, the gas channel/diffusion layer boundaries are permeable to the gases or liquid water, and the appropriate boundary conditions are set such that the mass fluxes of the gases, $\rho\vec{v}$, gas species, $\rho_i\vec{v}_i$, and liquid water, $\rho_w s\vec{v}$, are continuous across the boundaries.

3.1.3 Gas Diffusion Layers

As for the gas channels, flows of the gases and liquid water in the gas diffusion layers are determined by applying the fundamental laws of conservation in a porous medium with porosity φ (which is the volumetric fraction of open pore space in the porous medium), and with saturation $s_f = \varphi_f / \varphi$ of fluid f (where φ_f is the volumetric fraction of the fluid in the porous medium). The conservation of mass can be expressed in the form of the

steady-state equation of continuity for the fluid f, with density ρ_f, and superficial velocity $\vec{v}_f$, as follows (Nield & Bejan, 1992):

$$\vec{\nabla}\cdot\left(\rho_f \vec{v}_f\right) = S_f \tag{3.39}$$

In this equation, the source term S_f is the rate of mass production or consumption of fluid f per unit volume, which is positive for mass production. In the gas diffusion layers Equation (3.39) yields for the gases:

$$\vec{\nabla}\cdot\left(\rho \vec{v}\right) = S_g \tag{3.40}$$

(which is identical to Equation (3.7) for the gases in the gas channels) and for the liquid water:

$$\vec{\nabla}\cdot\left(\rho_w \vec{v}_w\right) = S_w \tag{3.41}$$

Note that the source terms in Equations (3.40) and (3.41) are non-zero since phase changes between water vapour and liquid water are taken into account.

In the gas diffusion layers, conservation of linear momentum is expressed in the form of Darcy's law for fluids in an isotropic porous medium (Nield & Bejan, 1992):

$$\vec{v}_f = -\frac{\kappa_{r,f}\kappa}{\mu_f}\vec{\nabla}P_f \tag{3.42}$$

where κ is the total permeability of the medium, κ_f is the permeability of the medium to fluid f with viscosity μ_f and pressure P_f, and $\kappa_{r,f} = \kappa_f/\kappa$ is the relative permeability of the medium to fluid f. In the gas diffusion layers, saturation of liquid water is

relatively small under normal PEM fuel cell operating conditions, such that the value of relative permeability (of the medium to the gases) is close to one and can be assumed independent of the liquid water saturation (Kaviany, 1995). This is also a justifiable simplification considering that the gas pressure gradients are small in the gas diffusion layers and gas transport is primarily by diffusion. Rewriting Equation (3.42) for the gases, in an equivalent form as Equation (3.8) for the gases in the gas channels, then yields:

$$\vec{\nabla}P = -\frac{\mu}{\kappa}\vec{v} \tag{3.43}$$

Substituting Equation (3.42) for the liquid water in the gas diffusion layers into Equation (3.41) yields:

$$\vec{\nabla}\cdot\left(\rho_w \frac{\kappa_{r,w}\,\kappa}{\mu_w}\vec{\nabla}P_w\right) + S_w = 0 \tag{3.44}$$

In Equation (3.44), the viscosity of liquid water is essentially constant for the typical variations in temperature and pressure found in PEM fuel cells, and the value of 4.04×10^{-4} kg (m s)$^{-1}$ at the operating temperature and pressure (Linstrom & Mallard, 2003) is used in the thesis model.

By definition, the reduced liquid water saturation is given in terms of the liquid water saturation, s, by (Kaviany, 1995):

$$s_r = \frac{s - s_{im}}{1 - s_{im} - s_{g,\,im}} \tag{3.45}$$

where s_{im} and $s_{g,\,im}$ are the immobile or irreducible saturations of the liquid water and gas phases, respectively. In general, the displacement of the wetting phase by the non-wetting phase in a porous medium is called drainage and the reverse is called imbibition. In the

case of the hydrophobic gas diffusion layers, drainage occurs since the wetting phase, which is the gases, is being displaced by the non-wetting liquid water phase produced as a result of the electrochemical reactions in the cathode. For drainage in porous media with large surface roughnesses (as is assumed to be the case in the gas diffusion layers), both liquid water and gas immobile saturations are found to be equal to zero (Kaviany, 1995) and the reduced liquid water saturation is simply equal to the liquid water saturation.

In general, pressures of the gases, P, and liquid water, P_w, are related to each other through the capillary pressure, P_c, which is given in terms of the Leverett J-function, $J(s)$. For the case of imbibition of a hydrophilic porous medium, the Leverett J-function is given by the expression in the square brackets below (Kaviany, 1995):

$$P_c = P_w - P = \left| \frac{\gamma \cos\theta}{(\kappa/\varphi)^{1/2}} \left[1.417\,(1-s) - 2.120\,(1-s)^2 + 1.263\,(1-s)^3 \right] \right| \qquad (3.46)$$

Both imbibition of a hydrophilic porous medium and drainage of a hydrophobic porous medium take place through the displacement of gases by the liquid water. Therefore this expression for the Leverett J-function is also assumed to apply to the gas diffusion layers in the thesis model, but where the hydrophobic nature of the gas diffusion layers is taken into account through the contact angle of liquid water, θ, in Equation (3.46). An estimate for the contact angle of liquid water in the gas diffusion layers is $\theta = 120°$ and an estimate for the surface tension between liquid water and the gases is $\gamma = 0.0644$ N m^{-1} (Nam & Kaviany, 2003). It is to be noted that the expression for the Leverett J-function in Equation (3.46) was derived using experimental results for the displacement of air by liquid water in unconsolidated sand, and is not relevant to gas diffusion layers, but it is used in the thesis model due to the lack of directly applicable experimental results.

Assuming that changes in the gas pressures are relatively small compared to changes in the liquid water pressure, since the viscosities of the gases are quite small relative to the viscosity of the liquid water, yields:

$$\vec{\nabla}P_c = \vec{\nabla}P_w - \vec{\nabla}P \cong \vec{\nabla}P_w \tag{3.47}$$

For liquid water, the relative permeability is given by $\kappa_{r,w} = s^3$ (Nam & Kaviany, 2003), and substituting this expression and Equation (3.47) into Equation (3.44) yields:

$$\vec{\nabla}\cdot\left(\rho_w \frac{s^3\kappa}{\mu_w}\frac{dP_c}{ds}\vec{\nabla}s\right) + S_w = 0 \tag{3.48}$$

where, using Equation (3.46), the derivative of the capillary pressure is given by:

$$\frac{dP_c}{ds} = \left|\frac{\gamma\cos\theta}{(\kappa/\varphi)^{1/2}}\left[-1.417 + 4.240\,(1-s) - 3.789\,(1-s)^2\right]\right| \tag{3.49}$$

The expression for the Leverett J-function, J, in Equation (3.46) and the absolute value of the derivative of this expression, $|dJ/ds|$ (i.e. the absolute value of the expression in the square brackets above), are shown as a function of liquid water saturation, s, in Figure 3.1.

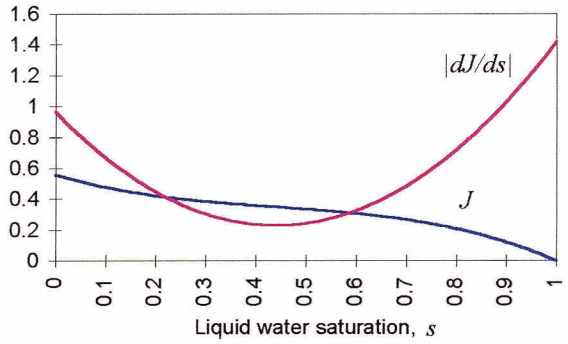

Figure 3.1 - Leverett J-function.

Equation (3.48) describes liquid water saturation in the gas diffusion layers consistent with Equation (3.29) for liquid water saturation in the gas channels. However, in the gas diffusion layers the source term S_w is non-zero since phase changes between water vapour and liquid water are taken into account. In this case the source term is given by $S_w = r_w$, where r_w is the rate of condensation of water vapour mass per unit volume, while the source term in Equation (3.40) is given by $S_g = -r_w$. In the thesis model r_w is given by:

$$r_w = c_s \max\left\{(1-s)\frac{P_{H_2O} - P_{sat}}{RT} M_{H_2O},\ -s\rho_w\right\} \tag{3.50}$$

where c_s is the constant rate of condensation per second. The first term in the brackets (Natarajan & Nguyen, 2001; Nam & Kaviany, 2003) accounts for the condensation of water vapour mass per unit volume from the gases with volumetric fraction $\varphi(1-s)$ in the porous medium. The second term accounts for the evaporation per unit volume of liquid water with volumetric fraction φs in the porous medium, where the rate of evaporation is assumed to be the same as the rate of condensation. Finally, both terms are combined in a manner which ensures a continuous function for the rate of condensation or evaporation of

water mass per unit volume. The porosity found in both terms is included in the rate of condensation or evaporation, which is a somewhat arbitrary constant that determines the deviation allowed in the value of water vapour partial pressure from the value of water vapour saturation pressure.

For gas and liquid water flow in a fixed isotropic porous medium, it is assumed that local thermal equilibrium applies, such that temperatures in the gas, liquid water and solid are equal at every point in the medium and can be replaced by a single temperature. It is also assumed that heat conduction in the gas, liquid water and solid takes place in parallel, such that there is no net heat transfer from one phase to the other. Conservation of energy then takes the similar form to Equation (3.12) (Bird, Stewart & Lightfoot, 2002; Nield & Bejan, 1992):

$$\vec{\nabla}\cdot\left(\rho h\vec{v} + \rho_w h_w \vec{v}_w\right) = \vec{\nabla}\cdot\left(k_{total}\vec{\nabla}T\right) + S_h \tag{3.51}$$

In the above equation, h_w is the enthalpy per unit mass of liquid water and:

$$k_{total} = \varphi(1-s)k + \varphi s k_w + (1-\varphi)k_s \tag{3.52}$$

where k_w and k_s are the thermal conductivities of liquid water and solid, respectively. For the gas diffusion layers in PEM fuel cells, the assumption of small liquid water saturations, and therefore small superficial velocities, allows the liquid water terms in Equations (3.51) and (3.52) to be neglected and the equations to be rewritten together as:

$$\vec{\nabla}\cdot\left(\rho h\vec{v}\right) = \vec{\nabla}\cdot\left\{\left[\varphi k + (1-\varphi)k_s\right]\vec{\nabla}T\right\} + S_h \tag{3.53}$$

This assumption is also justifiable on the basis that the value for thermal conductivity of carbon in the solid phase is at least two orders of magnitude greater than that of liquid water and the gases (Lide, 2003) and thus dominates the energy transport in the MEA.

In the gas diffusion layers the source term is given by:

$$S_h = r_w h_{wg} + \frac{i_s^2}{\sigma_s^{eff}} \tag{3.54}$$

Equation (3.54) takes into account the ohmic heat generated by electron flow in the solid matrix and the heat generated by phase changes of water. In the first term on the right hand side r_w is given by Equation (3.50) and h_{wg} is the latent heat of vaporisation per unit mass of water which, because of the small variations in temperature typical in PEM fuel cells, can be considered to be constant and equal to the value at the operating temperature and saturation pressure of 2.333×10^6 J kg^{-1} (Linstrom & Mallard, 2003).

The mass fractions of species in the gas diffusion layers are determined by applying the fundamental law of conservation of mass to each species in the isotropic porous medium, which also yields Equation (3.18), with the exception that the diffusion coefficients are replaced by effective coefficients, such that:

$$\hat{D}_{ij}^{eff} = \frac{\varphi(1-s)}{\Gamma}\hat{D}_{ij} = \frac{\varphi(1-s)}{\tau^2}\hat{D}_{ij} = \varphi^a(1-s)^b\hat{D}_{ij} \tag{3.55}$$

In Equation (3.55) $\Gamma = \tau^2$ is the so-called tortuosity factor and τ is the tortuosity, which is defined as the ratio of the average pore length (i.e. average length of pathways through the pores) to the length of the porous medium along the major diffusion axis (Epstein, 1988). The last expression on the right in Equation (3.55) is a generalisation of Bruggemann's approximation, found to apply for conductivity in electrolytes with a suspended insulating phase (De La Rue & Tobias, 1959). In the thesis model this expression will be used for simplicity where from the effective medium theory for packed spherical particles (i.e. carbon black particles), a = 1.5, and also if the pore structure does not change with water saturation, b = 1.5 (Nam & Kaviany, 2003). Also, using Equations

(3.27) and (3.55), the diffusion coefficients are given in terms of their values at the reference temperature of $T^\circ = 298.15$ K and pressure of $P^\circ = 1$ atm (101,325 Pa) by:

$$\hat{D}_{ij}^{eff} = \varphi^a (1-s)^b \hat{D}_{ij}^\circ \left(\frac{P^\circ}{P}\right)\left(\frac{T}{T^\circ}\right)^{1.75} \tag{3.56}$$

Note that Equation (3.56) can also be applied to the gas channels, where the porosity φ is equal to one, such that the presence of liquid water has an effect on the conservation of species, but not on mass, linear momentum and energy as discussed in Section 3.1.2. Finally, in Equation (3.18) for the gas diffusion layers, $S_{H_2O} = -r_w$ to account for the condensation of water vapour into liquid water, with r_w given by Equation (3.50).

In the gas diffusion layers, with the appropriate boundary conditions, Equations (3.40), (3.43), (3.53) and (3.18), together with the ideal gas law, can be solved for the gas superficial velocity, $\vec{v}$, density, ρ, pressure, P, temperature, T, and species mass fractions, y_i. Equation (3.48) with Equation (3.49) can be solved for the liquid water saturation, s. Also, Equation (3.2) applies to the gas diffusion layers, with the source term equal to zero since there are no electrochemical reactions, and this equation can be solved for the electrical potential in the carbon matrix, ϕ_s.

Similar to the bipolar plate/gas channel boundaries, the bipolar plates are assumed to form impermeable walls with the gas diffusion layers with the fluid flows obeying no-slip conditions, such that the superficial velocities of the gases and liquid water and diffusive mass fluxes (i.e. gradients in mass fractions) of the gas species are equal to zero at the bipolar plate/gas diffusion layer boundaries. Similar to the gas channel/gas diffusion layer boundaries, the gas diffusion layers are assumed to form boundaries with the catalyst layers across which the mass fluxes of the gases and liquid water, as well as of the gas species, are continuous. Note, however, that there are discontinuities in the total volumetric fraction of gases and liquid water at the boundaries of the gas diffusion layers

with the gas channels and catalyst layers. Discontinuities therefore also exist in the saturation of liquid water, since the saturation is defined as volumetric fraction of liquid water divided by the total volumetric fraction of gases and liquid water. In the case of the gas diffusion and catalyst layers, these values are the porosities, and in the case of the gas channels are equal to one. These discontinuities are determined assuming equilibrium and therefore continuity of capillary pressure across the boundaries.

Finally, for the conduction of electrons, similar to the bipolar plate/gas diffusion layer boundaries, superficial current densities of electrons are continuous at the gas diffusion/catalyst layer boundaries, although there can be discontinuities in the electrical potential due to contact resistances. Also, similar to the bipolar plate/gas channel boundaries, superficial current densities of electrons normal to the gas channel/gas diffusion layer boundaries are equal to zero, since the gases and liquid water act as electrical insulators.

The E-TEK division of De Nora North America Inc. manufactures ELAT® LT 1200-W carbon-cloth based gas diffusion layers. These layers have a thickness of 2.6×10^{-4} m, a permeability of $\kappa = 1.45 \times 10^{-11}$ m^2 and an effective electrical conductivity of $\sigma_s^{eff} = 2.4 \times 10^2$ S m^{-1} through-plane (i.e. normal to the gas diffusion/catalyst layer boundaries). These values are from the technical data sheet supplied by E-TEK (2004) and are used in the thesis model. Unfortunately, E-TEK does not supply complete data for their gas diffusion layers and, instead, a density of $\rho_s = 1.8 \times 10^3$ kg m^{-3} and a specific heat of $c_{P,s} = 7.1 \times 10^2$ J (kg K)$^{-1}$ are used, which are for carbon black (Lide, 2003). Finally, through- and in-plane data for carbon paper from Toray Industries Inc. (2004) are used to calculate an average thermal conductivity of $k_s = 12$ W (m K)$^{-1}$ for the thesis model. The data are also used to calculate a through- to in-plane electrical conductivity of 0.07, and this ratio is used to calculate an average electrical conductivity of $\sigma_s^{eff} = 1.8 \times 10^3$ S m^{-1} for the thesis model from the through-plane value given above for the ELAT® LT 1200-W gas diffusion layers.

3.1.4 Catalyst Layers

In the thesis model, it is assumed that gas and liquid water transport in the catalyst layers is similar to that in the gas diffusion layers. However, as reactants are transported through the catalyst layers, they also undergo electrochemical reactions at catalyst sites on the surface of the agglomerates, which are assumed to be surrounded by a thin film of polymer electrolyte, followed by a second thin film of liquid water. Thus before reaching the catalyst sites, reactants in the gas phase dissolve into the liquid water and diffuse across both the liquid water and polymer electrolyte films. The overall rates of reaction can be obtained by multiplying the Butler-Volmer equation for the rates of reaction, using the concentrations of dissolved reactants at the catalyst sites, by the surface area per unit volume of catalyst sites found on the surfaces of the agglomerates in contact with polymer electrolyte (i.e. active surface area). This requirement of an active surface area per unit volume is based on the lack of a well-defined geometry for the active surface and also the inherent averaging of physical properties in each of the grid cells in a CFD calculation.

In the thesis model, it is assumed that Reaction (1.2) in the cathode catalyst layer initially produces water vapour in the thin film of polymer electrolyte surrounding the catalyst sites, which then bubbles without changing phase through both the polymer electrolyte and liquid water films and into the gas in the cathode catalyst layer - with negligible resistance and no effect on the properties of the polymer electrolyte and liquid water. Once in the gas, the water vapour can condense to form liquid water, similar to processes in the gas diffusion layers. In the thesis model, it is also assumed that water vapour in the anode and cathode catalyst layer gases condenses into and evaporates out of the thin film of polymer electrolyte surrounding the catalyst sites through the thin film of liquid water, with no effect on the properties of the liquid water.

In the catalyst layers, Equation (3.18) with appropriate effective diffusion coefficients given by Equation (3.56) for the gas species mass fractions, y_i (which are reactants and products in the respective catalyst layers - i.e. hydrogen in the anode and oxygen and water vapour, respectively, in the cathode), now has source terms S_i for the rate of production or consumption of species mass per unit volume. These values are related by Reactions (1.1) and (1.2) in the anode and cathode catalyst layers, respectively, to the consumption or production of current of electrons per unit volume, S_s, which is positive for the production of current of electrons. In general, the non-zero source terms in the anode catalyst layer are given by:

$$\begin{aligned} S_{H_2} &= \frac{M_{H_2}}{2F} S_s \\ S_{H_2O} &= -r_w - r_m \end{aligned} \tag{3.57}$$

and the non-zero source terms in the cathode catalyst layer are given by:

$$\begin{aligned} S_{O_2} &= -\frac{M_{O_2}}{4F} S_s \\ S_{H_2O} &= \frac{M_{H_2O}}{2F} S_s - r_w - r_m \end{aligned} \tag{3.58}$$

allowing for phase changes of water between vapour and liquid in the anode and cathode catalyst layers, with r_w given by Equation (3.50). In Equations (3.57) and (3.58), r_m, as derived in the next section, is the source term for the rate of production or consumption of liquid water mass in the polymer electrolyte per unit volume by phase changes between water vapour and liquid water. This value is positive for the production of liquid water in the polymer electrolyte and, in combination with r_w, also accounts for the volumetric rate of mass transfer between liquid water and liquid water in the polymer electrolyte. Also, the gas velocities in the anode and cathode catalyst layers are given by Equation (3.40) with $S_g = S_{H_2} + S_{H_2O}$ using Equation (3.57) and $S_g = S_{O_2} + S_{H_2O}$ using Equation (3.58),

respectively. Finally, liquid water saturation is governed by Equations (3.48) and (3.49), with r_w as given by Equation (3.50).

The consumption or production of current of electrons per unit volume is given by the Butler-Volmer equation for the rate of a multistep, multi-electron electrochemical reaction (Bockris & Khan, 1993), which for Reaction (1.1) in the anode catalyst layer is given as:

$$\begin{aligned} S_s &= \xi\, i_{0,a} \left(e^{-\alpha_{c,a}\eta_a F/RT} - e^{\alpha_{a,a}\eta_a F/RT} \right) \\ &= \xi\, i_{0,a}^{ref} \left(\frac{c_{H_2}}{c_{H_2}^{ref}} \right)^{b_{H_2}} \left(e^{-\alpha_{c,a}\eta_a F/RT} - e^{\alpha_{a,a}\eta_a F/RT} \right) \end{aligned} \tag{3.59}$$

and which for Reaction (1.2) in the cathode catalyst layer is given as:

$$\begin{aligned} S_s &= \xi\, i_{0,c} \left(e^{-\alpha_{c,c}\eta_c F/RT} - e^{\alpha_{a,c}\eta_c F/RT} \right) \\ &= \xi\, i_{0,c}^{ref} \left(\frac{c_{O_2}}{c_{O_2}^{ref}} \right)^{b_{O_2}} \left(e^{-\alpha_{c,c}\eta_c F/RT} - e^{\alpha_{a,c}\eta_c F/RT} \right) \end{aligned} \tag{3.60}$$

Note that conservation of charge requires that the overall consumption of current of electrons in the anode, given by integrating Equation (3.59) over the volume of the anode catalyst layer, must have the same absolute value as the overall production of current of electrons in the cathode, given by integrating Equation (3.60) over the volume of the cathode catalyst layer.

In Equations (3.59) and (3.60), ξ is the active surface area per unit volume, which is assumed to be the same in both catalyst layers since, in the thesis model, the anode and cathode catalyst layers are identical. Also, anodic and cathodic exchange current densities, $i_{0,a}$ and $i_{0,c}$, respectively, depend on the catalytic activities per unit catalyst surface area and concentrations of the dissolved reactants and products, raised to powers (where b_{H_2} is

the exponent for dissolved hydrogen and b_{O_2} for dissolved oxygen), in Reactions (1.1) and (1.2), respectively. Thus the anodic and cathodic exchange current densities in Equations (3.59) and (3.60) are expressed in terms of the anodic and cathodic exchange current densities determined at reference concentrations c^{ref} of dissolved oxygen and hydrogen, $i_{0,a}^{ref}$ and $i_{0,c}^{ref}$, respectively, and the concentrations c of dissolved oxygen and hydrogen at the catalyst sites. Note that from electroneutrality and incompressibility arguments, the concentrations of dissolved protons and water are constant and equal to their reference concentrations and thus do not appear in Equations (3.59) and (3.60). The concentrations of dissolved hydrogen and oxygen at the catalyst sites are related (through the transport limitations of the thin films of liquid water and polymer electrolyte) to concentrations of dissolved hydrogen and oxygen at the outer surface of the liquid water film which, in turn, are related to partial pressures of hydrogen and oxygen, and their related mass fractions, in the adjacent gaseous phase by Henry's law. The effects of these transport limitations will be discussed in Chapter 4.

In Equations (3.59) and (3.60), $\alpha_{a,a}$ and $\alpha_{c,a}$ are the anodic and cathodic transfer coefficients in the anode catalyst layer, respectively, and $\alpha_{a,c}$ and $\alpha_{c,c}$ are the anodic and cathodic transfer coefficients in the cathode catalyst layer, respectively. Note that for one-step, one-electron reactions, the anodic and cathodic transfer coefficients have values between zero and one (usually one-half) and their sum is equal to one. However, for multistep, multi-electron reactions, the transfer coefficients can also have values greater than one. In this case, the sum of the transfer coefficients is equal to the number of electrons transferred divided by the number of times that the rate-determining step occurs, for each occurrence of the reaction, and this sum is in general not equal to one (Bockris & Khan, 1993).

Finally, in Equations (3.59) and (3.60), overpotentials driving the electrochemical reactions are related to potential differences between the solid matrix and polymer electrolyte phases in the anode catalyst layer by $\eta_a = \phi_s - \phi_m$, which is positive, and in the

cathode catalyst layer by $\eta_c = \phi_s - \phi_m - V_{oc}$, which is negative (Um et al., 2000). The electrical potential in the solid matrix of the catalyst layers, ϕ_s, is governed by Equation (3.2) with the source term given by Equations (3.59) and (3.60) for the anode and cathode catalyst layers, respectively. The equations which govern the electrical potential in the polymer electrolyte of the catalyst layers, ϕ_m, will be discussed in Section 3.1.5. The open-circuit potential, V_{oc}, of PEM fuel cells (in units of Volts) is given in terms of the reversible potential by the Nernst equation for Reaction (1.3) with product water assumed to be in the vapour phase (Larminie & Dicks, 2000):

$$V_{oc} = \frac{-\Delta \bar{g}_f^{\circ}}{4F} + \frac{RT}{4F} \ln\left(\frac{x_{H_2}^2 x_{O_2}}{x_{H_2O}^2}\right) + \frac{RT}{4F} \ln P \tag{3.61}$$

The term $\Delta \bar{g}_f^{\circ}$ = -4.530 × 10^8 J $kmol^{-1}$ (Chase et al., 1986) is the change in Gibbs free energy of formation in Reaction (1.3) at the reference pressure of 1 atm and the operating temperature, T, in units of Kelvin. The operating pressure, P, is in units of atmospheres. Using the mole fractions from Equations (3.35) and (3.36), Equation (3.61) yields V_{oc} = 1.20 V. However, as mentioned in Chapter 1, the open-circuit potential departs from its reversible value as a result of competing reactions setting up a mixed potential. According to the experimental data of Parthasarathy et al. (1992) this potential has a value of 1.12 V at a temperature of 343.15 K, and in the thesis model this value will be used instead of the reversible value.

According to Equations (3.59) and (3.60) at low overpotentials (i.e. low current densities) the Butler-Volmer equation becomes linear, whereas at high overpotentials (i.e. high current densities) one of the terms in the Butler-Volmer equation (i.e. the back reaction rate) becomes negligibly small yielding the Tafel approximation, as discussed in Chapter 2. At high overpotentials, according to Equations (3.59) and (3.60), the slope of a plot of overpotential versus logarithm of current density magnitude is given by $2.303RT/\alpha_{a,a}F$ and $-2.303RT/\alpha_{c,c}F$ in the anode and cathode catalyst layers,

respectively. This slope is commonly referred to as the Tafel slope. Thus values of ±30, ±60 and ±120 mV dec^{-1} for the Tafel slope at the reference temperature of $T^\circ = 298.15$ K correspond to values of 2, 1 and 1/2 for the transfer coefficients $\alpha_{a,a}$ and $\alpha_{c,c}$ in the anode and cathode catalyst layers, respectively.

Mello & Ticianelli (1997) measured a value of approximately 30 mV dec^{-1} for the Tafel slope of Reaction (1.1) at Nafion® covered platinum electrodes in acid solutions (i.e. under similar conditions as in anode catalyst layers of PEM fuel cells) at the reference temperature of $T^\circ = 298.15$ K. The experimental data of Mello & Ticianelli (1997) indicates that for Reaction (1.1) in anode catalyst layers of PEM fuel cells, $\alpha_{a,a} = 2$ in Equation (3.59). Croissant et al. (1998) interpret the experimental data of Mello & Ticianelli (1997) as indicating that Reaction (1.1) in anode catalyst layers results from an initial adsorption step of dissolved hydrogen onto the surface of the catalyst, which has to occur twice:

$$H_2 \rightarrow 2H_{ads} \tag{3.62}$$

This chemical step, which is commonly referred to as the Tafel step, is followed by a de-electronation step, which has to occur four times for each occurrence of Reaction (1.1):

$$H_{ads} \rightarrow H^+ + e^- \tag{3.63}$$

This one-electron electrochemical step is commonly referred to as the Volmer step. Croissant et al. (1998) interpret the experimental data of Mello & Ticianelli (1997) as indicating that the initial Tafel step is the rate-determining step for the Reaction (1.1) and that there is a high degree of catalyst surface coverage by adsorbed hydrogen. Based on this rate-determining step for the above set of steps, for each occurrence of Reaction (1.1), dividing the number of electrons transferred (i.e. 4) by the number of times that the rate-determining step occurs (i.e. 2) yields the sum of the transfer coefficients (i.e. 2).

Therefore for Reaction (1.1) in anode catalyst layers of PEM fuel cells, $\alpha_{c,a}$ = 0 in Equation (3.59). Also, based on this rate-determining step for the above set of steps, the value of b_{H_2} in Equation (3.59) is calculated to be equal to one-half (Bockris & Khan, 1993). Thus, based on the above results, values of $\alpha_{a,a}$ = 2, $\alpha_{c,a}$ = 0 and b_{H_2} = 1/2 are used in the thesis model.

Parathasarathy et al. (1992) measured values of approximately -60 mV dec^{-1} and -120 mV dec^{-1} for the Tafel slope of Reaction (1.2) at platinum microelectrodes in contact with Nafion® membranes near the reference temperature of T° = 298.15 K at low and high current densities, respectively. Similar values were measured by Floriano et al. (1994) at Nafion®-covered platinum electrodes in acid solutions near the same reference temperature. The experimental data of Parathasarathy et al. (1992) and Floriano et al. (1994), which is for similar conditions as in cathode catalyst layers of PEM fuel cells, indicate that for Reaction (1.2), $\alpha_{c,c}$ = 1 and $\alpha_{c,c}$ = 1/2 in Equation (3.60) at low and high current densities, respectively. Parathasarathy et al. (1992) interpret their experimental data as indicating that Reaction (1.2) in cathode catalyst layers results from the following initial one-electron electrochemical adsorption step of dissolved oxygen onto the surface of the catalyst:

$$O_2 + H^+ + e^- \rightarrow O_2H_{ads} \tag{3.64}$$

where Reaction (3.64) is the rate-determining step at high current densities. Parathasarathy et al. (1992) also suggest that there is a chemical step following Reaction (3.64) and that this chemical step is probably the rate-determining step at low current densities. Based on this set of steps, for each occurrence of Reaction (1.2), dividing the number of electrons transferred (i.e. 4) by the number of times that the rate-determining step occurs (i.e. 1) yields the sum of the transfer coefficients (i.e. 4). Therefore, for Reaction (1.2) in cathode catalyst layers of PEM fuel cells, $\alpha_{a,c}$ = 3 and $\alpha_{a,c}$ = 7/2 at low and high current densities, respectively. However, in the thesis model the value of

$\alpha_{c,c}$ is assumed to be constant (i.e. independent of current density), with $\alpha_{a,c} = 4 - \alpha_{c,c}$, and is not set a-priori, but is determined by fitting model results to the experimental data of Wang et al. (2003) - as discussed in more detail in Chapter 5. Finally, Sepa et al. (1981) note that experimental data support a value of $b_{O_2} = 1$ in Equation (3.60) and this value is used in the thesis model.

The dependence of cathode catalyst layer exchange current density on the temperature (in units of Kelvin) has been determined experimentally to be of the form:

$$i_{0,c}^{ref}(T) = i_{0,c}^{ref}(343.15)e^{\left[\frac{\Delta E}{R}\left(\frac{1}{343.15}-\frac{1}{T}\right)\right]} \tag{3.65}$$

where $\Delta E = 2.76 \times 10^7$ J kmol^{-1} is the activation energy at high current densities (Parathasarathy et al., 1992). This temperature dependence is small for variations around operating temperatures on the order of those typically found in PEM fuel cells. Thus temperature dependence of the exchange current density in the cathode catalyst layer has been neglected in the thesis model. Also, because of the much smaller effect that anode kinetics has on the overall performance of PEM fuel cells, temperature dependence of the exchange current density in the anode catalyst layer has been neglected as well.

Croissant et al. (1998) measured values of approximately 10^{-3} A cm^{-2} for the exchange current density of Reaction (1.1) at platinum electrodes in acid solutions at the reference temperature of $T^\circ = 298.15$ K. Parathasarathy et al. (1992) measured values of approximately 10^{-10} A cm^{-2} and 10^{-6} A cm^{-2} for the exchange current density of Reaction (1.2) at platinum microelectrodes in contact with Nafion® membranes near the same temperature, at low and high current densities, respectively. Thus the catalytic activity per unit surface area of platinum is approximately 10^7 and 10^3 times lower for Reaction (1.2) than Reaction (1.1) at low and high current densities, respectively. In the thesis model, however, the ratio of anodic to cathodic exchange current densities is assumed to be independent of current density and also temperature, and the average value of 10^5 is used.

Therefore, since the orders of $\left(c_{H_2}^{ref}\right)^{-b_{H_2}}$ and $\left(c_{O_2}^{ref}\right)^{-b_{O_2}}$ are similar (Croissant et al., 1998; Parathasarathy et al., 1992), in the thesis model the ratio of the value $\xi i_{0,a}^{ref}\left(c_{H_2}^{ref}\right)^{-b_{H_2}}$ (Equation (3.59)) divided by $\xi i_{0,c}^{ref}\left(c_{O_2}^{ref}\right)^{-b_{O_2}}$ (Equation (3.60)) is maintained at 10^5. The values are not set a-priori, but are determined by fitting model results to the experimental data of Wang et al. (2003) - as discussed in more detail in Chapter 5.

In the catalyst layers, Equation (3.53) for the conservation of energy applies, but with the rate of heat production, S_h, per unit volume of the medium including additional terms as compared to Equation (3.54). These additional terms arise from the latent heat associated with the phase change of water between vapour and polymer electrolyte phases, $r_m h_{wc}$, the ohmic heat generated by the current of protons in the polymer electrolyte, i_m^2/σ_m^{eff}, and the heat production due to the overpotentials, $|\eta_a S_s|$ and $|\eta_c S_s|$, associated with the destruction or generation of current of electrons in the respective catalyst layers. Also an additional term due to the reversible heat production associated with Reaction (1.1) in the anode catalyst layer is given by $-\left(T\Delta\bar{s}_a^{\circ}/F\right)|S_s|$ and, due to the reversible heat production associated with Reaction (1.2) in the cathode catalyst layer, is given by $-\left(T\Delta\bar{s}_c^{\circ}/F\right)|S_s|$.

At the reference temperature of 298.15 K and pressure of 1 atm (101,325 Pa), the change in entropy in Reaction (1.1) is $\Delta\bar{s}_a^{\circ}$ = 208 J (kmol K)$^{-1}$ and in Reaction (1.2), where the product water is assumed to be in liquid phase, is $\Delta\bar{s}_c^{\circ}$ = -326360 J (kmol K)$^{-1}$ (Lampinen & Fomino, 1993). Thus the reversible heat absorbed in the anode catalyst layer by Reaction (1.1) is very small compared to the heat produced in the cathode catalyst layer by Reaction (1.2) and is neglected in the thesis model. Also, the reversible heat produced in the cathode catalyst layer by Reaction (1.2) is almost identical to the heat produced by the overall Reaction (1.3).

Therefore, in the thesis model, it is assumed that the reversible heat production for the overall Reaction (1.3) is produced entirely in the cathode catalyst layer. Also, since the temperature and pressure variations in PEM fuel cells are relatively small, for the overall Reaction (1.3), the reversible molar heat production can be assumed to be constant and can therefore be expressed as a fraction, β, of the change in enthalpy of formation, $\Delta \bar{h}_f^\circ$, which can also be assumed to be constant. Thus the rate of heat production, S_h, per unit volume in the anode catalyst layer is given by:

$$S_h = (r_w + r_m)\, h_{wg} + \frac{i_s^2}{\sigma_s^{eff}} + \frac{i_m^2}{\sigma_m^{eff}} + |\eta_a S_s| \tag{3.66}$$

and in the cathode catalyst layer is given by:

$$S_h = (r_w + r_m)\, h_{wg} + \frac{i_s^2}{\sigma_s^{eff}} + \frac{i_m^2}{\sigma_m^{eff}} + |\eta_c S_s| - \beta \frac{\Delta \bar{h}_f^\circ}{4F} S_s \tag{3.67}$$

At the operating temperature and pressure with product water in vapour phase, $\Delta \bar{h}_f^\circ$ = -4.846 × 10^8 J $kmol^{-1}$ (Chase et al., 1986) and $-\Delta \bar{h}_f^\circ / 4F$ = 1.26 V. Finally, using the mixed potential value of 1.12 V rather than the reversible value of 1.20 V for the open-circuit potential, β = (1.26 V - 1.12 V)/1.26 V = 0.11.

For the boundary conditions at the membrane/catalyst layer boundaries, the mass transfer of the gases (other than the water vapour present in the PEM fuel cell through the membrane) is considered negligible. Additionally, mass transfer between liquid water and the water in the polymer electrolyte is considered to occur only through water vapour as an intermediary, and the phase change of water vapour to water in the polymer electrolyte is treated as source terms in the catalyst layers in the thesis model rather than as boundary conditions. The boundaries can then be considered to be walls impermeable to the gases and liquid water. Assuming no slip conditions as well, superficial velocities of the gases

and liquid water and diffusive mass fluxes of the gas species are therefore equal to zero at the boundaries. Finally, it is assumed that the membrane does not conduct electrons since polymer electrolyte is an insulator to the flow of electrons and, as a result, currents of electrons normal to the boundaries are equal to zero.

In the thesis model, it is assumed that the ELAT® LT 1200-W gas diffusion layers have catalyst layers consisting of carbon-black supported platinum and polymer electrolyte, with or without PTFE, deposited on them to form gas diffusion electrodes. Such electrodes are commercially available as ELAT® LT 120E-W gas diffusion electrodes and, in general, the ELAT® LT series gas diffusion layers and electrodes have similar properties, according to the technical data sheets supplied by E-TEK (2004), except for the mean pore sizes. This is because the catalysed carbon in the catalyst layers are bound into a similar agglomerate structure as the uncatalysed carbon in the gas diffusion layers. For similar amounts of catalysed and uncatalysed carbon in the catalyst and gas diffusion layers, the densities, specific heats and thermal conductivities of the solid matrix, and effective electrical conductivities of the medium, will be approximately the same - since the weight percentage of platinum on carbon-black support is assumed to be 20 wt % in the thesis model. Note that this value yields a platinum loading of 0.1 mg cm^{-2} for the assumed thickness of the catalyst layers (Ticianelli et al., 1988a). However, the catalyst layers have large enough polymer electrolyte loadings such that excess polymer electrolyte fills the macropores, reducing the mean pore sizes, and therefore also the porosities, compared to the gas diffusion layers, as has already been assumed in Section 3.1 for the thesis model (with $\varphi_{gdl} = 0.40$ and $\varphi_{cl} = 0.25$).

In contrast to the porosities, according to the technical data sheets supplied by E-TEK (2004), permeabilities of the gas diffusion layers and electrodes are similar, which is probably the result of a corresponding decrease in the tortuosity with the decrease in porosity, since $\kappa \propto \varphi/\tau^2$ (Epstein, 1988). Therefore, in the thesis model, permeabilities are assumed to be the same in the catalyst and gas diffusion layers. The similar φ/τ^2 or

φ^a dependence of the effective diffusion coefficients in Equation (3.55) is also assumed to be the same in the catalyst and gas diffusion layers - which yields $a = 1.0$ in the catalyst layers. However, in Equation (3.55), it is assumed that $b = 1.5$ in the catalyst layers, consistent with the value used in the gas diffusion layers. Finally, according to Baschuk & Li (2000), the active surface area per unit volume in the catalyst layers is given by first multiplying the platinum loading of 1.0 g m^{-2} by the surface area per unit mass for platinum, which for 20 wt % platinum is equal to 128 m^2 g^{-1} (according to the technical data sheets supplied by E-TEK (2004)). This value is then divided by the thickness of the catalyst layer (1.29×10^{-5} m) and multiplied by the fractional utilisation of platinum in the thin-film catalyst layer (0.454 - Cheng et al., 1999) yielding a value of $\xi = 4.50 \times 10^6$ m^{-1}.

3.1.5 Membrane

In the membrane and catalyst layers, transport of protons through water-filled pores of polymer electrolyte has to be considered. In general, the molar flux of a dilute charged species through an electrolyte is described by the Nernst-Planck equation (Bard & Faulkner, 2001), which is derived by assuming that Equation (3.19), with driving force given by Equation (3.22) for a binary system, applies to the charged species. The other component is considered to be the solvent, which in this case is the liquid water in the pores of the polymer electrolyte. It is further assumed that bulk properties of the binary system as a whole can be approximated as those of the solvent. With these assumptions, and applying Equations (3.19) and (3.22) to the protons in the polymer electrolyte (which is assumed to be an isotropic porous medium) the following equation for the superficial molar flux of the protons is derived:

$$\vec{N}_{H^+} = c_{H^+}\vec{v}_m - D_{H^+}^{eff}\vec{\nabla}c_{H^+} - \frac{F}{RT}c_{H^+}D_{H^+}^{eff}\vec{\nabla}\phi_m \tag{3.68}$$

where $\vec{v}_m$ is the superficial velocity of liquid water, c_{H^+} is the concentration of protons, $D_{H^+}^{eff}$ is the effective diffusion coefficient for protons and ϕ_m is the potential, in the polymer electrolyte. The three terms on the right represent convection, diffusion and migration, respectively, where the migration term is the contribution of the electric field to the transport of the protons. In the case of the polymer electrolyte, which has fixed negative charge sites attached to the polymer backbone, the physically justifiable assumption of electroneutrality means that the concentration of protons must be equal to the concentration of fixed negative charge sites, c_f. In an operating fuel cell stack the membrane is to a large extent volumetrically constrained, and therefore the effects of membrane swelling are small and can be neglected. Thus c_f is assumed to be constant. As a result, the concentration of protons is constant throughout the polymer electrolyte and the diffusion term in Equation (3.68) is equal to zero. Finally, although there is convection occurring in the polymer electrolyte of PEM fuel cells as discussed below, the effects of migration are typically much greater - since the contribution of the electric field to the transport of the protons is dominant. Thus Equation (3.68) yields:

$$\vec{i}_m = F\vec{N}_{H^+} = -\sigma_m \vec{\nabla}\phi_m \tag{3.69}$$

where $\vec{i}_m$ is the superficial current density of protons and, according to Ohm's law $\left(\text{i.e. } \vec{i}_m = -\sigma_m \vec{\nabla}\phi_m\right)$, $\sigma_m = F^2 c_f D_{H^+}^{eff}/RT$ is the protonic conductivity of the polymer electrolyte. It is important to note that Equation (3.69) applies to polymer electrolyte and therefore an effective conductivity is associated with the volumetric fraction of polymer electrolyte, φ_m, which is equal to 1 in the membrane, but in the thesis model is equal to 0.25 in the catalyst layers.

Substituting an effective conductivity into Equation (3.69) and taking the divergence yields:

$$\vec{\nabla}\cdot\left(\sigma_m^{eff}\vec{\nabla}\phi_m\right)+S_m=0 \tag{3.70}$$

where $S_m=\vec{\nabla}\cdot\vec{i}_m$ is the source term for rate of production or consumption of current of protons per unit volume, which is positive for the production of protons. Equation (3.70) is the analogous equation to Equation (3.2) where, in general, conservation of charge (i.e. $\vec{\nabla}\cdot\vec{i}_m=-\vec{\nabla}\cdot\vec{i}_s$), yields $S_m=-S_s$. Note that in the membrane the source terms are equal to zero since there are no electrochemical reactions, but that in the anode and cathode catalyst layers the source terms are given by Equations (3.59) and (3.60), respectively. Finally, at the catalyst/gas diffusion layer boundaries polymer electrolyte ends and the superficial current densities of protons are equal to zero, since polymer electrolyte is necessary for the transport of protons.

In the thesis model a fit to experimental data for a Nafion® PFSA polymer membrane N-117 manufactured by DuPont (Springer et al., 1991) is used for the protonic conductivity of the polymer electrolyte (in units of siemens per metre) as a function of water content and temperature (in units of Kelvin). The resulting effective conductivity is given by:

$$\begin{aligned}\sigma_m^{eff}&=\varphi_m^a(0.5139\lambda-0.326)e^{\left[1268\left(\frac{1}{303}-\frac{1}{T}\right)\right]},\quad \lambda>1\\ \sigma_m^{eff}&=\varphi_m^a(0.1879)e^{\left[1268\left(\frac{1}{303}-\frac{1}{T}\right)\right]},\quad \lambda\le 1\end{aligned} \tag{3.71}$$

where λ is the concentration of liquid water divided by the concentration of fixed negative charge sites in the polymer electrolyte. A generalisation of Bruggemann's approximation has been used to account for the volumetric fraction of polymer electrolyte (De La Rue & Tobias, 1959) in which, for simplicity, it is assumed that a = 1.0 - consistent with the value used for the diffusion coefficients in the thesis model catalyst layers.

The superficial mass flux of liquid water in polymer electrolyte, $\vec{J}_w$, is given by an equation of the following form (Bernardi & Verbrugge, 1991; Springer et al., 1991):

$$\vec{J}_w = \left(\frac{2.5}{22}\right) M_{H_2O} \frac{\vec{i}_m}{F} \lambda - \rho_w \frac{\kappa}{\mu_w} \vec{\nabla} P_w - \frac{\rho_{dry}}{M_{dry}} M_{H_2O} D_\lambda \vec{\nabla} \lambda \tag{3.72}$$

The first term on the right is an expression for electro-osmotic drag, which results from water being dragged along by the protonic current because of hydrogen bonding of water to the protons. The second term is Darcy's law for viscous convection applied to the porous polymer electrolyte, and the final term is Fick's first law for self-diffusion. In Equation (3.72), ρ_{dry} and M_{dry} are the density and equivalent weight of dry polymer electrolyte, respectively. The equivalent weight is defined as the dry polymer electrolyte density divided by the corresponding concentration of fixed negative charge sites, such that $c_f = \rho_{dry} / M_{dry}$. For polymer electrolyte, viscous convection is relatively small compared to the other terms in Equation (3.72) and therefore can be neglected (Fimrite, 2004), yielding:

$$\vec{J}_w = \left(\frac{2.5}{22}\right) M_{H_2O} \frac{\vec{i}_m}{F} \lambda - \frac{\rho_{dry}}{M_{dry}} M_{H_2O} D_\lambda \vec{\nabla} \lambda \tag{3.73}$$

It is important to note that Equation (3.73) applies to polymer electrolyte and therefore an effective diffusivity is associated with the volumetric fraction of polymer electrolyte which, when substituted into Equation (3.73) and the divergence is taken, yields:

$$\vec{\nabla} \cdot \left[\left(\frac{2.5}{22}\right) M_{H_2O} \frac{\vec{i}_m}{F} \lambda - \frac{\rho_{dry}}{M_{dry}} M_{H_2O} D_\lambda^{eff} \vec{\nabla} \lambda \right] = r_m \tag{3.74}$$

where the source term for rate of production or consumption of liquid water mass in the polymer electrolyte per unit volume is given by:

$$r_m = \vec{\nabla} \cdot \vec{J}_w \tag{3.75}$$

Note that in the membrane this source term is equal to zero since there is no production of liquid water in the polymer electrolyte. In the catalyst layers, Equation (3.74) is solved to yield r_m which is then used in Equations (3.57) and (3.58) to account for mass transfer of water (from water vapour in the gas pores to liquid water in the polymer electrolyte) and the associated rate of heat production in Equations (3.66) and (3.67).

In Equation (3.74), the effective Fick's first law self-diffusion coefficient, D_λ^{eff}, is determined using a linear fit (Dutta et al., 2001) to experimental data for a Nafion® PFSA polymer membrane N-117 (Springer et al., 1991). The coefficient is given in units of metres squared per second, with the associated dependence on temperature in units of Kelvin (Springer et al., 1991), as follows:

$$\begin{aligned}
D_\lambda^{eff} &= \varphi_m^a 10^{-10} e^{2416\left(\frac{1}{303}-\frac{1}{T}\right)}, \quad \lambda < 2 \\
D_\lambda^{eff} &= \varphi_m^a 10^{-10}\left(1+2(\lambda-2)\right) e^{2416\left(\frac{1}{303}-\frac{1}{T}\right)}, \quad 2 \le \lambda \le 3 \\
D_\lambda^{eff} &= \varphi_m^a 10^{-10}\left(3-1.67(\lambda-3)\right) e^{2416\left(\frac{1}{303}-\frac{1}{T}\right)}, \quad 3 < \lambda < 4.5 \\
D_\lambda^{eff} &= \varphi_m^a 1.25 \times 10^{-10} e^{2416\left(\frac{1}{303}-\frac{1}{T}\right)}, \quad \lambda \ge 4.5
\end{aligned} \tag{3.76}$$

where a generalisation of Bruggemann's approximation has been used with a = 1.0.

In the membrane, since there is no gaseous phase (i.e. the volumetric fraction of gases, φ, is equal to zero), Equation (3.53) for the conservation of energy simplifies to:

$$\vec{\nabla}\cdot\left(k_s\vec{\nabla}T\right)+S_h=0 \tag{3.77}$$

where k_s is thermal conductivity of the solid polymer and the membrane heat production per unit volume (due to ohmic heating) is given by:

$$S_h=\frac{i_m^2}{\sigma_m^{eff}} \tag{3.78}$$

Note that Equation (3.77) does not include the contribution of conductive heat transfer by liquid water in the membrane. However, the thermal conductivity of liquid water at the operating temperature and pressure is 0.66 W (m K)$^{-1}$ (Linstrom & Mallard, 2003), while that of Teflon® is only 0.25 W (m K)$^{-1}$ according to technical data sheets supplied by DuPont (2004). Note that equivalent data for Nafion® is not available, but Nafion® and Teflon® should have approximately equal thermal conductivities due to their similar compositions and structures. Using Equation (3.52) with s equal to one, the total thermal conductivity of the membrane is given by $k_{total}=\varphi k_w+(1-\varphi)k_s$. In this case φ is the volumetric fraction of liquid water in the membrane which, for a fully hydrated Nafion® PFSA polymer membrane N-117, has a value of 0.28 (Bernardi & Verbrugge, 1992), such that in Equation (3.77) a value of k_s = 0.36 W (m K)$^{-1}$ is assumed in order to represent the total thermal conductivity. Finally, note that the effect of convective heat transfer by liquid water is neglected in the thesis model, since the velocity of liquid water through the membrane is very small - as can be seen for example in Figure 2.5.

Since the polymer electrolyte in the catalyst layers is assumed to form thin films covering the agglomerates (which are in contact with thin films of liquid water or pores filled with gases and liquid water), the polymer electrolyte can be considered to be in equilibrium with the gases and liquid water. This should also be the case at the membrane/catalyst layer boundaries. In the thesis model, polymer electrolyte liquid water content in the catalyst layers and at the membrane/catalyst layer boundaries, as given by

λ, is related to partial water vapour pressure and liquid water saturation in the adjacent pores using an experimentally derived relationship for a Nafion® PFSA polymer membrane N-117 (Springer et al., 1991):

$$\begin{aligned} \lambda &= 0.043 + 17.81\,\hat{a} - 39.85\,\hat{a}^2 + 36.0\,\hat{a}^3, \quad 0 \le \hat{a} \le 1 \\ \lambda &= 14 + 1.4(\hat{a} - 1), \quad 1 < \hat{a} \le 3 \end{aligned} \tag{3.79}$$

where $\hat{a}$ is the activity of water vapour and liquid water, which is assumed to be given by (Eaton, 2001):

$$\hat{a} = \frac{P_{H_2O}}{P_{sat}} + 2s \tag{3.80}$$

Using Equations (3.79) and (3.80), the liquid water content in the polymer electrolyte is determined as a function of position in the catalyst layers, which also yields the gradient in liquid water content. Knowing λ and the temperature T, Equation (3.76) can be solved for D_λ^{eff}. Substitution of D_λ^{eff} into Equation (3.74), together with $\vec{\nabla}\lambda$ and knowledge of $\vec{i}_m$, yields the expression in square brackets in Equation (3.74) as a function of position and, therefore, also the divergence of the expression. This calculation then finally yields r_m in the catalyst layers.

DuPont manufactures Nafion® PFSA polymer membrane N-112. These membranes have a thickness of 5.1×10^{-5} m, a dry density of 1980 kg m^{-3} and a dry equivalent weight of 1100 kg kmol^{-1} (according to technical data sheets supplied by DuPont (2004)) and these values are used in the thesis model. Also, a specific heat of 1172 J (kg K)$^{-1}$, which is the value for Teflon®, is assumed, since equivalent data for Nafion® is not available but should be the same. Finally, the experimentally derived relationships for a Nafion® PFSA polymer membrane N-117 in Equations (3.71), (3.76) and (3.79) are assumed to apply for

the N-112 membrane in the thesis model, since they are identical except for the thickness values.

3.2 Implementation in FLUENT™ PEMFC Software Package

A PEM fuel cell model that has been developed at Fluent Inc. and has been implemented in the company's general purpose commercial CFD software package FLUENT™ (Fluent Inc., 2001) is presented by Li & Becker (2004). This implementation is herein referred to as the FLUENT™ PEMFC software package. The thesis model is similar to the model developed at Fluent Inc. and can be implemented in the FLUENT™ PEMFC software package by adjusting appropriate parameters in the software package. In the FLUENT™ PEMFC software package, standard conservation of mass, linear momentum, energy and species equations (Fluent Inc., 2001) are solved throughout the entire computational domain. These standard equations are given in Table 3.5. The conservation of mass equation in the FLUENT™ PEMFC software package is the same as Equations (3.7) and (3.40), which are equivalent, for the gas channels, gas diffusion layers and catalyst layers. Also, the species source terms in the FLUENT™ PEMFC software package are the same as in the thesis model. In the FLUENT™ PEMFC software package, the conservation of mass equation is applied to the bipolar plates and membrane as well, but the velocities of the gases and the source terms are set equal to zero as shown in Table 3.5.

The conservation of linear momentum equation in the FLUENT™ PEMFC software package is the same as Equation (3.8) for the gas channels, with the viscous stress tensor given by Equation (3.9). However, Darcy's law for porous media in the form of Equation (3.43) for the gas diffusion and catalyst layers is implemented in FLUENT™ as a source term in Equation (3.8), as shown in Table 3.5 (Fluent Inc., 2001). Unfortunately, this is not a physically justifiable formulation (Nield & Bejan, 1992), although the effects of the

convective term, $\vec{\nabla}\cdot(\rho\ \vec{v}\vec{v})$, and the viscous term, $\vec{\nabla}\cdot\tau$, are very small for the typical operating conditions in PEM fuel cells, such that Darcy's law still holds approximately.

In general, FLUENT™ also allows for the inclusion of a quadratic drag source term (Fluent Inc., 2001), the so-called Forchheimer term (Nield & Bejan, 1992), together with the linear Darcy's law source term although, for the typical operating conditions in PEM fuel cells, this term is negligible and is therefore set equal to zero. The conservation of linear momentum equation is also applied to the bipolar plates and membrane (which are assumed to be porous media with volumetric fractions of gases, φ, essentially set equal to zero), but the gas velocities, and therefore also the viscous stress tensors and Darcy's law source terms, are set equal to zero as shown in Table 3.5. The conservation of energy equation in the FLUENT™ PEMFC software package is the same as Equation (3.12) for the gas channels, with $\varphi = 1$, Equation (3.53) for the gas diffusion and catalyst layers, and Equations (3.5) and (3.77), which are equivalent, for the bipolar plates and membrane. The diffusive mass fluxes of gas species in the bipolar plates and membrane are essentially set equal to zero, as a result of the dependence on volumetric fraction of the gases through Equations (3.17) and (3.56). Also, energy source terms in the FLUENT™ PEM fuel cell software package are the same as in the thesis model.

Finally, the conservation of species equation in the FLUENT™ PEMFC software package is the same as Equation (3.18) for the gas channels, gas diffusion layers and catalyst layers, with the appropriate simplifications outlined in Section 3.1.2 and effective diffusion coefficients given by Equation (3.56). Also, the species source terms in the FLUENT™ PEMFC software package are the same as in the thesis model. In the FLUENT™ PEMFC software package the conservation of species equation is applied to the bipolar plates and membrane as well, but with the effective diffusion coefficients essentially set equal to zero, as a result of the dependence on the volumetric fraction of the gases, and the source terms set equal to zero.

In order for equations to be solved simultaneously throughout the entire computational domain in the FLUENT™ PEMFC software package, interior boundaries cannot be treated as walls if any transport is to occur through them. Therefore, bipolar plate/gas diffusion layer and membrane/catalyst layer boundaries, through which transport generally occurs, cannot be treated as no-slip impermeable walls for the gases like in the thesis model. No-slip impermeable wall boundary conditions are applied approximately in the FLUENT™ PEMFC software package by setting the velocities of the gases equal to zero and the diffusive mass fluxes of the gas species essentially equal to zero in the bipolar plates and membrane. In comparison, boundaries between the bipolar plates and gas channels can be treated as walls in the FLUENT™ PEMFC software package like in the thesis model, since no transport occurs through them.

In general, for an arbitrary scalar ϕ , FLUENT™ allows the implementation of a user-defined transport equation (Fluent Inc., 2001):

$$\vec{\nabla}\cdot\left(\vec{J}\phi - D\,\vec{\nabla}\phi\right) = S_{\phi} \tag{3.81}$$

where $\vec{J}$ is a user-defined flux, D is a diffusion coefficient and S_{ϕ} is a source term. In the FLUENT™ PEMFC software package, Equation (3.2) (for potential in the solid matrix of the bipolar plates, gas diffusion layers and catalyst layers, with constant effective electrical conductivities) and Equation (3.70) (for the potential in the polymer electrolyte in the catalyst layers and membrane, with effective electrical conductivity given by Equation (3.71)) are implemented as two user-defined transport equations - where $\vec{J}$ is equal to zero and D is the effective electrical conductivity. Source terms are those for the thesis model. Both scalar transport equations are solved throughout the entire computational domain, but with effective electrical conductivities essentially set equal to zero in regions where the equations do not physically apply and the source terms set equal to zero as shown in Table 3.6. Also, boundary conditions of zero superficial current densities of electrons (protons) at the internal membrane/catalyst layer (catalyst/gas diffusion layer)

boundaries are approximately set - by having effective electrical conductivities of electrons in the membrane and protons in the gas diffusion layers essentially set equal to zero.

In the FLUENT™ PEMFC software package, the saturation of liquid water is solved throughout the computational domain as a user-defined transport equation:

$$\vec{\nabla}\cdot\left(\rho_w\vec{v}\mathrm{s}-\rho_w\frac{s^3\kappa}{\mu_w}\frac{dP_c}{ds}\vec{\nabla}s\right)=S_w \tag{3.82}$$

where, from Equation (3.81), $\phi=\mathrm{s}$, $\vec{J}=\rho_w\vec{v}$ and $D=\left(\rho_w s^3\kappa/\mu_w\right)\left(dP_c/ds\right)$ with dP_c/ds given by Equation (3.49). In the case of liquid water flows in the gas channels, D is set equal to zero and Equation (3.82) simplifies to Equation (3.29). In the case of liquid water flows in the gas diffusion and catalyst layers, $\vec{J}$ is set equal to zero and Equation (3.82) simplifies to Equation (3.48). Equation (3.82) is also solved in the bipolar plates and membrane, but with liquid water saturation and source terms set equal to zero, such that boundary conditions of no-slip impermeable walls are set (approximately) at the internal bipolar plate/gas diffusion layer and membrane/catalyst layer boundaries.

Finally, in the FLUENT™ PEMFC software package, Equation (3.74) for λ (the content of liquid water in the polymer electrolyte in the catalyst layers and membrane) is solved throughout the computational domain as a user-defined transport equation where, from Equation (3.81), $\phi=\lambda$, $\vec{J}=\left(2.5/22\right)\left(M_{H_2O}\vec{i}_m/F\right)$ and $D=\rho_{dry}M_{H_2O}D_\lambda^{eff}/M_{dry}$, with D_λ^{eff} given by Equation (3.76). Equation (3.74) is also solved in the gas diffusion layers, gas channels and bipolar plates, but with λ and the source terms set equal to zero, such that boundary conditions of no-slip impermeable walls are set (approximately) at the internal catalyst/gas diffusion layer boundaries.

Table 3.5 - Standard equations in FLUENT™ PEMFC software package.

	Bipolar plates	Gas channels	Gas diffusion layers	Anode catalyst layer	Cathode catalyst layer	Membrane
Properties	$\varphi \cong 0$ $\vec{v} = 0$	$\varphi = 1$				$\varphi \cong 0$ $\vec{v} = 0$
Mass	$\vec{\nabla} \cdot (\rho\ \vec{v}) = S_g$					
	$S_g = 0$	$S_g = 0$	$S_g = -r_w$	$S_g = S_{H_2} + S_{H_2O}$	$S_g = S_{O_2} + S_{H_2O}$	$S_g = 0$
Linear momentum	$\vec{\nabla} \cdot (\rho\ \vec{v}\vec{v}) + \vec{\nabla} P + \vec{\nabla} \cdot \tau = \vec{S}$					
	$\vec{S} = 0$	$\vec{S} = 0$	$\vec{S} = -\frac{\mu}{\kappa}\vec{v}$	$\vec{S} = -\frac{\mu}{\kappa}\vec{v}$	$\vec{S} = -\frac{\mu}{\kappa}\vec{v}$	$\vec{S} = 0$
Energy	$\vec{\nabla} \cdot (\rho h \vec{v}) = \vec{\nabla} \cdot \left\{ \left[\varphi k + (1-\varphi) k_s \right] \vec{\nabla} T \right\} + S_h$					
	$S_h = \frac{i_s^2}{\sigma_s^{eff}}$	$S_h = 0$	$S_h = r_w h_{wg} + \frac{i_s^2}{\sigma_s^{eff}}$	$S_h = (r_w + r_m) h_{wg} + \frac{i_s^2}{\sigma_s^{eff}} + \frac{i_m^2}{\sigma_m^{eff}} + \lvert \eta_a S_s \rvert$	$S_h = (r_w + r_m) h_{wg} + \frac{i_s^2}{\sigma_s^{eff}} + \frac{i_m^2}{\sigma_m^{eff}} + \lvert \eta_c S_s \rvert - \beta \frac{\Delta \bar{h}_f^{\circ}}{4F} S_s$	$S_h = \frac{i_m^2}{\sigma_m^{eff}}$
Species	$\vec{\nabla} \cdot (\rho y_i \vec{v}) = \vec{\nabla} \cdot \left(\rho \hat{D}_{ii}^{eff} \vec{\nabla} y_i \right) + S_i$					
	$S_i = 0$	$S_i = 0$	$S_{H_2O} = -r_w$	$S_{H_2} = \frac{M_{H_2}}{2F} S_s$ $S_{H_2O} = -r_w - r_m$	$S_{O_2} = -\frac{M_{O_2}}{4F} S_s$ $S_{H_2O} = \frac{M_{H_2O}}{2F} S_s - r_w - r_m$	$S_i = 0$

Table 3.6 - Scalar transport equations in FLUENT™ PEMFC software package.

	Bipolar plates	Gas channels	Gas diffusion layers	Anode catalyst layer	Cathode catalyst layer	Membrane
Properties	$\sigma_m^{eff} \cong 0$ $s = 0$ $\lambda = 0$	$\sigma_s^{eff} \cong 0$ $\sigma_m^{eff} \cong 0$ $\lambda = 0$	$\sigma_m^{eff} \cong 0$ $\lambda = 0$	Fixed value for λ	Fixed value for λ	$\sigma_s^{eff} \cong 0$ $s = 0$
Solid potential	$\vec{\nabla} \cdot \left(\sigma_s^{eff} \vec{\nabla} \phi_s \right) + S_s = 0$					
	$S_s = 0$	$S_s = 0$	$S_s = 0$	$S_s = \xi \, i_{0,a}^{ref} \left(\frac{c_{H_2}}{c_{H_2}^{ref}} \right)^{b_{H_2}} \left(e^{-\alpha_{a,a} \eta_a F / RT} - e^{\alpha_{a,a} \eta_a F / RT} \right)$	$S_s = \xi \, i_{0,c}^{ref} \left(\frac{c_{O_2}}{c_{O_2}^{ref}} \right)^{b_{O_2}} \left(e^{-\alpha_{a,c} \eta_a F / RT} - e^{\alpha_{a,c} \eta_a F / RT} \right)$	$S_s = 0$
Membrane potential	$\vec{\nabla} \cdot \left(\sigma_m^{eff} \vec{\nabla} \phi_m \right) + S_m = 0$					
	$S_m = -S_s$					
Saturation	$\vec{\nabla} \cdot \left(\rho_w \vec{v} s - \rho_w \frac{s^3 \kappa}{\mu_w} \frac{dP_c}{ds} \vec{\nabla} s \right) = S_w$					
	$S_w = 0$	$S_w = 0$	$S_w = r_w$	$S_w = r_w$	$S_w = r_w$	$S_w = 0$
Water content	$\vec{\nabla} \cdot \left[\left(\frac{2.5}{22} \right) M_{H_2O} \frac{\vec{i}_m}{F} \lambda - \frac{\rho_{dry}}{M_{dry}} M_{H_2O} D_\lambda^{eff} \vec{\nabla} \lambda \right] = r_m$					
	$r_m = 0$	$r_m = 0$	$r_m = 0$	Solved for r_m	Solved for r_m	$r_m = 0$

Chapter 4

Multiple Thin-Film Agglomerate Model

As discussed in Chapter 2, an appropriate model to consider for PEM fuel cell catalyst layers is the multiple thin-film agglomerate model. In order to include the effects of the multiple thin-film agglomerate model, detailed modelling of the reactions in the catalyst layers is required in the thesis model. In general, reactions which occur at the interface between different phases are referred to as heterogeneous, whereas reactions that occur in a single phase are referred to as homogeneous. Thus Reactions (1.1) and (1.2), which occur at the interface between the surface of the solid catalyst phase (which conducts electrons) and the phases contacting the solid catalyst phase (which transport hydrogen and protons in the anode and oxygen and protons in the cathode) are heterogeneous reactions. Note that in the multiple thin-film agglomerate model, the phase contacting the catalyst sites is assumed to be polymer electrolyte since protons can only be transported through this medium (i.e. the transport of protons through gases and liquid water is negligible). If the same overall reaction, which in the case of PEM fuel cells is Reaction (1.3), can occur either homogeneously or be catalysed heterogeneously, the activation energy for the homogeneous reaction pathway is almost invariably greater than for the heterogeneous reaction pathway. However, in comparison to homogeneous reactions, which occur in the bulk fluid, heterogeneous catalysis involves chemical conversion at the catalyst surface influenced by the fact that reactants have to be transported to the surface and products away from it.

In PEM fuel cells, the solid phase remains unchanged, and it is possible to treat the heterogeneous Reactions (1.1) and (1.2) as pseudo-homogeneous reactions, since the concentration of reactants can be assumed to be nearly constant on the scale of the solid catalyst surface - such that a specific surface area of the catalyst surface per unit volume of combined solid-fluid phases can be defined. Thus, the catalysed carbon-black agglomerates, polymer electrolyte, liquid water and gases in the catalyst layers can be considered as a continuum, in which the reaction proceeds according to homogeneous kinetics. The effects of reactant adsorption on the catalyst surface, and conversion to and desorption of the products, can be contained in single expressions describing kinetics of the overall heterogeneous Reactions (1.1) and (1.2), which depend on local concentrations of reactants adjacent to the catalyst surface.

4.1 Introduction

In the multiple thin-film agglomerate model for the catalyst layers in PEM fuel cells, local concentrations of reactants adjacent to the catalyst surface are dependent on the reactant transport through both an outer liquid water film and an inner polymer electrolyte film. As a first approximation, in the thesis model, the thin film of polymer electrolyte is considered to have a constant thickness throughout the catalyst layers since the volumetric fraction occupied by polymer electrolyte in the catalyst layers is assumed to be uniform. However, transport of reactants will depend on the liquid water content in the polymer electrolyte, as given by the variable λ. In contrast, the thickness of the thin film of liquid water in the catalyst layers is a function of the saturation of liquid water, s. Both the liquid water content in the polymer electrolyte and the liquid water saturation in the catalyst layers are determined by the overall rate of Reaction (1.3) since, in the thesis model, water vapour is produced at the cathode catalyst sites and can condense into the thin film of liquid water in the cathode, changing its thickness.

Additionally, water vapour can condense into the polymer electrolyte in the (anode or cathode) catalyst layers and be transported through the membrane, evaporating to form water vapour in the opposite catalyst layer. The direction of water flow depends on the overall reaction rate and operating conditions of the fuel cell. This water transport through the fuel cell alters the liquid water content in the polymer electrolyte, and also the thickness of anode and cathode liquid water films, by altering the condensation of water vapour into liquid water. Finally, both local water production at the cathode catalyst sites and local water transport through the catalyst layers and membrane vary throughout the catalyst layers as a result of variations in the local rates of Reactions (1.1) and (1.2). Thus the polymer electrolyte liquid water content and liquid water saturation in the catalyst layers (i.e. the thickness of the liquid water film) (which effect reactant transport across the thin films of polymer electrolyte and liquid water, respectively) are functions of location in the catalyst layers, and are also dependent on overall reaction rate and operating conditions.

4.2 Stationary Film Model

In the multiple thin-film agglomerate model for catalyst layers in PEM fuel cells, the transport of reactants and products between the bulk gas and the external surface of catalysed carbon-black agglomerates is described by the stationary film model. The stationary film model is based on the observation that when fluid flows at low velocities over the surface of a solid or the interface of another immiscible fluid, the flow tends to be laminar. This is the case for water flow in the polymer electrolyte or in the thin film of liquid water in PEM fuel cells. In laminar flow, the fluid may be considered to be composed of thin layers following the surface contours without mixing with adjacent layers, except for the mixing which results from molecular diffusion. The relative fluid velocity in the layer adjacent to the solid or other immiscible fluid is essentially zero, while in layers at increasing distances from the interface the velocity progressively increases.

Thus there is a layer of fluid at the interface in which laminar flow, with zero relative velocity, is maintained. The thickness of this layer or film increases with decreasing flow velocity. In the catalyst layers of PEM fuel cells, velocities of the water in the thin films of polymer electrolyte and liquid water are relatively small and can be neglected, such that the films can be considered to be stationary (i.e. with zero relative velocity).

In general, because of the inherent averaging involved in CFD calculations for PEM fuel cells, physical parameters (including species concentrations, pressure and temperature in the gases) are uniform on a grid-cell basis. When dealing with mass transfer over length scales less than the dimensions of a grid cell, it is common to assume that these uniform physical parameters are the result of mixing in the flow. The differences between these bulk conditions in the flow and those at the surfaces of solids or the interfaces of another immiscible fluid located inside the grid cell can be assumed to occur across effective laminar and stationary boundary films. In the multiple thin-film agglomerate model the thin films of polymer electrolyte and liquid water are treated in this manner since these films typically have thicknesses less than the dimensions of a grid cell. Based on these assumptions, in the stationary film model, the fluid can be divided into 1) stationary films near the interfaces, across which mass transfer is considered to result from molecular diffusion under the influence of concentration gradients, and 2) a well-mixed bulk adjacent to the films in which no concentration gradients occur. Thus the mass transfer process is a stationary one and assuming that Fick's first law applies (Taylor & Krishna, 1993), linear concentration profiles are produced across the films, which is equivalent to using the linearised form of Fick's first law for a flat, thin film.

It is assumed that the transport of reactants (i.e. hydrogen in the anode and oxygen in the cathode) through the thin film of liquid water and through the water-filled pores of the thin film of polymer electrolyte is that of a dilute species through a solvent. Molar fluxes of the reactants are derived by assuming that Equation (3.19), with driving force given by Equation (3.23), applies to the dissolved reactant with the other component considered to be the solvent which, in this case, is water in the thin films of polymer electrolyte and

liquid water. As discussed in Chapter 3, for an ideal two-component system, Equations (3.19) and (3.23) are equivalent to Fick's first law as given by Equation (3.17), such that the Stefan-Maxwell binary diffusion coefficient in Equation (3.19) is equal to the Fick's diffusion coefficient. It is further assumed that bulk properties of the system as a whole can be approximated as those of the solvent and, as mentioned above, that water velocities in the thin films of polymer electrolyte and liquid water are relatively small and can be neglected. With these assumptions, Equations (3.19) and (3.23) yield the molar flux of reactant r through the thin film of liquid water:

$$N_{r,w} = -\frac{\mathcal{D}_{r\text{-}w}\,\Delta c_{r,w}}{l_w} \tag{4.1}$$

where $\mathcal{D}_{r\text{-}w}$ is the binary diffusion coefficient and $\Delta c_{r,w}$ is the total change in concentration of the dissolved reactant in the liquid water film of thickness l_w. Similarly, the molar flux of reactant r through the thin film of polymer electrolyte is given by:

$$N_{r,m} = -\frac{\mathcal{D}_{r\text{-}m}\,\Delta c_{r,m}}{l_m} \tag{4.2}$$

where $\mathcal{D}_{r\text{-}m}$ is the binary diffusion coefficient and $\Delta c_{r,m}$ is the total change in concentration of the dissolved reactant in the polymer electrolyte film of thickness l_m.

The binary diffusion coefficients of dissolved hydrogen and oxygen in liquid water and polymer electrolyte are given in units of metres squared per second by:

$$
\begin{aligned}
\mathcal{D}_{H_2\text{-}w} &= \left(3.34\times10^{-6}\right)e^{-\frac{1932}{T}} \\
\mathcal{D}_{O_2\text{-}w} &= \left(2.31\times10^{-6}\right)e^{-\frac{2055}{T}} \\
\mathcal{D}_{H_2\text{-}m} &= \left(7.16\times10^{-8}\right)\left(\frac{\lambda}{16.8}\right)e^{-\frac{1335}{T}} \\
\mathcal{D}_{O_2\text{-}m} &= \left(2.67\times10^{-6}\right)\left(\frac{\lambda}{16.8}\right)e^{-\frac{2870}{T}}
\end{aligned}
\tag{4.3}
$$

where the temperature T is in units of Kelvin. Note that the diffusion coefficients of dissolved hydrogen, $\mathcal{D}_{H_2\text{-}w}$ (Jahne et al., 1987), and oxygen, $\mathcal{D}_{O_2\text{-}w}$ (Himmelblau, 1964), in liquid water are approximately one order of magnitude greater, respectively, than the diffusion coefficients of dissolved hydrogen, $\mathcal{D}_{H_2\text{-}m}$ (Jiang & Kucernak, 2004), and oxygen, $\mathcal{D}_{O_2\text{-}m}$ (Parathasarathy et al., 1992), in polymer electrolyte. The diffusion coefficients in polymer electrolyte are given for fully hydrated Nafion® PFSA polymer membrane N-117 manufactured by DuPont and are assumed to be the same for the N-112 membrane in the thesis model, since the membranes differ only in thickness values. The dependence of the polymer electrolyte diffusion coefficients on water content (i.e. λ) in Equation (4.3) is based on the observation that $\mathcal{D}_{H_2\text{-}m}$ increases linearly with increasing water content (Yeo & McBreen, 1979) and the assumption that $\mathcal{D}_{O_2\text{-}m}$ behaves in a similar fashion (as supported by the experimental data of Parathasarathy et al. (1992)). According to Equation (3.79), λ has a maximum value of 16.8. Finally, the dependence of the diffusion coefficients on pressure is negligible for the typical operating pressures in PEM fuel cells (Taylor & Krishna, 1993).

4.3 Transport Limitations

In the multiple thin-film agglomerate model, concentrations in the Butler-Volmer equation for the consumption or production of current of electrons per unit volume (i.e.

Equation (3.59) in the anode catalyst layer and Equation (3.60) in the cathode catalyst layer) are the concentrations of dissolved reactant, c_r, at the catalyst sites located at the inner surface of the thin film of polymer electrolyte. This concentration is related to the concentration $c_{r,mw}$ at the outer surface of the thin film of polymer electrolyte through Equation (4.1), where $\Delta c_{r,m} = c_r - c_{r,mw}$. The concentration at the outer surface of the thin film of polymer electrolyte is assumed to be equal to the concentration at the inner surface of the thin film of liquid water. This is a justifiable assumption since, according to the experimental data of Jiang & Kucernak (2004), the solubility (i.e. concentration) of hydrogen in Nafion® membrane in equilibrium with hydrogen saturated liquid water is 0.89 times the solubility of hydrogen in liquid water at 333 K. Also, according to the experimental data of Parathasarathy et al. (1992), the solubility of oxygen in Nafion® membrane in equilibrium with pure oxygen at 5 atm pressure and a temperature of 343.15 K is 1.19 times the solubility of oxygen in liquid water (as calculated using Equation (4.7)). Finally, the concentration at the inner surface of the thin film of liquid water is related to the concentration $c_{r,b}$ at the outer surface of the thin film of liquid water through Equation (4.2), where $\Delta c_{r,w} = c_{r,mw} - c_{r,b}$. Since the molar fluxes in Equations (4.1) and (4.2) are equal for steady-state conditions (i.e. $N_{r,w} = N_{r,m} = N_r$), substituting the above expressions into Equations (4.1) and (4.2) and equating $c_{r,mw}$ yields the reactant molar flux:

$$N_r = \frac{1}{\left(l_w / \mathcal{D}_{r\text{-}w} + l_m / \mathcal{D}_{r\text{-}m}\right)}\left(c_{r,b} - c_r\right) \tag{4.4}$$

Multiplying Equation (4.4) by the active surface area per unit volume in the catalyst layers, ξ, and taking into account the superficial transport limitations of the thin films of liquid water and polymer electrolyte in each of the CFD grid cells - such that the diffusion coefficients in Equation (4.4) are replaced by effective diffusion coefficients - yields for steady-state conditions in the anode and cathode, respectively:

$$\begin{aligned}\frac{1}{\left(l_w/\mathcal{D}^{eff}_{H_2\text{-}w}+l_m/\mathcal{D}^{eff}_{H_2\text{-}m}\right)}\left(c_{H_2}-c_{H_2,b}\right)\xi &= \frac{S_s}{2F}\\ \frac{1}{\left(l_w/\mathcal{D}^{eff}_{O_2\text{-}w}+l_m/\mathcal{D}^{eff}_{O_2\text{-}m}\right)}\left(c_{O_2}-c_{O_2,b}\right)\xi &= -\frac{S_s}{4F}\end{aligned} \tag{4.5}$$

where use has been made of Reactions (1.1) and (1.2). In Equation (4.5), the effective diffusion coefficients - consistent with Equation (3.55) - are given by:

$$\begin{aligned}\mathcal{D}^{eff}_{r-w} &= \varphi_{cl}^{\,a}s^b\mathcal{D}_{r-w}\\ \mathcal{D}^{eff}_{r-m} &= \varphi_m^{\,a}\mathcal{D}_{r-m}\end{aligned} \tag{4.6}$$

since $\varphi_{cl}s$ is the volumetric fraction of liquid water and φ_m is the volumetric fraction of polymer electrolyte in the catalyst layers, and where the values of a and b are assumed to be the same as for the diffusion coefficients in the gases. Also, in Equation (4.5), S_s is given by Equations (3.59) and (3.60) in the anode and cathode catalyst layers, respectively. These equations are functions of the dissolved reactant concentrations at the catalyst sites (i.e. c_{H_2} and c_{O_2}, respectively).

It is assumed that gases in the catalyst layers are in equilibrium with liquid water in the thin films of both liquid water and polymer electrolyte. Henry's law for the solubility of reactant gas r in liquid water for both films is derived by equating fugacity of the reactant gas (with mole fraction x_r in the gas phase), $f_r = \gamma_r x_r P$, to fugacity of the dissolved reactant (with mole fraction $x_{r,w}$ in the liquid water phases in the thin films), $f_{r,w} = H_{r,w}x_{r,w}$ (Prausnitz et al., 1986). Ideal gases are also assumed, such that the gas-phase fugacity coefficient, γ_r, is equal to one and the term $x_r P$ is simply the partial reactant pressure in the gas phase. Bulk properties of the thin films as a whole are approximated as those of the liquid water solvent. Henry's law for the concentration of

dissolved reactant at the outer surface of the thin film of liquid water, in terms of the partial reactant pressure in the adjacent gaseous bulk phase, is given by:

$$c_{r,b} = c_w \frac{x_r P}{H_{r,w}} \tag{4.7}$$

where c_w is the concentration of liquid water, which changes negligibly for the typical temperature and pressure variations in PEM fuel cells. The value at the operating temperature and pressure of 54.28 kmol m^{-3} (Linstrom & Mallard, 2003) is used in the thesis model.

In Equation (4.7), $H_{r,w}$ is the Henry's law constant for solubility of the reactant in liquid water, which is independent of the reactant mole fraction in the gaseous phase and also the liquid water phase, provided that the mole fraction in the liquid water phase is sufficiently small, as is assumed to be the case here. Also, although in general this constant is dependent on temperature and, to a lesser degree, on total pressure, for the typical variations in temperature and for the relatively low pressures in PEM fuel cells, the variations in this constant are negligible. The values at the operating temperature and standard pressure of $H_{H_2,w} = 7.60 \times 10^9$ Pa and $H_{O_2,w} = 6.66 \times 10^9$ Pa (Lide, 2003) are used in the thesis model. Thus the Henry's law constants are uniform over the thin films and apply equally at the catalyst surfaces, assuming overall equilibrium. Equation (4.7) is used to replace dissolved reactant concentrations at the outer surface of the thin film of liquid water in Equation (4.5) by equivalent partial pressures in the adjacent gas phases (which are then replaced by mass fractions of reactants in the gases). Equation (4.7) is similarly used to replace dissolved reactant concentrations at catalyst surfaces in Equation (4.5). The resulting equations are given by:

$$\frac{\rho c_w}{\left(l_w/\mathcal{D}^{eff}_{H_2\text{-}w} + l_m/\mathcal{D}^{eff}_{H_2\text{-}m}\right)} \frac{RT}{H_{H_2,w}} \left(y_{H_2} - y_{H_2,b}\right)\xi = M_{H_2} \frac{S_s}{2F}$$
$$\frac{\rho c_w}{\left(l_w/\mathcal{D}^{eff}_{O_2\text{-}w} + l_m/\mathcal{D}^{eff}_{O_2\text{-}m}\right)} \frac{RT}{H_{O_2,w}} \left(y_{O_2} - y_{O_2,b}\right)\xi = -M_{O_2} \frac{S_s}{4F} \tag{4.8}$$

where the ideal gas law is assumed. Equation (4.8) is similar to the following equations used for diffusion-reaction balance in the PEM fuel cell model that has been developed at Fluent Inc. (Li & Becker, 2004):

$$\frac{\rho \mathcal{D}^{eff}_{H_2-H_2O}}{l}\left(y_{H_2} - y_{H_2,b}\right)\xi = M_{H_2} \frac{S_s}{2F}$$
$$\frac{\rho \mathcal{D}^{eff}_{O_2-N_2}}{l}\left(y_{O_2} - y_{O_2,b}\right)\xi = -M_{O_2} \frac{S_s}{4F} \tag{4.9}$$

except that the diffusional process occurring within each grid cell (on the left hand side of the equations given above) is considered to be in the gas phase.

Thus the diffusion-reaction balance of Li & Becker (2004) is similar to the no-film agglomerate model of Eikerling & Kornyshev (1998), in that it does not take into account the thin films of liquid water and polymer electrolyte and the reaction is considered to occur at the interface between the catalyst sites and the gas phase. However, unlike the no-film agglomerate model, the diffusion-reaction balance of Li & Becker (2004) does take into account a thin film of stationary gases surrounding the catalyst sites of thickness l. In the multiple thin-film model, the thin film of stationary gases is not taken into account - since transport limitations of such a film are negligible compared to transport limitations of the thin films of liquid water and polymer electrolyte. In effect, the thin film of stationary gas is assumed to be part of the bulk gases on a grid-cell basis.

In the diffusion-reaction balance of Li & Becker (2004), the thickness l of the thin film of stationary gases surrounding the catalyst sites in Equation (4.9) is given to a first order approximation as:

$$l = \frac{1}{\xi} \tag{4.10}$$

which is equivalent to assuming that the thickness of this thin film is on the order of the length scale between active catalyst surfaces. The macropores between catalyst layer agglomerates are similar in size to the agglomerates themselves and the active catalyst surfaces are found on the agglomerate surfaces, such that the length scale between active catalyst surfaces is similar to the size of the macropores. Thus Equation (4.10) is equivalent to assuming that the thin film of stationary gases is on the order of the size of the macropores. Therefore the diffusional process of the gaseous reactants in the catalyst layers can be considered to be one of axial diffusion along the main axis of the macropores as given by Equations (3.18) and (3.56), followed by one of radial (i.e. perpendicular to the main axis) diffusion to the active catalyst surfaces lining the macropores as given by Equations (4.9) and (4.10).

In the multiple thin-film agglomerate model for the catalyst layers, the thickness l of the thin film of stationary gases surrounding the catalyst sites in Equation (4.9) is replaced by the thicknesses l_m and l_w of the thin films of polymer electrolyte and liquid water, respectively, together with a correspondingly reduced thickness of the thin film of stationary gases (which is now assumed to be part of the bulk gases). Thus, assuming that thicknesses of the thin films of polymer electrolyte, liquid water and stationary gases surrounding the catalyst sites are proportional to the volumetric fractions of polymer electrolyte, φ_m, liquid water, $\varphi_{cl}s$, and stationary gases, $\varphi_{cl}(1-s)$, the thickness l_m of the thin film of polymer electrolyte is related to the thickness l of the thin film of stationary gases in Equation (4.9) by:

$$\frac{l_m}{l} = \frac{\varphi_m}{\varphi_{cl}(1-s)+\varphi_{cl}s+\varphi_m} = \frac{\varphi_m}{\varphi_{cl}+\varphi_m} \tag{4.11}$$

This can be justified on the assumption that polymer electrolyte uniformly covers the walls of the macropores, thus forming a film of constant thickness throughout the catalyst layers with the same contours as the macropores themselves. The thickness l_w of the thin film of liquid water is similarly related to the thickness l of the thin film of stationary gases in Equation (4.9) by:

$$\frac{l_w}{l} = \frac{\varphi_{cl}s}{\varphi_{cl}(1-s)+\varphi_{cl}s+\varphi_m} = \frac{\varphi_{cl}s}{\varphi_{cl}+\varphi_m} \tag{4.12}$$

This can be justified on the assumption that liquid water in the macropores uniformly covers randomly distributed hydrophilic regions of polymer electrolyte on the walls of the macropores, thus forming a film of constant thickness for a given saturation with the same contours as the macropores themselves.

Substituting Equations (4.6), (4.10), (4.11) and (4.12) into Equation (4.8) yields the following equations for transport limitations of the electrochemical reactions in the multiple thin-film agglomerate model:

$$\begin{aligned}
&\frac{(\varphi_{cl}+\varphi_m)\rho c_w}{\left[1/\left(\varphi_{cl}^{a-1}s^{b-1}\mathcal{D}_{H_2\text{-}w}\right)+1/\left(\varphi_m^{a-1}\mathcal{D}_{H_2\text{-}m}\right)\right]}\frac{RT}{H_{H_2,w}}\left(y_{H_2}-y_{H_2,b}\right)\xi^2 = M_{H_2}\frac{S_s}{2F} \\
&\frac{(\varphi_{cl}+\varphi_m)\rho c_w}{\left[1/\left(\varphi_{cl}^{a-1}s^{b-1}\mathcal{D}_{O_2\text{-}w}\right)+1/\left(\varphi_m^{a-1}\mathcal{D}_{O_2\text{-}m}\right)\right]}\frac{RT}{H_{O_2,w}}\left(y_{O_2}-y_{O_2,b}\right)\xi^2 = -M_{O_2}\frac{S_s}{4F}
\end{aligned} \tag{4.13}$$

Substituting Equation (4.10) into Equation (4.9), and using Equation (3.55), yields the following equations for the diffusion-reaction balance of Li & Becker (2004):

$$\begin{aligned} \rho\,\varphi_{cl}^{a}(1-s)^{b}\,\mathcal{D}_{H_2-H_2O}\left(y_{H_2}-y_{H_2,b}\right)\xi^{2} &= M_{H_2}\frac{S_s}{2F} \\ \rho\,\varphi_{cl}^{a}(1-s)^{b}\,\mathcal{D}_{O_2-N_2}\left(y_{O_2}-y_{O_2,b}\right)\xi^{2} &= -M_{O_2}\frac{S_s}{4F} \end{aligned} \tag{4.14}$$

which have been implemented in the FLUENT™ PEMFC software package.

4.4 Implementation in FLUENT™ PEMFC Software Package

Comparing Equations (4.13) and (4.14) reveals that the thin films of liquid water and polymer electrolyte in the multiple thin-film agglomerate model can be taken into account using the diffusion-reaction balance of Li & Becker (2004) since Equation (4.13) can be derived from Equation (4.14) by multiplying the left hand side of Equation (4.14) by the following expressions:

$$\begin{aligned} &\frac{\left(\varphi_{cl}+\varphi_{m}\right)c_w RT/H_{H_2,w}}{\varphi_{cl}^{a}(1-s)^{b}\,\mathcal{D}_{H_2-H_2O}\left[1/\left(\varphi_{cl}^{a-1}s^{b-1}\mathcal{D}_{H_2\text{-}w}\right)+1/\left(\varphi_{m}^{a-1}\mathcal{D}_{H_2\text{-}m}\right)\right]} \\ &\frac{\left(\varphi_{cl}+\varphi_{m}\right)c_w RT/H_{O_2,w}}{\varphi_{cl}^{a}(1-s)^{b}\,\mathcal{D}_{O_2-N_2}\left[1/\left(\varphi_{cl}^{a-1}s^{b-1}\mathcal{D}_{O_2\text{-}w}\right)+1/\left(\varphi_{m}^{a-1}\mathcal{D}_{O_2\text{-}m}\right)\right]} \end{aligned} \tag{4.15}$$

This is implemented through the use of user-defined functions, in which the default value of the variable ξ is multiplied by the square root of Equation (4.15).

Chapter 5

Effects of Transport Limitations

Improving the performance of PEM fuel cells depends on the optimisation of catalyst layer composition and structure for low transport resistances. This optimisation requires detailed modelling of the transport in catalyst layers in order to determine ways of increasing catalyst layer effectiveness. In Chapter 3, a PEM fuel cell model is presented which is implemented in the FLUENT™ PEMFC software package. In Chapter 4, the resulting implementation is further modified and improved by taking into account the detailed composition and structure of catalyst layers. Based on experimental observations and previous modelling studies, a multiple thin-film agglomerate model of catalyst layers is chosen for implementation in the FLUENT™ PEMFC software package. In this chapter, three-dimensional, multicomponent and multiphase CFD simulations are performed using the improved implementation, and the effects of the resulting transport limitations are investigated, by varying parameters associated with the multiple thin-film model. The results of the CFD simulations demonstrate that catalyst layer composition and structure have a significant effect on PEM fuel cell performance.

5.1 Geometry and Mesh for Thesis Model

The thesis model is based on the typical design for a single fuel cell with straight gas channels, a schematic of which is shown in Figure 1.1 together with an associated co-

ordinate system. The volume enclosed by boundaries marked with dashed lines in Figure 1.1 is extended throughout the PEM fuel cell in the positive and negative z-directions to the external boundaries. The resulting volume can be assumed to be representative of the fuel cell as a whole, and therefore is used as the thesis model volume. Figure 5.1 shows an outline of the geometry for the thesis model.

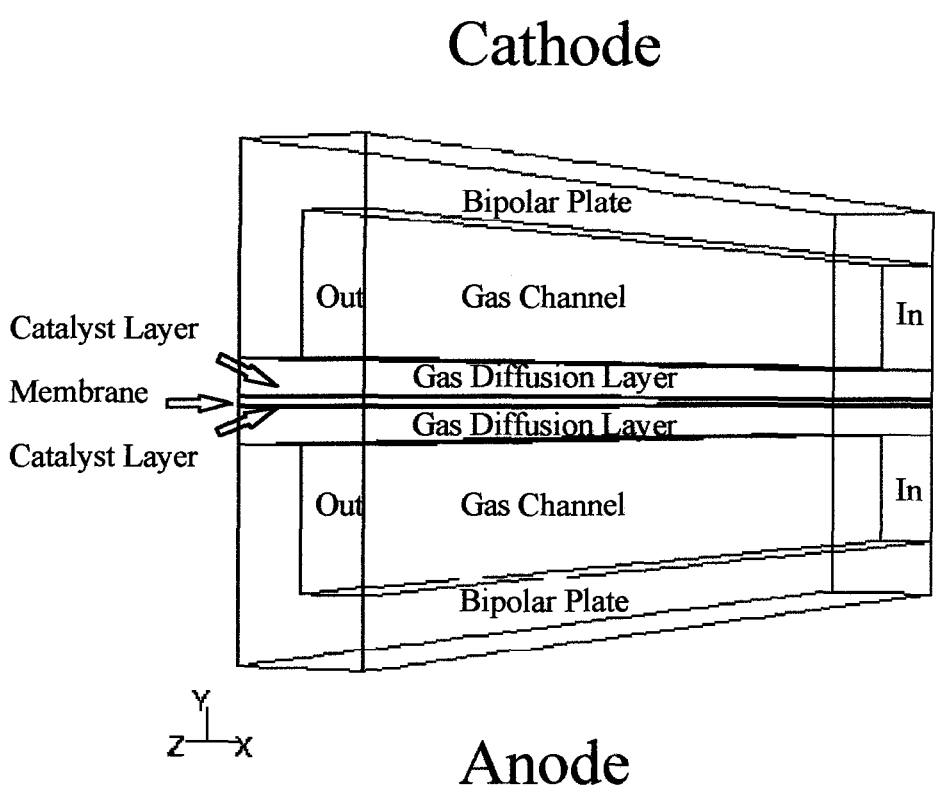

Figure 5.1 - Geometry for thesis model.

Note that Figure 5.1, which is an interior cross-sectional view along the z-axis of the PEM fuel cell from the inlets to the outlets of the gas channels, has been scaled by a factor of 1/7 in the z-direction in order to enhance the presentation of the geometry for the

thesis model. Other figures in Chapters 5 and 6 which are based on the geometry for the thesis model have also been scaled by a factor of 1/7 in the z-direction.

Figure 5.2 shows the mesh together with an enlargement revealing details in the catalyst layers and membrane.

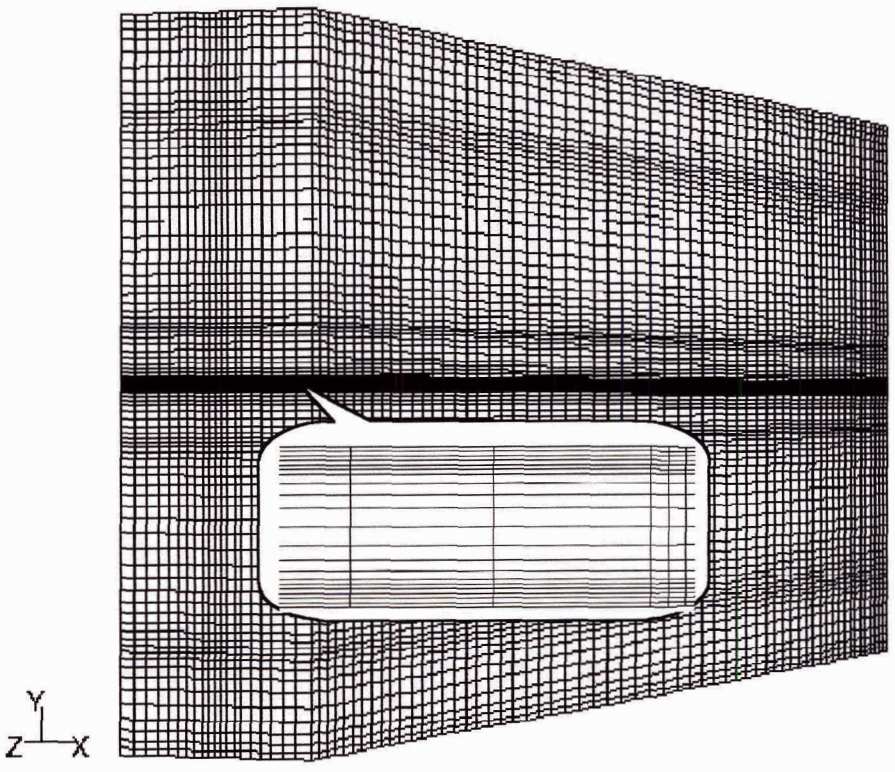

Figure 5.2 - Mesh for thesis model with magnification for corner region.

The mesh shown in Figure 5.2 is based on a grid sensitivity study performed for a model volume with similar dimensions as the thesis model (Sivertsen, 2003). In this study, at a cell voltage of 0.798 V, a coarse grid with 66,240 cells and a medium grid with 155,925 cells yield deviations of about 1.2 % and 0.9 % for the current density compared to a fine grid of 546,000 cells. In contrast to the thesis model, in the grid sensitivity study of

Sivertsen (2003), the bipolar plates are not modelled and the catalyst layers are not fully resolved. Therefore, based on this study, a similar coarse grid is used to mesh the thesis model in order to provide sufficient grid resolution while minimising computational resources. For the thesis model, the computational cells are distributed in a similar manner as for the meshes in the grid sensitivity study of Sivertsen (2003), except that additional cells are necessary in the bipolar plates and the catalyst layers. Thus, all simulations presented in Chapters 5 and 6 are performed using a grid consisting of 120,000 computational cells. The grid dimensions for the thesis model and the placement of the cells in the components of the model volume are presented in Table 5.1.

Table 5.1 - Grid dimensions for thesis model.

Components of model volume	Grid cells in x-, y- and z-directions	Number of cells
Bipolar plates (above and below gas channels)	20×10×60	2×12000
Bipolar plates (beside gas channels)	10×20×60	2×12000
Gas channels	10×20×60	2×12000
Gas diffusion layers	20×10×60	2×12000
Catalyst layers	20×6×60	2×7200
Membrane	20×8×60	9600

The grid dimensions presented in Table 5.1 are not uniform throughout the model volume components. As can be seen in Figure 5.2, the mesh for the thesis model is more dense near the bipolar plate/gas channel, bipolar plate/gas diffusion layer, gas channel/gas diffusion layer, gas diffusion layer/catalyst layer and catalyst layer/membrane boundaries

and the external boundaries in positive and negative y- and z-directions, including the gas channel inlets and outlets. The mesh for the thesis model is correspondingly less dense in the centre of model volume components and near the symmetry boundaries in the positive and negative x-directions. This is done in order to place more computational cells near regions with greater variation in the solution variables. This is accomplished by decreasing the cell dimensions in the normal direction towards the relevant boundaries except in the case of the catalyst layers which, because of their relatively small thickness, are given uniform cell dimensions in the y-direction but not in the x- and z-directions.

5.2 Comparison of Experimental and CFD Simulation Results

As mentioned in Chapter 3, Wang et al. (2003) provide experimental results for a single PEM fuel cell. The experimental results are in the form of a series of polarisation curves for different fuel cell operating temperatures and anode and cathode humidification temperatures and back pressures, which show the effects of the various operating conditions on the performance of the PEM fuel cell. The MEA of the PEM fuel cell has a superficial area of 7.2 × 7.2 cm^2. The MEA consists of a Nafion® PFSA polymer membrane, catalyst layers with platinum loadings of 0.4 mg cm^{-2} and carbon cloth gas diffusion layers. The MEA is positioned between two graphite plates, grooved with serpentine gas channels, and the entire fuel cell is pressed between two gold-plated copper plates. Reactant gases at regulated temperatures, with constant volumetric flow rates of 1200 sccm of pure hydrogen on the anode side and 2200 sccm of dry air on the cathode side, are humidified by passing through external water tanks. Regulating the water temperatures controls the humidification temperatures of the reactant gases. Reactant gas pressures are controlled by back pressure regulators. The polarisation curves are obtained for the PEM fuel cell by controlling the electronic load and measuring the voltage versus current response of the fuel cell. Figure 6 of Wang et al. (2003) provides an experimental

polarisation curve for operating conditions in Table 5.2 (herein referred to as "base case" operating conditions).

Table 5.2 - "Base case" operating conditions.

Operating condition	Value
Fuel cell temperature	70 °C
Anode humidification temperature	70 °C
Cathode humidification temperature	70 °C
Anode back pressure	3 atm
Cathode back pressure	3 atm
Anode flow rate	1200 sccm
Cathode flow rate	2200 sccm

CFD simulations are performed for similar operating conditions to the experimental "base case". Unfortunately, however, the dimensions given for the membrane, catalyst layers and gas diffusion layer in the PEM fuel cell of Wang et al. (2003) do not correspond to the dimensions of any Nafion® PFSA polymer membrane, typical catalyst layers with platinum loadings of 0.4 mg cm^{-2} or any commercially available carbon-cloth based gas diffusion layer. In order to overcome these discrepancies, and also to provide reliable data for the properties of these components, commercially available components from manufacturers which provide extensive property data are used in the thesis model, as outlined in Chapter 3. Thus a Nafion® PFSA polymer membrane N-112 manufactured by DuPont is used in the thesis model. ELAT® LT 120E-W gas diffusion electrodes composed of ELAT® LT 1200-W carbon-cloth based gas diffusion layers with catalyst layers (consisting of carbon-black supported platinum and polymer electrolyte and with or without PTFE) deposited on them, as manufactured by the E-TEK division of De Nora North America Inc., are also used in the thesis model. Finally, no information is given for

the graphite plates in the PEM fuel cell of Wang et al. (2003), except for the dimensions. Thus BMC 940 vinyl ester thermoset bipolar plates manufactured by Bulk Molding Compounds Inc. are assumed in the thesis model, but with the dimensions given by Wang et al. (2003).

As mentioned previously, the graphite plates of the PEM fuel cell of Wang et al. (2003) are grooved with serpentine gas channels and correspond to a superficial MEA area of 7.2 × 7.2 cm^2. In order to model this geometry, substantial computational resources would be required. Instead, an alternate design for a single PEM fuel cell (a schematic of which is shown in Figure 1.1) is assumed for the thesis model. This design uses a similar number of straight gas channels grooved into the graphite bipolar plates as compared with the number of straight sections in the serpentine gas channels (all of which are assumed to be 7.0 cm in length). Because gas flows in the serpentine channels of Wang et al. (2003) are different than gas flows in the straight channels of the thesis model, the constant volumetric flow rates of Wang et al. (2003) cannot be used in the thesis model. The constant volumetric flow rates in the serpentine gas channels of Wang et al. (2003) correspond to constant stoichiometric flow rates at a given current density. Assuming that the performance of PEM fuel cells is reaction-dominated and that characteristics of the gas flows have only a minor effect on the results, constant volumetric flow rates are set in the thesis model that correspond to identical stoichiometric flow rates at the same current density. Finally, it is assumed that the anode and cathode gas flows are in the same direction both in the PEM fuel cell of Wang et al. (2003) and the thesis model.

In order to match the experimental polarisation curve for "base case" operating conditions with CFD simulation results for the thesis model, it is necessary to vary some of the parameters associated with the thesis model. In general, polarisation curves can be fit with a five-parameter semi-empirical equation (Costamagna & Srinivasan, 2001b). Therefore it should only be necessary to vary up to five independent parameters associated with the thesis model. It is in fact found that varying two parameters is sufficient. This is because all of the other parameters associated with the thesis model have been given

values that have been accurately determined from separate experimental measurements, as discussed in Chapter 3.

In the thesis model, the ratio of the value $\xi i_{0,a}^{ref}\left(c_{H_2}^{ref}\right)^{-b_{H_2}}$ (Equation (3.59)) divided by $\xi i_{0,c}^{ref}\left(c_{O_2}^{ref}\right)^{-b_{O_2}}$ (Equation (3.60)) is maintained at 10^5, but the actual values are not accurately known and therefore are not set a-priori, as discussed in Chapter 3. This yields one parameter to vary in order to match the experimental results, and the values of $\xi i_{0,a}^{ref}\left(c_{H_2}^{ref}\right)^{-b_{H_2}}$ and $\xi i_{0,c}^{ref}\left(c_{O_2}^{ref}\right)^{-b_{O_2}}$ determined as a result are consistent with order of magnitude estimates of the actual values. Also, in Equation (3.60), the value of $\alpha_{c,c}$, with $\alpha_{a,c} = 4 - \alpha_{c,c}$, is not set a-priori, but yields a second parameter to vary, and the value of $\alpha_{c,c} = 2$, which yields $\alpha_{a,c} = 2$, is determined as a result. Identical values for $\alpha_{c,c}$ and $\alpha_{a,c}$ have been used in previous modelling studies (e.g. Bernardi & Verbrugge (1991, 1992)). Finally, the values of $\xi i_{0,a}^{ref}\left(c_{H_2}^{ref}\right)^{-b_{H_2}}$, $\xi i_{0,c}^{ref}\left(c_{O_2}^{ref}\right)^{-b_{O_2}}$, $\alpha_{c,c}$ and $\alpha_{a,c}$ determined as a result of matching the experimental polarisation curve for "base case" operating conditions with CFD simulation results for the thesis model are assumed to apply generally and are fixed in all other CFD simulations performed for this thesis, except for those in Section 5.3.1.1.

In this section, the CFD simulation results are for the thesis model as presented in Chapter 3, which does not include the multiple thin-film agglomerate model of catalyst layers presented in Chapter 4. However, the thesis model does include the diffusion-reaction balance of Li & Becker (2004) (Equation (4.14)), and this version is herein referred to as the DRB model. Figure 5.3 shows the experimental polarisation curve for "base case" operating conditions together with the matching CFD simulation results for the DRB model.

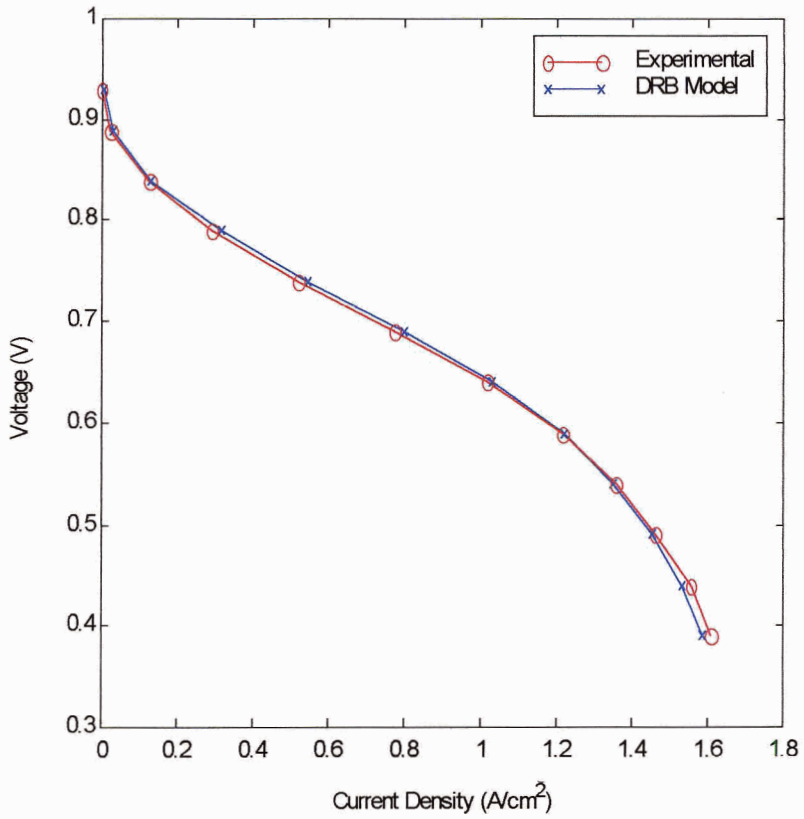

Figure 5.3 - Comparison of experimental (red) and DRB model (blue) polarisation curves for "base case" operating conditions.

As can be seen in Figure 5.3, the CFD simulation results match the experimental results to within a maximum deviation of 8.3 % at a voltage of 0.79 V. The CFD simulation results are slightly higher than the experimental results at low current densities and slightly lower than the experimental results at high current densities. This implies a slight underestimation of ohmic overpotential (probably due to high polymer electrolyte conductivity in the thesis model) and an overestimation of concentration overpotential (probably due to high model liquid water saturation).

The experimental results do not have error bounds associated with them (Wang et al., 2003). However, considering the complexity of the thesis model and the small number of parameters (i.e. two) varied in order to match the experimental results, this match is considered to be satisfactory because the polarisation curves have similar values and follow the same trend. This implies that the thesis model correctly accounts for the fundamental physics associated with PEM fuel cells. If more parameters were varied an even better match could be obtained, but that would entail varying parameters that have been given values accurately determined from separate experimental measurements, and therefore are not justifiable to change. Thus, in general, CFD simulations for the thesis model can produce results in the form of polarisation curves that satisfactorily match experimental results.

5.3 Multiple Thin-Film Agglomerate Model

In the preceding section, CFD simulation results in the form of polarisation curves for the DRB model are presented. In this section, the thesis model is further modified and improved by taking into account the detailed composition and structure of catalyst layers through the use of the multiple thin-film agglomerate model, and this version of the thesis model is herein referred to as the MTF model. CFD simulation results in the form of polarisation curves for the MTF model are presented in the next few sections and more detailed simulation results for the model variables are presented later in Section 5.3.4.

5.3.1 Comparison of Experimental and CFD Simulation Results

Figure 5.4 shows the experimental polarisation curve for "base case" operating conditions together with CFD simulation results for the MTF model.

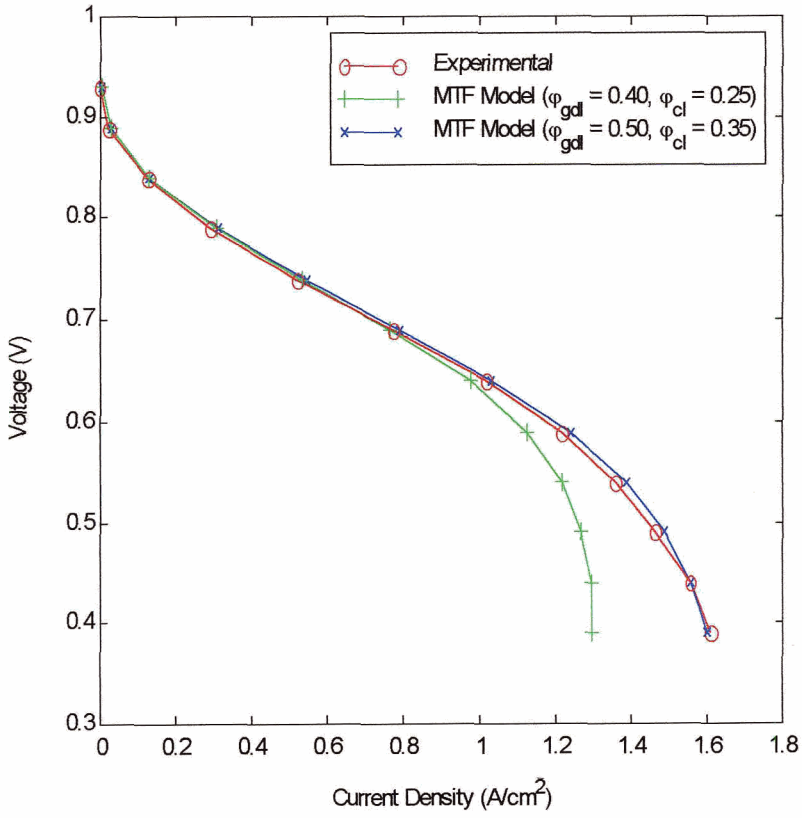

Figure 5.4 - Comparison of experimental (red) and MTF model polarisation curves for "base case" operating conditions. The model results are for φ_{gdl} = 0.40 and φ_{cl} = 0.25 (green), and φ_{gdl} = 0.50 and φ_{cl} = 0.35 (blue).

The parameter values used to generate the MTF model CFD simulation results in Figure 5.4 are all identical (except for the gas diffusion/catalyst layer porosities in the case of the blue curve) to the parameter values used in the DRB model (Figure 5.3). The only difference between the CFD simulation results in Figures 5.4 and 5.3 is the substitution of the multiple thin-film agglomerate model for the diffusion-reaction balance of Li & Becker (2004), as outlined in Chapter 4. As expected, the inclusion of the thin films of liquid water and polymer electrolyte in the multiple thin-film agglomerate model increases the

transport limitations compared to the diffusion-reaction balance. Thus in the case of the green curve with identical parameters, the CFD simulation results no longer match the experimental results, since the higher concentration overpotentials associated with the larger transport limitations yield poorer PEM fuel cell performance at higher current densities. In order to make up for the larger transport limitations associated with the multiple thin-film agglomerate model, it is found that it is necessary to increase the porosity of the gas diffusion layers, φ_{gdl}, from 0.40 to 0.50 and the porosity of the catalyst layers, φ_{cl}, from 0.25 to 0.35. These increases in gas diffusion and catalyst layer porosities are justifiable since porosities are not provided by Wang et al. (2003) for the experimental PEM fuel cell nor by E-TEK (2004) for the ELAT® LT series assumed in the thesis model. Increasing the porosities decreases the transport limitations, as discussed in Chapter 2. As can be seen in Figure 5.4, this yields CFD simulation results that match the experimental results to within a maximum deviation of 7.3 % at a voltage of 0.79 V. The CFD simulation results are slightly higher than the experimental results at low and medium current densities and slightly lower than the experimental results at the highest current densities. Similar to Figure 5.3, this implies a slight underestimation of ohmic overpotential (probably due to high polymer electrolyte conductivity in the thesis model) and an overestimation of concentration overpotential at the highest current densities (probably due to inclusion of the thin films of liquid water and polymer electrolyte).

In increasing the porosities of the gas diffusion and catalyst layers it is assumed that the volumetric fractions occupied by carbon in the gas diffusion layers and carbon/platinum in the catalyst layers remain the same (i.e. $\varphi_{C/Pt} = 0.40$). Thus the thermal characteristics and effective conductivity of electrons in the gas diffusion and catalyst layers will remain the same. Therefore, in order to account for the increase in gas diffusion layer porosity from 0.40 to 0.50, there must be a corresponding decrease in the PTFE volumetric fraction from 0.20 to 0.10. Based on the results outlined in Chapter 1, there is a minimum PTFE content at which the hydrophobic property of PTFE provides sufficient water expulsion. For contents above this minimum, the presence of excess PTFE

only has the effect of reducing porosity. Assuming that a PTFE volumetric fraction of 0.10 still provides ample hydrophobicity, such that the contact angle remains the same, the transport characteristics in the gas diffusion layers will remain the same except for the effect of increased porosity.

In the catalyst layers it is also assumed that the volumetric fraction of polymer electrolyte remains the same. Thus the active catalyst surface and the effective conductivity of protons in the catalyst layers will remain the same. Also, since polymer electrolyte acts as a binding agent similar to PTFE, the structure of the catalyst layers should also be similar and the transport characteristics in the catalyst layers will remain the same except for the effect of increased porosity. Therefore, in order to account for the increase in catalyst layer porosity from 0.25 to 0.35, there must be a corresponding decrease in the PTFE volumetric fraction from 0.10 to 0. Thin-film catalyst layers typically contain no PTFE and the multiple thin-film model actually implies that there is no PTFE present, since otherwise the resulting hydrophobicity would limit formation of the thin film of liquid water. Also, note that the hydrophobic backbone of the polymer electrolyte (made of PTFE) ensures that the contact angle remains the same in the catalyst layers for the randomly distributed regions where water expulsion is occurring.

Finally, for both the gas diffusion and catalyst layers, $\kappa \propto \varphi/\tau^2$ (Epstein, 1988), and assuming that the tortuosity remains the same, the permeability must be increased as the porosity is increased. However, the effect of permeability is small for the diffusion dominated transport in a PEM fuel cell, such that changes in permeability are neglected. Thus it is justifiable to increase the porosities of the gas diffusion and catalyst layers without changing any other parameter values associated with the thesis model. Therefore the values $\varphi_{gdl} = 0.50$ and $\varphi_{cl} = 0.35$ are used to generate all CFD simulation results presented subsequently for the MTF model.

As discussed in Chapter 4, for the diffusion-reaction balance of Li & Becker (2004), the thickness l of the thin film of stationary gases surrounding the catalyst sites is given to a first order approximation as $l = 1/\xi$, which is equivalent to assuming that the thickness of the thin film is on the order of the length scale between active catalyst surfaces. In the thesis model, the value of $\xi = 4.50 \times 10^6$ m^{-1} yields $l = 220$ nm. As mentioned in Chapter 4, this is equivalent to assuming that the thin film of stationary gases is on the order of the size of the macropores. According to Uchida et al. (1995), macropores range in size from 40 - 1000 nm. Assuming that the diffusional process of the gaseous reactants in the catalyst layers can be considered to be one of axial diffusion along the main axis of the macropores, followed by one of radial (i.e. perpendicular to the main axis) diffusion to the active catalyst surfaces lining the macropores, the thickness l of the thin film of stationary gases surrounding the catalyst sites is 20 - 500 nm. In the diffusion-reaction balance of Li & Becker (2004), the thickness l = 220 nm of the thin film of stationary gases surrounding the catalyst sites is a good first approximation since the thin film has only a negligible effect. However, in the multiple thin-film model, the thickness of the thin film of polymer electrolyte has a large effect as shown below in Section 5.3.2. Therefore the thickness l of the thin films of stationary gases, liquid water and polymer electrolyte surrounding the catalyst sites is set to be in the range of 20 - 500 nm, and a lower value of 36 nm is chosen. This corresponds to a thickness of the thin film of polymer electrolyte of 15 nm according to Equation (4.11).

5.3.1.1 Humidification Temperatures

Figures 3 and 4 of Wang et al. (2003) provide experimental polarisation curves for "base case" operating conditions, and also for variable anode and cathode humidification temperatures, respectively. However, the experimental polarisation curves for "base case" operating conditions from Figures 3 and 4 of Wang et al. (2003), although identical to each other, are different from the experimental polarisation curve for "base case"

operating conditions from their Figure 6. Thus different values of $\xi i_{0,a}^{ref}\left(c_{H_2}^{ref}\right)^{-b_{H_2}}$ and $\xi i_{0,c}^{ref}\left(c_{O_2}^{ref}\right)^{-b_{O_2}}$ are determined as a result of matching CFD simulation results for the MTF model to the experimental results in Figures 3 and 4 of Wang et al. (2003), versus to those in their Figure 6. However, the same values of $\alpha_{c,c}$ and $\alpha_{a,c}$ are found to apply. In this section, after matching CFD simulation results to the experimental results for "base case" operating conditions, the predictive capabilities of the simulations are tested by varying the simulation anode and cathode humidification temperatures in an attempt to match the experimental polarisation curves for variable anode and cathode humidification temperatures.

Figure 5.5 shows the experimental polarisation curve for "base case" operating conditions from Figure 3 of Wang et al. (2003) together with the matching CFD simulation results for the MTF model. Figure 5.5 also shows the experimental and simulated polarisation curves for "base case" operating conditions, except for an anode humidification temperature of 40 °C. In the simulations, the composition of the gas entering the anode gas channel for the 40 °C case is set based on a saturation pressure of water vapour value of 0.0731 atm (Equation (3.34)). According to Equation (3.35), this yields mole and mass fractions of the gas species at the operating pressure of 3 atm of $x_{H_2O} = 0.0244$, $x_{H_2} = 0.9756$, $y_{H_2O,a} = 0.1825$ and $y_{H_2} = 0.8175$. Using Equation (3.37), the corresponding mass flow rate is $Q_a = 2.97 \times 10^{-8}$ kg s^{-1}.

As can be seen in Figure 5.5, for "base case" operating conditions, the CFD simulation results match the experimental results to within a maximum deviation of 5.4 % at a voltage of 0.79 V. The CFD simulation results are slightly higher than the experimental results at low and medium current densities and slightly lower than the experimental results at the highest current densities, the reasons for which have been discussed previously for the similar results in Figure 5.4.

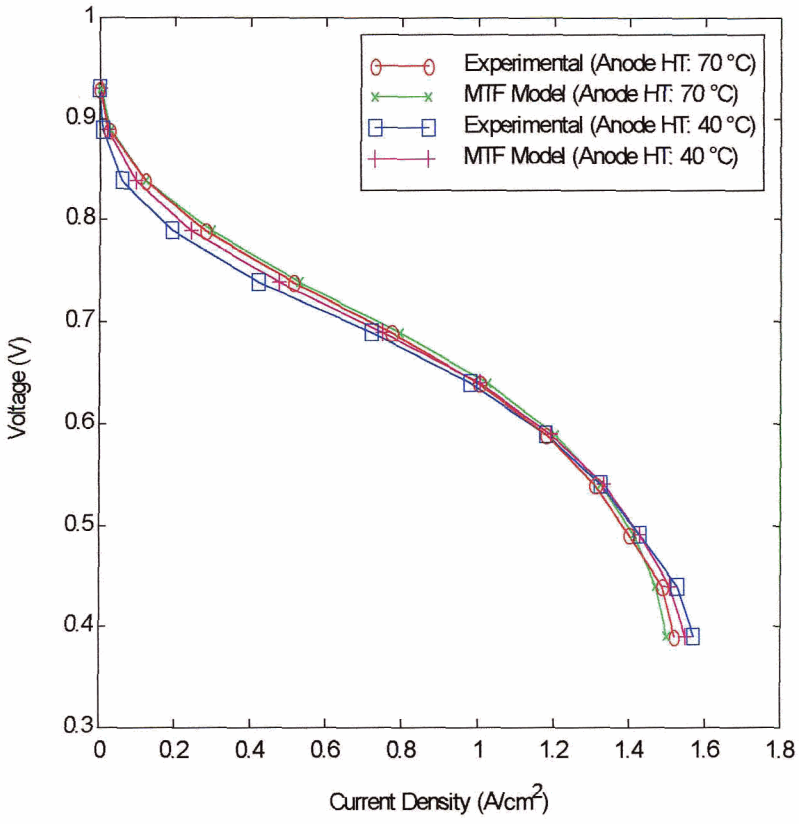

Figure 5.5 - Comparison of experimental and MTF model polarisation curves for "base case" operating conditions, and also for variable anode humidification temperature (HT). The experimental results are for an anode HT of 70 °C (red) and 40 °C (blue), and the model results are for an anode HT of 70 °C (green) and 40 °C (magenta).

Also, from Figure 5.5 it can be seen that for an anode humidification of 40 °C, the CFD simulation results similarly match the corresponding experimental results, with the simulation results higher than the experimental results at low and medium current densities and lower than the experimental results at the highest current densities. However, in this case, deviations between the simulation and experimental results are in general larger than

for the "base case" results, with a maximum deviation of 37 % at a voltage of 0.84 V. Thus the numerical accuracy of the predicted CFD simulation results versus the experimental results decreases as variations in operating conditions from the "base case" values increase. However, qualitatively, the predictive capability of the CFD simulations in this case is reasonable as the simulations correctly predict the cell voltage (i.e. between 0.54 and 0.59 V) at which the PEM fuel cell performance for an anode humidification of 40 °C changes from being worse to being better than that for an anode humidification of 70 °C. The CFD simulations also follow the same trend as the experimental results.

Note that the PEM fuel cell performance is worse at low current densities for an anode humidification of 40 °C versus 70 °C because less water vapour in the anode catalyst layer results in less water content in the polymer electrolyte and greater ohmic resistances. At higher current densities, the PEM fuel cell performance is better for an anode humidification of 40 °C versus 70 °C because less water vapour in the anode catalyst layer results in less water being transported through the membrane to the cathode catalyst layer by electro-osmotic drag. There is therefore less liquid water saturation and its associated transport limitations in the cathode. The results in Figure 5.5 imply that the effect of the underestimation of ohmic overpotential (probably due to high polymer electrolyte conductivity in the thesis model) for "base case" operating conditions, as discussed previously for the similar results in Figure 5.4, is enhanced for the lower anode humidification temperature (probably due to relatively higher model conductivity). However, the effect of the overestimation of concentration overpotential is similar for "base case" operating conditions and the lower anode humidification temperature.

Figure 5.6 shows the experimental polarisation curve for "base case" operating conditions from Figure 4 of Wang et al. (2003) together with the matching CFD simulation results for the MTF model. Figure 5.6 also shows the experimental and simulated polarisation curves for identical operating conditions as the "base case" operating conditions, except for a cathode humidification temperature of 40 °C. In the simulations, Equation (3.36) yields mole and mass fractions of the gas species entering the

cathode gas channel for the 40 °C case of x_{H_2O} = 0.0244, x_{O_2} = 0.2049, x_{N_2} = 0.7707, $y_{H_2O,\,c}$ = 0.0154, y_{O_2} = 0.2293 and y_{N_2} = 0.7553. Using Equation (3.38), the corresponding mass flow rate is Q_c = 6.48 × 10^{-7} kg s^{-1}.

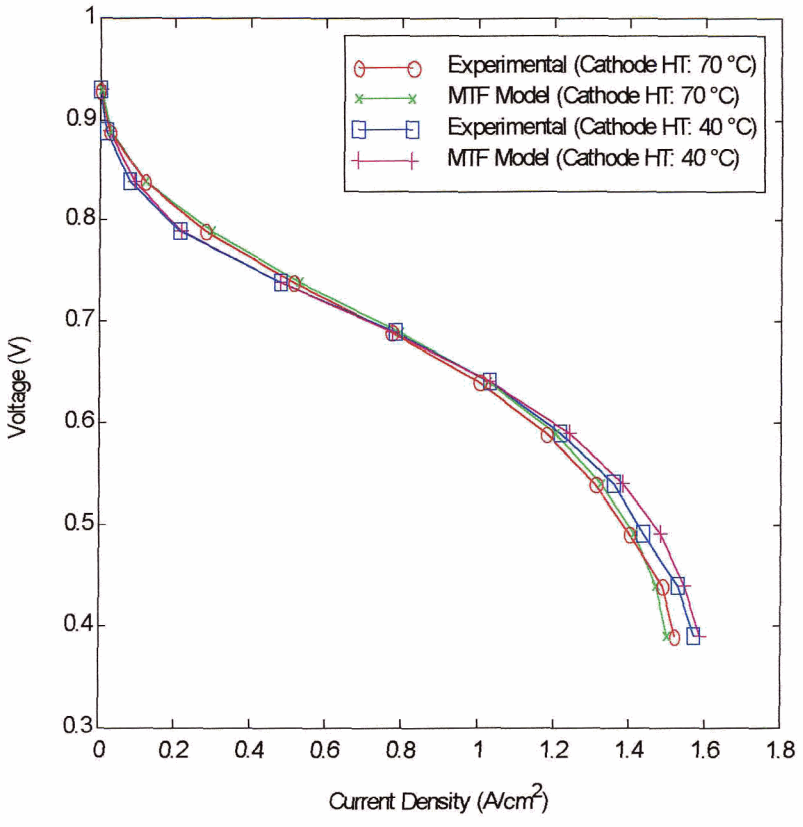

Figure 5.6 - Comparison of experimental and MTF model polarisation curves for "base case" operating conditions, and also for variable cathode humidification temperature (HT). The experimental results are for a cathode HT of 70 °C (red) and 40 °C (blue), and the model results are for a cathode HT of 70 °C (green) and 40 °C (magenta).

In Figure 5.6, the experimental polarisation curve for "base case" operating conditions from Figure 4 of Wang et al. (2003) and the corresponding CFD simulation results are the same as those in Figure 5.5. Also, from Figure 5.6 it can be seen that for a cathode humidification temperature of 40 °C, the CFD simulation results are slightly higher than the corresponding experimental results at all current densities, including even at the highest current densities. In this case, deviations between the simulation and experimental results are in general only slightly larger than for the "base case" results, with a maximum deviation of 13 % at a voltage of 0.84 V. Thus the numerical accuracy of the predicted CFD simulation results versus the experimental results is much better than that for the anode humidification temperature of 40 °C in Figure 5.5 and decreases only slightly as variations in operating conditions from the "base case" values increase. Also, the CFD simulations qualitatively follow the same trend as the experimental results and correctly predict the cell voltage (i.e. approximately 0.69 V) at which the PEM fuel cell performance for a cathode humidification of 40 °C changes from being worse to being better than that for a cathode humidification of 70 °C.

Note that the PEM fuel cell performance is worse at low current densities for a cathode humidification of 40 °C versus 70 °C because less water vapour in the cathode catalyst layer results in less water content in the polymer electrolyte and greater ohmic resistances. At higher current densities, the PEM fuel cell performance is better for a cathode humidification of 40 °C versus 70 °C because less water vapour in the cathode catalyst layer results in more liquid water evaporation and therefore less saturation and its associated transport limitations in the cathode. The results in Figure 5.6 imply that the effect of the underestimation of ohmic overpotential (probably due to high polymer electrolyte conductivity in the thesis model) is similar for "base case" operating conditions and the lower cathode humidification temperature. However, the overestimation of concentration overpotential at the highest current densities seen for the "base case" operating conditions becomes an underestimation for the lower cathode humidification temperature (probably due to relatively low model liquid water saturation).

5.3.2 Polymer Electrolyte

Figure 5.7 shows CFD simulation results for the MTF model in the form of polarisation curves for "base case" operating conditions, and with variable thickness, l_m, of the thin film of polymer electrolyte.

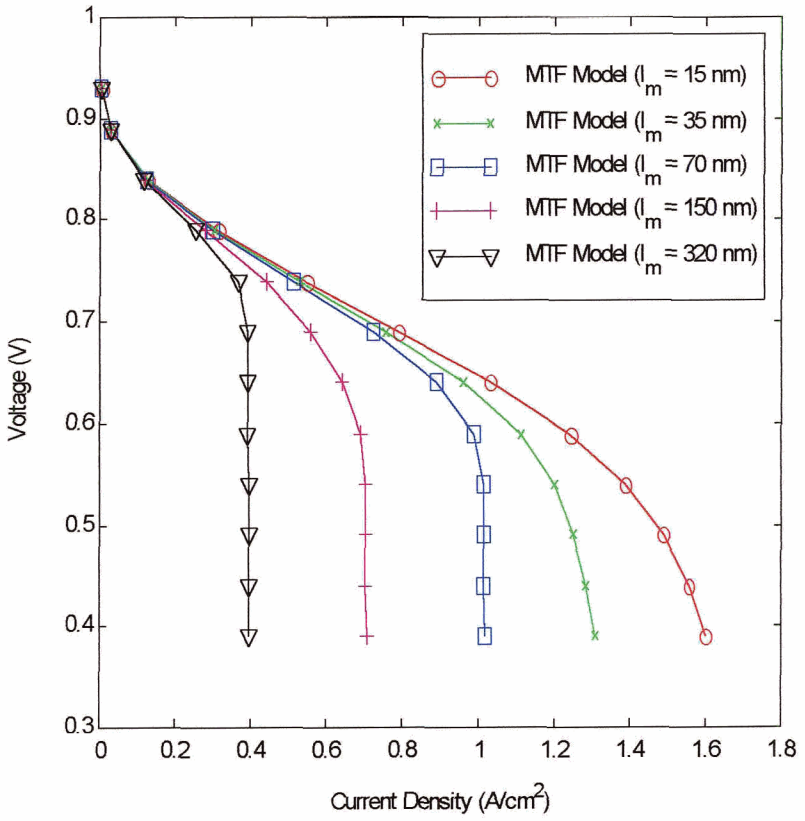

Figure 5.7 - Comparison of MTF model polarisation curves for "base case" operating conditions, and with variable thickness, l_m, of the thin film of polymer electrolyte of 15 nm (red), 35 nm (green), 70 nm (blue), 150 nm (magenta) and 320 nm (black).

The red curve in Figure 5.7 is the CFD simulation results from Figure 5.4 for the values $\varphi_{gdl} = 0.50$ and $\varphi_{cl} = 0.35$. As discussed in Section 5.3.1, the thickness of the thin film of polymer electrolyte in this case is 15 nm. For the other polarisation curves in Figure 5.7, the thickness of the thin film of polymer electrolyte in the CFD simulations is increased to 35, 70, 150 and 320 nm, while all other parameter values are kept the same. According to Equation (4.11), this corresponds to an increased thickness l of the thin films of stationary gases, liquid water and polymer electrolyte surrounding the catalyst sites of 84, 168, 360 and 768 nm for a 0.25 volumetric fraction of polymer electrolyte and a porosity of 0.35. Assuming that the diffusional process of the gaseous reactants in the catalyst layers can be considered to be one of axial diffusion along the main axis of the macropores, followed by one of radial diffusion to the active catalyst surfaces lining the macropores, this corresponds to increased macropore sizes of 168, 336, 720 and 1536 nm. According to Uchida et al. (1995), macropores range in size from 40 - 1000 nm and, therefore, the value of 1536 nm corresponds to a length scale greater than the maximum macropore size. Thus, in this case, the assumed structure in the multiple thin-film agglomerate model of the catalyst layers starts to become invalid - since the 320 nm thickness of the thin film of polymer electrolyte probably occupies a volumetric fraction that is greater than 0.25, with a corresponding decrease in the porosity, and these effects need to be taken into account in the model.

As can be seen in Figure 5.7, increasing the thickness of the thin film of polymer electrolyte in the multiple thin-film model has a substantial negative effect on PEM fuel cell performance This is because of increased transport limitations associated with the large decrease in diffusion coefficients of the reactants in the polymer electrolyte versus gas phase. For a 320 nm thickness of the thin film of polymer electrolyte, a maximum current density of only about 0.4 A cm^{-2} is predicted by the CFD simulations. If the thickness could be increased without varying any other parameters, the maximum current density would approach zero as the thickness increases above approximately 1000 nm. Thus the results in Figure 5.7 agree with those discussed in Chapter 2 where it is noted

that, according to experimental results, the layer of polymer electrolyte surrounding the catalyst sites cannot exceed 1000 nm in thickness.

5.3.3 Liquid Water

Figure 5.8 shows CFD simulation results for the MTF model in the form of polarisation curves for "base case" operating conditions, and with variable volume-averaged (in the cathode gas diffusion and catalyst layers) liquid water saturation.

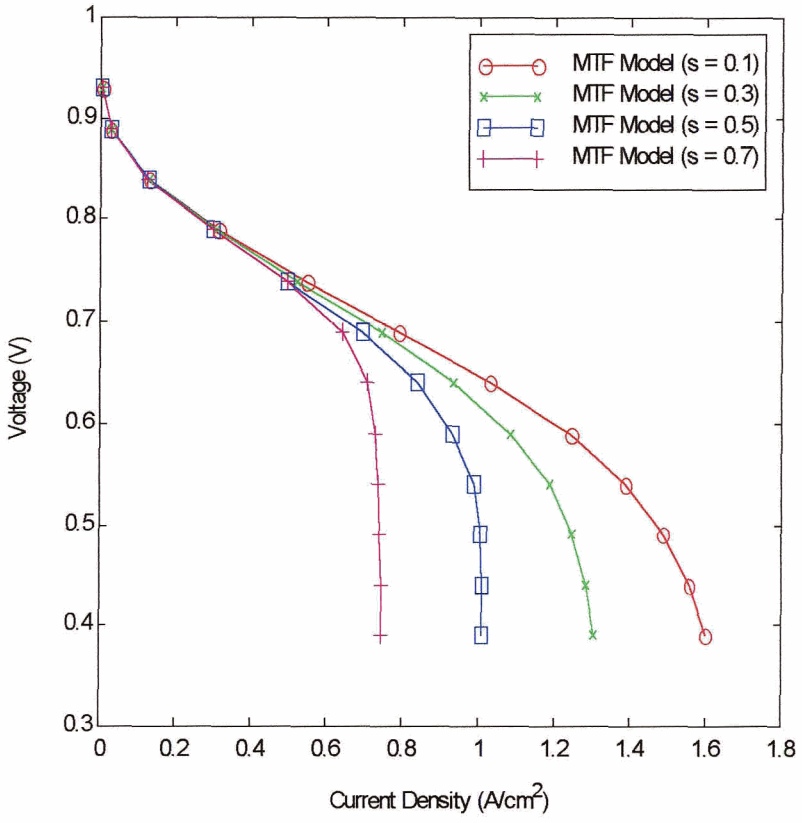

Figure 5.8 - Comparison of MTF model polarisation curves for "base case" operating conditions, and with variable volume-averaged (in the cathode gas diffusion and catalyst layers) liquid water saturation, s, at a voltage of 0.39 V of 0.1 (red), 0.3 (green), 0.5 (blue) and 0.7 (magenta).

As in Figure 5.7, the red curve in Figure 5.8 is the CFD simulation results from Figure 5.4 for the values $\varphi_{gdl} = 0.50$ and $\varphi_{cl} = 0.35$. As discussed in Chapter 4, the thickness l_w of the thin film of liquid water is proportional to the liquid water saturation, s. In general, it is found that volume-averaged (in the cathode gas diffusion and catalyst layers) liquid water saturation increases monotonically from zero at low current densities to a maximum at the highest current densities. However, even for a fully flooded catalyst layer at the highest current densities (i.e. $s = 1$) from Equations (4.11) and (4.12), the thickness of the thin film of liquid water is only 1.4 times the thickness of the thin film of polymer electrolyte. Thus since the diffusion coefficients of the dissolved reactants in liquid water are approximately one order of magnitude greater than the diffusion coefficients of the dissolved reactants in polymer electrolyte, as discussed in Chapter 4, the maximum transport limitations associated with the thin film of liquid water will be approximately 1/10 the transport limitations associated with the corresponding thin film of polymer electrolyte. The effect of the thin film of liquid water is therefore small compared to the effect of the thin film of polymer electrolyte.

Note that the results in Figure 5.7 already include the transport limitations associated with the thin film of liquid water. However, the presence of liquid water in the gas diffusion and catalyst layers also decreases the pore space available for the transport of gases as shown in Equation (3.56), where the effective diffusion coefficients in the gas phase approach zero as the liquid water saturation approaches one. For the CFD simulation results shown in Figure 5.7, the parameter values which affect liquid water saturation are not varied. Thus all the results are for volume-averaged (in the cathode gas diffusion and catalyst layers) liquid water saturations of 0.1 at a voltage of 0.39 V. In Figure 5.8, the diffusion coefficient associated with liquid water transport from Equation (3.82) is decreased in order to produce larger liquid water saturations by decreasing the total permeability of the media. Note, however, that the small effect varying the permeability has on the convection of gases in the porous media (as expressed through

Darcy's law) is neglected. Thus, for the other polarisation curves in Figure 5.8, the diffusion coefficient associated with liquid water transport is decreased such that volume-averaged (in the cathode gas diffusion and catalyst layers) liquid water saturation is increased to 0.3, 0.5 and 0.7 at a voltage of 0.39 V, while all other parameter values are kept the same.

As can be seen in Figure 5.8, increasing the liquid water saturation in the cathode, which also increases the thickness of the thin film of liquid water in the multiple thin-film model, has a substantial negative effect on PEM fuel cell performance. This is because of the increased transport limitations associated with the large decrease in the diffusion coefficients of the reactants in the gas phase. For liquid water saturations of approximately 0.7, the maximum current density is less than half that at saturations of 0.1 and as the saturation approaches one (i.e. the gas diffusion and catalyst layers are fully flooded) the CFD simulations predict that the maximum current density approaches zero. Thus the results in Figure 5.8 agree with those discussed in Chapter 2, where it is noted that flooding of the cathode has a severe negative effect on PEM fuel cell performance.

5.3.4 CFD Simulation Results for Model Variables

In general, the thesis model equations presented in Chapter 3 are solved in the CFD simulations for superficial velocity, $\vec{v}$, pressure, P, temperature, T, species mass fractions, y_i, solid phase electrical potential, ϕ_s, polymer-electrolyte phase electrical potential, ϕ_m, liquid water saturation, s, and polymer electrolyte water content, λ. All other variables are known functions of these variables. The MTF model for "base case" operating conditions and the values $\varphi_{gdl} = 0.50$ and $\varphi_{cl} = 0.35$ (herein referred to as the "base case" MTF model) - the polarisation curve for which is shown in Figure 5.4 - is used in this section to generate CFD simulation results for model variables. Results are presented for low, medium and high current densities at voltages of 0.84 V, 0.69 V and

0.39 V, respectively. The figures in this section are based on the geometry for the thesis model shown in Figure 5.1, which has been scaled by a factor of 1/7 in the z-direction. Although the model variables are solved throughout the entire computational domain as outlined in Chapter 3, they are only shown in the following figures for the components of the model volume where they have physical significance.

Figure 5.9 shows superficial velocity, $\vec{v}$, in the anode and cathode gas channels, gas diffusion layers and catalyst layers at a voltage of 0.84 V.

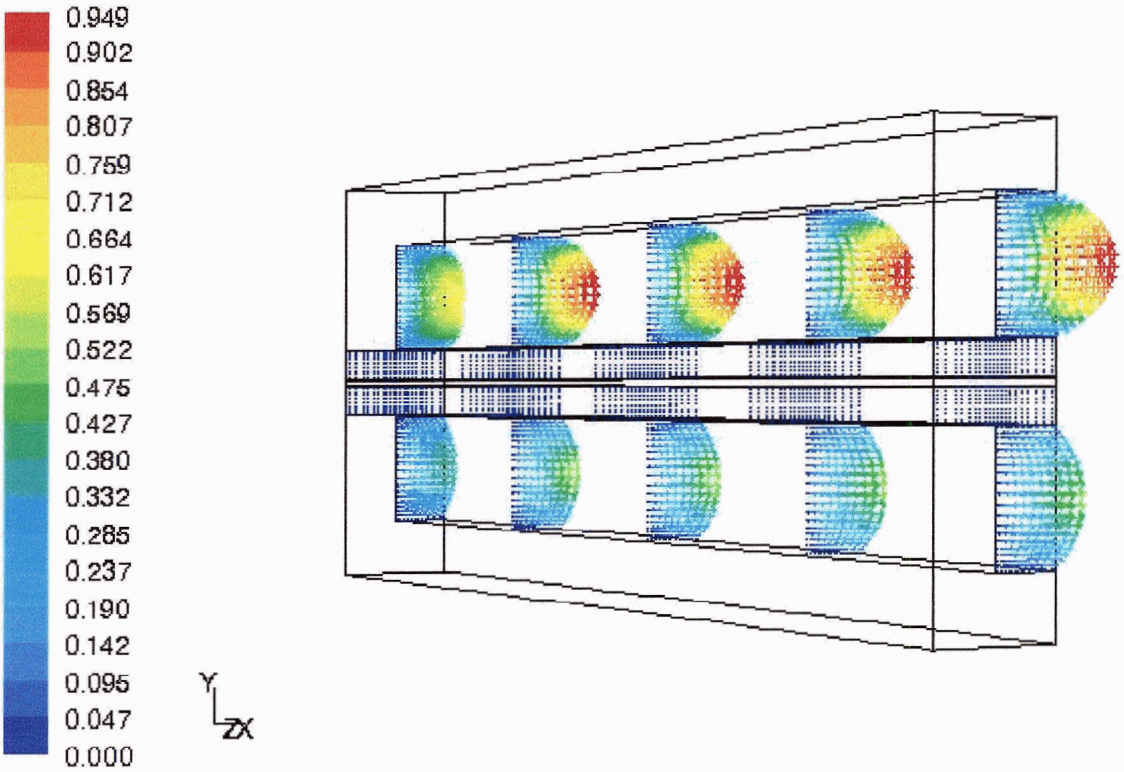

Figure 5.9 - Superficial velocity vectors (coloured by velocity magnitude) in units of m s^{-1} in the anode and cathode gas channels, gas diffusion layers and catalyst layers for the "base case" MTF model at a voltage of 0.84 V.

Note that Figure 5.9 is rotated to the right as compared to Figure 5.1 in order to enhance the presentation of the vectors. The superficial velocity in Figure 5.9 is that of gases, although in the thesis model the intrinsic velocity of liquid water is assumed to be equal to the superficial gas velocity in the gas channels. In the thesis model, the mean gas velocities are 0.252 m s^{-1} and 0.462 m s^{-1}, respectively, at the inlets of the anode and cathode gas channels. For square gas channels, the ratio of the mean velocity to the maximum velocity for fully developed flow is approximately 0.473 (Kakac et al., 1987) and therefore, in the thesis model, the maximum gas velocities are 0.533 m s^{-1} and 0.977 m s^{-1}. These values agree reasonably well with the maximum velocities shown in Figure 5.9 considering that there is a small penetration of the flow in the porous gas diffusion layers which will produce smaller maximum velocities.

The results at medium and high current densities are found to be identical to the results shown in Figure 5.9 at low current densities. This is expected since the velocity profiles are primarily determined by the mass flow rates set at the gas channel inlets, which do not vary with current density. Note that there is negligible gas velocity in the gas diffusion and catalyst layers since the normal component of the gas velocity is zero at the boundaries in the positive and negative x-directions and the gas velocity is zero at the boundaries in the positive and negative z-directions and at the membrane/catalyst layer boundaries. These boundary conditions, together with the resistance of the porous media, cause the velocity to rapidly decrease from its values in the gas channels towards zero values at the boundaries. Thus the results here show that, for the thesis model, the gas transport in the gas diffusion and catalyst layers is primarily by diffusion. Finally, as discussed in Chapter 3, the flow in the anode and cathode gas channels is fully developed after 0.8 % and 5.8 % of the gas channel length from the inlets, respectively, and this is seen in Figure 5.9 where the flow is fully developed almost immediately upon entering the gas channels.

Figure 5.10 shows pressure, P, in the anode and cathode gas channels, gas diffusion layers and catalyst layers at a voltage of 0.39 V.

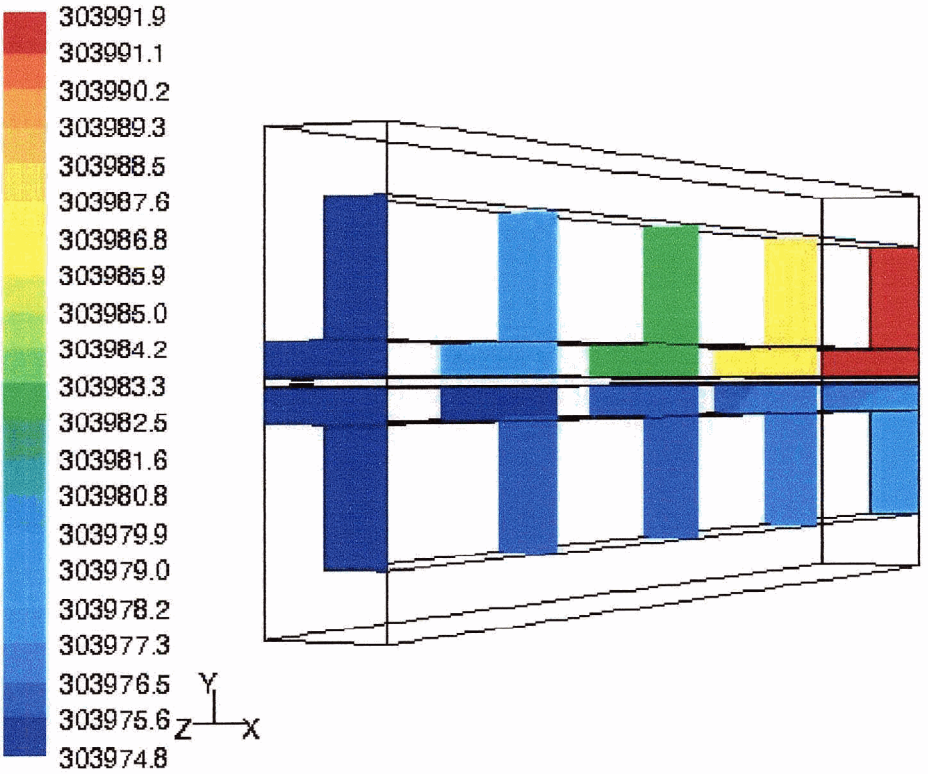

Figure 5.10 - Pressure contours in units of Pa in the anode and cathode gas channels, gas diffusion layers and catalyst layers for the "base case" MTF model at a voltage of 0.39 V.

The pressure in Figure 5.10 is that of gases, although in the gas diffusion and catalyst layers liquid water pressure is related to gas pressure through capillary pressure. The results at low and medium current densities are almost identical to the results shown in Figure 5.10 at high current densities. However, the pressure-drops in the z-direction towards the gas channel outlets, which are greater in the cathode than the anode due to higher velocities, are progressively larger at smaller current densities due to less consumption of reactants and therefore less decrease in velocity. Also, note that pressure-

drops in the x- and y-directions towards the catalyst layers located under the bipolar plates are less than those in the z-direction towards the gas channel outlets. In Figure 5.10, it can be seen that the pressures of gases leaving the anode and cathode gas channels are set to 3 atm (303,975 Pa). Also, although the thesis model is not isobaric, an approximate operating pressure of 303,975 Pa is maintained throughout the PEM fuel cell since the results in Figure 5.10 show that pressure variations around the operating pressure are negligible. These results justify the assumption made previously in the thesis that gas pressure gradients in PEM fuel cells are relatively small and can be neglected.

Figure 5.11 shows temperature, T, in the entire fuel cell at a voltage of 0.39 V.

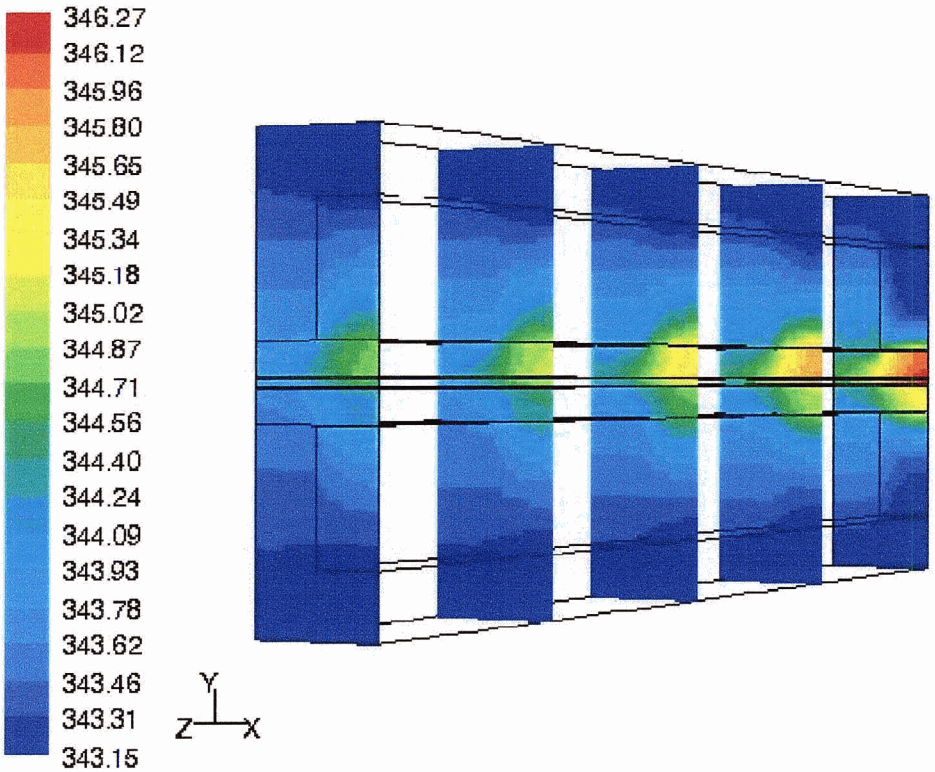

Figure 5.11 - Temperature contours in units of K in the entire fuel cell for the "base case" MTF model at a voltage of 0.39 V.

Note that in the thesis model it is assumed that local thermal equilibrium applies, such that gas, liquid water and solid temperatures are equal at every point in the fuel cell and can be replaced by a single temperature. As discussed in Chapter 3, although the thesis model is not isothermal, an approximate operating temperature of 70 °C (343.15 K) is maintained by setting the temperatures of gases entering the gas channels and at the external boundaries in the positive and negative y-directions to 343.15 K, as can be seen in Figure 5.11. Also, the effects of the boundary conditions of no conductive heat fluxes (i.e. zero gradients of temperature) in the positive and negative x- and z-directions (except for the gas channel inlets and outlets) can be seen in Figure 5.11, where the contours of temperature are perpendicular to these boundaries. The maximum temperature of 346.27 K in Figure 5.11 represents a 0.9 % variation from the operating temperature at high current densities. Results at low and medium current densities show that this maximum temperature variation decreases as the current density decreases. These results justify the assumption used throughout the thesis that temperature gradients in PEM fuel cells are relatively small.

From Figure 5.11, it is observed that the heat generated due to reactions in the PEM fuel cell is concentrated in the catalyst layers under the gas channel inlets - where most of the reactions are occurring at high current densities, as outlined subsequently in Chapter 6. Also more heat is generated by the reactions in the cathode than in the anode. This is expected since, in the thesis model, it is assumed that the reversible heat production for the overall Reaction (1.3) is produced entirely in the cathode catalyst layer. Also, less irreversible heat is generated by the anode catalyst layer reactions because of the smaller overpotential. As can be seen in Figure 5.11, heat released by the cathode reactions is flowing out the bipolar plates in the positive and negative y-directions and also out the gas channel inlets. The results at low and medium current densities besides having smaller temperature variations also vary due to the location where reactions are occurring in the catalyst layers. Reaction distributions in the catalyst layers are shown in Chapter 6.

In general, although the thesis model equations presented in Chapter 3 are solved in the CFD simulations for species mass fractions, y_i, using the ideal gas law, species concentrations, c_i, and mole fractions, x_i, are known functions of species mass fractions, y_i, (and pressure, P, and temperature, T). The Butler-Volmer equation for the reaction rates depends on the concentration of hydrogen, c_{H_2}, in the anode catalyst layer (Equation (3.59)) and the concentration of oxygen, c_{O_2}, in the cathode catalyst layer (Equation (3.60)). Thus the concentrations of hydrogen and oxygen are presented in the following figures.

Also, in polymer electrolyte, effective conductivity (Equation (3.71)) and superficial mass flux of liquid water (as given by electro-osmotic drag and Fick's first law for self-diffusion) depend on the water content (Equations (3.74) and (3.76)). In the thesis model, polymer electrolyte water content, λ, in the catalyst layers and at the membrane/catalyst layer boundaries is a known function of water vapour mole fraction, x_{H_2O}, (and pressure, P, temperature, T, and liquid water saturation, s) in the adjacent pores using Equations (3.34), (3.35), (3.79) and (3.80). Thus the water vapour mole fraction is presented in the following figures.

Figure 5.12 shows hydrogen concentration, c_{H_2}, in the anode gas channel, gas diffusion layer and catalyst layer at a voltage of 0.69 V. The results at low and high current densities are almost identical, with similar profiles, to the results shown in Figure 5.12 at medium current densities.

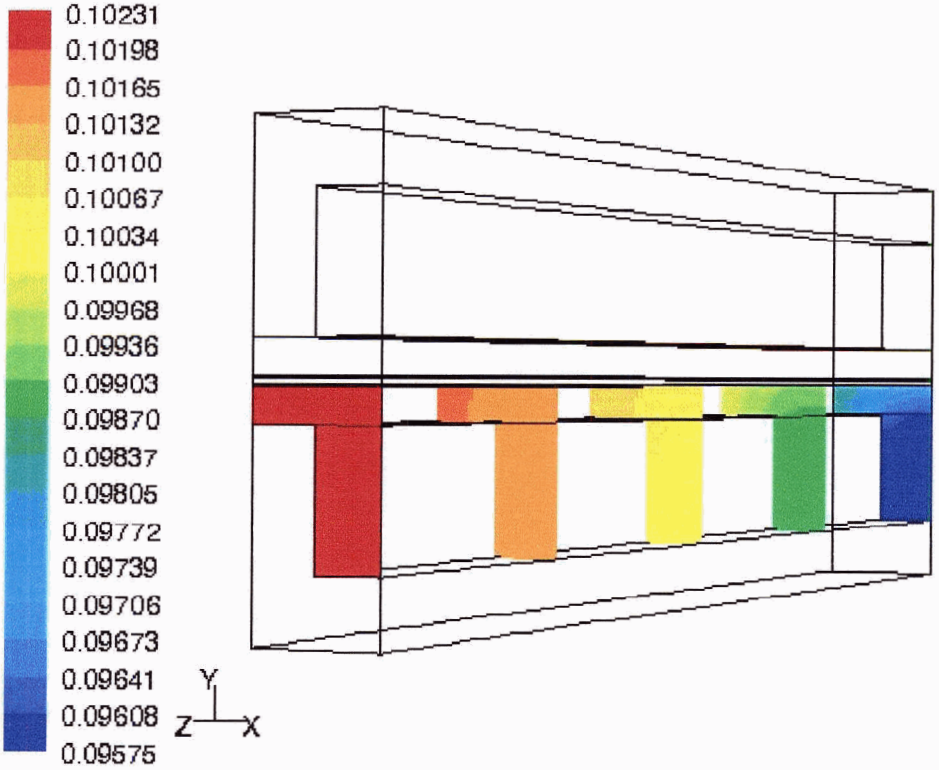

Figure 5.12 - Hydrogen concentration contours in units of kmol m^{-3} in the anode gas channel, gas diffusion layer and catalyst layer for the "base case" MTF model at a voltage of 0.69 V.

Using the ideal gas law, the mole fraction of x_{H_2} = 0.898 set at the anode gas channel inlet (Equation (3.35)) corresponds to a concentration of c_{H_2} = 0.0957 kmol m^{-3} at the operating temperature of 70 °C (343.15 K) and pressure of 3 atm (303,975 Pa) in agreement with the results shown in Figure 5.12. This concentration is the minimum concentration as shown in Figure 5.12 and is also found to be the minimum concentration at low and high current densities. However, the maximum concentration is found to be 0.0979 kmol m^{-3} at a voltage of 0.84 and 0.10517 kmol m^{-3} at a voltage of 0.39 V, and therefore increases with current density, although the range is only 7.2 %. These results are expected since the PEM fuel cell is essentially isobaric and isothermal as discussed for

the results in Figures 5.10 and 5.11, yielding a constant overall concentration using the ideal gas law. As shown subsequently for the results in Figure 5.14, the water vapour mole fraction in the anode decreases towards the gas channel outlet and the catalyst layers under the bipolar plate because electro-osmotic drag transports water from the anode to the cathode, causing a corresponding increase in hydrogen mole fraction. However, from Equation (3.35) the water vapour mole fraction is relatively small and therefore as it decreases, it causes only small increases in hydrogen mole fraction, and also because of the constant overall concentration, small increases in hydrogen concentration. Finally, electro-osmotic drag increases with current density, causing larger decreases in water vapour mole fraction and corresponding increases in hydrogen concentration.

Figure 5.13 shows oxygen concentration, c_{O_2}, in the cathode gas channel, gas diffusion layer and catalyst layer at voltages of 0.84 V and 0.39 V.

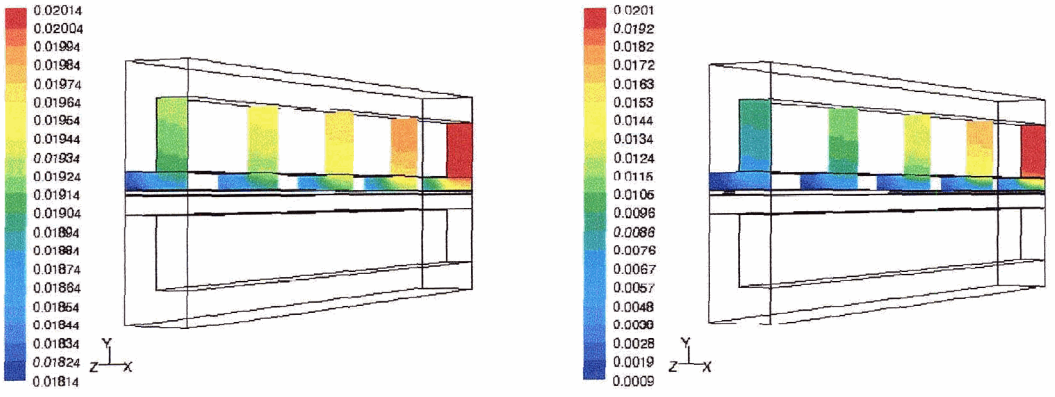

Figure 5.13 - Oxygen concentration contours in units of kmol m^{-3} in the cathode gas channel, gas diffusion layer and catalyst layer for the "base case" MTF model at voltages of 0.84 V (left) and 0.39 V (right).

Using the ideal gas law, the mole fraction of x_{O_2} = 0.189 set at the cathode gas channel inlet (Equation (3.36)) corresponds to a concentration of c_{O_2} = 0.0201 kmol m^{-3} at the operating temperature of 70 °C (343.15 K) and pressure of 3 atm (303,975 Pa) in agreement with the results shown in Figure 5.13. This concentration is the maximum concentration as shown in Figure 5.13 at low and high current densities and is also found to be the maximum concentration at medium current densities. However, according to the results in Figure 5.13, the minimum concentration is 0.0181 kmol m^{-3} at a voltage of 0.84 and 0.0009 kmol m^{-3} at a voltage of 0.39 V, and therefore decreases substantially with current density. Thus the results show the expected decrease in oxygen concentration associated with the transport resistances of nitrogen and liquid water, which increase as the current density is increased, causing large concentration overpotentials at high current densities. Also, note that the concentration is lower under the bipolar plate and towards the outlet (i.e. further away from the gas channel inlets) because of the longer diffusion length scales.

Figure 5.14 shows water vapour mole fraction, x_{H_2O}, in the anode gas channel, gas diffusion layer and catalyst layer at voltages of 0.84 V and 0.69 V.

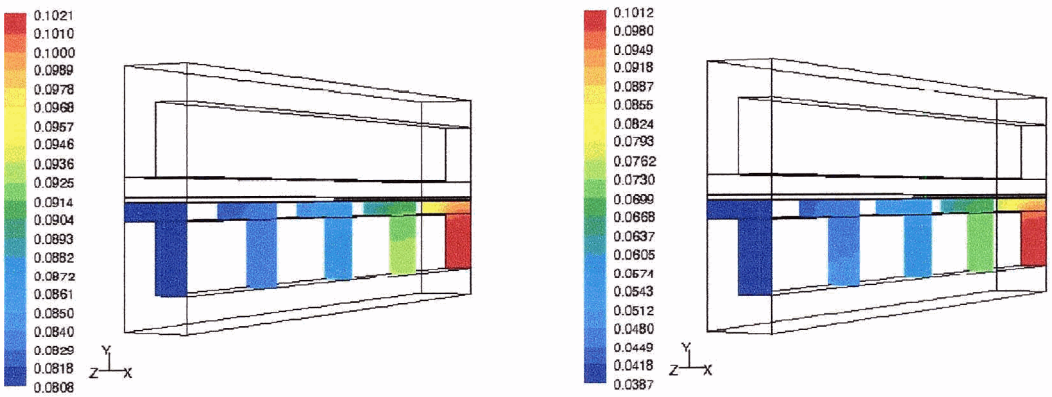

Figure 5.14 - Water vapour mole fraction contours in the anode gas channel, gas diffusion layer and catalyst layer for the "base case" MTF model at voltages of 0.84 V (left) and 0.69 V (right).

The mole fraction of x_{H_2O} = 0.102 set at the anode gas channel inlet (Equation (3.35)) is in agreement with the results shown in Figure 5.14. This mole fraction is the maximum mole fraction in the anode at low and medium current densities and is also found to be the maximum mole fraction at high current densities. As shown in Figure 5.14 at medium current densities, the minimum water vapour mole fraction (i.e. 0.0387) is lower than at low current densities (i.e. 0.0808) and, at high current densities, the minimum value is found to be even lower (i.e. 0.0119). Thus the water vapour mole fraction decreases with increasing current density, as expected, since electro-osmotic drag increases with current density (Equation (3.74)). Also, as discussed previously, the water vapour mole in the anode decreases along the gas channel and towards the gas diffusion and catalyst layers because electro-osmotic drag transports water through the membrane from the anode to the cathode.

In the cathode, the mole fraction of x_{H_2O} = 0.102 set at the gas channel inlet (Equation (3.36)) is found to be in agreement with the results shown in Figure 5.14. However, in this case, this mole fraction is found to be the minimum mole fraction at all current densities. The maximum value increases with current density, although it is limited by the formation of liquid water (Equation (3.50)) to its fully saturated value of x_{H_2O} = 0.102 at the operating temperature and x_{H_2O} = 0.117 at the maximum temperature of 346.27 K from Figure 5.11 at high current densities (Equations (3.34) and 3.36)). In the cathode at low to high current densities maximum values for the water vapour mole fraction of 0.10739 to 0.1294 are found, which deviate approximately 5 % to 10 % from the physically correct fully saturated values. Considering that the mole fraction of water vapour is relatively small in the cathode (i.e. x_{H_2O} = 0.102 from Equation (3.36)) this excess water vapour mole fraction in the CFD simulations (found where the reactions are occurring in the cathode catalyst layer) is only on the order of a maximum of 1 % and therefore has a negligible effect on the overall results.

Figure 5.15 shows solid phase electrical potential, ϕ_s, in the anode and cathode bipolar plates, gas diffusion layers and catalyst layers at a voltage of 0.39 V.

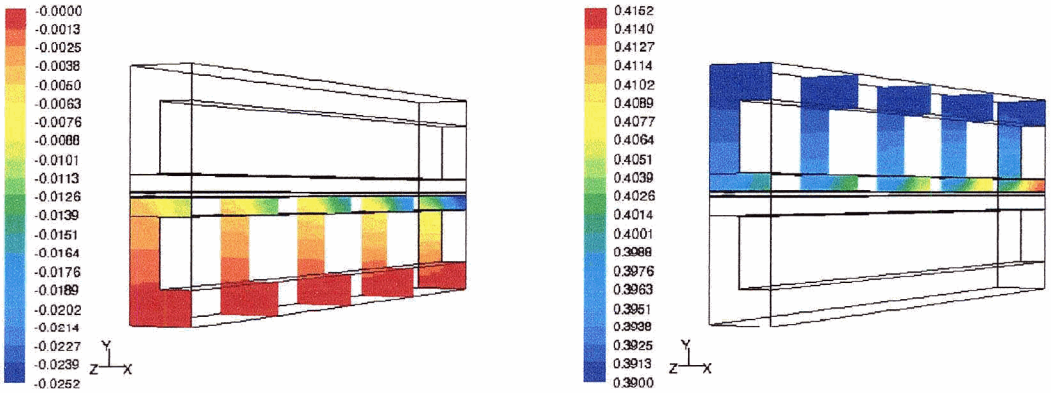

Figure 5.15 - Solid phase electrical potential contours in units of V in the bipolar plates, gas diffusion layers and catalyst layers of the anode (left) and cathode (right) for the "base case" MTF model at a voltage of 0.39 V.

The solid phase electrical potential of ϕ_s = 0 V and ϕ_s = 0.39 V set at the anode and cathode bipolar plate boundaries in the negative and positive y-directions, respectively, are in agreement with the results shown in Figure 5.15 at high current densities. Values of ϕ_s = 0 V and ϕ_s = 0.84 V, and ϕ_s = 0 V and ϕ_s = 0.69 V set at low and medium current densities, respectively, are also found to be in agreement with CFD simulation results. The effects of the boundary conditions of zero normal current density at the symmetry boundaries and gas channel walls in the positive and negative x-directions and external walls in the positive and negative z-directions can be seen in Figure 5.15, where the contours of electrical potential are perpendicular to these boundaries.

As shown in Figure 5.15, anode and cathode electrical potentials have identical maximum absolute potential differences of 0.0252 V at high current densities; maximum absolute potential differences of 0.00119 V and 0.00893 V (identical in the anode and cathode) are also found at low and medium current densities, respectively. Therefore the maximum absolute potential differences increase as the current density is increased, as expected from Equation (3.1). Also, using Equation (3.1), the flow of electrons (which is in the opposite direction to the current density of electrons) is in the direction of increasing potential. This is in agreement with the results shown in Figure 5.15 (and also found at low and medium current densities), where the potential is decreasing (increasing) from the bipolar plates to the catalyst layers under the gas channels in the anode (cathode) since electrons are flowing out of the anode catalyst layer and into the cathode catalyst layer through the bipolar plates.

Note that at a given current density, maximum absolute potential differences are expected to be identical in the anode and cathode since they have the same bipolar plates, gas diffusion layers and catalyst layers (i.e. solid phase electrical conductivities), and the overall current in the anode must equal that in the cathode due to electroneutrality. Finally, in Figure 5.15, the maximum absolute potential difference occurs in the catalyst layers under the inlets of the gas channels where most of the reactions are occurring at high current densities, as outlined subsequently in Chapter 6.

Figure 5.16 shows superficial current density of electrons, $\vec{i}_s$, in the anode and cathode bipolar plates, gas diffusion layers and catalyst layers at a voltage of 0.84 V.

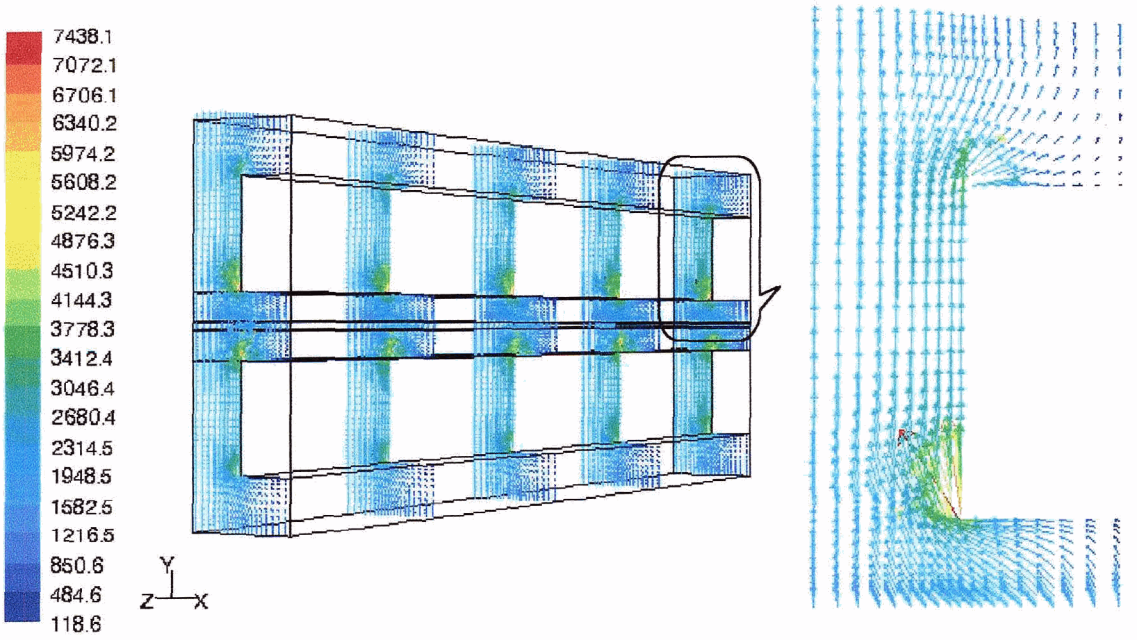

Figure 5.16 - Superficial current density of electron vectors (coloured by current density magnitude) in units of A m^{-2} in the anode and cathode bipolar plates, gas diffusion layers and catalyst layers for the "base case" MTF model at a voltage of 0.84 V.

The current density in Figure 5.16, although at a voltage of 0.84 V, corresponds qualitatively to the anode and cathode electrical potentials shown in Figure 5.15 at a voltage of 0.39 V. The balloon in Figure 5.16 is an enlargement of the cathode bipolar plate, gas diffusion layer and catalyst layer adjacent to the inlet of the gas channel. This enlargement reveals details of the vectors.

As discussed for the results shown in Figure 5.15, in the cathode, the flow of electrons (which is in the opposite direction to the current density of electrons shown in Figure 5.16) is from the bipolar plate to the catalyst layer. In general, the overall resistance in the bipolar plates, gas diffusion layers and catalyst layers is proportional to the conduction path length and inversely proportional to the conduction area associated with the flow of

electrons. Thus, in order to reduce the overall resistance, electrons tend to flow along the shortest path length while still flowing through the largest area available. Therefore electrons do not flow evenly into the cathode bipolar plate in Figure 5.16, but preferentially flow into the region that is not above the gas channel - since the conduction path length of this region is less than that of the region above the gas channel. In contrast, electrons still flow into the region of the bipolar plates above the gas channel in order to maximise the conduction area. These electrons must flow around the corner of the gas channel, resulting in current density flares at the corner as shown in Figure 5.16, where the current density and the associated ohmic heating reach a maximum. Similar flares occur at the corner of the gas channel adjacent to the gas diffusion layer, since the electrons spread out in the gas diffusion layer in order to maximise the conduction area. Finally the flow of electrons into the catalyst layer is determined by where the reactions are occurring and, as indicated in a comparison of the results in Figure 5.16 versus those in Figure 5.11, the reactions are more uniform at low current densities than at high current densities.

Also, in Figure 5.11, the ohmic heating associated with the flares is not noticeable since reaction heating and the ohmic heating associated with the current density of protons in polymer electrolyte dominate in a PEM fuel cell. CFD simulation results also show that the z-component of current density at a voltage of 0.84 V has a maximum magnitude of 5.47 A m^{-2} which is only approximately 5 % of the minimum current density magnitude of 118.6 A m^{-2} from Figure 5.16. This, together with other CFD simulation results at medium and high current densities, indicate that the z-component of current density is relatively small. Thus the current density vectors shown in Figure 5.16 are essentially two-dimensional.

Figure 5.17 shows polymer-electrolyte phase electrical potential, ϕ_m, in the membrane and anode and cathode catalyst layers at voltages of 0.84 V and 0.39 V.

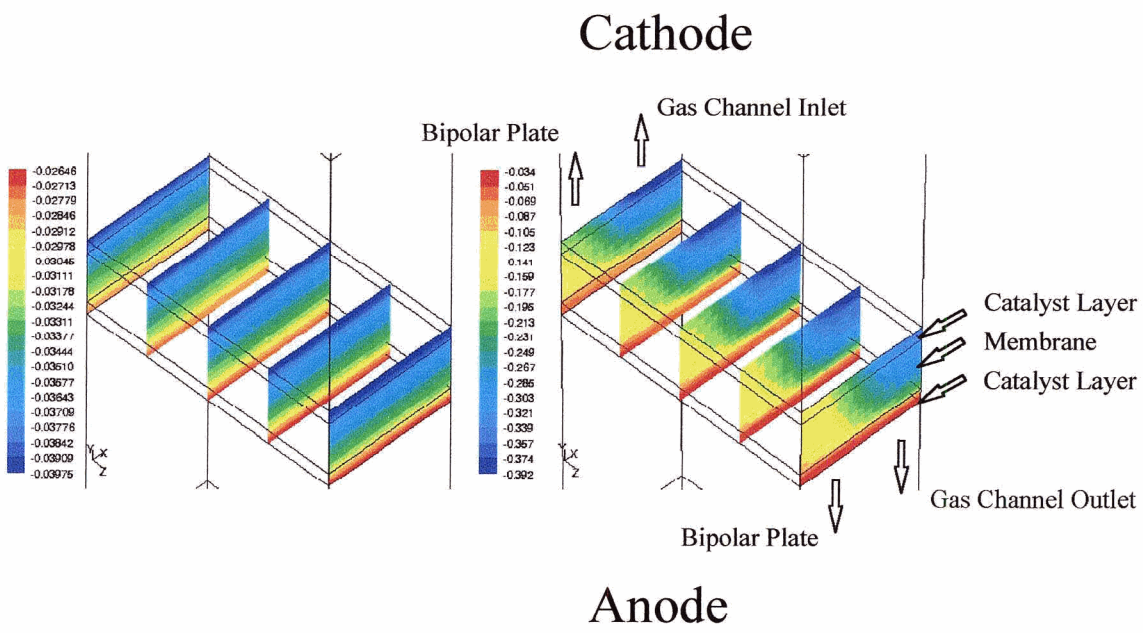

Figure 5.17 - Polymer-electrolyte phase electrical potential contours in units of V in the membrane and anode and cathode catalyst layers for the "base case" MTF model at voltages of 0.84 V (left) and 0.39 V (right).

Figure 5.17 has not only been scaled by a factor of 1/7 in the z-direction in order to enhance the presentation of the geometry for the thesis model, but it has also been scaled by a factor of 5 in the x-direction and a factor of 40 in the y-direction to reveal detailed results in the catalyst layers and membrane. Note that Figure 5.17 is also rotated to the right as compared to Figure 5.1. The effects of the boundary conditions of zero normal proton current density at the symmetry boundaries in the positive and negative x-directions and external walls in the positive and negative z-directions can be seen in Figure 5.17, where the contours of electrical potential are perpendicular to these boundaries.

As shown in Figure 5.17, the maximum absolute potential difference is 0.0133 V and 0.3580 V at low and high current densities, respectively. The maximum absolute potential

difference is also found to be 0.1106 V at medium current densities. Therefore the maximum absolute potential difference increases as the current density is increased, as expected from Equation (3.69). Also, using Equation (3.69), the flow of protons (which is in the same direction as the current density) is in the direction of decreasing potential. This is in agreement with the results shown in Figure 5.17 (and also found at medium current densities), where the potential is decreasing from the anode to the cathode catalyst layer since protons are flowing out of the anode catalyst layer, through the membrane, and into the cathode catalyst layer.

Figure 5.18 shows liquid water saturation, s, in the anode and cathode gas channels, gas diffusion layers and catalyst layers at a voltage of 0.39 V.

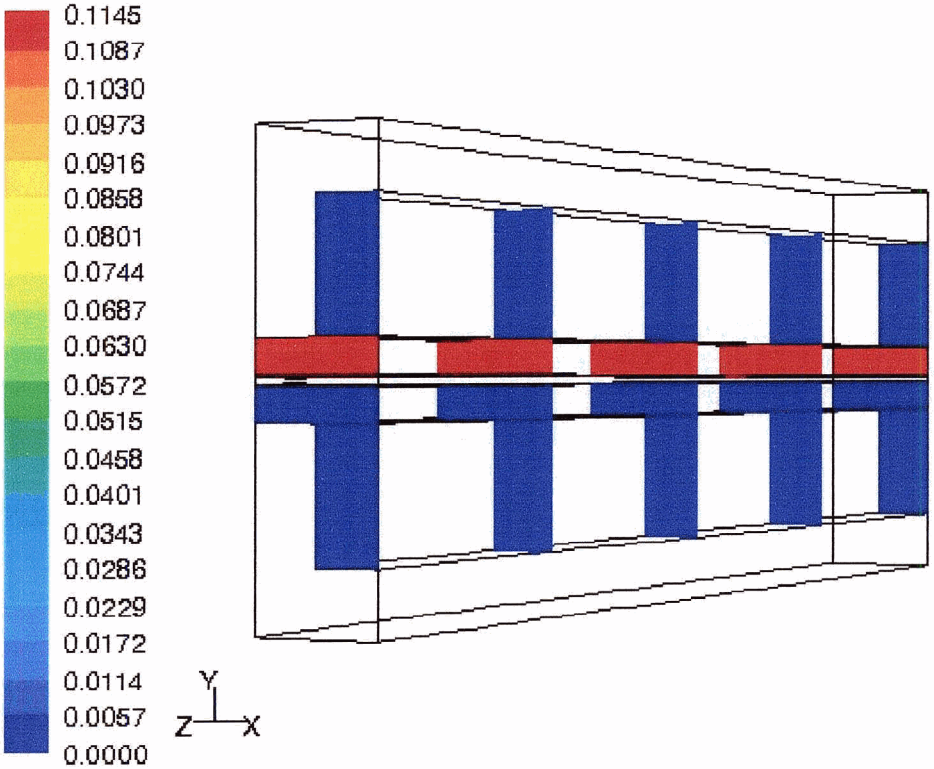

Figure 5.18 - Liquid water saturation contours in anode and cathode gas channels, gas diffusion layers and catalyst layers for the "base case" MTF model at a voltage of 0.39 V.

As shown in Figure 5.18, volume-averaged saturation in the cathode gas diffusion and catalyst layers is approximately 0.1 at high current densities. Values of 0.04 and 0.08 are also found at low and medium current densities, respectively. Note that the saturation profile in the cathode gas diffusion and catalyst layers as shown in Figure 5.18 is essentially flat; similar profiles are also found at low and medium current densities. This is because the capillary pressure driving force for liquid water transport (Equations (3.48) and (3.49)) is found to be relatively large, such that only small gradients in saturation are necessary to transport liquid water through the gas diffusion and catalyst layers after it has condensed. Also, as shown in Figure 5.18, there is only a small amount of liquid water in the cathode gas channel adjacent to the gas diffusion layer. Thus the assumed transport of liquid water in the gas channels (i.e. as a fine mist with the same velocity as the gases) is found to easily allow for liquid water to be transported in the cathode through the gas channel from the gas diffusion layer to the gas channel outlet. Finally, as shown in Figure 5.18, there is no liquid water in the anode. This is because the water vapour mole fraction is below the fully saturated value at low and medium current densities, as shown in Figure 5.14, and this is also found to be the case at high current densities.

Figure 5.19 shows polymer electrolyte water content, λ, in the membrane and anode and cathode catalyst layers at a voltage of 0.39 V. Similar to Figure 5.17, Figure 5.19 has been scaled by a factor of 5 in the x-direction, and factors of 40 and 1/7 in the y- and z-directions, respectively. Using Equations (3.79) and (3.80) for a fully saturated cathode catalyst layer (as shown to be the case at all current densities from CFD simulation results), and a volume-averaged liquid water saturation in the cathode catalyst layer of approximately 0.04 at low current densities, yields a water content of 14.1 in agreement with the maximum value shown in Figure 5.19. From Equations (3.79) and (3.80), water content only varies from 14.0 to 16.8 over the entire range of liquid water saturation, and therefore CFD simulation results show that water content in the cathode catalyst layer is essentially constant at all current densities, since liquid water saturation remains relatively

small. However, water content has a minimum of 6.93, as shown in Figure 5.19; minimum values of 3.01 and 1.57 are also found at medium and high current densities, respectively. These minimum values are all found in the anode catalyst layers, where the low water vapour mole fraction (as indicated in Figure 5.14) and zero liquid water saturation (as indicated in Figure 5.18) yield low water content.

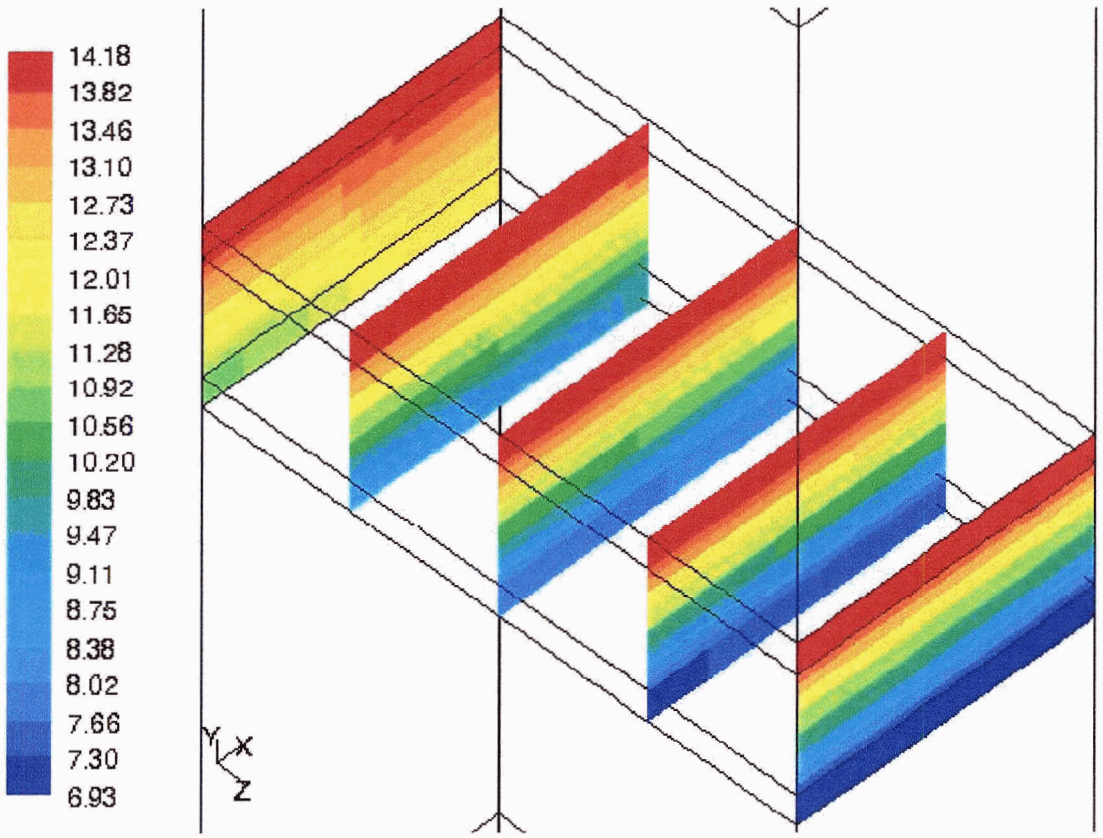

Figure 5.19 - Polymer electrolyte water content contours in the membrane and anode and cathode catalyst layers for the "base case" MTF model at a voltage of 0.84 V.

As shown in Figure 5.19, the water content decreases from the fully saturated maximum value in the cathode catalyst layer through the membrane towards the minimum value in

the anode catalyst layer near the gas channel outlet. Similar profiles are found at all current densities since they are determined by the water vapour mole fraction distribution in the anode catalyst layer, as shown in Figure 5.14, which is found to be similar at all current densities.

In summary, in this section the "base case" MTF model is used to generate CFD simulation results for model variables. These results confirm the capability of the CFD simulations in predicting accurate detailed results associated with the MTF model. The accuracy of the MTF model CFD simulations in predicting experimental results in the form of polarisation curves has already been confirmed in Section 5.3.1. In the next section in Chapter 6, "base case" MTF model simulation results for variables that are known functions of the model variables are presented in order to show reaction distributions in the catalyst layers.

Chapter 6

Effects of Non-Uniform Catalyst Loading

Improving the performance of PEM fuel cells depends on the optimisation of catalyst layer composition and structure for large reaction surfaces. This optimisation requires a detailed modelling of the reactions in catalyst layers in order to find ways to increase the effectiveness of catalyst layers for a given precious metal loading. From previous modelling studies, it is well known that the distribution of electrochemical reactions in catalyst layers is highly dependent on the complex interaction of activation and ohmic effects as well as contributions from transport limitations and variations in local and overall current densities. In this chapter, available data on catalyst layer composition and structure are used in CFD simulations to predict reaction rate distributions. Based on these results, variations in local catalyst loading are implemented in CFD simulations for the same overall catalyst loading in an attempt to improve PEM fuel cell performance.

6.1 Reaction Distributions for "Base Case" MTF Model

In this section, results are presented for the distribution of reaction rates in the anode and cathode catalyst layers. Since reaction rates depend on model variables, a brief review

of findings from Chapter 5 follows. The reaction rate, as given by the Butler-Volmer equation, can be expressed in terms of production or consumption of current of electrons per unit volume, S_s, which is positive for production. The absolute value of production or consumption of current of electrons per unit volume, $|S_s|$, is herein referred to as transfer current. Using Equations (3.59) and (3.60), respectively, transfer current is a known function in the anode catalyst layer of hydrogen concentration, c_{H_2}, and overpotential, η_a, and in the cathode catalyst layer of oxygen concentration, c_{O_2}, and overpotential, η_c. Note that transfer current is the negative of the variable S_s in the anode catalyst layer (i.e. electrons are produced and current of electrons is consumed) and the positive of the variable S_s in the cathode catalyst layer (i.e. electrons are consumed and current of electrons is produced). Also, note that anode and cathode transfer current volume integrals are equal due to conservation of charge.

MTF model CFD simulation results for hydrogen concentration are shown in Figure 5.12 in the anode gas channel, gas diffusion layer and catalyst layer at medium current densities. The hydrogen concentration set at the anode gas channel inlet, which does not vary with current density, is shown in Figure 5.12 to be the minimum concentration and is also found to be the minimum concentration at low and high current densities. The variation in hydrogen concentration throughout the entire anode is found to increase with current density, but even at high current densities it is only found to be 9.4 %. Thus the hydrogen concentration is essentially uniform throughout the anode catalyst layer and also has the same approximate value at all current densities. Therefore the distribution of transfer current in the anode catalyst layer is determined by the distribution of overpotential.

MTF model CFD simulation results for oxygen concentration are shown in Figure 5.13 in the cathode gas channel, gas diffusion layer and catalyst layer at low and high current densities. The oxygen concentration set at the cathode gas channel inlet, which does not vary with current density, is shown in Figure 5.13 to be the maximum concentration and is

also found to be the maximum concentration at medium current densities. However, according to the results in Figure 5.13, the minimum concentration decreases substantially with current density. Thus the results show the expected decrease in oxygen concentration associated with the transport resistances of nitrogen and liquid water, which increase as the current density is increased, causing the concentration to be lower under the bipolar plate and towards the outlet (i.e. further away from the gas channel inlet) because of the longer diffusion length scales. Therefore the distribution of transfer current in the cathode catalyst layer is determined by the distribution of both overpotential and oxygen concentration. Note that both oxygen and hydrogen concentrations are bulk gas concentrations and therefore do not include the effects of transport limitations associated with the thin films of liquid water and polymer electrolyte in the multiple thin-film agglomerate model.

The overpotentials driving the reactions in the anode and cathode catalyst layers are known functions of solid and polymer-electrolyte phase electrical potentials (i.e. $\eta_a = \phi_s - \phi_m$ and $\eta_c = \phi_s - \phi_m - V_{oc}$, respectively). In the thesis model, it is assumed that the open-circuit potential, V_{oc}, is equal to 1.12 V. Figure 5.15 shows solid phase electrical potential in the anode and cathode bipolar plates, gas diffusion layers and catalyst layers at high current densities. Figure 5.17 shows polymer-electrolyte phase electrical potential in the membrane and anode and cathode catalyst layers at low and high current densities. The results shown in these figures, together with results generated using the "base case" MTF model at other current densities, yield anode and cathode overpotentials. Note that in the catalyst layers in the thesis model, effective solid phase conductivity (i.e. $\sigma_s^{eff} = 1.8 \times 10^3$ S m^{-1}) is approximately three orders of magnitude greater than the maximum effective polymer-electrolyte phase conductivity at the PEM fuel cell operating temperature as given by Equation (3.71) (i.e. $\sigma_m^{eff} = 3.4$ S m^{-1}). Thus, for similar current densities of electrons and protons, the solid phase potential differences are negligible compared with those in the polymer-electrolyte phase and the solid phase electrical potentials in the catalyst layers are essentially uniform. Therefore overpotential distributions in the catalyst

layers are determined entirely by the distribution of the polymer-electrolyte phase electrical potential.

Finally, results for overpotentials and hydrogen and oxygen concentrations yield anode and cathode transfer currents. The results for overpotentials and transfer currents are presented in this section at voltages of 0.84 V, 0.69 V and 0.39 V, which correspond to low, medium and high current densities, respectively. Using Equations (3.59) and (3.60), in order for electrons to be produced in the anode and consumed in the cathode, overpotential is positive in the anode and negative in the cathode. Therefore transfer current increases as overpotential increases (i.e. becomes more positive) in the anode and decreases (i.e. becomes more negative) in the cathode. Similar to Figure 5.17, the figures in this section have been scaled by factors of 5 and 1/7 in the x- and z-directions, respectively, but by a factor of 120 in the y-direction.

Figure 6.1 shows overpotential in the anode, η_a, and cathode, η_c, catalyst layers at a voltage of 0.84 V.

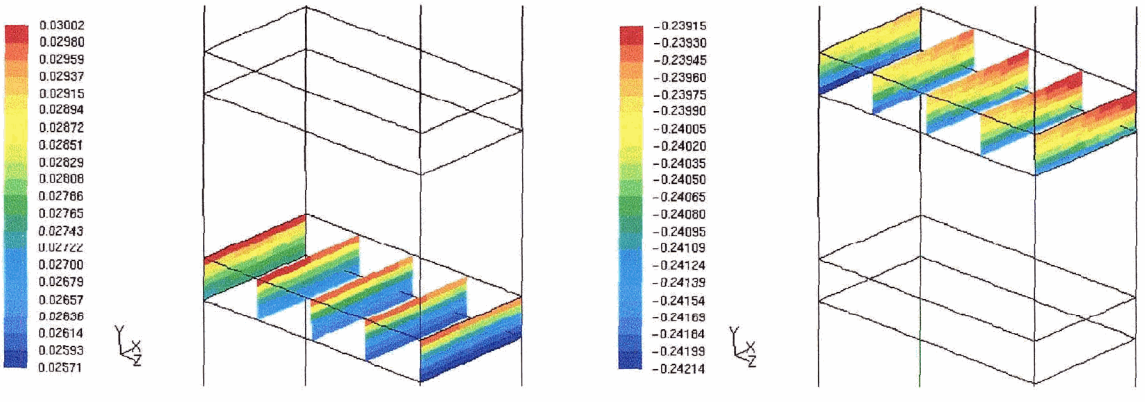

Figure 6.1 - Overpotential contours in units of V in the anode (left) and cathode (right) catalyst layers for the "base case" MTF model at a voltage of 0.84 V.

As shown in Figure 6.1, absolute values of overpotential are approximately an order of magnitude larger in the cathode than in the anode. This is predicted using Equations (3.59) and (3.60) for similar anode and cathode transfer currents (required by conservation of charge) since the ratio of the value $\xi i_{0,a}^{ref}\left(c_{H_2}^{ref}\right)^{-b_{H_2}}$ divided by $\xi i_{0,c}^{ref}\left(c_{O_2}^{ref}\right)^{-b_{O_2}}$ is maintained at 10^5 in the thesis model. As shown in Figure 6.1, the variation in overpotential is 15.5 % in the anode and only 1.2 % in the cathode. Note that overpotential variations in the catalyst layers are determined entirely by electrical potential differences in the polymer-electrolyte phase and that potential differences are larger in the anode than cathode due to lower water content (Figure 5.19) and therefore lower electrical conductivity in the polymer-electrolyte phase.

As stated previously, overpotential distributions in the catalyst layers are determined entirely by the distribution of the polymer-electrolyte phase electrical potential. According to the results shown in Figure 5.17 at low current densities, polymer-electrolyte phase electrical potential in the anode and cathode catalyst layers is approximately uniform in the x-direction under the bipolar plates and gas channels. Electrical potential in the catalyst layers decreases in the y-direction towards the membrane in the anode and towards the gas diffusion layer in the cathode. Finally, electrical potential in the catalyst layers increases (anode) and decreases (cathode) in the z-direction towards the gas channel outlets. Similar overpotential distributions are observed in Figure 6.1 except that overpotential is proportional to the negative of polymer-electrolyte phase electrical potential and therefore the overpotential distributions are the negative of the electrical potential distributions. Thus, in agreement with the results shown in Figure 5.17 at low current densities for the electrical potential distributions, overpotentials in the anode and cathode are approximately uniform in the x-direction under the bipolar plates and gas channels. Overpotential also increases in the y-direction towards the membrane in the anode and towards the gas diffusion layer in the cathode, and decreases (anode) and increases (cathode) in the z-direction towards the gas channel outlets.

Figure 6.2 shows overpotential in the anode, η_a, and cathode, η_c, catalyst layers at a voltage of 0.39 V.

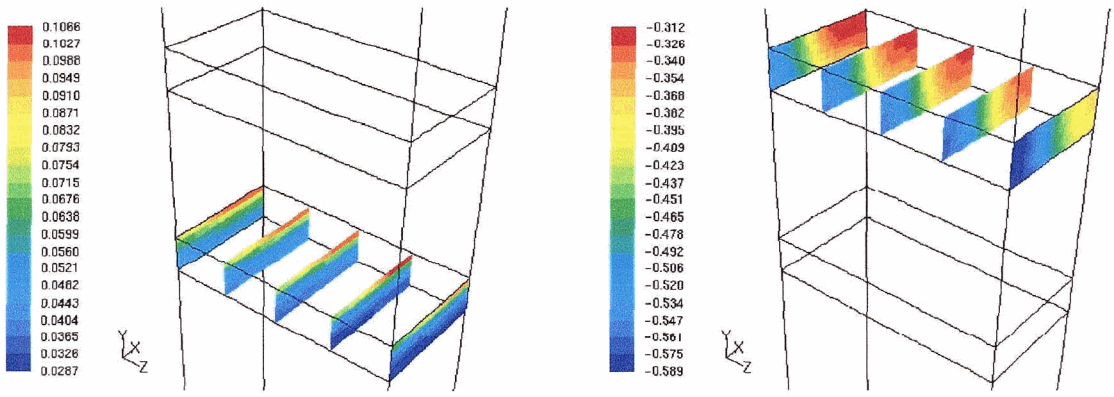

Figure 6.2 - Overpotential contours in units of V in the anode (left) and cathode (right) catalyst layers for the "base case" MTF model at a voltage of 0.39 V.

In Figure 6.2, similar to Figure 6.1, absolute values of overpotential are approximately an order of magnitude larger in the cathode than in the anode. Also, in comparing the results in Figure 6.2 to those in Figure 6.1, it is observed that absolute values of anode and cathode overpotentials increase with current density as required by Equations (3.59) and (3.60). As shown in Figure 6.2, the variation in overpotential is larger in the anode (i.e. 115 %) than in the cathode (i.e. 61 %) as expected, and these variations are much larger than those found at low current densities. This is in agreement with the increase in maximum absolute potential difference in the polymer-electrolyte phase as current density is increased, as expected from Equation (3.69).

According to the results shown in Figure 5.17 at high current densities, polymer-electrolyte phase electrical potential in the catalyst layers is decreasing in the x-direction towards the gas channel in the anode and even more so in the cathode. Electrical potential in the catalyst layers decreases in the y-direction towards the membrane in the anode, but

is more uniform in the cathode. Finally, electrical potential in both the anode and cathode catalyst layers increases in the z-direction towards the gas channel outlets. Similar overpotential distributions are observed in Figure 6.2 except that the overpotential distributions are the negative of the electrical potential distributions. Thus, in agreement with the results shown in Figure 5.17 at high current densities for the electrical potential distributions, overpotential is increasing in the x-direction towards the gas channel in the anode and even more so in the cathode. Overpotential also increases in the y-direction towards the membrane in the anode, but is more uniform in the cathode, and decreases in the z-direction towards the gas channel outlets in both the anode and cathode.

In general, the distribution of overpotential in the anode catalyst layer is found to be qualitatively similar at both low and medium current densities and is approximately uniform in the x-direction under the bipolar plate and gas channel, and also increases in the y-direction towards the membrane and decreases in the z-direction towards the gas channel outlet. At high current densities anode overpotential distribution is similar to that at low and medium current densities, except that overpotential is increasing in the x-direction towards the gas channel. In contrast, the distribution of overpotential in the cathode catalyst layer changes more with current density. In the x-direction cathode overpotential is approximately uniform at low current densities, but increases towards the gas channel at high current densities. In the y-direction cathode overpotential increases towards the gas diffusion layer at low current densities, but is approximately uniform at high current densities. Finally, in the z-direction cathode overpotential increases towards the gas channel outlet at low current densities, but decreases towards the outlet at high current densities.

Figure 6.3 shows transfer current, $|S_s|$, in the anode and cathode catalyst layers at a voltage of 0.84 V.

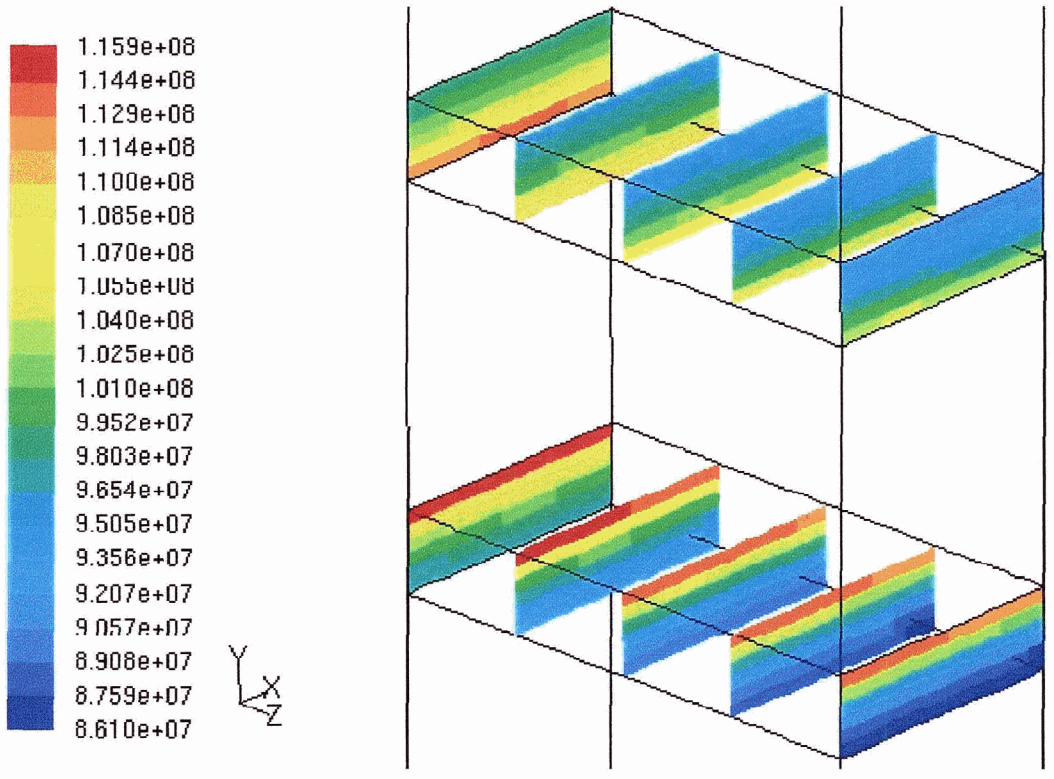

Figure 6.3 - Transfer current contours in units of A m^{-3} in the anode and cathode catalyst layers for the "base case" MTF model at a voltage of 0.84 V.

As noted previously, hydrogen concentration is essentially uniform throughout the anode catalyst layer and also has the same approximate value at all current densities. Therefore the distribution of transfer current in the anode catalyst layer is determined by the distribution of overpotential. At low current densities the distribution of overpotential in the anode is found to be approximately uniform in the x-direction under the bipolar plate and gas channel, and increases in the y-direction towards the membrane and decreases in the z-direction towards the gas channel outlet. Since transfer current increases as overpotential increases in the anode, the distribution of transfer current should be similar and this is shown to be the case at low current densities in Figure 6.3. Thus transfer current is approximately uniform in the x-direction under the bipolar plate and gas

channel, and increases in the y-direction towards the membrane and decreases in the z-direction towards the gas channel outlet.

At low current densities, the oxygen concentration as shown in Figure 5.13 varies by only 10.4 %, and therefore oxygen concentration is essentially uniform throughout the cathode catalyst layer. Therefore in this case the distribution of transfer current in the cathode catalyst layer is determined by the distribution of overpotential. Note that since transfer current increases as overpotential decreases in the cathode, the transfer current distribution is the negative of the overpotential distribution. At low current densities in the cathode catalyst layer overpotential is approximately uniform in the x-direction, and increases in the y-direction towards the gas diffusion layer and in the z-direction towards the gas channel outlet. This agrees with the results for the distribution of transfer current in the cathode catalyst layer in Figure 6.3, which shows that transfer current is approximately uniform in the x-direction, and decreases in the y-direction towards the gas diffusion layer and in the z-direction towards the gas channel outlet.

Figure 6.4 shows transfer current, $|S_s|$, in the anode and cathode catalyst layers at a voltage of 0.69 V. Since the distribution of transfer current in the anode catalyst layer is determined by the distribution of overpotential, which is found to be qualitatively similar at low and medium current densities, similar results for the anode transfer current distribution are expected at medium (Figure 6.4) versus low (Figure 6.3) current densities. This is observed to be the case in Figure 6.4 since transfer current is approximately uniform in the x-direction under the bipolar plate and gas channel, and increases in the y-direction towards the membrane and decreases in the z-direction towards the gas channel outlet.

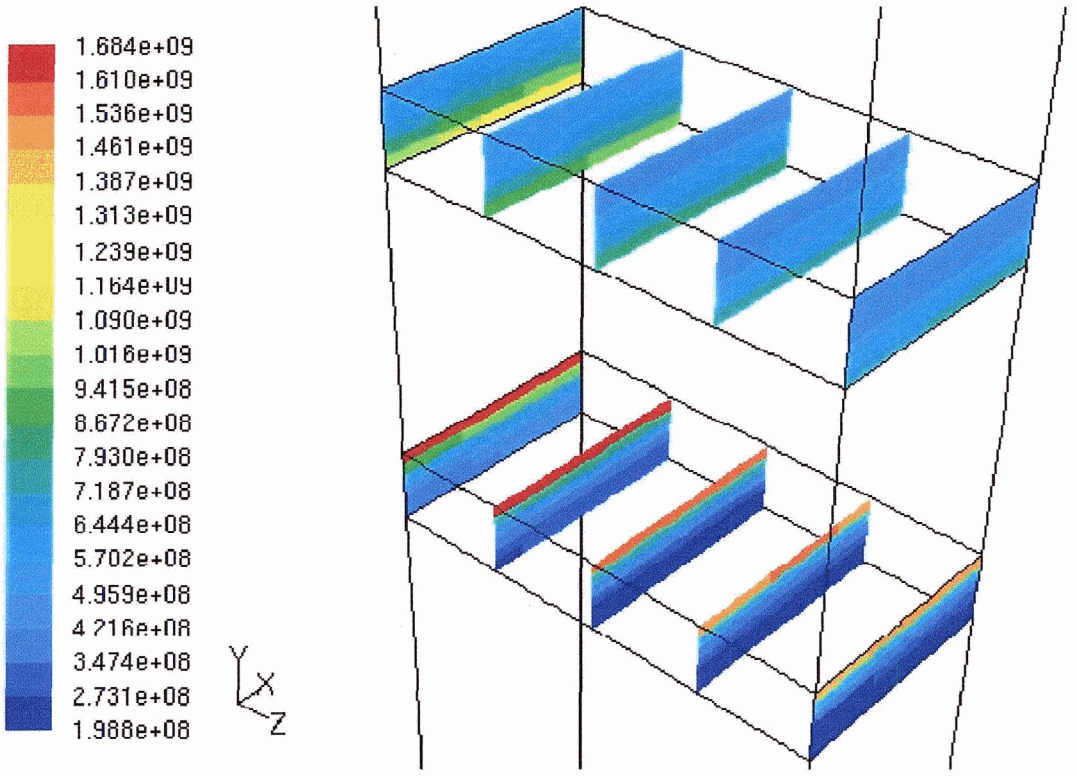

Figure 6.4 - Transfer current contours in units of A m^{-3} in the anode and cathode catalyst layers for the "base case" MTF model at a voltage of 0.69 V.

At medium current densities the oxygen concentration is found to vary by 88 % and therefore is no longer uniform throughout the cathode catalyst layer. Thus the distribution of transfer current in the cathode catalyst layer is potentially determined by the distributions of both overpotential and oxygen concentration. At medium current densities, oxygen concentration is found to increase in the x-direction towards the gas channel and decrease in the z-direction towards the gas channel outlet, but because the diffusion length scale in the y-direction is negligible compared to that in the x- and z-directions, oxygen concentration is approximately uniform in the y-direction. At medium current densities, overpotential is found to be approximately uniform in the x- and z-direction, and increases in the y-direction towards the gas diffusion layer. According to the results shown in Figure 6.4, transfer current is approximately uniform in the x- and z-directions,

and decreases in the y-direction towards the gas diffusion layer. Since transfer current distribution is the negative of overpotential distribution in the cathode, the transfer current distribution shown in Figure 6.4 is similar to the overpotential distribution. Also, since transfer current increases as oxygen concentration increases using Equation (3.60), the transfer current distribution should be similar to the oxygen distribution - if oxygen concentration is dominant - and this is not observed to be the case in Figure 6.4. Thus the results in Figure 6.4 show that at medium current densities, transfer current distribution in the cathode catalyst layer is determined by overpotential distribution and therefore the effect of overpotential is more important at medium current densities than the effect of oxygen concentration.

In general, since at low and medium current densities the transfer current distributions in both the anode and cathode are determined by overpotential distributions and (as shown in Figures 6.1 and 6.2) overpotential variations are larger in the anode than in the cathode, the variation in transfer current is larger in the anode than in the cathode (as observed in Figure 6.3 and 6.4). As mentioned previously, overpotential variations in the catalyst layers are larger in the anode than cathode due to lower water content and therefore lower electrical conductivity in the polymer-electrolyte phase. Thus the larger transfer current variation in the anode, which indicates that reactions are more concentrated in the anode than in the cathode, is due to drying of the polymer electrolyte in the anode causing large ohmic resistances. Therefore, in order to minimise ohmic resistances, most of the reactions in the anode occur near the gas channel inlet where water content is found to be the highest and towards the membrane where the conduction path length is the shortest.

Figure 6.5 shows transfer current, $|S_s|$, in the anode and cathode catalyst layers at a voltage of 0.39 V.

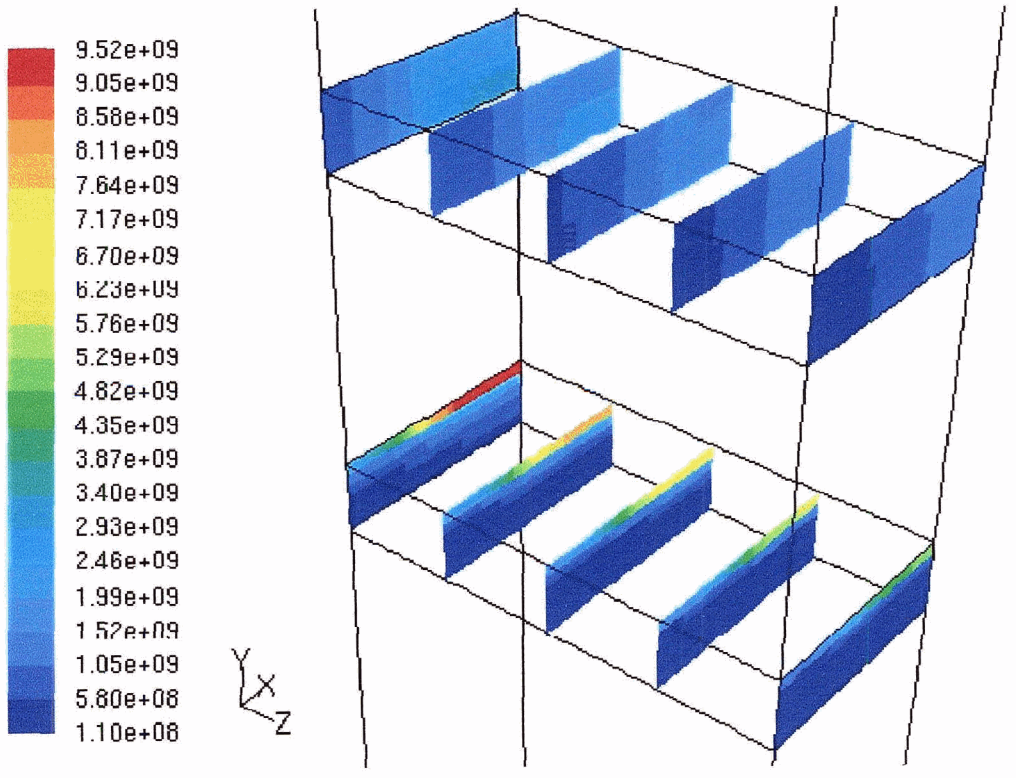

Figure 6.5 - Transfer current contours in units of A m^{-3} in the anode and cathode catalyst layers for the "base case" MTF model at a voltage of 0.39 V.

At high current densities the anode overpotential distribution is similar to that at low and medium current densities, except that overpotential is increasing in the x-direction towards the gas channel. Therefore, similar to the results for anode transfer current distribution shown in Figure 6.3 at low current densities and Figure 6.4 at medium current densities, the results in Figure 6.5 show that, at high current densities, the anode transfer current increases in the y-direction towards the membrane and decreases in the z-direction towards the gas channel outlet. In contrast, the results in Figure 6.5 show that anode transfer current increases in the x-direction towards the gas channel. Also, in order to minimise ohmic losses due to drying of the polymer electrolyte in the anode (which is found to increase with current density), the reactions in the anode become more concentrated near the gas channel inlet (where water content is found to be the highest)

and towards the membrane (where the conduction path length is the shortest) as current density increases. This effect is observed in the results shown in Figures 6.3, 6.4 and 6.5 as an increase in transfer current variation with current density.

At high current densities, the oxygen concentration (as shown previously in Figure 5.13) varies by almost two orders of magnitude. According to results shown in Figure 5.13, oxygen concentration increases in the x-direction towards the gas channel and decreases in the z-direction towards the gas channel outlet, but is approximately uniform in the y-direction. The results in Figure 6.5 show a similar transfer current distribution as expected for oxygen concentration as the dominant effect. In contrast, for a distribution determined by overpotential, the transfer current would decrease in the x-direction towards the gas channel and increase in the z-direction towards the gas channel outlet, although it would still be approximately uniform in the y-direction. Therefore, the results in Figure 6.5 show that the effect of oxygen concentration is dominant.

In general, although the cathode transfer current distribution at high current densities is no longer determined by the overpotential distribution, the variation in transfer current is still larger in the anode than in the cathode as shown in Figure 6.5. Thus the anode reactions are more concentrated near the gas channel inlet and towards the membrane than the cathode reactions are concentrated near the gas channel inlet. Therefore, drying in the anode has a larger effect on reaction distributions than oxygen transport limitations in the cathode even at high current densities. As a result, reactions are more uniform in the cathode than in the anode at all current densities.

6.2 Non-Uniform Anode Catalyst Loading

According to the results shown in Figures 6.3 and 6.4, the transfer current distribution in the anode catalyst layer is similar at low and medium current densities. In these cases,

transfer current is approximately uniform in the x-direction, and increases in the y-direction towards the membrane and decreases in the z-direction towards the gas channel outlet. The results in Figure 6.5 show that the anode transfer current distribution at high current densities is similar to that at low and medium current densities, except that the transfer current distribution is increasing in the x-direction towards the gas channel.

Therefore, the reaction distribution in the anode catalyst layer is highly non-uniform and not all the catalyst sites are being utilised. According to Figure 6.3 for low current densities, the variation in anode transfer current is only 29.5 %. Thus at low current densities in the anode, the reaction rate and therefore the utilisation of catalyst sites is relatively uniform. However, according to Figure 6.4 for medium current densities and Figure 6.5 for high current densities, respectively, the minimum transfer current in the anode is approximately one and two orders of magnitude less than the maximum transfer current. Thus anode reactions become more concentrated near the gas channel inlet and towards the membrane as current density increases due to increased drying of the polymer electrolyte. Therefore catalyst site utilisation near the gas channel inlet and towards the membrane increases and catalyst site utilisation near the outlet and towards the gas diffusion layer decreases as current density increases.

Using Equations (3.59) and (3.60), transfer current is proportional to the active surface area per unit volume, ξ, which in the thesis model is assumed to be the same in both catalyst layers. As discussed in Chapter 3, the active surface area per unit volume in the catalyst layers in the thesis model is given by first multiplying the platinum loading of 1.0 g m^{-2} by the surface area per unit mass for platinum, which for 20 wt % platinum is equal to 128 m^2 g^{-1} (according to the technical data sheets supplied by E-TEK (2004)). This value is then divided by the thickness of the catalyst layer (1.29×10^{-5} m) and multiplied by the fractional utilisation of platinum in the thin-film catalyst layer (0.454 - Cheng et al., 1999) yielding a value of $\xi = 4.50 \times 10^6$ m^{-1}. Thus, in general, transfer current is proportional to the overall precious metal loading, although for all the CFD

simulation results presented in this thesis the overall platinum loading has the same value of 1.0 g m^{-2}. Also, in general, transfer current is inversely proportional to the catalyst layer thickness, although for all the CFD simulation results presented in this thesis the catalyst layer thickness has the same value of 1.29×10^{-5} m.

The value for the fractional utilisation of platinum used to calculate the active surface area per unit volume in the catalyst layers is an experimentally derived value and is the maximum value that is found if all the available catalyst sites are being utilised. Although in general the maximum fractional utilisation of platinum is a function of polymer electrolyte content (Sasikumar et al., 2004), for all the CFD simulation results presented in this thesis the content of polymer electrolyte in the catalyst layers has the same value. Note that maximum fractional utilisation of platinum is a function of polymer electrolyte content since active catalyst sites are limited to those in contact with polymer electrolyte (as discussed in Chapter 1). According to the results shown in Section 6.1 not all of the active catalyst sites are being utilised and the actual utilisation is a function of location in the anode and cathode catalyst layers. Thus, although the maximum fractional utilisation of platinum has the same value for all the CFD simulation results presented in this thesis, the actual utilisation varies for the same overall platinum loading. However, the results also show that reactions become more concentrated near the gas channel inlet and towards the membrane in the anode as current density increases and the reactions in these locations could potentially be limited by the maximum fractional utilisation of platinum. Therefore, if active surface area per unit volume is increased in these locations (i.e. where reactions are concentrated), then reactions in these locations should also increase. Conversely, if active surface area per unit volume is decreased in locations where reactions are not concentrated, then since reactions in these locations are not limited by the maximum fractional utilisation of platinum, the actual utilisation can increase such that the reactions should not change. The overall result will be an increase in reactions and an improvement in PEM fuel cell performance.

In order to vary active surface area per unit volume as a function of location for the same overall platinum loading, the local platinum loading is varied. In order to vary the local platinum loading without varying the surface area per unit mass for platinum, which varies with wt % platinum, the same value of 20 wt % platinum is assumed for all the CFD simulation results presented in this thesis. The local platinum loading is varied linearly between the values of 0 to 2.0 g m^{-2} such that the average value of 1.0 g m^{-2} corresponds to the same overall platinum loading. For 20 wt % platinum, local platinum loading values of 0, 1.0 and 2.0 g m^{-2} correspond to local catalysed carbon loading values of 0, 4.0 and 8.0 g m^{-2}, respectively. In order for the overall and local carbon content to remain constant in the catalyst layers - such that the structure, total thermal conductivity and effective solid phase electrical conductivity remain the same - local catalysed carbon loading values of 0, 4.0 and 8.0 g m^{-2} are assumed to be supplemented by local uncatalysed carbon loading values of 8.0, 4.0 and 0 g m^{-2}, respectively. This yields an active surface area per unit volume which varies linearly from 0 to 9.0×10^6 m^{-1} with an average value of 4.50×10^6 m^{-1}.

The variations in active surface area per unit volume (local catalyst loading) are implemented in CFD simulations for the "base case" MTF model for the same overall catalyst loading. In this section, linear variations in local anode catalyst loading in the positive and negative x-, y- and z-directions are implemented individually in separate CFD simulations. These results are compared with uniform anode catalyst loading, yielding seven cases altogether. Uniform cathode catalyst loading is maintained for all cases. Similarly, in Section 6.3, linear variations in local cathode catalyst loading are implemented individually in separate CFD simulations and the results compared with uniform cathode catalyst loading. Uniform anode catalyst loading is maintained for all cases.

Figure 6.6 shows CFD simulation results for the MTF model in the form of polarisation curves for "base case" operating conditions, and with uniform versus non-uniform anode catalyst loading (cathode catalyst loading is uniform).

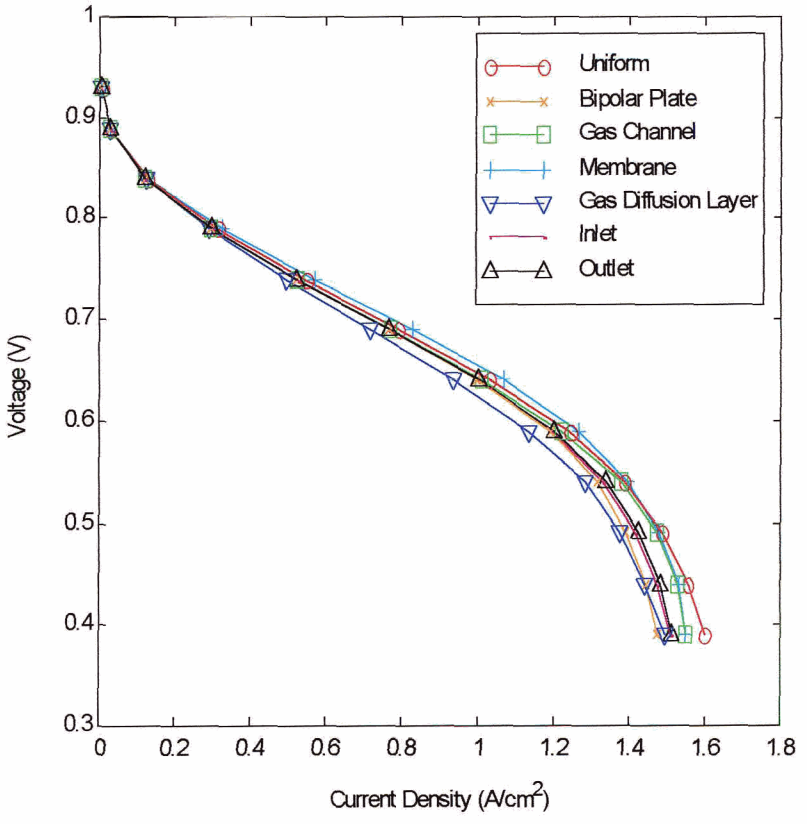

Figure 6.6 - Comparison of MTF model polarisation curves for "base case" operating conditions, and with uniform cathode catalyst loading. Anode catalyst loading is uniform (red) and linearly variable in one dimension (at the same overall loading) with maximum loading under the bipolar plate (orange), under the gas channel (green), adjacent to the membrane (cyan), adjacent to the gas diffusion layer (blue), towards the gas channel inlet (magenta) and towards the gas channel outlet (black).

In general, as shown in Figure 6.6, at low current densities the results are approximately equal and relative differences between the polarisation curves are not obvious. Thus for the discussion of the results at low current densities in this section and Section 6.3, the actual numerical values are compared. According to the results shown in Figure 6.6, the polarisation curve for local catalyst loading increasing in the x-direction towards the gas channel is lower at low current densities and higher at medium and high current densities than the polarisation curve for local catalyst loading decreasing towards the gas channel (i.e. with maximum loading under the bipolar plate). The polarisation curves cross at a voltage between 0.74 and 0.79 V. These results are expected (as discussed previously) since transfer current is approximately uniform in the x-direction at low current densities (although these results indicate that transfer current is decreasing very slightly towards the gas channel due to the increase in hydrogen concentration found in the opposite direction) and is increasing towards the gas channel at high current densities. Thus, increasing local anode catalyst loading in the locations where reactions are concentrated (i.e. under the bipolar plate at low current densities and under the gas channel at high current densities) yields improved fuel cell performance. The improvements at low current densities for maximum loading under the bipolar plate are relatively small (i.e. less than 0.2 %), but at high current densities for maximum loading under the gas channel are larger, reaching a maximum of approximately 5.7 % at voltages of 0.44 and 0.49 V.

As shown in Figure 6.6, the polarisation curve for local catalyst loading increasing in the y-direction towards the membrane is higher at all current densities than the polarisation curve for local catalyst loading decreasing towards the membrane (i.e. with maximum loading adjacent to the gas diffusion layer). These results are expected (as discussed previously) since transfer current is increasing in the y-direction towards the membrane at all current densities. Thus, increasing local anode catalyst loading in the locations where reactions are concentrated (i.e. adjacent to the membrane at all current densities) yields improved fuel cell performance. The improvement is the largest at

medium current densities and reaches a maximum of approximately 14 % at a voltage of 0.69 V.

According to the results shown in Figure 6.6, the polarisation curve for local catalyst loading increasing in the z-direction towards the gas channel outlet is lower at low and medium current densities and higher at high current densities than the polarisation curve for local catalyst loading decreasing towards the gas channel outlet (i.e. with maximum loading towards the gas channel inlet). The polarisation curves cross at a voltage between 0.59 and 0.64 V, although the difference between the curves is never more than 0.8 %. The results at low and medium current densities are expected (as discussed previously) since transfer current is decreasing in the z-direction towards the gas channel outlet at all current densities. Thus, increasing local anode catalyst loading in the locations where reactions are concentrated (i.e. towards the gas channel inlet) yields improved fuel cell performance at low and medium current densities.

In contrast, the results at high current densities are not expected (as discussed previously), since increasing local anode catalyst loading towards the gas channel inlet where reactions are concentrated yields worse fuel cell performance. These results can be explained in general, however, since increasing local catalyst loading in locations where reactions are concentrated also has the detrimental effect of decreasing local catalyst loading in locations where reactions are not concentrated. If reactions are limited by the maximum fractional utilisation of catalyst in the locations where reactions are concentrated, then increasing local catalyst loading in these locations causes an increase in reactions, improving fuel cell performance. Otherwise the reactions and fuel cell performance will not change. In contrast, decreasing local catalyst loading in locations where reactions are not concentrated below actual utilisation will cause a decrease in reactions, causing worse fuel cell performance. Thus it is possible that the overall reactions will decrease (causing worse fuel cell performance) for cases of increased local catalyst loading in locations where reactions are concentrated - since the gain of catalyst

sites in these locations can have less of an effect than the loss of catalyst sites in locations where reactions are not concentrated.

As shown in Figure 6.6, this is also the case for the polarisation curve with uniform catalyst loading. This polarisation curve is higher than all the other polarisation curves at all current densities except for the polarisation curve with maximum catalyst loading adjacent to the membrane at low and medium current densities (which is higher for voltages exceeding a value between 0.49 and 0.54 V). Thus the polarisation curve with uniform catalyst loading shows that, in general, the uniformity of catalyst loading is a dominant effect. Also, as discussed in Chapter 2, fuel cell performance improves as reactions in a given catalyst layer become more uniform. Therefore, in general, both uniform catalyst loading and reactions improve fuel cell performance.

In Figure 6.6, the polarisation curve for maximum catalyst loading adjacent to the membrane is the highest at low and medium current densities and is the second highest at high current densities (below the polarisation curve for uniform catalyst loading). The improvement (over the polarisation curve for uniform catalyst loading) is the largest at medium current densities and reaches a maximum of approximately 4.7 % at a voltage of 0.74 V. In contrast, the polarisation curve for maximum catalyst loading adjacent to the gas diffusion layer is the lowest for all but the lowest and very highest current densities. The polarisation curves for maximum catalyst loading under the bipolar plate at low current densities and under the gas channel at medium and high current densities are the next highest. Finally, the polarisation curves for maximum catalyst loading towards the gas channel inlet and outlet are lower than all others except the cases of maximum catalyst loading adjacent to the gas diffusion layer and under the bipolar plate at medium and high current densities.

These results indicate that the effect of ohmic resistance associated with conduction path length towards the membrane is dominant, such that increasing local catalyst loading adjacent to the membrane (shortest path length) has the most beneficial effect whereas

increasing local catalyst loading adjacent to the gas diffusion layer (longest path length) has the most detrimental effect. The next most important effect is associated with the increase in water content and electrical conductivity in polymer electrolyte from under the bipolar plate to under the gas channel. Increasing local catalyst loading under the gas channel at medium and high current densities has the next most beneficial effect and under the bipolar plate a large detrimental effect. Finally, the least important effect is the decrease in water content and electrical conductivity in polymer electrolyte towards the gas channel outlet. In this case, the non-uniformity of the local catalyst loading is the dominant effect as it is for all the polarisation curves in general.

6.3 Non-Uniform Cathode Catalyst Loading

According to the results shown in Figures 6.3 and 6.4, the transfer current distribution in the cathode catalyst layer is similar at low and medium current densities. In these cases, transfer current is approximately uniform in the x-direction, and decreases in the y-direction towards the gas diffusion layer and in the z-direction towards the gas channel outlet. The results in Figure 6.5 show that the cathode transfer current at high current densities increases in the x-direction towards the gas channel, is approximately uniform in the y-direction and decreases in the z-direction towards the gas channel outlet. Thus the transfer current distribution changes from being uniform in the x-direction at low and medium current densities, to increasing in the x-direction towards the gas channel at high current densities. In the y-direction the transfer current distribution changes from decreasing towards the gas diffusion layer at low and medium current densities to being uniform at high current densities. Finally, in the z-direction the transfer current is decreasing towards the gas channel outlet at all current densities.

Therefore the reaction distribution in the cathode catalyst layer is non-uniform and not all the catalyst sites are being utilised. As mentioned previously, the variation in transfer

current is smaller in the cathode than in the anode at all current densities. Thus, at low current densities (Figure 6.3) the variation in cathode transfer current is less than the 29.5 % variation in anode transfer current, and therefore the utilisation of catalyst sites is relatively uniform. However, according to Figure 6.4 at medium current densities and Figure 6.5 at high current densities, even though the variation in cathode transfer current is less than that for the anode, it is still increasing with current density - such that the minimum cathode transfer current is approximately one order of magnitude less than the maximum at high current densities. Thus cathode reactions become more concentrated near the gas channel inlet as current density increases due to increased oxygen transport limitations. Therefore catalyst site utilisation near the gas channel inlet increases and catalyst site utilisation near the outlet decreases with increasing current density.

Figure 6.7 shows CFD simulation results for the MTF model in the form of polarisation curves for "base case" operating conditions, and with uniform versus non-uniform cathode catalyst loading (anode catalyst loading is uniform). According to the results shown in Figure 6.7, the polarisation curve for local catalyst loading increasing in the x-direction towards the gas channel is lower at low and medium current densities and higher at high current densities than the polarisation curve for local catalyst loading decreasing towards the gas channel (i.e. with maximum loading under the bipolar plate). The polarisation curves cross at a voltage between 0.54 and 0.59 V. The improvements at low current densities for maximum loading under the bipolar plate are relatively small (i.e. less than 0.3 %), but at high current densities for maximum loading under the gas channel are larger, reaching a maximum of approximately 13.5 % at a voltage of 0.39 V. Thus these results are similar to those for the anode catalyst layer (as expected since the transfer current distribution in the x-direction is similar in both the anode and cathode at all current densities), except that the polarisation curves cross at a higher current density and differ by a larger margin.

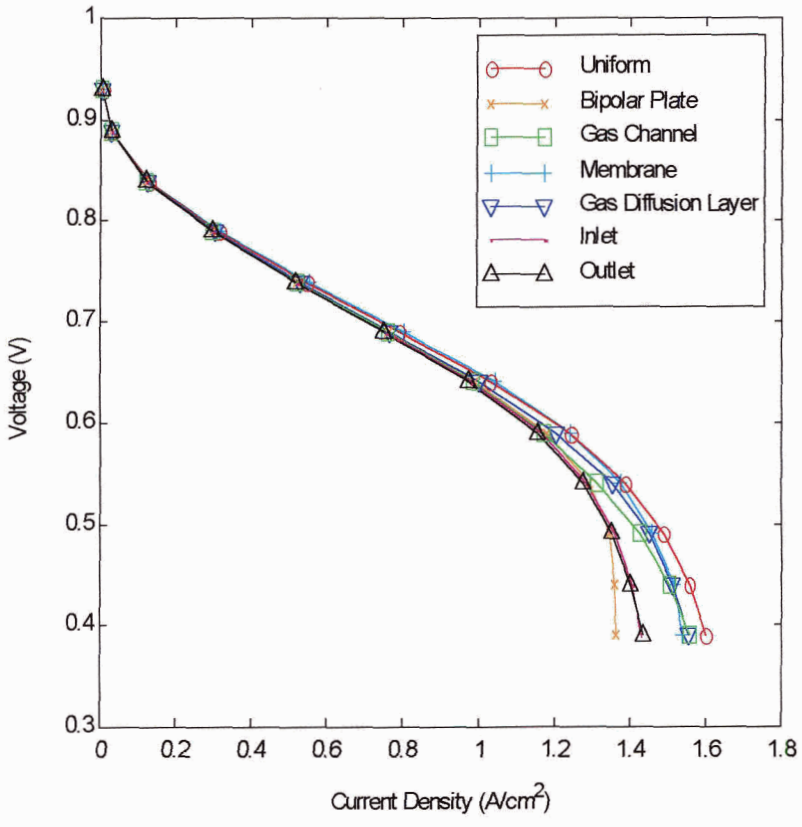

Figure 6.7 - Comparison of MTF model polarisation curves for "base case" operating conditions, and with uniform anode catalyst loading. Cathode catalyst loading is uniform (red) and linearly variable in one dimension (at the same overall loading) with maximum loading under the bipolar plate (orange), under the gas channel (green), adjacent to the membrane (cyan), adjacent to the gas diffusion layer (blue), towards the gas channel inlet (magenta) and towards the gas channel outlet (black).

As shown in Figure 6.7, the polarisation curve for local catalyst loading increasing in the y-direction towards the gas diffusion layer is lower at low and medium current densities and higher at the very highest current densities than the polarisation curve for local catalyst loading decreasing towards the gas diffusion layer (i.e. with maximum

loading adjacent to the membrane). These results are expected (as discussed previously) since in the y-direction transfer current is decreasing towards the gas diffusion layer at low and medium current densities and is approximately uniform at high current densities. Note, however, that these results indicate that transfer current is increasing very slightly towards the gas diffusion layer at high current densities due to a small increase in oxygen concentration found in this direction. Thus increasing local cathode catalyst loading in the locations where reactions are concentrated (i.e. towards the membrane at low and medium current densities and towards the gas diffusion layer at high current densities) yields improved fuel cell performance. The improvement at medium current densities for maximum loading towards the membrane reaches a maximum of approximately 4.7 % at a voltage of 0.69 V, while at high current densities for maximum loading towards the gas diffusion layer, the improvement is 1.0 % at a voltage of 0.39 V.

According to the results shown in Figure 6.7, the polarisation curve for local catalyst loading increasing in the z-direction towards the gas channel outlet is lower at low and medium current densities and higher at the very highest current densities than the polarisation curve for local catalyst loading decreasing towards the gas channel outlet (i.e. with maximum loading towards the gas channel inlet). The polarisation curves cross at a voltage between 0.39 and 0.44 V, although the difference between the curves is never more than 1.1 %. The results at all current densities except the very highest current densities are expected (as discussed previously) since transfer current is decreasing in the z-direction towards the gas channel outlet at all current densities. Thus increasing local cathode catalyst loading in the locations where reactions are concentrated (i.e. towards the gas channel inlet) yields improved fuel cell performance for all but the very highest current densities.

In Figure 6.7, similar to Figure 6.6, the polarisation curve for uniform catalyst loading is higher than all others at all current densities except for the case of maximum catalyst loading adjacent to the membrane. This polarisation curve is higher at low and medium current densities for voltages exceeding a value between 0.54 and 0.59 V. The

improvement (over the polarisation curve for uniform catalyst loading) is the largest at medium current densities and reaches a maximum of approximately 1.6 % at a voltage of 0.69 V. However, in contrast to Figure 6.6, the polarisation curve for maximum catalyst loading adjacent to the membrane is no longer the second highest at the very highest current densities, since the effect of oxygen transport limitations becomes more dominant and the polarisation curves for maximum catalyst loading adjacent to the gas diffusion layer and under the gas channel are now higher. Also, the polarisation curve for maximum catalyst loading adjacent to the gas diffusion layer is now higher than that for maximum catalyst loading under the bipolar plate at all current densities. Finally, the polarisation curves for maximum catalyst loading towards the gas channel inlet and outlet are lower than all others except the case of maximum catalyst loading under the bipolar plate at high current densities.

These results indicate that the effect of ohmic resistance associated with conduction path length towards the membrane is still important at low and medium current densities, such that increasing local catalyst loading adjacent to the membrane (shortest path length) has the most beneficial effect. However concentration overpotential due to oxygen transport limitations is also important and becomes a dominant effect at the highest current densities. Concentration overpotential causes decreasing reactions under the bipolar plate compared to under the gas channel, and towards the membrane compared to towards the gas diffusion layer, such that increasing local catalyst loading under the gas channel and towards the gas diffusion layer at high current densities have the most beneficial effects after uniformity. In contrast, increasing local catalyst loading under the bipolar plate has a large detrimental effect. Finally, the decrease in oxygen concentration towards the gas channel outlet does not have as much of an effect as might be expected as evidenced by the fact that increases in local catalyst loading towards the gas channel inlet do not improve fuel cell performance significantly relative to increases towards the outlet. In this case, similar to the results shown in Figure 6.6, the non-uniformity of the local catalyst loading is the dominant effect.

Chapter 7

Conclusions

The performance of PEM fuel cells (i.e. reaction rates) is not only dependent on operating conditions such as gas pressure, temperature and humidity, but is also strongly dependent on the composition (i.e. carbon supported platinum, polymer electrolyte and PTFE), structure (i.e. porosity, tortuosity, pore size and pore size distribution) and fabrication method of the catalyst layers. In PEM fuel cells, platinum or platinum alloys provide the best catalytic activity for both hydrogen oxidation at the anode and oxygen reduction at the cathode. Unfortunately, platinum is prohibitively expensive, and in order to optimise performance at minimum cost, PEM fuel cells require high platinum utilisation. State-of-the-art PEM fuel cell catalyst layers with high performance for low platinum loadings of 0.1 mg cm^{-2} in the cathode and 0.05 mg cm^{-2} in the anode are fabricated by deposition of very thin catalyst layers (on the order of 10 μm and 5 μm, respectively) on either the gas diffusion layers or membrane, before hot-pressing the electrodes and membrane in a MEA. The catalyst layers are composed of highly inter-mixed carbon supported platinum and polymer electrolyte, and sometimes PTFE. As discussed in Chapter 1, optimal fuel cell performance is achieved by increasing catalyst utilisation through improved contact between catalyst sites and polymer electrolyte. The performance of PEM fuel cells depends not only on catalyst utilisation, but also on improved reactant transport through increased porosity and wet-proofing (i.e. PTFE content), improved proton conductivity through increased polymer electrolyte content and

improved electron conductivity through increased carbon content. In general, reactant transport and proton and electron conductivities influence the reaction rate distribution, which in turn influences fuel cell performance. As discussed in Chapter 1, optimal fuel cell performance is achieved for specific polymer electrolyte and PTFE contents, although the optimisation of composition, which determines the structure of the catalyst layer, changes depending on operating current density.

Thus increasing PEM fuel cell performance depends on the optimisation of the catalyst layer composition and structure for large active surfaces with low resistances to the transport of reactants and conduction of protons and electrons. One way of contributing to a fundamental understanding of the effects of catalyst layer composition and structure on the physical and electrochemical phenomena occurring in PEM fuel cells (that determine reaction rate distributions and fuel cell performance) is through modelling. Modelling studies provide a valuable tool for the optimisation of MEA composition and structure and also fuel cell operating conditions in order to attain maximum performance. This optimisation for maximum performance requires a detailed modelling of the reactions and mass transport in catalyst layers in order to find ways to increase the effectiveness of the catalyst layers for a given precious metal loading.

As discussed in Chapter 2, many studies of PEM fuel cells which concentrate on regions other than the catalyst layers have implemented simplified models by treating the catalyst layers as infinitely thin interfaces between the gas diffusion layers and membrane, relegating them to boundary conditions for the solution of the model. In contrast, Bernardi & Verbrugge (1991, 1992) and Springer et al. (1993), among others, presented macro-homogenous models for the catalyst layers based on similar models previously applied to catalyst layers in contact with aqueous acid electrolyte. These models of charge and mass transport coupled to electrochemical reactions in the catalyst layers assume that polymer electrolyte fully penetrates the catalyst layers and completely fills the void spaces of the porous matrix. In this case the catalyst layers are a homogeneous domain of polymer

electrolyte and solid matrix in which the transport of dissolved reactants, and conduction of protons and electrons, are simply superimposed onto each other.

As discussed in Chapter 1, experimental results contradict the fundamental assumption of the macro-homogeneous model - that polymer electrolyte completely fills the void spaces of the porous matrix - and suggest that a trade-off exists between proton conductivity and reactant mass-transport as the limiting processes in catalyst layers since polymer electrolyte enhances proton conductivity, but restricts reactant mass-transport. Thus, Rho et al. (1994), Bevers et al. (1997) and Baschuk & Li (2000), among others, have shown that the agglomerate model (i.e. catalyst layers contain interconnected gas-filled macropores through which reactants diffuse before reacting at catalyst sites on the surfaces of polymer electrolyte bound agglomerates) is more appropriate than the macro-homogeneous model, as the former model better explains the reactant diffusion process in catalyst layers. Also, as discussed in Chapter 2, comparisons of polarisation curves derived from simulations using the same model parameters for both agglomerate and macro-homogenous models show that agglomerate models better match experimental results.

In the studies based on catalyst layer agglomerate models discussed in Chapter 2, effects of compositional and structural parameters such as platinum loading, polymer electrolyte content, porosity and catalyst layer thickness have been analysed. The results show that for low polymer electrolyte content, proton conductivity is the limiting process and reactions occur predominately in thin regions adjacent to the membrane. In contrast, for low porosity, mass transport of the reactants is the limiting process and reactions occur predominately in thin regions adjacent to the gas diffusion layers. In either case, faster reaction kinetics (i.e. increased platinum loading) cause even thinner reaction regions, while increases in the current density cause the reaction regions to expand. Thus optimising platinum loading and reducing costs through better catalyst utilisation is accomplished by causing reaction regions to expand and fill the entire catalyst layers, which can be done by decreasing the catalyst layer thickness, since this has the added

benefit of reducing proton resistivity and reactant mass-transport limitations due to the shorter transport pathways.

7.1 Contributions and Results

In Chapter 3, a fully three-dimensional, multicomponent and multiphase model is presented for PEM fuel cells. The set of equations governing transport of reactants in the gas channels, gas diffusion layers and catalyst layers includes Fick's first law for diffusion - with effective diffusion coefficients calculated using an approximate solution to the full set of Stefan-Maxwell equations. Ohm's law is used for both electron conduction in the bipolar plates, gas diffusion layers and catalyst layers, and proton conduction in the catalyst layers and membrane. Liquid water transport through the membrane is governed by electro-osmotic drag and diffusion. In the gas diffusion and catalyst layers liquid water transport is described by Darcy's law, taking into account capillary pressure and relative permeability (as a function of liquid water saturation) and phase changes between water vapour and liquid water. The transport limitations caused by the presence of liquid water on the diffusion of reactants (due to a reduced volumetric fraction of gas) is also taken into account. The temperature distribution in the PEM fuel cell is governed by the conservation of energy equation, taking into account local heat production in the catalyst layers due to activation overpotentials and reversible changes in entropy of the electrochemical reactions. Local heat production due to phase changes in the gas diffusion and catalyst layers, and to ohmic resistances (associated with electron conduction in the bipolar plates, gas diffusion layers and catalyst layers, and proton conduction in the catalyst layers and membrane) are also taken into account. Reaction rates in the catalyst layers are given by the Butler-Volmer equation.

In general, because the governing equations in the model are strongly non-linear, analytical solutions are only available under simplified conditions. In order to obtain general solutions for the model, a CFD implementation is necessary. Based on

compatibility, a new PEM fuel cell implementation (Li & Becker, 2004) in the general purpose commercial CFD software package FLUENT™ (Fluent Inc., 2001) is chosen for the implementation of the model.

As concluded in Chapter 2, the most appropriate model for PEM fuel cell catalyst layers is the multiple thin-film agglomerate model of Baschuk & Li (2000). In this model, local concentrations of reactants adjacent to catalyst sites on the surfaces of the polymer-electrolyte bound agglomerates are dependent on reactant transport through both an outer thin film of liquid water caused by flooding in the catalyst layer and an inner thin film of polymer electrolyte surrounding the catalyst sites. The model of Baschuk & Li (2000) is one-dimensional and isothermal. A fully three-dimensional and non-isothermal version of this model is presented in Chapter 4. In this version, the thin film of polymer electrolyte is considered to have a constant thickness throughout the catalyst layers, although the thickness can be varied. In contrast, the thickness of the thin film of liquid water is a function of the liquid water saturation. Henry's law is used for dissolution of gaseous reactants into the thin film of liquid water. Transport of dissolved reactants through the thin films of liquid water and polymer electrolyte is modelled using Fick's first law, in its flat thin-film approximation, with diffusion coefficients of reactants in liquid water and polymer electrolyte, respectively.

The CFD implementation of the PEM fuel cell model presented in Chapter 3 is further improved in Chapter 4 by taking into account the detailed composition and structure of the catalyst layers. This is done by adapting the version of the multiple thin-film agglomerate model presented in Chapter 4 for use in the CFD implementation. In Chapters 5 and 6, simulation results generated using the CFD implementation of the PEM fuel cell model, with the multiple thin-film agglomerate model for catalyst layers, are presented in the form of polarisation curves and more detailed model variable results. Experimental PEM fuel cell results (Wang et al., 2003) in the form of a polarisation curve for the operating conditions in Table 5.2 can be accurately matched with CFD simulation results to within a maximum deviation of 7.3 % by varying two parameters associated with the

PEM fuel cell model. The other parameters associated with the PEM fuel cell model have been given values that have been accurately determined from separate experimental measurements, as discussed in Chapter 3.

After matching CFD simulation results to the experimental results for the operating conditions in Table 5.2, the predictive capabilities of the simulations are tested by varying the humidification of the gases in the anode and cathode in an attempt to match experimental polarisation curves for similarly varied operating conditions. It is found that numerical accuracy of the predicted CFD simulation results versus the experimental results decreases as variations from the operating conditions in Table 5.2 increase. However, qualitatively, the predictive capability of the CFD simulations is reasonable as the simulations correctly follow the same trend as the experimental results.

The effects of the transport limitations associated with the multiple thin-film agglomerate model for catalyst layers are investigated by varying the thickness of the thin film of polymer electrolyte in the CFD simulations between 15 and 320 nm, while all other parameter values are kept the same. The resulting polarisation curves show that increasing the thickness of the thin film of polymer electrolyte in the multiple thin-film model has a substantial negative effect on PEM fuel cell performance. This is because of increased transport limitations associated with the large decrease in reactant diffusion coefficients in polymer electrolyte versus gas. For a 320 nm thickness of the thin film of polymer electrolyte, a maximum current density of only about 0.4 A cm^{-2} is predicted by the CFD simulations. If the thickness could be increased without varying any other parameters, the maximum current density would approach zero as the thickness increases above approximately 1000 nm, and this limit agrees with the experimental results discussed in Chapter 2.

In the multiple thin-film agglomerate model for catalyst layers the transport limitation associated with the thickness of the thin film of liquid water is found to be small compared to that associated with the thickness of the thin film of polymer electrolyte. However, the

presence of liquid water in the gas diffusion and catalyst layers also decreases the volumetric fraction available for the transport of gaseous reactants. The effect of the resulting transport limitations is investigated by varying the diffusion coefficient associated with liquid water transport such that volume-averaged (in the cathode gas diffusion and catalyst layers) liquid water saturation varies between 0.1 and 0.7 at a voltage of 0.39 V, while all other parameter values are kept the same. The resulting polarisation curves show that increasing cathode liquid water saturation has a substantial negative effect on PEM fuel cell performance. For liquid water saturations of 0.7, the maximum current density is less than half that at saturations of 0.1 and, as the saturation approaches one (i.e. the gas diffusion and catalyst layers are fully flooded), the CFD simulations predict that the maximum current density approaches zero - in agreement with the results of previous modelling studies discussed in Chapter 2.

In general, simulation results for model variables generated using the CFD implementation of the PEM fuel cell model with the multiple thin-film agglomerate model confirm the capability of the CFD simulations in accurately predicting detailed results. The results show that temperature and gas pressure gradients in PEM fuel cells are relatively small such that PEM fuel cells are to a first approximation isothermal and isobaric. Also, hydrogen concentration gradients in the anode are relatively small. In contrast, cathode oxygen concentration decreases substantially with current density due to the transport resistances of nitrogen and liquid water, and is lower under the bipolar plate and towards the gas channel outlet (i.e. further away from the inlet) because of longer diffusion length scales. Anode water vapour mole fraction is lower under the bipolar plate and towards the gas channel outlet because electro-osmotic drag transports water from the anode to the cathode. In the cathode, excess water vapour condenses into liquid water, limiting the mole fraction to its fully saturated value. Thus, in the cathode catalyst layer, polymer electrolyte water content is high, whereas in the anode water content is relatively low. Finally, anode and cathode gradients of electrical potential are much smaller in the solid phase than in the polymer-electrolyte phase since effective conductivity is approximately three orders of magnitude greater in the solid phase than in the polymer-electrolyte phase.

In Chapter 6, simulation results for model variables (i.e. solid phase and polymer-electrolyte phase electrical potentials and hydrogen and oxygen concentrations) generated using the CFD implementation of the PEM fuel cell model, with the multiple thin-film agglomerate model, are used to predict reaction rate distributions in catalyst layers. In general, due to polymer electrolyte drying, anode reactions change from being more concentrated under the bipolar plate at low current densities to being more concentrated under the gas channel at high current densities, and become more concentrated adjacent to the membrane and near the gas channel inlet as current density increases. Also, due to oxygen transport limitations, cathode reactions change from being more concentrated under the bipolar plate at low current densities to being more concentrated under the gas channel at high current densities. Cathode reactions also change from being more concentrated adjacent to the membrane at low current density to being more concentrated adjacent to the gas diffusion layer at high current densities, and become more concentrated near the gas channel inlet as current density increases.

In general, reaction rates are proportional to catalyst loading. In Chapter 6 the effect (on PEM fuel cell performance) of varying catalyst loading as a function of location is studied for the same overall platinum loading. The local catalyst loading in the anode or cathode is increased linearly between the values of 0 and 2.0 g m^{-2} in the positive and negative x-, y- and z-directions individually while all other parameter values are kept the same in separate CFD simulations. The results in the form of polarisation curves are compared to those for uniform catalyst loading in the anode and cathode. In general, according to the results for variable anode and cathode catalyst loading, increasing local catalyst loading in regions of more concentrated reactions yields improved fuel cell performance relative to increasing local catalyst loading in regions of less concentrated reactions. Thus, in the anode, maximum catalyst loading under the gas channel and adjacent to the membrane yields improved fuel cell performance (as current density increases) relative to maximum catalyst loading under the bipolar plate and adjacent to the gas diffusion layer. This is because ohmic resistance due to polymer electrolyte drying

(which increases as current density increases) is higher under the bipolar plate and adjacent to the gas diffusion layer. Also, in the cathode, maximum catalyst loading under the gas channel and adjacent to the gas diffusion layer yields improved fuel cell performance (as current density increases) relative to maximum catalyst loading under the bipolar plate and adjacent to the membrane. This is because concentration overpotential due to oxygen transport limitations (which increases as current density increases) is higher under the bipolar plate and adjacent to the membrane.

However, polarisation curves for maximum anode and cathode catalyst loading near the gas channel outlets are higher at high current densities than those for maximum catalyst loading near the gas channel inlets - even though reactions are more concentrated near the gas channel inlets as current density increases. Thus the effect of increased polymer electrolyte drying in the anode, and decreased oxygen concentration in the cathode, towards the gas channel outlet is not as important as might be expected. In this case, the non-uniformity of the local catalyst loading has a dominant detrimental effect. The associated beneficial effect of uniform catalyst loading is seen in the polarisation curves in general, since the polarisation curve for uniform catalyst loading is the highest at all current densities except for those cases of maximum catalyst loading adjacent to the membrane (which are the highest at low current densities). Thus, as mentioned previously, optimising platinum loading and reducing costs through better catalyst utilisation is accomplished primarily by causing the reaction regions to expand and fill the entire catalyst layers.

7.2 Improvements and Recommendations

The PEM fuel cell model presented in Chapter 3 is a fully three-dimensional, multicomponent and multiphase model. The set of equations used in the model is comprehensive, but improvements can still be made to the model by taking into account:

- Knudsen diffusion and surface migration and the Stefan-Maxwell equations for ordinary molecular diffusion for gas transport in the catalyst and gas diffusion layers. The model presented in Chapter 3 uses Fick's first law for diffusion (with effective diffusion coefficients calculated using an approximate solution to the Stefan-Maxwell equations) based on the assumption that gas transport is primarily through macropores. The inclusion of Knudsen diffusion (i.e. dusty gas, mean transport-pore or binary friction models) and surface migration is important if transport is primarily through micropores.
- Capillary pressure (i.e. Leverett J-function) and relative permeability expressions (as functions of liquid water saturation) for liquid water transport in the gas diffusion and catalyst layers which are for porous gas diffusion electrodes. The experimentally derived relationships presented in Chapter 3 are for the displacement of air by liquid water in unconsolidated sand.
- Liquid water transport in gas channels based on the experimentally observed formation of droplets on gas diffusion layer surfaces (leading to bridging and the eventual blocking of entire gas channels by plugs for large liquid water saturations, resulting in temporary failures of PEM fuel cells until the plugs are cleared) rather than as a fine mist in the gases.
- Convection and diffusion (if the concentration of protons is not constant due to swelling of polymer electrolyte) in the Nernst-Planck equation for transport of protons through polymer electrolyte. In the model presented in Chapter 3, convection and diffusion are assumed to be equal to zero, yielding Ohm's law.
- Darcy's law for viscous convection (Bernardi & Verbrugge, 1991) in the expression for liquid water transport in polymer electrolyte governed by electro-osmotic drag and Fick's first law for self-diffusion (Springer et al., 1991). In the model presented in Chapter 3, viscous convection is assumed to be equal to zero.
- Polymer-electrolyte phase electrical conductivity, electro-osmotic drag coefficient and effective Fick's self-diffusion coefficient expressions (as functions of water content (i.e. water activity) and temperature) for Nafion® 112. The experimentally derived

relationships presented in Chapter 3 are for Nafion® 117 (Springer et al., 1991; Dutta et al., 2001).

- Reaction rate expressions (as described by the Butler-Volmer equation) that include the dependence of exchange current density and transfer coefficients in the cathode on current density (Parathasarathy et al., 1992).
- Boundary conditions for the conservation of energy equation which are derived using experimental data for a PEM fuel cell.
- The actual geometry and gas flows for a PEM fuel cell with serpentine channels. Due to the substantial computational resources required in order to model such a geometry it is assumed in Chapter 5 that the performance of PEM fuel cells is reaction-dominated and that characteristics of the gas flows have only a minor effect on the results, such that corresponding stoichiometric flow rates are used in a PEM fuel cell with straight channels.
- Non-isotropic values for permeabilities, and electrical and thermal conductivities in the gas diffusion and catalyst layers (E-TEK, 2004) and conductivities in the bipolar plates (Bulk Molding Compounds Inc., 2001). Averages of these non-isotropic values are used in the model presented in Chapter 3.

These improvements are of varying importance. Transport models which take into account Knudsen diffusion, surface migration and the Stefan-Maxwell equations are relatively complicated and have not proven to be very useful as discussed in Chapter 1. Instead experimentally measured effective bulk diffusion coefficients in porous gas diffusion electrodes for use in Fick's first law (which lump together all relevant transport phenomena and include the effects of porosity and tortuosity) are of greater value. In contrast, capillary pressure and relative permeability expressions for porous gas diffusion electrodes are necessary in order to properly model the significant effect that water transport has on PEM fuel cell performance. In this regard, liquid water transport in gas channels is also important but would be difficult to model.

Considering the importance of the membrane in a PEM fuel cell, comprehensive and self-consistent models for transport processes in polymer electrolyte (that take into account convection, diffusion and migration in the expressions for both the transport of protons and liquid water) should be included in future CFD implementations. Experimentally derived relationships for the convection, diffusion and migration coefficients associated with these models should also be included in future CFD implementations. As evidenced by the discrepancies between the experimentally derived values for the cathode transfer coefficients (i.e. $\alpha_{c,c} = 1$ and $\alpha_{c,c} = 1/2$ at low and high current densities, respectively) and the value found in Chapter 5 (i.e. $\alpha_{c,c} = 2$), including the dependence of cathode transfer coefficients (and exchange current density) on current density in the Butler-Volmer equation is also of importance. The actual geometry, gas flows and thermal boundary conditions for PEM fuel cells should be modelled since the characteristics of complicated gas flows, and especially the thermal boundary conditions, could have large effects on fuel cell performance. Finally, although non-isotropic values of permeabilities, and solid phase electrical and thermal conductivities, would have only minor effects for the PEM fuel cell design presented in Chapter 3 (which is dominated by diffusion and polymer-electrolyte phase electrical conductivity, and is essentially isothermal - according to the results presented in Chapter 5), they could have more significant effects for different fuel cell designs.

In this thesis, a comprehensive three-dimensional, multicomponent and multiphase model of the transport processes and reactions in PEM fuel cells has been presented. The model has been further improved by taking into account the detailed composition and structure of the catalyst layers using a multiple thin-film agglomerate model. Both models have been implemented in the FLUENT™ PEMFC software package (Fluent Inc., 2001; Li & Becker, 2004). In general, simulation results for model variables generated using the CFD implementation of the PEM fuel cell model, with the multiple thin-film agglomerate model, confirm the capability of the CFD simulations to accurately predict detailed results. Experimental PEM fuel cell results (Wang et al., 2003) in the form of polarisation curves

can also be accurately matched with CFD simulation results. Further, the predictive capabilities of the CFD simulations are tested for variable operating conditions, and it is found that numerical accuracy of predicted simulation results versus experimental results decreases as changes in operating conditions increase, but that simulation results qualitatively predict experimental trends. Thus, for changes in model parameters the CFD simulation results should be qualitatively accurate, successfully predicting general trends.

In this thesis available data on catalyst layer composition and structure are used in CFD simulations. According to the simulation results, the transport limitations associated with the low concentration of oxygen in air and the restriction of the porous media to gas transport (due to the presence of liquid water in the cathode gas diffusion and catalyst layers) have substantial negative effects on PEM fuel cell performance. For the multiple thin-film agglomerate model, it is also found that the presence of the thin film of polymer electrolyte has a substantial negative effect on PEM fuel cell performance. These results confirm that agglomerate models for PEM fuel cell catalyst layers are more appropriate than macro-homogeneous models. Finally, variations in local catalyst loading are implemented in the CFD simulations for a given precious metal loading. In general, the results show that uniform catalyst loading provides the best fuel cell performance, since the polarisation curve for uniform catalyst loading is the highest at all current densities except for those cases of maximum catalyst loading adjacent to the membrane (which are the highest at low current densities).

In general, the performance of PEM fuel cells depends on the composition and structure of the catalyst layers. Thus, improving the performance of PEM fuel cells depends on the optimisation of catalyst layer composition and structure. Future CFD simulations should therefore continue to investigate the effects of varying parameters associated with catalyst layer composition and structure. Parameters can be uniform or vary as a function of location for the same overall value (as done for catalyst loading in Chapter 6) and the overall value can also be changed. Maximum fuel cell performance should be achieved for specific compositional and structural parameter values, although

these optimal values will change with current density. The optimal values should also change depending on operating conditions such as gas pressure, temperature, humidification and flow rates.

State-of-the-art PEM fuel cell catalyst layers are primarily composed of platinum, carbon and polymer electrolyte, and therefore the contents of these compositional parameters should be varied to investigate their effects on the performance of PEM fuel cells. In general, both increased platinum loading and polymer electrolyte content reduce activation overpotential through larger active surfaces and faster reaction kinetics. Both increased carbon loading and polymer electrolyte content reduce ohmic overpotential through larger effective electrical conductivities. Structural parameters that should be varied to investigate their effects on the performance of PEM fuel cells include porosity and tortuosity. Concentration overpotential decreases for increasing porosity and decreasing tortuosity through larger effective diffusion coefficients and shorter transport path lengths, respectively. Note that the effect of a 0.1 increase in porosity in the gas diffusion and catalyst layers has already been investigated in Chapter 5. Finally, the effect of catalyst layer thickness on the performance of PEM fuel cells should also be investigated, since both ohmic and concentration overpotentials increase (i.e. longer conduction and transport path lengths, respectively) while activation overpotential decreases (i.e. larger active surfaces) for increasing thickness.

In general, the compositional and structural parameters and the thickness of the catalyst layers are all strongly interrelated and this interdependence must be considered when varying parameters. Thus, although a full parametric study of the effects of catalyst layer composition and structure can be performed using the CFD implementation of the PEM fuel cell model, with the multiple thin-film agglomerate model, more work is required. Finally, an actual optimisation of composition and structure for maximum PEM fuel cell performance based on CFD simulations, although feasible, would require substantial computational resources.

References

J. C. Amphlett, R. M. Baumert, R. F. Mann, B. A. Peppley, P. R. Roberge, T. J. Harris, Journal of the Electrochemical Society 142 (1995) 1.

A. J. Bard, L. R. Faulkner, Electrochemical Methods: Fundamentals and Applications, 2nd Ed., Wiley, New York, 2001.

J. J. Baschuk, X. Li, Journal of Power Sources 86 (2000) 181.

D. M. Bernardi, M. W. Verbrugge, American Institute of Chemical Engineers Journal 37 (1991) 1151.

D. M. Bernardi, M. W. Verbrugge, Journal of the Electrochemical Society 139 (1992) 2477.

T. Berning, D. M. Lu, N. Djilali, Journal of Power Sources 106 (2002) 284.

D. Bevers, M. Wohr, K. Yasuda, K. Oguro, Journal of Applied Electrochemistry 27 (1997) 1254.

R. B. Bird, W. E. Stewart, E. N. Lightfoot, Transport Phenomena, 2nd Ed., Wiley, New York, 2002.

J. O' M. Bockris, S. U. M. Khan, Surface Electrochemistry: A Molecular Level Approach, Plenum, New York, 1993.

K. Broka, P. Ekdunge, Journal of Applied Electrochemistry 27 (1997) 281.

Bulk Molding Compounds Inc., Typical Data - BMC 940, Chicago, 2001.

P. Capek, A. Seidel-Morgenstern, Applied Catalysis A: General 211 (2001) 227.

M. W. Chase, C. A. Davies, J. R. Downey, D. J. Frurip, R. A. McDonald, A. N. Syverud, JANAF Thermochemical Tables, 3rd Ed., American Institute of Physics, New York, 1986.

X. Cheng, B. Yi, M. Han, J. Zhang, Y. Qiao, J. Yu, Journal of Power Sources 79 (1999) 75.

P. Costamagna, Chemical Engineering Science 56 (2001) 323.

P. Costamagna, S. Srinivasan, Journal of Power Sources 102 (2001a) 242.

P. Costamagna, S. Srinivasan, Journal of Power Sources 102 (2001b) 253.

M. J. Croissant, T. Napporn, J.-M. Leger, C. Lamy, Electrochimica Acta 43 (1998) 2447.

E. L. Cussler, Diffusion - Mass Transfer in Fluid Systems, 2nd Ed., Cambridge University Press, Cambridge, 1997.

R. E. De La Rue, C. W. Tobias, Journal of the Electrochemical Society 106 (1959) 827.

N. Djilali, D. M. Lu, International Journal of Thermal Sciences 41 (2002) 29.

DuPont (E. I.) de Nemours and Company, Nafion® PFSA Membranes: Product Information, Wilmington, DE, 2004.

S. Dutta, S. Shimpalee, J. W. Van Zee, Journal of Applied Electrochemistry 30 (2000) 135.

S. Dutta, S. Shimpalee, J. W. Van Zee, International Journal of Heat and Mass Transfer 44 (2001) 2029.

B. M. Eaton, One Dimensional, Transient Model of Heat, Mass, and Charge Transfer in a Proton Exchange Membrane, M.Sc. Thesis, Virginia Polytechnic Institute and State University, Blacksburg, 2001.

M. Eikerling, A. A. Kornyshev, Journal of Electroanalytical Chemistry 453 (1998) 89.

N. Epstein, Chemical Engineering Science 44 (1989) 777.

S. Escribano, P. Aldebert, Solid State Ionics 77 (1995) 318.

E-TEK division of De Nora North America Inc., Commercial Product Catalog, Somerset, NJ, 2004.

J. Fimrite, Transport Phenomena in Polymer Electrolyte Membranes, M.A.Sc. Thesis, University of Victoria, 2004.

A. Fischer, J. Jindra, H. Wendt, Journal of Applied Electrochemistry 28 (1998) 277.

J. B. Floriano, E. A. Ticianelli, E. R. Gonzalez, Journal of Electroanalytical Chemistry 367 (1994) 157.

Fluent Inc., FLUENT 6.1 User's Guide and UDF Manual, Lebanon, NH, 2001.

T. F. Fuller, J. Newman, Journal of the Electrochemical Society 140 (1993) 1218.

J. Giner, C. Hunter, Journal of the Electrochemical Society 116 (1969) 1124.

L. Giorgi, E. Antolini, A. Pozio, E. Passalacqua, Electrochimica Acta 43 (1998) 3675.

F. Gloaguen, R. Durand, Journal of Applied Electrochemistry 27 (1997) 1029.

F. Gloaguen, P. Convert, S. Gamburzev, O. A. Velev, S. Srinivasan, Electrochimica Acta 43 (1998) 3767.

S. Gottesfeld, J. Pafford, Journal of the Electrochemical Society 135 (1988) 2651.

V. Gurau, H. Liu, S. Kakac, American Institute of Chemical Engineers Journal 44 (1998) 2410.

W. He, J. S. Yi, T. V. Nguyen, American Institute of Chemical Engineers Journal 46 (2000) 2053.

D. M. Himmelblau, Chemical Reviews 64 (1964) 527.

J. T. Hinatsu, M. Mizuhata, H. Takenaka, Journal of the Electrochemical Society 141 (1994) 1493.

R. P. Iczkowski, M. B. Cutlip, Journal of the Electrochemical Society 127 (1980) 1433.

B. Jahne, G. Heinz, W. Dietrich, Journal of Geophysical Research 92 (1987) 10767.

J. Jiang, A. Kucernak, Journal of Electroanalytical Chemistry 567 (2004) 123.

S. Kakac, R. K. Shah, W. Aung, Handbook of Single-Phase Convective Heat Transfer, Wiley, New York, 1987.

M. Kaviany, Principles of Heat Transfer in Porous Media, 2nd Ed., Springer-Verlag, New York, 1995.

A. A. Kulikovsky, J. Divisek, A. A. Kornyshev, Journal of the Electrochemical Society 146 (1999) 3981.

A. A. Kulikovsky, Electrochemistry Communications 4 (2002a) 318.

A. A. Kulikovsky, Electrochemistry Communications 4 (2002b) 845.

G. S. Kumar, M. Raja, S. Parthasarathy, Electrochimica Acta 40 (1995) 285.

M. J. Lampinen, M. Fomino, Journal of the Electrochemical Society 140 (1993) 3537.

J. Larminie, A. Dicks, Fuel Cell Systems Explained, Wiley, New York, 2000.

S. Li, U. Becker, A Three Dimensional CFD Model for PEMFC, Fluent Inc., Lebanon, NH, 2004.

D. R. Lide, Ed. in Chief, CRC Handbook of Chemistry and Physics, 84th Ed., CRC Press, Boca Raton, FL, 2003.

P. J. Linstrom, W. G. Mallard, Eds., NIST Standard Reference Database Number 69, National Institute of Standards and Technology, Gaithersburg, MD, 2003.

V. Mehta, J. S. Cooper, Journal of Power Sources 114 (2003) 32.

R. M. Q. Mello, E. A. Ticianelli, Electrochimica Acta 42 (1997) 1031.

J. H. Nam, M. Kaviany, International Journal of Heat and Mass Transfer 46 (2003) 4595.

D. Natarajan, T. V. Nguyen, Journal of the Electrochemical Society 148 (2001) A1324.

D. Natarajan, T. V. Nguyen, Journal of Power Sources 115 (2003) 66.

J. S. Newman, C. W. Tobias, Journal of the Electrochemical Society 109 (1962) 1183.

T. V. Nguyen, R. E. White, Journal of the Electrochemical Society 140 (1993) 2178.

D. A. Nield, A. Bejan, Convection in Porous Media, Springer-Verlag, New York, 1992.

H.-F. Oetjen, V. M. Schmidt, U. Stimming, F. Trila, Journal of the Electrochemical Society 143 (1996) 3838.

A. A. M. Oliveira, M. Kaviany, Progress in Energy and Combustion Science 27 (2001) 523.

A. Parathasarathy, S. Srinivasan, A. J. Appleby, C. R. Martin, Journal of the Electrochemical Society 139 (1992) 2530.

J. M. Prausnitz, R. N. Lichtenthaler, E. G. de Azevedo, Molecular Themodynamics of Fluid-Phase Equilibria, 2nd Ed., Prentice-Hall, Englewood Cliffs, CA, 1986.

Y. W. Rho, S. Srinivasan, Y. T. Kho, Journal of the Electrochemical Society 141 (1994) 2089.

S. J. Ridge, R. E. White, Y. Tsou, R. N. Beaver, G. A. Eisman, Journal of the Electrochemical Society 136 (1989) 1902.

G. Sasikumar, J. W. Ihm, H. Ryu, Journal of Power Sources 132 (2004) 11.

T. J. Schmidt, H. A. Gasteiger, R. J. Behm, Journal of the Electrochemical Society 146 (1999) 1296.

D. B. Sepa, M. V. Vojnovic, A. Damjanovic, Electrochimica Acta 26 (1981) 781.

S. Shimpalee, S. Dutta, Numerical Heat Transfer Part A: Applications 38 (2000) 111.

N. P. Siegel, M. W. Ellis, D. J. Nelson, M. R. von Spakovsky, Journal of Power Sources 115 (2003) 81.

D. Singh, D. M. Lu, N. Djilali, International Journal of Engineering Science 37 (1999) 431.

B. R. Sivertsen, CFD-Based Modelling of Proton Exchange Membrane Fuel Cells, M.Sc. Thesis, Norwegian University of Science and Technology, Trondheim, 2003.

T. E. Springer, T. A. Zawodzinski, S. Gottesfeld, Journal of the Electrochemical Society 138 (1991) 2334.

T. E. Springer, M. S. Wilson, S. Gottesfeld, Journal of the Electrochemical Society 140 (1993) 3513.

J. M. Stockie, K. Promislow, B. R. Wetton, International Journal for Numerical Methods in Fluids 41 (2003) 577.

R. Taylor, R. Krishna, Multicomponent Mass Transfer, Wiley, New York, 1993.

E. A. Ticianelli, C. R. Derouin, S. Srinivasan, Journal of Electroanalytical Chemistry 251 (1988a) 275.

E. A. Ticianelli, C. R. Derouin, A. Redondo, S. Srinivasan, Journal of the Electrochemical Society 135 (1988b) 2209.

E. A. Ticianelli, J. G. Beery, S. Srinivasan, Journal of Applied Electrochemistry 21 (1991) 597.

Toray Industries Inc., Toray Carbon Fiber Paper TGP-H: Basic Data, Tokyo, 2004.

M. Uchida, Y. Aoyama, N. Eda, A. Ohta, Journal of the Electrochemical Society 142 (1995) 4143.

M. Uchida, Y. Fukuoka, Y. Sugawara, N. Eda, A. Ohta, Journal of the Electrochemical Society 143 (1996) 2245.

S. Um, C.-Y. Wang, K. S. Chen, Journal of the Electrochemical Society 147 (2000) 4485.

J. W. Veldsink, R. M. J. van Damme, G. F. Versteeg, W. P. M. van Swaaij, Chemical Engineering Journal 57 (1995) 115.

L. Wang, A. Husar, T. Zhou, H. Liu, International Journal of Hydrogen Energy 28 (2003) 1263.

Z. H. Wang, C.-Y. Wang, K. S. Chen, Journal of Power Sources 94 (2001) 40.

A. C. West, T. F. Fuller, Journal of Applied Electrochemistry 26 (1996) 557.

F. M. White, Fluid Mechanics, 4th Ed., McGraw-Hill, New York, 1999.

M. S. Wilson, J. A. Valerio, S. Gottesfeld, Electrochimica Acta 40 (1995) 355.

M. Wohr, K. Bolwin, W. Schnurnberger, M. Fischer, W. Neubrand, G. Eigenberger, International Journal of Hydrogen Energy 23 (1998) 213.

R. S. Yeo, J. McBreen, Journal of the Electrochemical Society 126 (1979) 1682.

J. S. Yi, T. V. Nguyen, Journal of the Electrochemical Society 145 (1998) 1149.

J. S. Yi, T. V. Nguyen, Journal of the Electrochemical Society 146 (1999) 38.

L. You, H. Liu, International Journal of Hydrogen Energy 26 (2001) 991.

L. You, H. Liu, International Journal of Heat and Mass Transfer 45 (2002) 2277.

Appendix A

List of Parameters

	Parameter	Value
Bipolar Plates	Density of solid, ρ_s	1.8×10^3 kg m^{-3}
	Effective electrical conductivity, σ_s^{eff}	7.5×10^3 S m^{-1}
	Specific heat of solid, $c_{P,s}$	9.4×10^2 J (kg K)$^{-1}$
	Thermal conductivity of solid, k_s	31.5 W (m K)$^{-1}$
Catalyst/Gas Diffusion Layers	Density of solid, ρ_s	1.8×10^3 kg m^{-3}
	Effective electrical conductivity, σ_s^{eff}	1.8×10^3 S m^{-1}
	Porosity of catalyst layers, φ_{cl}	0.25/0.35
	Porosity of gas diffusion layers, φ_{gdl}	0.40/0.50
	Permeability, κ	1.45×10^{-11} m^2
	Specific heat of solid, $c_{P,s}$	7.1×10^2 J (kg K)$^{-1}$
	Thermal conductivity of solid, k_s	12 W (m K)$^{-1}$
	Volumetric fraction of carbon in gas diffusion layers and carbon and	0.40

	platinum in catalyst layers, $\varphi_{C/Pt}$	
	Volumetric fraction of polymer electrolyte in catalyst layers, φ_m	0.25
Constants	Faraday's constant, F	9.6485×10^7 C kmol^{-1}
	Gas constant, R	8314.3 J (kmol K)$^{-1}$
Dimensions	Length of gas channels, l_{gc}	7×10^{-2} m
	Side dimensions of gas channels, d_{gc}	1×10^{-3} m
	Superficial area of MEA, s_{mea}	7×10^{-5} m^2
	Thickness of gas diffusion layers, t_{gdl}	2.6×10^{-4} m
	Thickness of catalyst layers, t_{cl}	1.29×10^{-5} m
	Thickness of membrane, t_m	5.1×10^{-5} m
Electrochemistry	Active surface area per unit volume in catalyst layers, ξ	4.50×10^6 m^{-1}
	Anodic transfer coefficient in anode catalyst layer, $\alpha_{a,a}$	2
	Anodic transfer coefficient in cathode catalyst layer, $\alpha_{a,c}$	2
	Cathodic transfer coefficient in anode catalyst layer, $\alpha_{c,a}$	0
	Cathodic transfer coefficient in cathode catalyst layer, $\alpha_{c,c}$	2
	Exponent of hydrogen concentration in anodic exchange current density, b_{H_2}	1/2
	Exponent of oxygen concentration in	1

	cathodic exchange current density, b_{O_2}	
	Open-circuit potential, V_{oc}	1.12 V
Gas Channel Inlets	Liquid water saturation, s	0
	Mass flow rate at anode, Q_a	4.90×10^{-8} kg s^{-1}
	Mass flow rate at cathode, Q_c	6.82×10^{-7} kg s^{-1}
	Mass fraction of water vapour at anode, $y_{H_2O,a}$	0.505
	Mass fraction of hydrogen, y_{H_2}	0.495
	Mass fraction of water vapour at cathode, $y_{H_2O,c}$	0.066
	Mass fraction of oxygen, y_{O_2}	0.218
	Mass fraction of nitrogen, y_{N_2}	0.716
	Nitrogen/oxygen mole ratio, x_{N_2}/x_{O_2}	0.79/0.21
	Operating pressure, P	303,975 Pa
	Operating temperature, T	343.15 K
	Relative humidity, RH	100 %
	Stoichiometric flow rate at anode, ζ_a	3.32
	Stoichiometric flow rate at cathode, ζ_c	2.56
Heat	Change in Gibbs free energy of formation in Reaction (1.3) at operating temperature and reference pressure, $\Delta \bar{g}_f^\circ$	-4.530×10^8 J kmol^{-1}
	Change in enthalpy of formation in Reaction (1.3) at operating temperature and pressure, $\Delta \bar{h}_f^\circ$	-4.846×10^8 J kmol^{-1}

	Fraction of change in enthalpy of formation in Reaction (1.3) released as heat in cathode catalyst layer, β	0.11
	Latent heat of vaporisation per unit mass of water at operating temperature and saturation pressure, h_{wg}	2.333×10^{6} J kg^{-1}
Membrane	Density of dry polymer electrolyte, ρ_{dry}	1980 kg m^{-3}
	Equivalent weight of dry polymer electrolyte, M_{dry}	1100 kg kmol^{-1}
	Specific heat of solid, $c_{P,s}$	1172 J (kg K)$^{-1}$
	Thermal conductivity of solid, k_s	0.36 W (m K)$^{-1}$
Multiphase	Contact angle, θ	120°
	Density of liquid water at operating temperature and pressure, ρ_w	977.9 kg m^{-3}
	Surface tension, γ	0.0644 N m^{-1}
	Viscosity of liquid water at operating temperature and pressure, μ_w	4.04×10^{-4} kg (m s)$^{-1}$
Transport	Binary diffusion coefficient at reference state, $\mathcal{D}^{\circ}_{H_2-H_2O}$	8.79×10^{-5} m^2 s^{-1}
	Binary diffusion coefficient at reference state, $\mathcal{D}^{\circ}_{H_2O-O_2}$	2.64×10^{-5} m^2 s^{-1}
	Binary diffusion coefficient at reference state, $\mathcal{D}^{\circ}_{H_2O-N_2}$	2.64×10^{-5} m^2 s^{-1}
	Binary diffusion coefficient at reference	2.07×10^{-5} m^2 s^{-1}

state, $\mathcal{D}^{\circ}_{O_2-N_2}$	
Concentration of liquid water at operating temperature and pressure, c_w	54.28 kmol m^{-3}
Exponent of porosity in effective diffusion coefficients for catalyst/gas diffusion layers, a	1.0/1.5
Exponent of gas saturation in effective diffusion coefficients, b	1.5
Henry's law constant for the solubility of hydrogen in liquid water, $H_{H_2,w}$	7.60×10^9 Pa
Henry's law constant for the solubility of oxygen in liquid water, $H_{O_2,w}$	6.66×10^9 Pa